

UNIVERSITAT DE VALÈNCIA

Departament d'Astronomia i Astrofísica

**Linear and non-linear
Kelvin-Helmholtz instabilities in
relativistic flows**

Application to extragalactic jets



UNIVERSITAT DE VALÈNCIA

**TESI DOCTORAL
PRESENTADA PER**

Manuel Perucho Pla

2005

José María Martí Puig, Professor Titular del Departament d'Astronomia i Astrofísica de la Universitat de València,

CERTIFICA:

Que la present memòria: **Linear and non-linear Kelvin-Helmholtz instabilities in relativistic flows, Application to extragalactic jets**, ha estat realitzada, sota la meua direcció, per **D. Manuel Perucho Pla**, i que constitueix la seua Tesi Doctoral per optar al grau de Doctor en Física.

I perquè en prengueu coneixement i tinga els efectes que corresponguen, signe el present certificat en Burjassot, a vint-i-dos de Febrer de 2005.

Signat: José María Martí Puig

Als meus pares i a Desirée

*Déu meu, com és de bell el riu en aquest llit,
Més delitós per beure que els llavis de donzella.
Sembla una polsera, amb flors a les vores
Talment la Via Làctia. És cristal·lí
Com un fil d'argent sobre una túnica verda.
Pestanyes en un ull blau, el brancatge
que el voreja entre carícies de brisa.
L'or del crepuscle rellisca damunt l'aigua platejada.
Quantes vegades, Déu meu, a la vora d'aquest riu
he convidat a un vi clar els meus estimats companys.*
Ibn Kafaja (sobre el Xúquer al seu pas per Alzira, any 1100)

*Jo em meravell com no es veu qui ulls ha
e cell qui ou per què no vol entendre
e qui no sap per què no vol aprendre
e cell qui pot e sap com bé no fa.*
Pere March

I no obstant, es mou.
Galileu Galilei

*Ha d'ésser possible
viure en dignitat.
Han d'ésser possibles
vents de llibertat.*
Vicent Andrés Estellés

*El Cosmos és tot el que és, el que va ser i el que serà en algún moment.
Les nostres contemplacions més tèbies de l'Univers ens commouen,
un calfred recorre la nostra espina dorsal, la veu se'ns quebra,
hi ha una sensació dèbil, com la d'un record llunyà o la de caure des de l'alt.
Sabem que ens estem apropant al major dels misteris.*
Carl Sagan

Agraïments

En primer lloc, vull donar les gràcies al meu director, per la seua paciència, per tractar-me com un amic, escoltar-me i ajudar-me quan ho necessitava, renyir-me quan no feia les coses com el mètode científic mana, i ensenyar-me a ser pacient (açò darrer no sé si ho ha aconseguit). Vull agrair-li especialment la dedicació dels últims dies a la finalització de la correcció de la memòria. Aquest treball és també seu.

Vull agrair a Michał la seua col·laboració i ajuda, ànims i hospitalitat. Moltes de les idees en les que es fonamenta aquest treball són seues. *Dziękuję, Michał.*

També han participat en un moment o altre una sèrie de persones que, desinteressadament, han estat clau del resultat. Jose, sempre disposat a ajudar-te, Miguel Ángel, amb l'ajuda de qui vaig programar el codi en tres dimensions i que m'ha pegat les *perolades* més grans (però interessants) d'aquestos anys, Andrei, amb qui he estat col·laborant en els últims mesos, m'ha ajudat pacientment en la sol·licitud de contractes... i amb qui m'ho vaig passar molt bé veient l'eurocopa i bebent vodka a sa casa (més pel vodka que pel futbol, és clar), Arnau, qui em va ajudar a entendre el mètode de Muller, Leo Scheck, que em va enviar les rutines de l'equació d'estat per gasos relativistes, Nicolás Pardo García, un xicot del politècnic al qual ni tan sols conec i qui em va enviar unes rutines per calcular les funcions de Bessel en variable complexa que ell havia desenvolupat. I, especialment Joan Antoni, a qui li vaig plantejar el problema més gros que hem patit al llarg d'aquestos quatre anys i la següent cosa que vaig saber d'ell és que l'havia resolt, Luís i Pablo, amb la seua ajuda numèrico-militar en la desesperació dels *Not a Number* i els *Arithmetic overflow*, Iván, per la seua hospitalitat, ànims i amistat, i Vicent, el meu *supervisor* (literalment) en temes de programació, i amic. A tots aquests genis, gràcies.

A José María, li vull agrair el fer tot el que pot, o li deixen, per nosaltres, per a que seguim amb il·lusió i, sobre tot, amb una faena pagada... En un

ambient (el científic) ple de gent que només busca i vol reconeixement i glòria (diners no hi ha), trobar una persona que partint de no res ha fet un grup respectat arreu del Món i no se'n vanaglòria és un autèntic plaer, malauradament no molt comú.

A Arturo (quasi-company de despatx), li done les gràcies per les pelis i els jocs. A Toni, per la música. A Ramon, per totes les coses que ens ensenya. A Pepe i Joan per les converses dels dinars. A Joan Antoni Morales, perquè som del València. Al personal d'administració del departament, Manel i Emi, per la seua eficiència. A Enric, per l'ajuda informàtica que m'ha donat. Al personal del Servei d'Informàtica per mantindre les màquines que s'han usat per realitzar els càlculs d'aquest treball: Tiberio i Cerca.

Als meus amics, Carlos, Chelo, David, Edu, Esteban, Emilio, Franz, Jean-Marie, Jorge, Juamba, Trini, Yannick, Yasmín i resta d'amics, els done les gràcies pels moments i l'amor. A la família de Desirée, vull agrair-los l'afecte i la seua ajuda en el nostre pis mentre jo estava enfeinat escrivint açò.

L'any passat ens va deixar mon tio, un dels principals *culpables* d'aquest treball, potser qui em va obrir els ulls a l'Univers (i des d'aleshores encara no he parat d'obrir-los i meravellar-me). M'haguera agradat que haguera tingut a les mans aquest treball. A la seua memòria el dedique, i també a la dels meus avis (Paco, Lola, Vicenta i Manolo), als quals de segur els haguera fet il·lusió veure com el seu net es doctorava. Tampoc no vull oblidar Homer, l'únic *germà* que he tingut i que sempre tindrà un lloc al meu cor. Vull dedicar també una part del meu esforç als meus cosins i tíos que sempre han estat prop, i molt especialment a Paco.

Per últim, agraisc als meus pares, als quals dedique aquest treball, el deixar-me pensar lliurement, un tresor que ja mai es pot furta, aguantar el meu mal geni, i haver-me recolçat en aquesta aventura que sembla, de vegades, absurda, però que no puc evitar seguir (com va dir un dia Ramon quan li vaig preguntar, parlant de la seua afició a la música, si seria músic si tornara a nàixer: "No, jo seria físic"). Ah! i pel saxo!

I per a Desi, el meu amor, qui ha suportat els meus nervis, m'ha recolçat i ha estat sempre al meu costat, només vull transcriure per a ella una dedicatòria de Carl Sagan a la seua dona: *en la vastitud de l'espai i la immensitat del temps, la meua alegria és compartir un planeta i una època amb tu.*

Per un Xúquer i una Albufera vius. A tots, GRÀCIES.

RESUM

Introducció

Aquest treball de tesi doctoral es centra en un fenomen particular (dolls relativistes) dins d'un més general conegut com AGN (acrònim de l'anglès *Active Galactic Nuclei*). Aquest darrer és un dels processos més energètics de l'Univers, en el que es posen en joc energies de fins a 10^{47} erg/s al llarg d'escala de temps cosmològiques, i amb emissió en tot l'espectre electromagnètic. Al llarg dels anys 40 i 50 del passat segle van ser trobades diverses fonts d'aparença estel·lar amb forta emissió en freqüències de ràdio, cosa poc típica dels estels. Descoberta la seua naturalesa extragalàctica quan Maarten Schmidt va mesurar el corriment al roig de les línies d'hidrogen al quàsar 3C 273, es va obrir el debat sobre quin tipus de procés físic podria generar semblant quantitat d'energia. A més, estudiant la variabilitat en l'emissió, hom podia saber que la regió on es produïra aquesta devia ser molt menuda (menys de 100 pc). Eddington va proposar el model més acceptat hui dia respecte a l'origen d'aquesta radiació, explicant-la com emesa per la matèria que cau per atracció gravitatòria en un objecte central. Fent uns senzills càlculs per trobar la massa de l'objecte capaç d'acretar la quantitat de matèria suficient per explicar la radiació emesa, es troba que deu ser d'al voltant de $10^8 M_{\odot}$.

La teoria estàndard ens presenta el fenomen AGN com el procés d'emissió de radiació per part de les partícules que cauen en un forat negre supermassiu (*Supermassive Black Hole*, SMBH) al centre de la galàxia activa. La matèria forma un disc, conegut com disc d'acreció, al voltant del forat i, al seu temps, el disc es troba rodejat per un torus de matèria que l'alimenta. L'existència de diferents famílies de galàxies actives s'associa al punt de vista de l'observador respecte a aquest torus, depenent de si ens amaga les regions centrals o no, a

més de la potència intrínseca de la font.

En un subgrup dels AGN, s'observen ejeccions de matèria sorgint de la regió activa. Aquestes ejeccions (dolls) emeten radiació sincrotró principalment en freqüències de ràdio, i són observats amb tècniques interferomètriques (per exemple, *Very Long Baseline Interferometry*, VLBI, en les escales del pàrsec, o *Very Large Array*, VLA, en les escales del kilopàrsec). No obstant l'emissió es produeix també en l'òptic, i, per radiació Compton inversa, en raigs X i raigs gamma, els més energètics de l'espectre electromagnètic. Gràcies a diferents evidències observacionals i a l'elevada precisió de les mesures interferomètriques sabem que les estructures en aquests dolls es mouen a velocitats properes a la de la llum (o relativistes).

El fenomen doll no només està associat als AGN, sinó que és molt general a l'Univers, i ocorre allà on es puga trobar un disc d'acreció al voltant d'un objecte massiu central. Aquest escenari és el que trobem en situacions tan diferents com un estel en formació, una binària de raigs X, o també en un estel en col·lapse. Evidentment les propietats dels dolls canvien radicalment d'uns a altres, en velocitats (de centenars de quilòmetres per segon als primers a velocitats properes a la de la llum als darrers o als AGN) i composició (de mol·lècules i àtoms als estels en formació a electrons, positrons i protons als dolls dels AGN). La formació està motivada per processos magnetohidrodinàmics encara no del tot ben entesos. La seua generalitat junt amb el desconeixement que encara existeix respecte a la física fonamental que impliquen fa d'aquest camp un dels més interessants de l'Astrofísica actual.

Els dolls en AGNs viatgen al llarg de centenars de milers de parsecs, portant grans quantitats de matèria i energia cap al medi intergalàctic durant escales de temps cosmològiques. Presenten estructures semblants en escales de pàrsec i kilopàrsec, amb components d'emissió en moviment, o components estacionàries. Les primeres són generalment superlumíniques en escales del pàrsec degut a les velocitats ultrarelativistes amb que es mouen, combinades amb un angle menut amb la direcció d'observació. Les components s'associen a ones de xoc o a pertorbacions propagant-se al llarg dels dolls. Pel que fa a les escales del kilopàrsec, els dolls es classifiquen, segons la seua morfologia, en fonts FRI (més difuses a gran escala) i FRII (més col·limades i amb emissió més intensa en les regions externes).

Les estructures i inhomogeneïtats observades i les propietats d'estabilitat a llarg terme han estat associades des d'els anys 70 (Turland i Scheuer 1976, Blandford i Pringle 1976) a les inestabilitats Kelvin-Helmholtz, que es desenvolupen en la superfície de contacte entre dos fluids amb velocitat relativa. Des d'aleshores la teoria lineal d'inestabilitats Kelvin-Helmholtz (KH) per a fluids relativistes ha estat desenvolupada i estudiada en diferents situacions (e.g., Ferrari et al. 1978, Payne and Cohn 1985, Birkinshaw 1991a,b, Hardee 1987, Hardee et al. 1998, Hardee 2000). En el domini dels fluids relativistes, les conclusions principals d'aquests treballs ens diuen que els dolls amb temperatures més altes i velocitats menors desenvolupen les inestabilitats més ràpidament, amb el que es dedueix que són més inestables, contràriament als més ràpids i freds, amb ritmes de creixement més baixos. També es conclou que si la transició entre el doll i el medi ambient és continua, els ritmes de creixement dels modes tendeixen a ser més menuts que en el cas on la transició siga discontinua. Les inestabilitats KH, segons la seua geometria, generen estructures simètriques (successives expansions i contraccions del doll), helicoidals, el·líptiques, triangulars, etc. Cadascuna d'aquestes geometries inclou un nombre infinit de modes, depenent de la longitud d'ona transversal, el mode *fonamental* sense cap zero en l'ona entre l'eix i la superfície, i els modes de *reflexió*, que presenten estructura transversal amb zeros, el nombre dels quals ens dona l'ordre del mode. Respecte al règim no lineal, els treballs d'estudi sobre l'efecte de les inestabilitats KH en els dolls han estat bàsicament realitzats en el règim subrelativista (e.g., Norman i Hardee 1988, Hardee i Norman 1988, Bodo et al. 1994, 1995) fins 1998, quan van aparèixer les primeres publicacions aplicant els coneixements en teoria lineal a simulacions de dolls relativistes (Hardee et al. 1998, Rosen et al. 1999). Les conclusions derivades d'aquests treballs van concloure que els dolls més ràpids i amb majors energies internes són més estables, contràriament al que prediu la teoria lineal.

L'estabilitat dels fluids relativistes pot donar llum a alguns dels problemes que la física dels dolls extragalàctics ens planteja, com la dicotomia FRI/FRII o les estructures dels dolls en escales del pàrsec. Per altra banda, encara que s'entenen parcialment una sèrie de fenòmens associats a aquests objectes, encara no ha aparegut una imatge conjunta dels processos que hi tenen lloc. El nostre objectiu últim és entendre què ocorre en un doll relativista, què hi ha darrere de la seua emissió i quines són les seues propietats i paràmetres.

Aquesta tesi doctoral es centra en l'estabilitat dels dolls, un dels aspectes fonamentals en aquest camp, com hem dit abans. Altres aspectes com l'acceleració de partícules, l'emissió en altes energies o la composició seran afegits en el futur.

Així doncs, en aquest treball s'ha aprofundit en l'estudi de l'efecte de les inestabilitats KH en dolls relativistes. Mitjançant l'ús d'un codi numèric que descriurem al llarg de la memòria, hem estat capaços de seguir el creixement de pertorbacions des de la fase lineal (çò és, quan les pertorbacions són petites), comprovant que els nostres càlculs estan d'acord amb les prediccions teòriques, fins el règim no lineal (on les pertorbacions són grans comparades amb els valors d'equilibri inicial). El règim no lineal inclou la física que escapa a un tractament analític, amb processos turbulents i caòtics que fan necessària la utilització de codis numèrics per a realitzar els càlculs amb ordinadors.

El treball consta de dues parts, una primera dedicada a un estudi general de les inestabilitats KH en fluids relativistes, i una segona en la que hem començat a plantejar-nos situacions astrofísiques reals, fent ús de l'experiència acumulada en l'evolució lineal i no lineal de les inestabilitats.

Estabilitat (transició discontinua)

Amb la fi d'estudiar la influència dels paràmetres dels dolls relativistes en la seua estabilitat a llarg terme, hem realitzat simulacions per a diferents factors de Lorentz i energies internes (temperatures) dels mateixos, considerant-los separats del medi per una discontinuïtat, la situació teòrica més estudiada en el règim lineal.

En el capítol corresponent, i en primer lloc, presentem el desenvolupament de la teoria lineal en el cas conegut com *vortex sheet*, és a dir, quan el doll i el medi ambient es troben separats per una discontinuïtat en velocitat i densitat. Es considera que el sistema doll/medi es troba en equilibri de pressions i s'estudia l'efecte d'una petita pertorbació en el sistema. La pertorbació de les equacions ens porta a equacions d'ones (de propagació de la pertorbació) en el doll i el medi, que, adequadament empalmades en la superfície de contacte, resulten en una relació de dispersió que relaciona la freqüència amb el nombre d'ona de les inestabilitats. La relació de dispersió es resol amb l'ajut del

mètode numèric de Newton-Rapson, explicat als Apèndix del treball. Resolent aquesta equació trobem l'estructura de les pertorbacions (longitud o nombre d'ona i freqüència) que són inestables, és a dir, que creixen en el sistema.

Aquestes pertorbacions inestables es poden estudiar des de dos punts de vista: aquell en que creixen en l'espai (estudi espacial), on la freqüència és real i el nombre d'ona complexa, sent la part imaginària la que ens dóna el creixement de la pertorbació; i aquell en que creixen en el temps (estudi temporal), on la freqüència és complexa i el nombre d'ona és real, sent la part imaginària de la freqüència la que ens dona el *ritme de creixement* de la pertorbació. En el nostre cas, ens centrem en l'estudi temporal, ja que, a l'hora de la realització de les simulacions numèriques permet l'ús de major resolució, com expliquem més avant.

Els resultats de la relació de dispersió són compatibles amb els estudis d'estabilitat lineal esmentats a la introducció d'aquest resum, que apunten cap als dolls més calents i/o lents com aquells en què les inestabilitats es desenvolupen més ràpidament respecte als dolls més freds i/o ràpids. El domini de paràmetres estudiat comprén des de factor de Lorentz 5 fins factor de Lorentz 20 i des d'energia interna específica $0.08 c^2$ (doll tebi) fins $60 c^2$ (doll calent, on c és la velocitat de la llum), fixant la raó de densitats de massa a 0.1 (amb el doll deu vegades menys dens que el medi). És dir, des de dolls mitjanament relativistes tant cinemàtica com termodinàmicament fins dolls altament relativistes en els dos aspectes.

Després d'estudiar els resultats de l'anàlisi lineal, passem a descriure les simulacions numèriques realitzades. Aquestes simulacions es fan prenent una porció d'un doll teòricament infinit (amb condicions de contorn periòdiques a l'eix de propagació), al que es pertorba. La pertorbació creix en el temps (estudi temporal) en aquestes simulacions. Açò ens permet centrar-nos en una part menuda del doll (del tamany de la longitud d'ona de la pertorbació), augmentant la resolució numèrica respecte als estudis espacials, als quals cal simular el doll en tota la seua extensió o seguir la seua evolució.

Com s'ha esmentat abans, es presenta un estudi de la resposta del codi front a pertorbacions petites, comparant el resultat amb els resultats teòrics de l'apartat anterior. Amb aquest objectiu, escollim una pertorbació de les

solucions i l'apliquem al doll. El resultat d'aquest estudi ens indica que el codi és capaç de seguir el desenvolupament de les inestabilitats tal i com prediu la teoria, sempre que la resolució numèrica siga suficientment alta. En cas contrari, la viscositat generada pel mètode numèric esmorteix el creixement, donant una estabilitat artificial al doll.

Un altre problema associat a aquest és el de l'estabilitat inicial del doll. Per pertorbar el doll, aquest deu estar en perfecte equilibri amb el medi. Numèricament açò és impossible si tractem la superfície com una discontinuïtat, de manera que, a l'hora de fer les simulacions, hem d'incloure una transició continua, però al mateix temps, el suficientment estreta per a que la teoria de transició discontinua siga aplicable.

Una vegada trobat l'equilibri entre resolució numèrica i amplària de la transició, presentem una sèrie de simulacions numèriques per a dolls amb el rang de paràmetres expressat més amunt, pertorbant el primer mode corporal simètric en tots ells, en tal d'estudiar la seua resposta no lineal a les pertorbacions. Els resultats més interessants d'aquesta part del treball són:

- En el règim lineal i post-lineal: hem confirmat el resultat de Hanasz (1995, 1997), qui va predir teòricament la saturació del creixement quan l'amplitud de la pertorbació en velocitat s'acosta a la velocitat de la llum. La fase lineal acaba quan la pertorbació en velocitat axial, en el sistema de referència del doll, arriba a una amplitud propera a aquesta velocitat límit. Després d'aquest moment, les pertorbacions en velocitat transversal i pressió segueixen creixent, encara que no indefinidament. Entre la fase lineal i la no lineal, trobem una fase de transició, marcada per la saturació de la velocitat transversal, i la generació d'una ona de xoc.
- Règim no lineal: Les condicions físiques del doll en el moment de la saturació condicionen l'estabilitat en el règim no lineal. L'ona de xoc generada en la transició de la fase lineal a la no lineal és més forta i destructiva per als dolls més lents i freds. Després de la formació de l'ona de xoc, comença un procés turbulent de transferència de moment del doll al medi extern i de mescla dels dos medis. Depenent de la intensitat de l'ona de xoc, el procés acaba per frenar i refredar el doll degut a la càrrega de material més dens i fred del medi extern.

El fet que l'ona de xoc siga més intensa per als dolls més freds és en part conseqüència de l'equilibri de pressions imposat al començament de la simulació. Açò ocorre perquè si el doll és més fred, el medi també ho és (degut a que hem fixat la raó de densitats), i per tant la velocitat del so és més baixa. Quan la pertorbació en velocitat supera la velocitat del so, es propaga de forma supersònica, generant una ona de xoc. Evidentment, quant menor siga la velocitat del so en el medi, més fàcil és que la pertorbació siga supersònica. Aquest fet ens va portar a fer un sèrie de noves simulacions, fixant les propietats físiques del medi extern, i modificant l'energia interna i la densitat de massa del doll de manera que es respectara l'equilibri de pressions. Aquestes simulacions no han fet més que afermar les conclusions exposades en els punts anteriors. No obstant, es remarca la importància del factor de Lorentz en l'estabilitat dels dolls, per damunt de les seues propietats termodinàmiques.

A més, exposem un anàlisi complet de les estructures transversals generades per les inestabilitats en el règim no lineal, i agrupem els dolls segons aquestes propietats i les magnituds promitjades com la quantitat de moment longitudinal conservat pel doll o l'amplària de la regió de mescla. Així, trobem quatre regions d'estabilitat que depenen bàsicament del factor de Lorentz i la raó d'entalpia específica entre el doll i el medi extern. Una primera regió comprén els dolls més freds i amb menors factors de Lorentz, els quals pateixen un procés de trencament i mescla ràpid després del xoc. Un altra regió inclou els dolls més calents i amb factors de Lorentz baixos, per als quals es dona un procés similar al del grup anterior, mantenint però una part central, prop de l'eix, sense mesclar i amb temperatures i velocitats elevades; aquest fet es mostra, no obstant, com possiblement degut a la baixa resolució axial utilitzada en les simulacions. El tercer grup inclou els dolls més ràpids i calents, els quals mostren una pèrdua gradual de moment longitudinal i un procés de mescla també lent, associat amb una eficient conversió d'energia cinètica en energia interna, que produeix una transferència continua d'energia i moment al medi extern. I el quart grup, en el que hi ha aquells dolls amb majors factors de Lorentz, però més freds que els anteriors, els quals són els més estables, en mantindre's col·limats i amb una porció elevada de la seua velocitat inicial.

Al final del capítol resumit ací es presenten simulacions realitzades per a quatre models representatius de l'exposat anteriorment, amb pertorbacions antisimètriques per provar la simetria del codi (en la qual es va treballar de

forma especial a nivell numèric) i estudiar l'efecte d'aquestes inestabilitats comparades amb les simètriques. Dues de les simulacions confirmen l'esperat partint dels resultats obtinguts amb pertorbacions simètriques. No obstant, en les altres dues apareixen, potser degut a un canvi de les condicions inicials (ampliació del tamany de la transició i canvi de resolució numèrica), uns creixements lineals anòmals de les pertorbacions. Aquest fet ens planteja la pregunta de l'origen de les anomalies (descartat un problema numèric), el qual s'explica en la secció següent.

En definitiva, hem fet un treball d'estudi i classificació de les inestabilitats Kelvin-Helmholtz en fluids relativistes, que ens permetrà abordar escenaris més generals i realistes amb una base de gran valor a l'hora d'analitzar els resultats obtinguts. A més hem pogut comprovar que les conclusions derivades dels treballs en el règim lineal, des de la suposició que les inestabilitats amb creixements més ràpids són les més disruptives, no es corresponen amb les conclusions derivades del règim no lineal, on veiem que, independentment del valor dels ritmes de creixement, l'estabilitat final del doll depèn de la transició entre un règim i l'altre, i, en particular, de la intensitat de l'ona de xoc generada en aquest moment. També demostrem que els dolls més calents no tenen per què ser els més estables com anteriors estudis numèrics havien conclòs (Hardee et al. 1998, Rosen et al. 1999). Els resultats han estat publicats als articles Perucho et al. 2004a i 2004b.

Estabilitat (transició continua)

El primer pas cap a escenaris més propers als sistemes reals passa per suavitzar l'exigència de transicions discontinües entre els medis, situació senzilla, i per tant interessant, baix un punt de vista teòric, però allunyada de l'interès pràctic. En el nostre cas, un altra motivació a l'hora d'enfrontar-nos a aquest problema es troba als resultats obtinguts en el cas de modes anti-simètrics.

En aquest cas de transició continua, la pertorbació de les equacions de la hidrodinàmica relativista ens porta a una equació diferencial per a la pertorbació en pressió que hem de resoldre numèricament. El mètode utilitzat per resoldre-la és conegut com *shooting method* o mètode del tir. El mètode del tir consisteix a donar condicions de contorn a l'equació diferencial, i, amb una

solució prova, integrar-la (amb el mètode Runge-Kutta de pas variable) des de una condició de contorn fins l'altra, comprovant si la solució prova compleix la segona. Si ho fa, hem trobat una solució de l'equació, i si no és així, s'utilitza el mètode de Muller per buscar una solució prova més propera a la solució vertadera.

Al començament del capítol corresponent, es presenten els resultats de l'anàlisi lineal d'una sèrie de models en els que es combinen diferents paràmetres com factor de Lorentz, energia interna específica i amplària de la transició. El primer resultat destacable, que confirma el mètode utilitzat, és la convergència entre els resultats obtinguts amb la relació de dispersió del problema de transició discontinua i la solució de l'equació diferencial de transició continua si aquesta és suficientment estreta.

La inclusió de transicions contínues entre un doll relativista i el medi ambient dona com resultat una disminució dels ritmes de creixement dels modes de reflexió d'ordre més baix. La disminució és més important quant més ampla és la transició. Pel que fa als modes de reflexió d'ordre més alt, presenten unes resonàncies molt pronunciades a les longituds d'ona més llargues per a les que comencen a ser inestables, és a dir, quan tenen ritmes de creixement majors que zero. Aquestes resonàncies, depenent dels paràmetres físics del model, són més o menys importants respecte als ritmes de creixement dels modes de reflexió d'ordre més baix: són particularment importants en els dolls més ràpids (amb factors de Lorentz ~ 20). Les resonàncies desapareixen a mesura que l'amplària de la transició es fa gran. El mode fonamental presenta dos comportaments diferenciats a longituds d'ona curtes i a longituds d'ona llargues. Per a les primeres els ritmes de creixement augmenten quan la transició creix, mentre que per a les segones la influència de la transició no es deixa sentir mentre l'amplària d'aquesta siga menuda comparable amb el tamany de la ona.

Es plantegen una sèrie de simulacions numèriques en el mateix domini de paràmetres termodinàmics i cinemàtics que les esmentades anteriorment, però incloent també models amb un factor de Lorentz 2.5. L'amplària de la transició en les simulacions és d'un 20% del radi del doll, i les pertorbacions s'inclouen com un conjunt d'ones simètriques i antisimètriques.

L'anàlisi de la fase lineal de les simulacions ens mostra la competició entre els diferents modes, la qual es mostra clarament mitjançant els efectes en la morfologia del doll en la fase immediatament posterior a la fi del règim lineal (fase de saturació). En els models amb factor de Lorentz inicial major, s'aprecia l'evolució de modes de reflexió d'alt ordre i longitud d'ona menuda que creixen més ràpidament que els demés modes, i que són excitats com armònics de les ones pertorbades explícitament per nosaltres. Hem comprovat que aquestos modes es corresponen amb les resonàncies trobades a la solució del problema lineal mitjançant una comparació de l'estructura generada per una de les resonàncies (teòricament) i l'estructura trobada a les pertorbacions de les simulacions, amb resultats positius. No obstant açò, els ritmes de creixement trobats a les simulacions són majors que els donats teòricament, sense que encara haguem trobat una explicació definitiva per a aquest fet. Potser estiga provocat per efectes no lineals d'interacció entre modes o per un creixement no homogeni d'aquestos modes al través del doll.

La importància de les resonàncies es fa palesa en la transició al règim no lineal. La presència d'ones de longitud d'ona curta que suposa l'aparició dels modes resonants, i que a més dominen el creixement de les pertorbacions, fa que qualsevol estructura de tamany majors siga trencada per aquestes ones més petites, evitant la formació de les ones de xoc que podrien provocar la disrupció del fluxe. Per tant, la saturació de les pertorbacions de velocitat transversal i pressió es produeix de forma suau. L'estructura de les resonàncies és tal que les amplituds de les ones són majors cap a la transició amb el medi. El creixement d'aquestes ones en la transició genera una conversió eficient d'energia cinètica en energia interna, formant-se una regió d'energia interna molt elevada (per damunt de la del doll mateix), que envolta el doll, aïllant-lo del medi. Així, els dolls que presenten aquest tipus d'evolució es mantenen col·limats i amb velocitats elevades.

Pel que fa als dolls més lents, per als que les resonàncies no apareixen a les simulacions d'acord amb els seu ritmes de creixement relatius (respecte als modes de longituds d'ona majors) més baixos, els processos són molt semblants al que s'ha dit respecte a les simulacions de dolls amb transició discontinua. En la major part dels cassos, després de la formació de l'ona de xoc, el material dels dolls es mescla amb el medi extern, com a conseqüència del qual els dolls són frenats i refredats. No obstant, hi ha un grup de dolls que pateixen

un procés de mescla més lent, en forma gradual. Els darrers preserven una quantitat important del seu moment longitudinal i no són mesclats amb el medi immediatament després de generar-se l'ona de xoc, però s'enceta en eixe moment un procés que, convertint energia cinètica en interna, desfa l'equilibri entre el doll i el medi i genera una vorticitat que dóna com a resultat la mescla i la transferència de moment longitudinal cap al medi extern, frenant-se així el doll. Aquesta família de dolls formen una regió de transició entre els dos grups esmentats abans, amb comportaments molt estables o molt inestables.

Al final del capítol, donem un gràfic en el que situem tots els dolls simulats en un pla factor de Lorentz - nombre de Mach relativista. En ell es demostra clarament la dependència de l'estabilitat dels dolls en aquestos paràmetres. Per demostrar el caràcter general del resultat, hem inclòs també els dolls de les simulacions del capítol anterior.

Finalment, es presenta una discussió en la que comparem els resultats d'aquestes simulacions amb els dolls extragalàctics reals, on es comparen els dolls que són frenats i mesclats amb els FRI, i els col·limats amb els FRII. Aquesta comparació és una simplificació molt gran, doncs no tenim en consideració efectes importants com la propagació dels dolls per un medi de densitat decreixent, o d'altres. No obstant, l'estudi no lineal d'aquestos fluids ens diu clarament quins són els més estables front a pertorbacions. Els resultats es troben en procés de publicació en aquestos moments (Perucho et al. 2005a,b).

Aplicacions astrofísiques

La darrera part del treball es centra en les possibles aplicacions de l'estudi realitzat a dolls extragalàctics, tant de l'escala del pàrsec com del kilopàrsec.

En primer lloc, hem provat de fer simulacions aplicades a dolls d'escala del pàrsec. Lobanov i Zensus (2001) van interpretar les estructures observades al doll d'escala del pàrsec del quàsar 3C 273 com produïdes per inestabilitats Kelvin-Helmholtz, i aplicant la teoria lineal, van obtindre un conjunt de paràmetres que el describien. Nosaltres hem realitzat dues simulacions en tres dimensions fent ús d'eixos paràmetres. Les simulacions comencen amb dolls estacionaris que són pertorbats amb l'objectiu d'estudiar les estructures que es

generen i comparar-les amb les trobades en el treball esmentat. A la primera simulació, les pertorbacions s'inclouen en la injecció del doll, amb estructures el·líptiques i helicoidals, com les identificades per Lobanov i Zensus, i es deixen evolucionar al llarg del doll (estudi espacial). Les estructures generades deuen ser comparades amb les observacions mitjançant transformacions que donen compte dels efectes de projecció relativistes i d'observació. És important per tant, conèixer la velocitat amb que es mouen les estructures per tal de fer les transformacions de forma adequada. La incertesa en aquest valor fa que la comparació siga complicada, encara que, estimant la velocitat de les ones, hem arribat a valors de longitud d'ona de les estructures generades comparables als observats. No obstant això, la simulació presenta un problema, com és que les inestabilitats acaben trencant el fluid, contràriament a les observacions que ens diuen que el doll del quàsar 3C 273 arriba col·limat fins ben fora de la galàxia progenitora. Al text es donen diverses hipòtesis per explicar el fet que el doll de la simulació es trenque, com la possibilitat de que hi haja errors acumulats en l'anàlisi lineal o la no inclusió de camps magnètics en la teoria i en les simulacions. No obstant això la resposta haurà d'esperar noves simulacions.

La segona simulació està basada en pertorbar el doll incloent fets observacionals com l'ejecció de components superlumíniques amb una freqüència anual, i la precessió del forat negre central amb un període d'uns 15 anys. En aquest cas el tamany físic simulat és menor que en la primera simulació, ja que la nostra prioritat en aquesta simulació era buscar estructures lineals comparables a les observades. D'aquesta manera hem observat que calen components amb factors de Lorentz majors (que els que nosaltres considerem) per explicar les estructures que Lobanov i Zensus expliquen com conseqüència de la precessió, i, a més, que aquestes components podrien explicar també algun dels modes de menor longitud d'ona observats pels mateixos autors. Degut a l'objectiu esmentat abans per a aquesta segona simulació, el doll no és el suficientment llarg com per deixar créixer les pertorbacions fins el règim no lineal, i, per tant, no podem saber si aquestes trencarien o no el doll. L'estabilitat a llarg terme del doll de 3C 273 serà estudiada amb més detall en futures simulacions.

En ambdós simulacions, es tracta de primeres aproximacions al problema de l'estabilitat en dolls reals, amb mancances tant teòriques com computacionals, però aquest tipus d'estudi és d'utilitat a l'hora de fer una crítica

constructiva del mètode utilitzat per obtindre els paràmetres del doll, potser comprovant la seua validesa o donant punts febles que millorar. Hem vist que, efectivament, hi ha mancances, però és a partir d'aquestes simulacions que ho podem saber i que podem tractar de superar-les amb noves ferramentes teòriques i amb millores en el codi.

Pel que fa als dolls d'escala del kilopàrsec, basant-nos en una sèrie de treballs de Laing i Bridle (2002a,b), estem fent una simulació per a l'evolució dels dolls de la radiofont FRI 3C 31. Aquests autors obtenen un model cinemàtic axisimètric per als dolls de 3C 31, tenint en compte també informació del medi extern obtinguda observacionalment (Hardcastle et al. 2002). En la nostra simulació hem incorporat aquesta informació per a un medi amb perfil radial de densitat. A més, hem treballat sobre el codi per tal de poder incloure tota la complexitat termodinàmica que el problema requereix, ja que els autors diferencien un medi extern, fred i bariònic, del doll, compost per partícules relativistes termodinàmicament (electrons i positrons). D'aquesta manera, hem usat l'equació d'estat de Synge per a gasos relativistes, que permet tractar amb electrons/positrons i protons, i per tant treballar amb diferents combinacions d'aquestes partícules.

Aquesta simulació està sent una de les més llargues de la tesi, amb una durada, fins l'escriptura d'aquestes línies, de quaranta-set dies, treballant amb vuit processadors de la màquina SGI Altix 3000 *CERCA*.

Els resultats parcials d'aquesta simulació ens mostren la propagació del doll al llarg dels primers milers de parsecs de la seua evolució, i ens han permès reproduir de forma qualitativa el model evolutiu de Laing i Bridle. L'evolució del doll ve marcada per una primer fase d'expansió adiabàtica i acceleració en el medi extern, fins que es troba amb una pressió menor que la del medi i pateix un procés de focalització (o compressió), que genera una forta disminució de la velocitat del doll i un increment de la densitat i la pressió, que afavoreixen l'augment de l'emissió. En acabant, s'enceta un segon procés d'expansió i refocalització, que es pot entendre com una oscil·lació al voltant de l'equilibri de pressions, del qual ja es troba prop després d'aquesta segona fase.

La comparació completa entre la simulació i els models teòrics no es podrà realitzar fins que el doll haja evolucionat durant més temps i l'evolució del

seu cap deixi d'influenciar les regions que volem estudiar. Aquesta influència ve donada per l'efecte de la resistència del medi extern a l'evolució del doll, per exemple, mitjançant un rebot de les partícules en forma de contrafluxe o matèria que es mou cap a darrere pels costats del doll, pertorbant-lo. Fins que aquestos efectes deixen de ser importants el doll no és estacionari i no podem comparar els resultats amb els models teòrics. De moment, com hem esmentat abans, açò només ho hem pogut fer per a les regions més internes. En l'anàlisi final de la simulació deurem tindre en compte la càrrega de matèria del medi ambient en el doll, ja que les teories més acceptades per a l'evolució dels dolls de FRI postulen aquesta càrrega com la causa de la pèrdua de velocitat i de col·limació dels dolls.

Conclusions

Aquest treball de tesi doctoral tenia com objecte aprofundir en el coneixement del règim lineal i obrir el camí del coneixement en el camp no lineal de l'estabilitat de fluids relativistes, sempre amb l'objectiu d'adreçar-nos als dolls extragalàctics en últim terme. La part principal de la tesi s'ocupa del primer i segon aspectes. Al llarg d'aquest treball s'han desenvolupat les eines tant teòriques com numèriques per dur-lo a terme, a més de fer les millores pertinents en el codi amb que treballem per tal d'optimitzar-lo i fer simulacions amb major resolució i en menys temps. El resultat d'aquest esforç ha estat clarament positiu com s'aprecia a les publicacions en revistes científiques especialitzades que ha motivat el treball.

Les conclusions i resultats més importants del treball són les següents:

- El codi numèric és capaç de reproduir el creixement lineal de les inestabilitats Kelvin-Helmholtz, sempre que utilitzem la resolució adequada (que minimitze els efectes de la viscositat numèrica) al problema.
- Hem confirmat la hipòtesi de Hanasz (1995, 1997) segons la qual les inestabilitats en fluids relativistes saturen quan l'amplitud de la pertorbació en velocitat s'acosta a la velocitat de la llum en el sistema de referència del doll.
- Hem separat l'evolució de les inestabilitats Kelvin-Helmholtz en dolls relativistes en tres fases: fase lineal, fase de saturació, i fase no lineal. Hem

estudiat la influència de la resolució numèrica en les fases lineal/saturació i no lineal.

- Hem estudiat i classificat l'evolució no lineal de les inestabilitats Kelvin-Helmholtz de forma quantitativa, mitjançant variables com la quantitat de moment total en el doll o l'amplària de la regió on es mescla amb el medi extern.
- Hem descobert l'existència de modes resonants en fluids relativistes amb transicions contínues que tenen una gran importància en l'estabilitat a llarg terme dels dolls.
- Hem donat un mapa de l'estabilitat dels dolls relativistes, depenent del seu nombre de Mach relativista i del seu factor de Lorentz inicial, demostrant que els dolls amb valors grans d'aquests paràmetres tendeixen a ser més estables que la resta.
- Hem realitzat dues simulacions numèriques del doll d'escala del pàrsec de 3C 273 amb l'objectiu de confirmar o corregir els resultats de Lobanov i Zensus (2001), qui, usant la teoria lineal (e.g., Hardee 2000), expliquen les estructures observades al doll com conseqüència del desenvolupament d'inestabilitats.
- Hem començat una simulació d'evolució de llarg terme per estudiar l'evolució dels dolls de la radiogalàxia 3C 31, en particular de la seua evolució per dins de la galàxia progenitora i l'eixida al medi intergalàctic, seguint els paràmetres donats als models de Laing i Bridle (2002 a,b). Pretenem posar a prova aquest model i fer un estudi de l'estabilitat dels dolls que es propaguen per medis amb perfils de densitat, que ens obliga el camí cap a un seguit de simulacions d'aquest tipus orientades a la recerca de la dicotomia FRI/FRII. Els resultats parcials són encoratjadors i ens han permès identificar les diferents fases incloses pels models esmentats, encara que deurem esperar fins el final de la simulació per obtindre comparacions definitives entre aquesta i les diferents teories que proven d'explicar la morfologia de les fonts FRI, entre les que trobem els models de Laing i Bridle.

Pel que fa als punts menys positius del treball, no entenem encara perquè els ritmes de creixement d'aquestes en les simulacions són majors que els teòrics, així com tampoc hem trobat una solució per a l'estabilitat a llarg

termini del doll en el quàsar 3C 273. Aquestos aspectes seran, no obstant, motiu d'estudi en el futur immediat.

El futur d'aquesta recerca està preparat amb les millores introduïdes en el codi (equació d'estat o versió del codi en tres dimensions) i amb el desenvolupament de teoria lineal d'instabilitats Kelvin-Helmholtz per a casos encara no estudiats, com el de dolls amb rotació diferencial. La inclusió de camps magnètics (element fonamental en certes simulacions) en el treball serà també possible en un futur proper.

Contents

1	INTRODUCTION	5
1.1	Jets in the Universe	5
1.2	AGN's and jets	6
1.3	The Standard Model	9
1.3.1	AGN unification	9
1.3.2	Jet formation and collimation	12
1.3.3	Jet models	13
1.3.4	Radiation mechanisms	18
1.4	The role of Kelvin-Helmholtz instabilities in jets	20
1.5	Motivation of the work	23
1.6	Methodology	24
1.7	Organization of the work	24
2	STABILITY IN THE VORTEX SHEET LIMIT	27
2.1	Linear analysis	27
2.1.1	Equilibrium state for the linear stability analysis	29
2.1.2	Dispersion relation	30
2.1.3	Solution	34
2.1.4	Modes	35
2.1.5	Surface and body modes	37
2.2	Note on temporal versus spatial approach	39
2.3	Numerical simulations	41
2.4	Results	48
2.4.1	Linear phase	48
2.4.2	Saturation phase	51
2.4.3	Non-linear phase	59

2.4.4	Influence of numerical resolution in the non-linear evolution	82
2.5	Conclusions	86
2.6	Single antisymmetric mode simulations	90
3	STABILITY OF SHEARED FLOWS	97
3.1	Linear analysis	98
3.2	Numerical simulations	111
3.3	Results	116
3.3.1	Linear phase	116
3.3.2	Saturation and transition to non-linear phase	123
3.3.3	Non-linear regime	127
3.4	Cylindrical jet simulations	139
3.5	Discussion	147
3.5.1	Non-linear stability	147
3.5.2	Astrophysical implications	152
3.6	Conclusions	154
4	ASTROPHYSICAL APPLICATIONS	157
4.1	Pc scale jets. Numerical simulations on 3C 273	157
4.1.1	Introduction	157
4.1.2	Linear Analysis	161
4.1.3	Simulation 3C273-A	163
4.1.4	Simulation 3C273-B	170
4.1.5	Conclusions	176
4.2	Kpc scale jets. Numerical simulations on 3C 31	177
4.2.1	Introduction	177
4.2.2	Setup for the numerical simulation	181
4.2.3	Results	184
4.2.4	Discussion and Conclusions	191
5	CONCLUSIONS	199
A	Numerical code	203
B	Numerical methods	211
B.1	Newton-Raphson method	211
B.2	Muller's method	212

B.3 Shooting method	213
C Special relativity in extragalactic jets	215
C.1 Beaming and its effects	216
C.2 Superluminal motion	217
D Linear stability problem for sheared jets	221
D.1 Slab jet	222
D.2 Cylindrical rotating jet	224
D.3 Conical rotating jet	226

Chapter 1

INTRODUCTION

1.1 Jets in the Universe

Outflows and jets represent a common feature in the Universe. They appear associated to accreting objects, ranging, in the case of galactic jets, from stars in the process of formation (Herbig-Haro objects, see e.g., Pudritz 2002, Calvet 2002, Hartmann 2002) to compact objects, like neutron stars and black holes in binary stars (e.g., X-ray binaries or microquasars, see e.g., Mirabel and Rodriguez 1994, 1998, 1999, Mirabel et al. 1998), or in the case of extragalactic jets, emerging from supermassive black holes (SMBH) in the nuclei of active galaxies (AGN, see e.g., Begelman, Blandford and Rees 1984, Zensus 1997, Ferrari 1998). Some models and observations point towards jets appearing also in stellar explosions and gamma-ray bursts (GRBs, see e.g., Piran 1999), when the central core accretes matter from its environments. The variety of scenarios in which they are present makes them an interesting topic through which we can try to understand the physics of their sources and surroundings.

The properties of jets depend critically on the scenario we consider. Particles in jets from young stellar objects (YSOs) have velocities of the order of hundreds of km s^{-1} , whereas those in AGN's present Lorentz factors close to $\gamma \simeq 10$ (γ is the Lorentz factor), i.e. relativistic speeds, and those in GRBs may have $\gamma > 100$. Jet composition is also very different from YSOs to AGNs, as the former consist on molecules and atoms, whereas in the latter, electrons, positrons and protons are the most likely ingredients. Therefore, relativistic jets in AGNs represent an excellent laboratory for relativistic plasma physics.

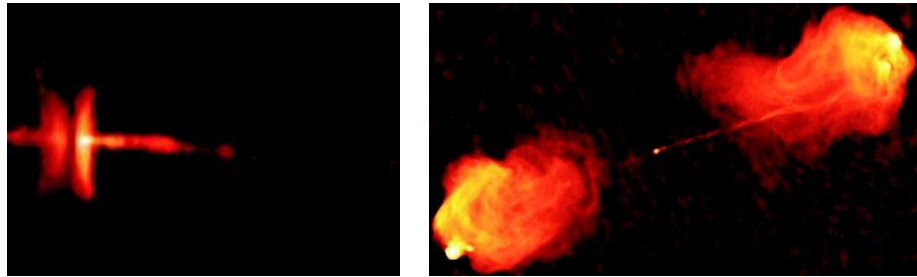


Figure 1.1: From the smallest to the largest. Jets in a forming star system (left, Hubble Space Telescope, HST) and in radiogalaxy Cygnus A (right, Very Large Array, NRAO).

Despite those differences, it is thought that all these scenarios have something fundamental in common. A magnetohydrodynamic process is supposed to generate all these different jets and outflows, the degree of collimation, velocities and composition depending on the properties of the central object, the accretion disk and its surroundings (Pudritz 2002, Camenzind 2002).

1.2 AGN's and jets

AGN phenomena (see, e.g., Krolik 1999, Peterson 1995) were discovered in 1943 by Carl Seyfert, when he realized that some galaxies (Seyfert galaxies) presented very high surface brightness at their nuclei and very strong line emission. Few years later, Woltjer (1959) deduced that all the emitted energy appeared to be originated at a very small region of about 100 pc across, where about 10% of the mass of the whole galaxy was concentrated.

Another piece of the puzzle appeared soon after, in the form of *radio-stars*, i.e., star-like objects with strong emission in radio frequencies, also known as *quasars*. These objects also showed emission lines at frequencies where they had never been observed in stars. Maarten Schmidt (1963) found that these were redshifted lines due to their cosmological distances, showing that quasars were not stars, but powerful, distant galaxies. It was then deduced that one of the first quasars discovered, 3C 273, was intrinsically 100 brighter than a typical spiral galaxy.

The origin of this energy coming from a very central region in some galaxies was thought to be due to the energy outcome from an accretion process by a

central object. The typical mass of such an object was deduced by Sir Arthur Eddington. The argument used was to consider that the gravitational field generated by it has to be equal or larger than the radiation pressure of the observed luminosity, in order that the accretion process is not stopped. The result showed that this mass has to be of the order of $10^8 M_{\odot}$. This was one of the first direct evidences of the existence of black holes, due to the enormous mass of the body and the small size of the region where it has to be embedded. If the energy outcome is due to the loss of gravitational energy by the accreted particles, we can easily estimate that the efficiency of the process could be about 16%, compared to 0.7% in the case of nuclear fusion. These arguments show that we deal with one of the most violent and energetic processes in the Universe.

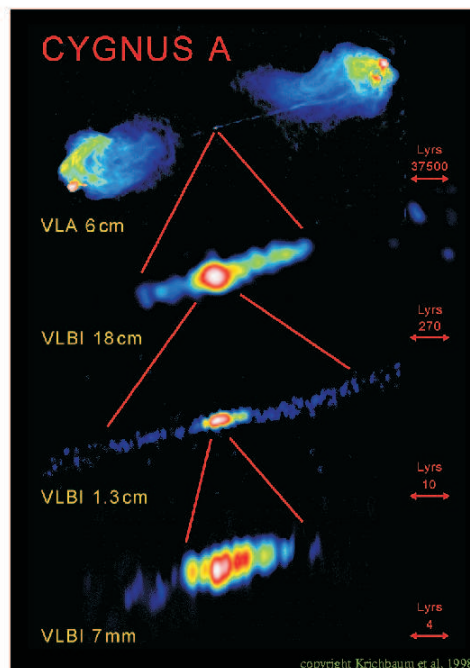


Figure 1.2: Cygnus A, observed at different wavelengths. Extragalactic jets show strong self similarity in very different scales (Krichbaum et al. 1998).

It is widely thought that SMBHs are present in the cores of AGNs, and observational evidences of this fact have been found (e.g., Biretta et al. 2002).

Due to their large mass and presence in the nuclei of galaxies, their origin could be in a very early epoch after the Big Bang (primordial black holes). Therefore, SMBHs are a key point in the formation of galaxies and clusters of galaxies. SMBHs not only appear in AGNs, but observations suggest that they are also in the nuclei of all galaxies, the mass of the object being smaller in the case of non active galaxies, e.g., the SMBH found in the center of our Galaxy has a mass of the order of $10^5 M_{\odot}$ (e.g., Ghez et al. 2000).

AGNs emit radiation in the whole electromagnetic spectrum and appear in a different set of luminosities, line emissions, spectral distributions and morphologies. A first division can be given between those AGNs with intense radio emission (which have also larger bolometric luminosities) and those with weak or no radio emission. Among these, two more divisions can be done, one related with the presence or not of broad lines in the spectrum and another with the bolometric luminosity. A very important step in the understanding of AGNs was done when all these apparently different objects were unified under a single physical process (Blandford and Rees 1978, see section 1.3).

Among the weak radio emitters we find Seyfert 1 and 2 galaxies, with Seyfert 1 galaxies showing broad lines, and radio quiet quasars, among others. Regarding strong radio emitters, we find radio galaxies (Narrow Line and Broad Line), quasars and blazars, from less to more luminous.

A fraction of AGNs, mainly those with intense radio emission, show extended emission in jet-like features arising from the nuclei. Radio emission seems to be originated in these jets, so they are the main difference between strong radio emitter AGNs and weak radio emitter AGNs. Jets are elongated emission regions with linear sizes up to 1 Mpc, and are channels through which large quantities of particles and energy is transported to the intergalactic medium. In the large scale, two types of source are identified, depending on their morphological features (Fanaroff and Riley 1974):

- FRI radio galaxies: low power radiogalaxies ($P_{178\text{MHz}} < 10^{25}\text{W/Hz}$). Their most luminous regions are towards the center (limb-darkened) and they end up in a diffuse external zone.
- FR II radio galaxies: large power radiogalaxies ($P_{178\text{MHz}} > 10^{25}\text{W/Hz}$). They are limb-brightened, terminating in bright hot-spots in the collision region with the ambient medium, and jets have a clearly collimated structure.

The other two main types of AGN where jets are present are:

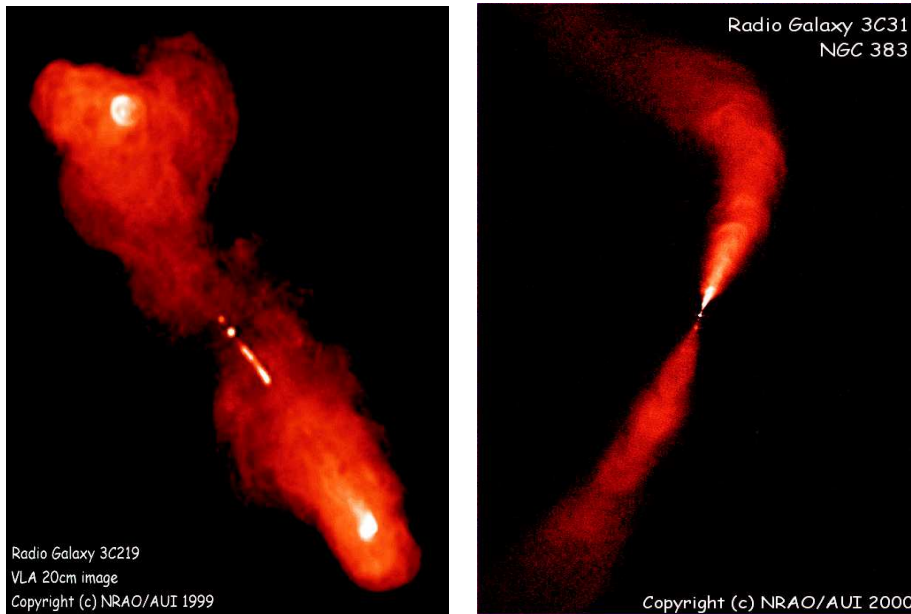


Figure 1.3: Radiogalaxies 3C219 (FRII, left) and 3C31 (FRI, right) (NRAO).

- Quasars are more intense than radiogalaxies in the optical and narrow and broad lines are observed. These sources are very variable in radio frequencies, and the jets appear unidirectional, although some times a second or counter hot-spot is observed.
- Blazars are the most variable (even intra-day) emitting sources in the whole spectrum. Jets in blazars are very compact and one-sided. These objects emit even in the most energetic part of the spectrum, at energies that can reach TeV (gamma rays). Blazars include OVV (optically variable violent) quasars, very powerful sources, and BL Lacs, with no emission lines and less powerful than Blazars.

1.3 The Standard Model

1.3.1 AGN unification

As stated above, AGN emission is due to the accretion process onto a SMBH in the center of the galaxies. Then, what is the reason for such a variety

of objects inside the same phenomenon? The unification schemes (Blandford and Rees 1978, Blandford and Payne 1982, Ghisellini et al. 1993, Urry and Padovani 1995) claim that the presence of broad lines in the spectra and the observed power is a consequence of the angle to the line of sight of the observer. The unified scheme includes two basic ingredients in order to explain this fact: i) relativistic beaming and ii) tori of gas and dust surrounding the central black hole and accretion disk.

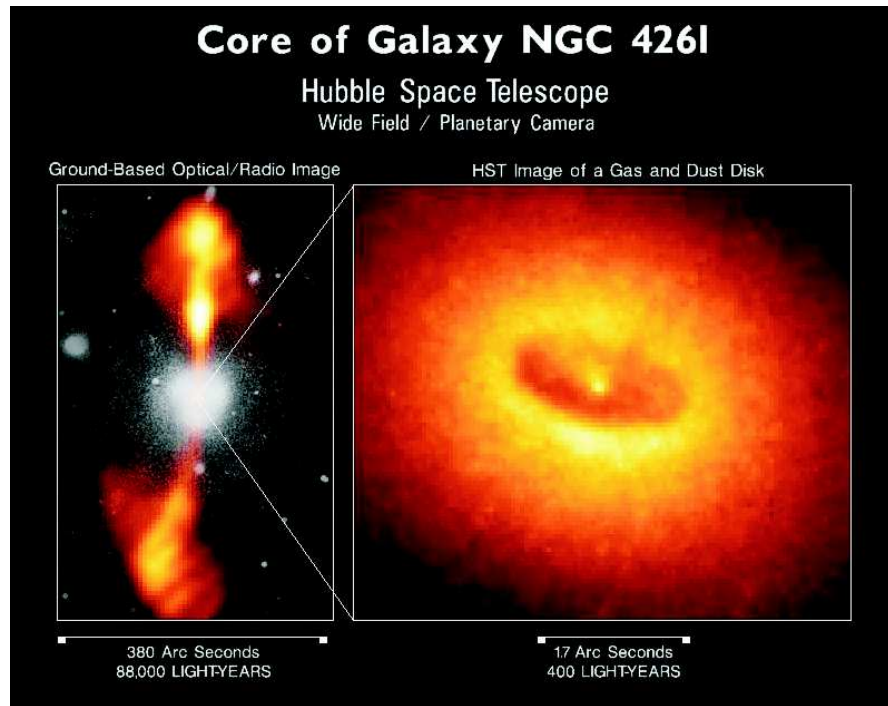


Figure 1.4: The torus in the core of radiogalaxy NGC4261 (HST).

A torus of dust and gas is supposed to surround the SMBH-disk system and obscure broad line emission, which would be located towards the center of the source (Broad Line Region). This fact is confirmed by the velocities of the emitting gas implied by the widths of broad lines (larger than $\sim 1000 \text{ km s}^{-1}$), as corresponds to material moving closer to the gravitational source, compared to that of narrow lines ($\sim 100 \text{ km s}^{-1}$, Narrow Line Region).

Regarding relativistic beaming (Blandford and Rees 1974, Rybicki and Lightman 1979, see also Appendix C), it is due to the anisotropic emission

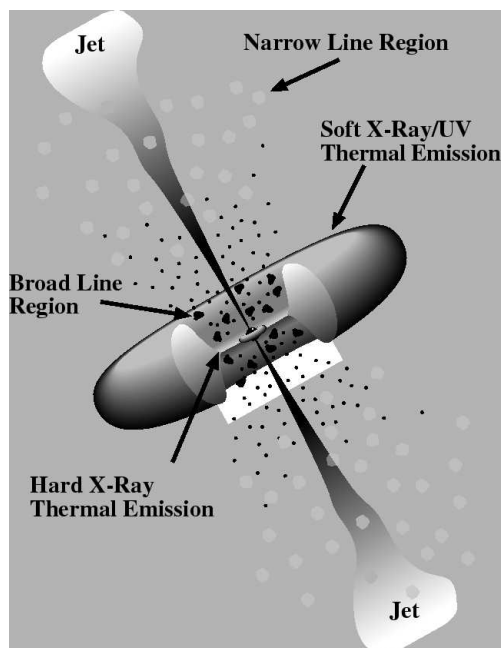


Figure 1.5: Schematic view of an AGN (Urry and Padovani 1995).

by relativistic particles, which favors the direction of motion in such a way that if the particle comes in the direction of observation (inside a cone of semi angle $1/\gamma$), the measured intensity will be larger than if it travels along further directions to the line of sight. The factor expressing this relativistic effect is the Doppler factor: $\delta = \gamma(1 - \beta \cos\theta)$, with β the velocity of the emitting material in units of the speed of light, and θ the angle to the line of sight. The measured intensity from a particle radiating at a direction close to the line of sight is increased by a factor proportional to δ^3 the radiated intensity. This would explain the apparent larger intensity from those sources which are observed in the direction of the relativistic jet and one-sidedness of these jets (e.g., blazars compared with radiogalaxies). They appear to have large variability in short timescales, implying that we observe emission from very compact regions, close to the active nucleus.

Possible intrinsic effects would explain power or morphological differences between sources seen under similar angles, like those appearing between individual sources belonging to the same kind, or between FRIs and FRIIs.



Figure 1.6: Caption from a simulation of jet formation in the surroundings of a SMBH; lines stand for magnetic field (Meier et al. 2001).

1.3.2 Jet formation and collimation

The process of jet formation and collimation is not still well understood, as it occurs in a very compact region and observations have not still resolved it. Junor et al. (1999) showed that the innermost collimation region in M87 is located at about $30 r_S$ (r_S is the Schwarzschild radius). Nevertheless, it is widely accepted that a magnetohydrodynamic process is behind the origin of jets. The original idea is due to Blandford and Payne (1982) and Shibata and Uchida (1985). The problem of the bed in a rotating wire has been suggested as an example of how particles are extracted from the disk: there is an angle for which, at a given rotation velocity, the bed starts to move outwards. In our case, we know that plasma particles are frozen to magnetic fields, so the parallelism is evident: the magnetic field acts as a wire allowing for particle transport. Thus, a magnetic field crossing the accretion disk with a given angle would provide a physical mechanism to extract particles and angular momentum from it. The extraction of angular momentum is crucial from the point of view of accretion, as there has to be loss of momentum in order

to have accretion due to momentum conservation law. Differential rotation velocity from the surface of the disk to further regions over the disk causes twisting of the field lines. In the model, collimation of the jet occurs due to this twisting creating an inwards Lorentz force transversal to the jet direction, which brings the frozen particles to the axis. Recently, Koide et al. (1998) have performed simulations including General Relativistic Magnetohydrodynamics, and found generation of some mildly relativistic outflow. However, they report numerical problems after some rotational periods of the disk. Their results suggest pressure along with magnetic driven outflows, depending on the region of extraction, and that a rotating SMBH (Kerr) is more likely to generate a faster jet than a static Schwarzschild SMBH if the black hole counter-rotates with respect to its accretion disk (see also Meier et al. 2001).

Other models have been proposed, like jets being formed in a magnetic Penrose process, where energy is directly extracted from a spinning (Kerr) black hole (Penrose 1969, Blandford and Znajek 1977), for which recent numerical simulations exist (Komissarov 2005, Koide et al. 2002); purely hydrodynamic processes, in which the flow would be accelerated down a pressure gradient, or models suggesting that plasmas are accelerated by a Poynting flux, i.e., through interaction with radiation (see Celotti and Blandford 2001 for further references on this topic).

1.3.3 Jet models

First models of jet kinematics idealized them as a funnel in which particles travel freely outwards (Blandford and Rees 1974, Scheuer 1974). However, interferometric techniques used in VLA (Very Large Array), MERLIN and VLBI (Very Long Baseline Interferometry), showed that jets have a knotty structure of stationary and moving features. Some moving components were also found to have superluminal motion ($\sim 2 - 5 h^{-1}c$, with h the normalized Hubble constant), what was explained by Rees (1966) as a relativistic effect of radiating particles moving close to the line of sight (Rybicki and Lightman 1979, see also Appendix C). Stationary components were considered to be associated with beaming due to helical motions approaching to the line of sight (Walker et al. 2001). It is believed that helical motions may arise due to precession of the SMBH or due to the jet being generated in a binary SMBH. Moving components were linked to shocks travelling through the jets by the so called *shock-in-jet* models (Blandford and Königl 1979, Marscher and Gear 1985, Gómez et al. 1993). This has been proven by numerical simulations

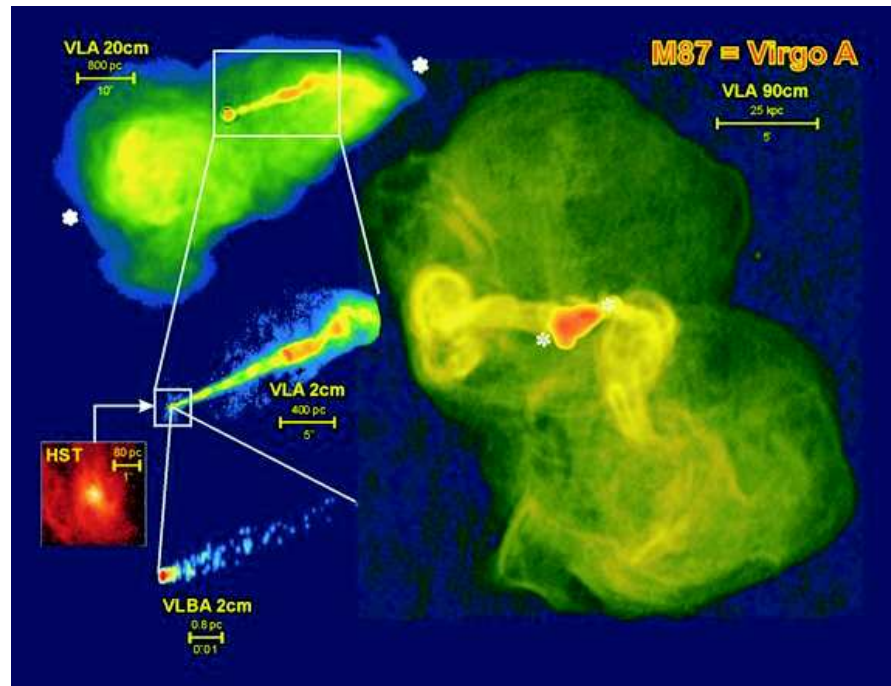


Figure 1.7: M87, from kiloparsec scales to the active nucleus (NRAO/AUI).

which combined relativistic hydrodynamics and emission mechanisms (see, e.g., Gómez et al. 1995, 1997, Agudo et al. 2001). Recent papers by Hardee (2003) and Hardee et al. (2005) also suggest that moving features could be associated to the downstream propagation of instabilities.

Progressively better resolution observations show a less idealized picture of strong coupling of jet evolution with its source and the ambient medium through which it moves, including accelerations and decelerations or interaction between components. Recent observations by Marscher et al. (2002) have shown that superluminal component ejections are associated to dips in X-ray emission, which imply a more intense accretion activity, thus showing that these travelling perturbations have their origin in the SMBH environment. Also, Gómez et al. (2000) interpreted bends in the jet of 3C 120 as caused by the interaction with a cloud in the ambient medium. Numerical codes have turned into a very valid approach to parsec scale jets (Agudo et al. 2001), as they permit dealing with these complex, non-linear systems.

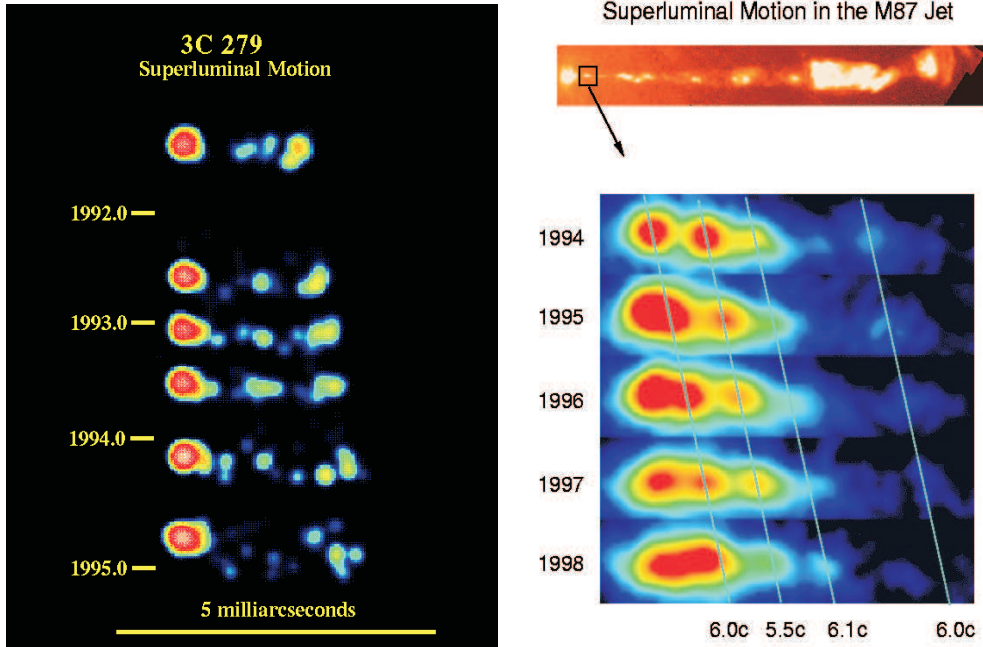


Figure 1.8: Observations of radio sources (quasar 3C279 at 22 GHz, left, and M87, right), showing superluminal motion. The outer component in 3C279 moved 25 projected light years during a six year interval and components in M87 move at about $6c$ (Wehrle et al. 1998, left, Biretta 1999, right).

On top of the difficulties for understanding such physical systems, we have to keep in mind that relativistic effects may show up as strong bends and deformations of the jet (see Appendix C). A small bend in the jet reference frame can appear as a 90° change of direction if the jet is observed at a sufficiently small angle.

Emission from jets is mainly due to two processes (see subsection 1.3.4), giving rise to the two peaks in the typical spectrum of an extragalactic jet:

- synchrotron radiation due to relativistic particles being accelerated by magnetic fields, responsible for emission from radio to optical wavelengths,
- synchrotron self, or external, inverse Compton radiation (depending on

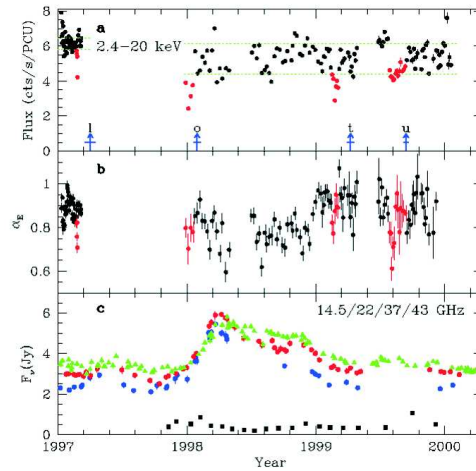


Figure 1.9: Disk-jet connection. Emission at X-ray energies and radio wavelengths from an AGN., where correlation between X-ray dips and radio bursts was shown for 3C 120 (Marscher et al. 2002).

the origin of the photons, from local synchrotron or from external sources -which may be cosmological microwave background radiation, CMB, emission from the SMBH corona, from the accretion disk..., respectively), responsible for high energy emission in the X-ray and gamma-ray bands, mostly in blazars.

Parsec scale jets present usually a flat spectrum in the radio band, due to the superposition of spectra from different components, which will be explained in next subsection. Jets present a two peak spectral distribution, the first shows up from the millimeter to the X-ray region, and the second in the MeV-TeV gamma-ray band.

Observations of kiloparsec scale jets allowed for studies in the radio (VLA) and up to optical (HST) bands. However, since the last decade, X-ray satellite Chandra has allowed for observations in this range in near kiloparsec scale jet (3C 273, see Section 4.1 and references therein, or M 87). These observations show very energetic emission far from the core, posing the problem of particle acceleration along the jet (Kirk and Duffy 1999). Several hypothesis have been proposed for the origin of this radiation, as explained in detail for 3C

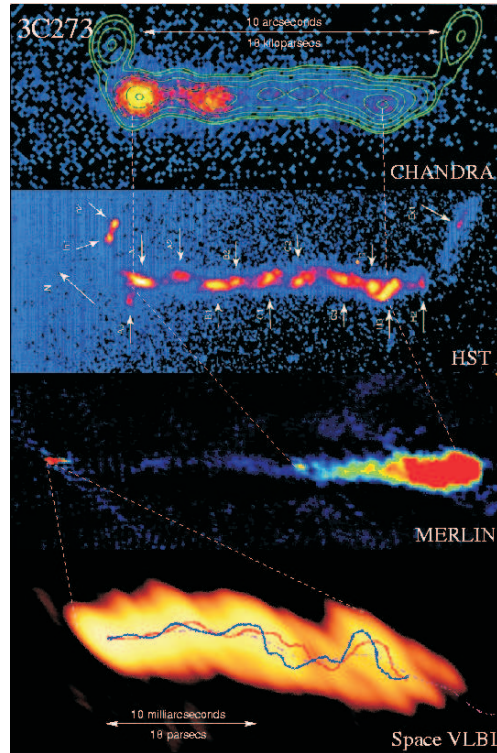


Figure 1.10: Jet in quasar 3C273 observed at different wavelengths.

273 in section 4.1, suggesting inverse Compton scattering of CMB photons, synchrotron self Compton or synchrotron radiation from ultrarelativistic electrons. Whatever the origin is, particles involved have to be relativistic, so the need for a model explaining particle acceleration and evolution of high energy particles in the jet (e.g., Jones et al. 2002, Agudo 2002, Mimica et al. 2004) is evident.

Another problem concerning kiloparsec scale jets is the *stability problem*, i.e., how to keep particles in jets collimated along hundreds of kiloparsecs. In the case of FRIs (e.g., 3C 31), jets are disrupted and have turbulent motion, being transonic or subsonic in kiloparsec scales. On the other hand, jets in FRIIs (e.g., Cygnus A) appear collimated up to the hot-spot, where they collide with the intergalactic medium. Despite this difference, they seem to have similar Lorentz factors in the parsec scales. We know that some (magneto)-

hydrodynamic instabilities, mostly Kelvin-Helmholtz instabilities, develop in systems like jets, so there must be a stabilizing effect which avoids their disruption in FRIIs.

1.3.4 Radiation mechanisms

Synchrotron

Synchrotron radiation is produced by charged particles accelerated around a magnetic field (Rybicki and Lightman 1979, Longair 1994). The power emitted by a single particle, taking mean angle of motion with respect to the magnetic field lines, is:

$$P = \frac{4}{3}\sigma_{\text{T}}c\beta^2\gamma^2U_{\text{B}}, \quad (1.1)$$

where $\sigma_{\text{T}} = 8\pi r_0^2/3$ is the Thomson cross-section (for the collision of an electron and a photon at low energies), with $r_0 = e^2/m_e c^2$ the classic electron radius, e the electron charge, m_e the mass of the electron and c is the speed of light, γ is the Lorentz factor of the electron, β the speed in units of c and $U_{\text{B}} = B^2/8\pi$ is the magnetic field energy density. It can be shown that this power is proportional to m^{-4} , so the synchrotron emission is mainly by lower mass particles, i.e., electrons and positrons, being negligible that from protons.

The power emitted by a single particle, Eq. (1.1), can be shown to be basically emitted at the critical frequency:

$$\nu_{\text{c}} = \frac{3}{4\pi}\gamma^3\omega_{\text{B}}\sin\alpha, \quad (1.2)$$

with ω_{B} being the gyration frequency of the electron around the magnetic field:

$$\omega_{\text{B}} = \frac{eB}{\gamma m_e c}, \quad (1.3)$$

and α the angle between the magnetic field line and the velocity vector of the particle.

This emission has a dipolar pattern in the reference frame of the relativistic particle, but if we make a transformation to the observer's frame, we find that this pattern is stretched towards the front lobe to a small cone of semiangle $1/\gamma$, with the axis in the direction of motion.

If we have a group of electrons with energies between E and $E + dE$ (γ and $\gamma + d\gamma$) with a power law distribution, where the number density is given

by:

$$N(E)dE = CE^{-p}dE, \text{ or } N(\gamma)d\gamma = C\gamma^{-p}d\gamma, \quad (1.4)$$

where C is a constant, the total power depends on the frequency of emission as follows:

$$P_{\text{tot}}(\nu) \propto \nu^{-(p-1)/2}. \quad (1.5)$$

Making $s = (p - 1)/2$, we finally have:

$$P_{\text{tot}}(\nu) \propto \nu^{-s}, \quad (1.6)$$

with s the spectral index.

Emitted synchrotron photons may be absorbed by particles in the system (synchrotron self-absorption). An opacity coefficient, which depends on the physical conditions of the emitting region and on the photon frequency, can be calculated (Rybicki and Lightman 1979). When this coefficient is larger than one, the source becomes optically thick and it can be shown that the spectrum is $\propto \nu^{5/2}$ in that range of frequencies. Typical spectra of isolated compact sources has a peaked spectrum, with an absorbed low frequency part, and a typical synchrotron higher frequency region, the peak being at the frequency where the opacity is equal to unity, i.e., where the spectra invert. If we observe a compact source composed by different components, they may have their individual spectral peaks at different frequencies, e.g., the denser and more intense the component (the closer to the formation), the higher the frequency at which the peak occurs. The resulting spectrum shows up as a flat one due to the combination of all the component spectra, effect known as *cosmic conspiracy* (Cotton et al. 1980, Marscher 1987).

Inverse Compton

Inverse Compton radiation is produced when a photon collides with a high energy electron and gains energy in the process. This collision can convert a radio frequency photon in an X-ray or even gamma-ray photon, and is the origin of the high energy radiation from extragalactic jets, and responsible for electron energy losses. In the observer's frame, the photon gains energy proportionally to the square of the Lorentz factor of the electron $E' \sim \gamma^2 E$, with $E = h\nu$ the original energy of the photon. The total power radiated by inverse Compton scattering can be shown to be (Rybicki and Lightman 1979):

$$P_{\text{Compton}} = \frac{4}{3}\sigma_T c(\gamma\beta)^2 U_{ph}, \quad (1.7)$$

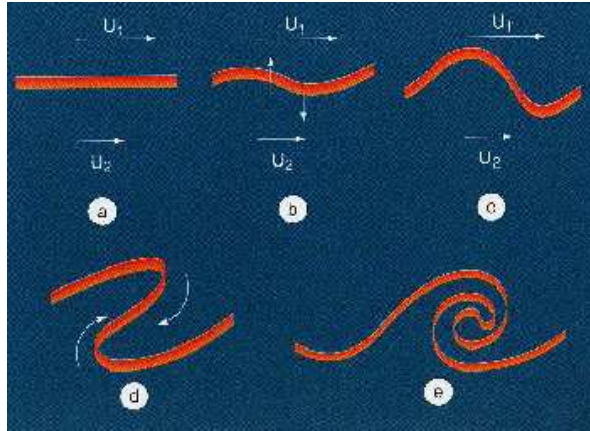


Figure 1.11: Development of Kelvin-Helmholtz instability.

with U_{ph} the source photon energy density.

Depending on the origin of the up-scattered photons, the emission generated is called *synchrotron self Compton* (SSC), if photons were originated as synchrotron photons in the source, or *external Compton* (EC), if photons arrive to the radio-source from an external radiation field like CMB.

1.4 The role of Kelvin-Helmholtz instabilities in jets

Kelvin-Helmholtz instabilities (Gill 1965, Chandrasekhar 1961) grow in the contact discontinuity or transition (shear instability) between two flows with relative speed. Figure 1.11 sketches how a perturbation grows in the interface between both fluids and the typical "ocean wave" morphology it develops. Many natural scenarios meet the conditions to be subject to KH instability (sea-air, cloud-air...), but also some more extreme physical scenarios like astrophysical jets.

These instabilities grow under any small perturbation, what can easily happen in the case of extragalactic jets, as these propagate embedded in an ambient medium where winds, clouds or any other obstacle can give rise to that perturbation. The dynamical interaction of the jet matter with the ambient medium leads to the formation of shocks, turbulence, acceleration of charged particles and subsequent emission of a broad-range electromagnetic radiation, which makes jets observable. The complex nature of flow instabili-

ties arising in these systems, especially the Kelvin-Helmholtz (KH) instability, makes difficult to distinguish effects which are directly related to the central object from those which are due to the interaction of jets with the ambient medium. As an example one can invoke the wavelike patterns in jets, which may result from the precession of the rotation axis of the accretion disk at the jet base, or from KH instability, which finds favorable conditions at the interface of jet and external medium (Trussoni, Ferrari and Zaninetti, 1983). Very recently, the KH instability theory has been successfully used to interpret the structure of the pc-scale jet in the radio source 3C273 (Lobanov and Zensus 2001). Also, it has been shown that any destabilization of the accretion disk creating a shock wave in the base of the jet excites KH instabilities (trailing components, Agudo et al. 2001).

At kiloparsec scales, the surprisingly stable propagation of relativistic jets in some sources (e.g., Cyg A) contrasts with the deceleration and decollimation observed in other sources (e.g. 3C31). These two sources are representative examples of Fanaroff-Riley type I (FRI, the latter) and Fanaroff-Riley type II (FR II, the former) radio sources (Fanaroff and Riley 1974). The morphological dichotomy of FRI and FR II sources may be related to the stability properties of relativistic jets with different kinetic powers (Rawlings and Saunders 1991).

This complex situation motivated us to study the interaction of relativistic jets with their ambient medium and more specifically the KH instability in detail, by applying linear stability analysis along with numerical simulations.

The linear analysis of KH instability in relativistic jets started with the work of Turland and Scheuer (1976) and Blandford and Pringle (1976) who derived and solved a dispersion relation for a single plane boundary between the relativistic flow and the ambient medium. Next, Ferrari, Trussoni and Zaninetti (1978) and Hardee (1979) examined properties of KH instability in relativistic cylindrical jets by following the derivation of the dispersion relation in the nonrelativistic case, in the vortex sheet approximation, done by Gill (1965). They numerically solved the dispersion relation, found unstable KH modes and classified them into the fundamental (surface) and reflection (body) family of modes. The classification is related to the number of nodes, across the jet, of sound waves reflecting in between jet boundaries. An internal wave pattern is formed by the composition of oblique waves, for which the jet interior is a resonant cavity. The physical meaning of KH instability in supersonic jets has been discussed by Payne and Cohn (1985), who have shown that the presence of instability is associated with the overreflection of soundwaves (the

modulus of reflection coefficient is larger than 1) on the sheared jet boundaries.

Subsequent studies include effects of magnetic field (Ferrari, Trussoni and Zaninetti 1981), the effects of the shear layer, replacing the vortex sheet in the nonrelativistic planar case (Ferrari, Massaglia and Trussoni 1981; Ray 1982; Roy Choudhury and Lovelace 1984), and conical and cylindrical jet geometry (Birkinshaw 1984; Hardee 1984, 1986, 1987). The effects of a cylindrical shear layer have been examined by Birkinshaw (1991a) in the nonrelativistic case, attempted by Urpin (2002) in the relativistic case and the presence of multiple components (jet + sheath + ambient medium) was investigated by Hanasz and Sol (1996, 1998). Other authors have investigated current-driven modes in magnetized jets (Appl and Camenzind 1992; Appl 1996) in addition to KH modes.

An extension of the linear stability analysis in the relativistic case to the weakly non-linear regime has been performed by Hanasz (1995) and led to the conclusion that Kelvin-Helmholtz instability saturates at finite amplitudes due to various non-linear effects. An explanation of the nature of the mentioned non-linearities has been proposed by Hanasz (1997). The most significant effect results from the relativistic character of the jet flow, namely from the fact that the velocity perturbation cannot exceed the speed of light.

A more recent approach is to perform a linear stability analysis in parallel with numerical simulations and to compare the results of both methods in the linear regime and then to follow the non-linear evolution of the KH instability resulting from numerical simulations. Hardee and Norman (1988) and Norman and Hardee (1988) have made such a study for nonrelativistic jets in the spatial approach and Bodo et al. (1994) in the temporal approach. In the relativistic case this kind of approach was applied for the first time by Hardee et al. (1998) in the case of axisymmetric, cylindrical jets and then extended to the 3D case by Hardee et al. (2001).

Similarly to the linear stability analysis, the numerical simulations of jet evolution can be performed following both the spatial and the temporal approach, depending on the particular choice of initial and boundary conditions. In the temporal approach one considers a short slice of jet limited by periodic boundaries along the jet axis, and adds some specific perturbation, eg. an eigenmode resulting from the linear stability analysis. Due to the periodic boundary conditions the growing perturbations can only be composed of modes having a wavelength equal to the length of the computational box and/or its integer fractions (Bodo et al. 1994, 1995, 1998). Whereas the spa-

tial approach appears more appropriate to analyze the global dynamics and morphology of the whole jet, the temporal approach is suitable for the comparison between the numerical results and analytical studies of the jet stability because, due to the fact that only part of the jet is simulated, a high effective numerical resolution is achievable with limited computer resources.

Numerical simulations (Martí et al. 1997; Hardee et al. 1998, Rosen et al. 1999) demonstrate that jets with high Lorentz factors and high internal energy are influenced very weakly by the Kelvin-Helmholtz instability. Moreover, Hardee et al. (1998), Rosen et al. (1999) note that contrary to the cases with lower Lorentz factors and lower internal energies, the relativistically hot and high Lorentz factor jets do not develop modes of KH instability predicted by the linear theory. They interpret this fact as the result of a lack of appropriate perturbations generating the instability in the system. In the limit of high internal energies of the jet matter the Kelvin-Helmholtz instability is expected to develop with the highest growth rate.

Recently, KH linear theory has been successfully applied to the interpretation of observed features in extragalactic jets (Lobanov and Zensus 2001, Lobanov et al. 2003, Hardee 2003, Hardee et al. 2005), where, under some assumptions regarding the validity of the linear regime in jets, the authors have interpreted the structures in the jets in 3C 273, M 87 and 3C 120, and have derived the physical parameters governing the flow.

1.5 Motivation of the work

Jet research is immediately related to several fundamental astrophysical phenomena: the jets are composed of particles moving at relativistic speeds, and they can serve as a laboratory for high energy plasma physics (e.g., Kirk and Duffy 1999); the jets are formed in the vicinity of accretion disks and SMBHs in AGNs, and studies of the jet physics on sub-parsec to parsec scales can bring some light to the formation of powerful relativistic outflows in AGN (e.g., Meier et al. 2001); the formation and evolution of galaxies is also influenced by the presence of jets (e.g., Rawlings and Jarvis 2004), for they represent a funnel through which matter and energy are transported outwards from the source galaxies; the jets interact with the interstellar medium and intergalactic medium as they evolve, and therefore they can be used as a probe of the physical conditions of these media (e.g., Gómez et al. 2000). Researching the extragalactic jets is therefore not only important by itself, but also has

a much wider impact on a number of astrophysical fields.

This thesis is an approach to one of the pieces of the puzzle of jet physics, an academic exercise in order to fill a gap in the understanding of the non-linear evolution of instabilities in relativistic jets, a crucial and still not understood problem in extragalactic jet physics. This may help us not only to learn more on this topic, but also, through the coupling we mentioned above, to investigate on the properties of the ambient media in which these objects evolve.

1.6 Methodology

In previous sections we have summarized the state-of-the-art in extragalactic jets. One of the conclusions that can be derived from them is that the better observations we are able to perform, the more complex the problem seems to be. Simple analytical models are very useful for a first approach to the understanding of jet physics, but they are far not sufficient for the next steps, as jet formation, propagation and interactions between components in the jet or with the external medium, particle acceleration and energy losses involve non-linear effects, turbulent dynamics and microphysics. Numerical simulations allow us to try to solve problems which are impossible to solve under analytical assumptions.

Numerical codes only give an approximation to real systems, they idealize systems by dividing them in computational cells, what creates an artificial viscosity which hides many microscopic processes, and, even, in the case of this PhD thesis, our code only solves relativistic hydrodynamic systems, without taking into account magnetic fields, relativistic particle transport... However, we have seen that jet emission requires the presence of magnetic fields or high energy particle population, and that jets move through complex ambient media, composed by clouds, stars, black holes... among other *realistic* features that we have not included in this work. Nevertheless, the only way to complete the puzzle we have at hand is to study each of the pieces, very carefully, understand it, and then place it along with the rest.

1.7 Organization of the work

This work is divided in three main parts. In Chapter 2 we review our results in the linear and non-linear regime for the stability of relativistic flows in the

vortex sheet approximation for slab jets, where we also include discussion on the nature of Kelvin-Helmholtz modes and their structures; in Chapter 3 we present results for the case of sheared relativistic jets with slab and cylindrical geometry in more general setups, and Chapter 4 we review results on two possible astrophysical applications of the work, to parsec and kiloparsec scale jets.

Chapter 2

STABILITY IN THE VORTEX SHEET LIMIT

In this Chapter we present the results obtained from the study of the stability of slab, relativistic jets, in the vortex sheet limit, in both the linear and non-linear regimes. These results were published in Perucho et al. (2004a) and Perucho et al. (2004b).

2.1 Linear analysis

Following the standard procedure (see eg. Gill 1965; Ferrari, Trussoni and Zaninetti 1978; Hardee 1979) we derive the dispersion relation for the Kelvin-Helmholtz modes. We focus on the simplest geometrical configuration of two-dimensional (X,Z) planar relativistic jets (moving in the Z direction) and apply the temporal stability analysis.

The full set of equations describing the current problem consists of the set of relativistic equations of hydrodynamics for a perfect fluid, (e.g. Ferrari, Trussoni and Zaninetti 1978)

$$\gamma^2 \left(\rho + \frac{p}{c^2} \right) \left[\frac{\partial \mathbf{v}}{\partial t} + (\mathbf{v} \cdot \nabla) \mathbf{v} \right] + \nabla p + \frac{\mathbf{v}}{c^2} \frac{\partial p}{\partial t} = 0, \quad (2.1)$$

$$\gamma \left(\frac{\partial \rho}{\partial t} + \mathbf{v} \cdot \nabla \rho \right) + \left(\rho + \frac{p}{c^2} \right) \left[\frac{\partial \gamma}{\partial t} + \nabla \cdot (\gamma \mathbf{v}) \right] = 0, \quad (2.2)$$

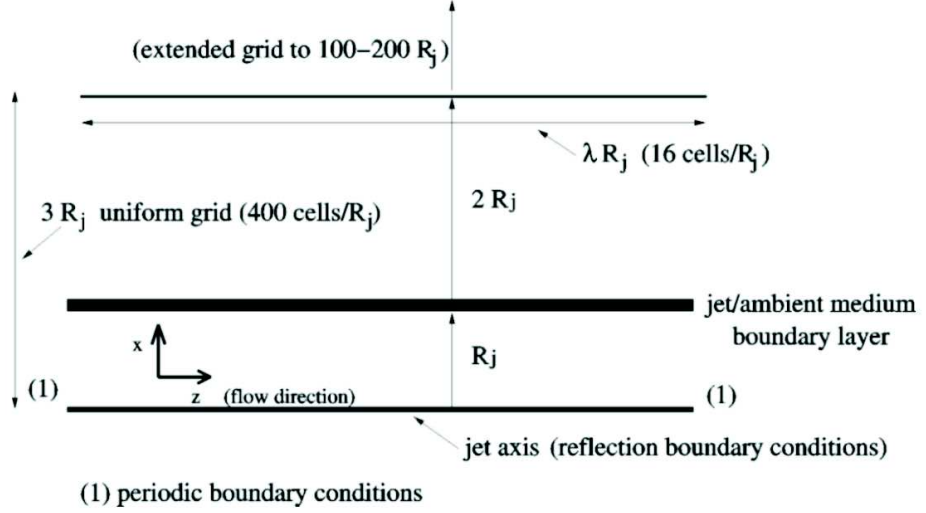


Figure 2.1: The geometry of the flow considered in the linear stability analysis and the numerical simulations (see Sect. 2.3), including a description of the boundary conditions.

and an (adiabatic) equation of state

$$p\rho_0^{-\Gamma} = \text{const.} \quad (2.3)$$

In the preceding equations, c is the speed of light, ρ_0 is the particle rest mass density (i.e., $\rho_0 \equiv mn$, where m is the particle rest mass and n the number density in the fluid rest frame). ρ stands for the relativistic density which is related to the particle rest mass density and the specific internal energy, ε , by $\rho = \rho_0(1 + \varepsilon/c^2)$. The enthalpy is defined as $w = \rho + p/c^2$, the sound speed is given by $c_s^2 = \Gamma p/w$, where Γ is the adiabatic index. The relation between pressure and the specific internal energy is $p = (\Gamma - 1)\varepsilon\rho_0$. The velocity of the fluid is represented by \mathbf{v} and γ is the corresponding Lorentz factor.

The assumed geometry of the jet considered in the forthcoming linear stability analysis and the numerical simulations is sketched in Fig. 2.1. First

of all the considered jet is 2D-planar and symmetric with respect to the $x = 0$ plane. The flow in the jet moves in the positive z direction and its matter forms a contact discontinuity (a vortex sheet) with the matter of external medium at $x = -R_j$ and $x = R_j$. From now on all quantities representing the jet will be assigned with the 'j' subscript and the quantities representing the ambient medium will be assigned with 'a'.

The following matching conditions are imposed on the interface between the jet and the ambient medium

$$p_a = p_j \quad \text{for} \quad |x| = R_j \quad (2.4)$$

$$h_a = h_j \quad \text{for} \quad |x| = R_j. \quad (2.5)$$

The matching conditions express the assumption of equality of the jet and ambient pressures and the equality of transversal displacements of jet (h_j) and ambient (h_a) fluid elements adjacent to the jet boundary (at $|x| = R_j$).

In addition, the Sommerfeld radiation condition (expressing the disappearance of perturbations at the infinity) will be applied for linear perturbations.

2.1.1 Equilibrium state for the linear stability analysis

We assume that the initial state is an equilibrium configuration. The initial equilibrium can be described by the following set of independent parameters: the Lorentz factor corresponding to the unperturbed longitudinal jet velocity, v_j , $\gamma = (1 - v_j^2/c^2)^{-1/2}$, the particle rest mass density of the jet ρ_{0j} (the particle rest mass density of the ambient medium is normalized to unity: $\rho_{0a} = 1$) and the specific internal energy of the jet ε_j . The ambient medium is assumed to be at rest ($v_a = 0$).

The other dependent parameters describing the equilibrium state are: the internal jet Mach number $M_j = v_j/c_{sj}$ corresponding to the initial jet longitudinal velocity, the relativistic rest mass density contrast:

$$\nu = \frac{\rho_{0j}(1 + \varepsilon_j)}{\rho_{0a}(1 + \varepsilon_a)}, \quad (2.6)$$

or, equivalently, the enthalpy contrast:

$$\eta = \frac{w_j}{w_a} = \frac{\rho_{0j}(1 + (\Gamma_j - 1)\varepsilon_j/(1 + \varepsilon_j))}{\rho_{0a}(1 + (\Gamma_a - 1)\varepsilon_a/(1 + \varepsilon_a))}, \quad (2.7)$$

and the specific internal energy of the ambient medium

$$\varepsilon_a = \frac{(\Gamma_j - 1)\rho_{0j}}{(\Gamma_a - 1)\rho_{0a}} \varepsilon_j, \quad (2.8)$$

which is related to the specific internal energy of the jet through the pressure balance condition.

2.1.2 Dispersion relation

The first step towards the dispersion relation (see Hanasz and Sol 1996) is to reduce the equations (2.1) - (2.5) to the dimensionless form through the normalization of spatial coordinates to the jet radius R_j , velocities to the sound speed of the jet material c_{sj} , time to the dynamical time R_j/c_{sj} and pressure to the equilibrium pressure.

The next step is to decompose each dependent quantity into the equilibrium value and the linear perturbation. After the reduction of equations to the dimensionless form and substitution of the perturbed quantities in equations (2.1)-(2.5), we obtain the following set of dimensionless linearized equations. In the following the dimensionless quantities will be assigned the same symbols as the previous dimensional ones. The subscript '1' stands for the linear perturbation of the corresponding variable. For the jet medium we get

$$\Gamma_j \gamma^2 \left(\frac{\partial \mathbf{v}_{j1}}{\partial t} + (\mathbf{v}_j \cdot \nabla) \mathbf{v}_{j1} \right) + \nabla p_{j1} + \frac{\mathbf{v}_j}{c^2} \frac{\partial p_{j1}}{\partial t} = 0, \quad (2.9)$$

$$\begin{aligned} \frac{\partial p_{j1}}{\partial t} + \mathbf{v}_j \cdot \nabla p_{j1} + \Gamma_j \nabla \cdot \mathbf{v}_{j1} \\ + \gamma^2 \Gamma_j \frac{\mathbf{v}_j}{c^2} \left(\frac{\partial \mathbf{v}_{j1}}{\partial t} + (\mathbf{v}_j \cdot \nabla) \mathbf{v}_{j1} \right) = 0 \quad , \end{aligned} \quad (2.10)$$

where \mathbf{v}_j is the initial (unperturbed) jet velocity in units of jet internal sound speed, c is the speed of light in units of the sound speed and the normalized pressure $p_0 = 1$ is omitted in the equations. For the ambient medium we get

$$\frac{\Gamma_j}{\eta} \frac{\partial \mathbf{v}_{a1}}{\partial t} + \nabla p_{a1} = 0, \quad (2.11)$$

$$\frac{\partial p_{a1}}{\partial t} + \Gamma_a \nabla \cdot \mathbf{v}_{a1} = 0. \quad (2.12)$$

The linearized matching conditions (2.4) and (2.5) at the jet interface read

$$p_{a1} = p_{j1} \quad \text{for } |x| = 1 \quad (2.13)$$

$$h_{a1} = h_{j1} \quad \text{for } |x| = 1, \quad (2.14)$$

where the displacements of fluid elements adjacent to the contact interface in the linear regime are related to transversal velocities by the following formulae

$$v_{jx1} = \left(\frac{\partial}{\partial t} + v_j \frac{\partial}{\partial z} \right) h_{j1}, \quad (2.15)$$

$$v_{ax1} = \frac{\partial}{\partial t} h_{a1}. \quad (2.16)$$

The following wave equations can be derived from the equations (2.9) - (2.12), respectively for the jet

$$\begin{aligned} \gamma^2 \left(\frac{\partial}{\partial t} + v_j \frac{\partial}{\partial z} \right)^2 p_{j1} - \frac{\partial^2 p_{j1}}{\partial x^2} \\ - \gamma^2 \left(\frac{\partial}{\partial z} + \frac{v_j}{c^2} \frac{\partial}{\partial t} \right)^2 p_{j1} = 0, \end{aligned} \quad (2.17)$$

and for the ambient medium

$$\frac{\partial^2 p_{a1}}{\partial t^2} - \frac{\eta \Gamma_a}{\Gamma_j} \left(\frac{\partial^2 p_{a1}}{\partial x^2} + \frac{\partial^2 p_{a1}}{\partial z^2} \right) = 0. \quad (2.18)$$

It is apparent that Eq. (2.17) and (2.18) describe propagation of oblique sound waves in the jet and ambient medium respectively.

The next step is to substitute perturbations of the form

$$\delta_{j1} = [\delta_j^+ F_j^+(x) + \delta_j^- F_j^-(x)] \exp i(k_{\parallel} z - \omega t) + c.c. \quad (2.19)$$

with $F_j^{\pm}(x) = \exp(\pm i k_{j\perp} x)$ to describe waves propagating in positive and negative x -directions in the beam. Here we use k_{\parallel} and $k_{a,j\perp}$ for longitudinal and transverse wavenumbers. Perturbations in the external medium are of the form

$$\delta_{a1} = \delta_a^+ F_a^+(x) \exp i(k_{\parallel} z - \omega t) + c.c. \quad (2.20)$$

where $F_a^+(x) = \exp(ik_{a\perp}x)$ for $|x| > 1$. Assuming that $\text{Re}(k_{a\perp}) > 0$, only outgoing waves are present in the ambient medium. After the substitution of the explicit forms of pressure perturbations to equations (2.17) and (2.18) we obtain the following expressions for the perpendicular components of wavevectors

$$k_{a\perp} = \left(\frac{\Gamma_j}{\eta\Gamma_a} \omega^2 - k_{\parallel}^2 \right)^{1/2} \quad (2.21)$$

$$k_{j\perp} = (\omega'^2 - k_{\parallel}'^2)^{1/2} \quad (2.22)$$

which are standard relations for linear sound waves in both media (note that $\eta\Gamma_a/\Gamma_j$ is the squared sound speed of ambient medium in units of the sound speed of jet), $\omega' = \gamma(\omega - v_j k_{\parallel})$ and $k_{\parallel}' = \gamma(k_{\parallel} - \frac{v_j}{c^2} \omega)$ are frequency and wavenumber of the internal sound wave in the reference frame comoving with the jet. The wavevectors $\mathbf{k}_j = (k_{j\perp}, k_{j\parallel})$ and $\mathbf{k}_a = (k_{a\perp}, k_{a\parallel})$ determine the direction of propagation of sound waves in the jet and ambient medium respectively. Vanishing of $k_{j\perp}$, for instance, would mean that the jet internal sound waves move in the axial direction. In cases $k_{j\perp} \neq 0$ and/or $k_{a\perp} \neq 0$ the propagation of the sound waves is oblique with respect to the jet axis.

The corresponding perturbation of the jet surface can be written as

$$h_{a1} = h_{j1} = h \exp i(k_{\parallel}z - \omega t) + c.c., \quad (2.23)$$

which after the substitution to equations (2.15) and (2.16) reads

$$v_{jx1} = -i(\omega - v_j k_{\parallel}) h_{j1}, \quad (2.24)$$

$$v_{ax1} = -i\omega h_{j1}. \quad (2.25)$$

With the aid of the above perturbations the whole system of partial differential equations is reduced to a set of homogeneous linear algebraic equations. The dispersion relation appears as solvability condition of the mentioned set of equations, namely it arises from equating the determinant of the linear problem to zero. Within the present setup, the dispersion relation for the Kelvin-Helmholtz instability in supersonic, relativistic, two-dimensional slab jets can be written as (Hanasz and Sol 1996, Turland and Scheuer 1976, Bland-

ford and Pringle 1976)

$$\begin{aligned} \frac{1}{\nu\Gamma_j} \frac{\omega}{\omega'} \frac{(\omega'^2 - k_{\parallel}^{\prime 2})^{1/2}}{\left(\frac{\omega^2}{\nu\Gamma_a} - k_{\parallel}^2\right)^{1/2}} &= \\ &= \begin{cases} \coth i(\omega'^2 - k_{\parallel}^{\prime 2})^{1/2} & \text{for } s = 1 \\ \text{th } i(\omega'^2 - k_{\parallel}^{\prime 2})^{1/2} & \text{for } s = -1 \end{cases} \end{aligned} \quad (2.26)$$

where $s = \pm 1$ is the symmetry of perturbation. We will focus on symmetric perturbations ($s = 1$).

Dispersion relation in cylindrical coordinates is derived in the same way. However differential equations corresponding to eqs. (2.17) and (2.18) are:

$$\begin{aligned} \gamma^2 \left(\frac{\partial}{\partial t} + v_j \frac{\partial}{\partial z} \right)^2 p_{j1} - \frac{\partial^2 p_{j1}}{\partial r^2} - \frac{1}{r} \frac{\partial p_{j1}}{\partial r} \\ - \gamma^2 \left(\frac{\partial}{\partial z} + \frac{v_j}{c^2} \frac{\partial}{\partial t} \right)^2 p_{j1} = 0, \end{aligned} \quad (2.27)$$

$$\frac{\partial^2 p_{a1}}{\partial t^2} - \frac{\eta\Gamma_a}{\Gamma_j} \left(\frac{\partial^2 p_{a1}}{\partial r^2} + \frac{1}{r} \frac{\partial p_{a1}}{\partial r} + \frac{\partial^2 p_{a1}}{\partial z^2} \right) = 0. \quad (2.28)$$

These can be written in the form of Bessel equations. Therefore, and due to the imposed boundary conditions, the solution to the first is a Bessel function and that of the second is a Hankel function (which tends to zero at infinity, accomplishing the Sommerfeld condition). Using the match of pressure and displacement values at the jet boundaries as before, we obtain (Ferrari et al. 1978, Hardee 1979, 1987):

$$\frac{\omega^2 \beta_j}{\eta \omega'^2 \beta_a} \frac{J'_n(\beta_j R_j)}{J_n(\beta_j R_j)} = \frac{H_n^{(1)'}(\beta_a R_j)}{H_n^{(1)}(\beta_a R_j)}, \quad (2.29)$$

where

$$\beta_j = \left(\omega'^2 - k_{\parallel}^{\prime 2} \right)^{1/2}, \quad (2.30)$$

with ω' and k_{\parallel}' equivalent to previous ω' and k_{\parallel}' respectively,

$$\beta_a = \left(\omega^2 - k_{\parallel}^2 \right)^{1/2}, \quad (2.31)$$

J_n and H_n are Bessel and Hankel functions, and primes denote derivatives with respect to their arguments.

2.1.3 Solution

In order to solve equation (2.26) we can consider one of these two possibilities:

- The spatial approach. Real frequency and complex wave-number are assumed, where the real part of the wavenumber gives the wavelength of the perturbation and the imaginary part is the growth length. The latter represents the inverse of the distance needed for the perturbation amplitude to e-fold (see Equation 2.19). These are therefore spatially growing wave-form perturbations, so in order to study their effects on the flow one must follow their evolution downstream.
- The temporal approach. Real wave-number and complex frequency are assumed, where the real part of the frequency is the frequency of the wave and the imaginary part is the growth rate. This is the inverse of the time needed for the perturbation to e-fold. These are temporally growing wave-form perturbations, and in order to study them one must follow the temporal evolution of the perturbed portion of the flow.

Equation 2.26 was solved numerically with the aid of the Newton-Raphson method (Press et al. 1992, see also Appendix B) using the temporal approach, for a series of flow parameters which were going to be used in numerical simulations (see Table 2.1). We obtained the complex frequency (ω_r, ω_i) as a function of the parallel component of the wavenumber k_{\parallel} . Solutions are plotted in Figs. 2.2-2.6. Newton-Raphson method is used in the following way: we start with a grid of initial guess points in the complex (ω_r, ω_i) plane and look for solutions around them. Solutions are called eigenmodes of the system, and any small perturbation in the flow can excite those having the same frequency or wavelength. Normally, out of the eigenmodes excited at a given frequency or wavelength, that with the largest growth rate or smaller growth length will dominate the development of the instability. As a consequence of this development, portions of fluid are displaced from their stationary flow line, and, globally, this leads to distortions of the whole flow. The form in which the flow is distorted depends on the properties of the excited mode.

Results show that growth rates for surface and body modes are higher for hotter (and therefore higher relativistic density ratio in our approach) and/or slower jets, and that, for colder and/or faster jets, instabilities appear at longer wavelengths.

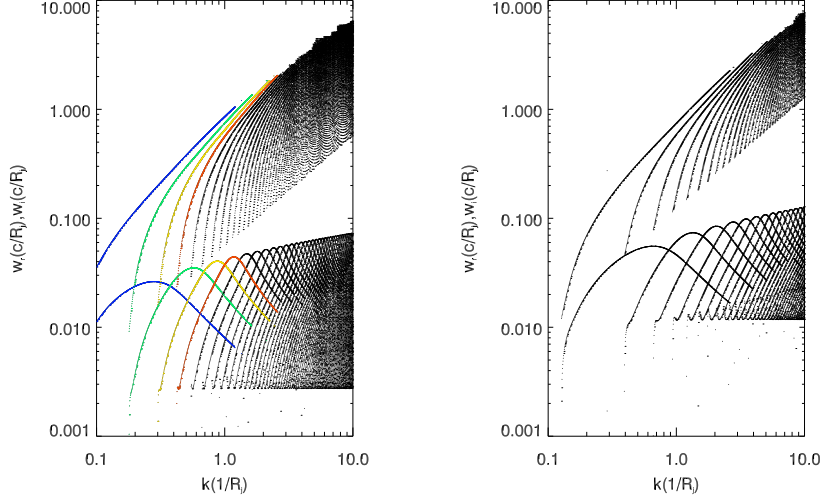


Figure 2.2: Symmetric solutions of the dispersion relation for slab jets with $\gamma = 5$, $\varepsilon = 0.07 c^2$ and $\nu = 0.11$ (left panel) and $\gamma = 5$, $\varepsilon = 0.4 c^2$ and $\nu = 0.14$ (right panel). Top lines represent the real part of frequency, and lower lines stand for the corresponding imaginary part of the modes. In left panel colors identify real and imaginary parts of single modes as an example for the reader.

2.1.4 Modes

Solutions to the dispersion relation depend on the characteristics of the perturbation. In the previous section, we have shown the derivation of dispersion relations for slab (planar symmetry) and cylindrical flows. In the former, we have two different main kinds of solutions, symmetric and antisymmetric, whereas in the latter we find an infinite number of modes, depending on the number of wave nulls caused by the perturbation in the jet surface (see Fig. 2.7). If no nulls are found in the surface ($n = 0$ in equation (2.29)), the mode is called 'pinching' mode, as it pinches the flow, which is also the name given to symmetric perturbations in slab jets ($s = 1$ in equation (2.26)). If there is one null the mode is called 'helical', as it generates helical patterns, and this is also the name given to antisymmetric modes in slab jets. If the number of nulls is larger than one, the modes are called 'fluting' modes, and depending on the number of nulls they may be elliptical ($n = 2$), triangular ($n = 3$)

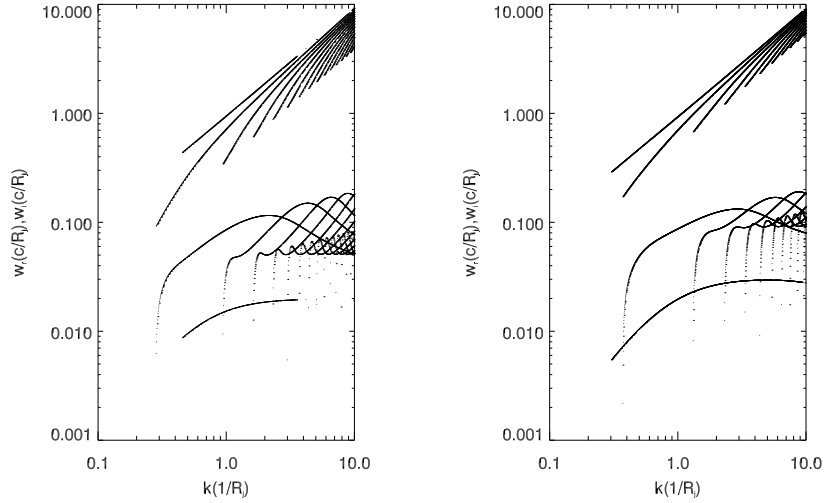


Figure 2.3: Same as Fig. 2.2 for jets with $\gamma = 5$, $\varepsilon = 6.1 c^2$ and $\nu = 0.44$ (left panel) and $\gamma = 5$, $\varepsilon = 60 c^2$ and $\nu = 0.87$ (right panel).

and so on (see Birkinshaw 1991b). Also, the angle of propagation of a mode wave along the jet depends on this azimuthal wave-number $\theta = \tan^{-1}(n/kR)$ (Hardee 2000), being k here wave-number along flow direction. This means that the lower the order of the mode, the more *longitudinal* its propagation is.

The disruptive character of a mode relies on its capability to extract kinetic energy from the jet. Generation of transversal displacements in the fluid cause the transfer of longitudinal momentum to the external medium in contact regions. The generation of transversal momentum results from the conversion of kinetic energy of the flow into internal energy, which overpressures the parts of the jet where it occurs with respect to others, thus generating transversal waves. These waves bounce once and again in the jet axis and the boundary layer, and instabilities arise when the transmission and reflection coefficients of the waves in that layer become larger than one (Payne and Cohn 1985). This fact makes that outgoing and incoming waves get larger and larger amplitudes, thus generating the instability.

Payne and Cohn (1985) define reflection and transmission coefficients in terms of the acoustic impedances (Z_j and Z_a , the ratio between pressure and

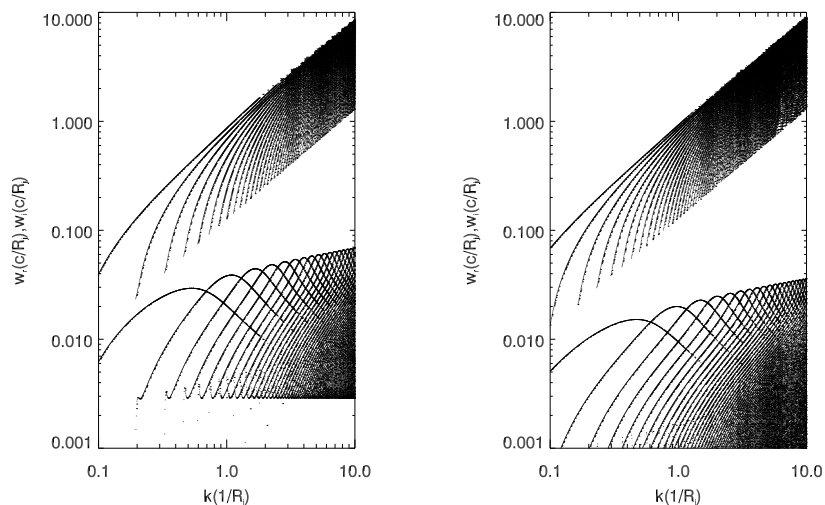


Figure 2.4: Same as Fig. 2.2 for jets with $\gamma = 10$, $\varepsilon = 0.4 c^2$ and $\nu = 0.14$ (left panel) and $\gamma = 20$, $\varepsilon = 0.4 c^2$ and $\nu = 0.14$ (right panel).

transversal speed) in both media:

$$\begin{aligned}\mathcal{R} &= \frac{Z_a - Z_j}{Z_j + Z_a} \\ \mathcal{T} &= \frac{2 Z_a}{Z_j + Z_a}\end{aligned}\tag{2.32}$$

If we write the impedances in terms of perturbations and these in terms of mode propagation angle, we find that maximum reflection and transversal coefficients arise for perturbations colliding with the contact surface with the Mach angle, producing resonances or peaks in the mode profile.

2.1.5 Surface and body modes

We have seen in Figs. 2.2-2.6 that for each of the symmetric solutions, many different solutions in the form of continuous lines appear. These are the sub-modes of each different kind of perturbation, which includes one surface (or fundamental) mode and an infinite number of body (or reflection) modes. The type of sub-mode is determined by the number of nulls the wave has

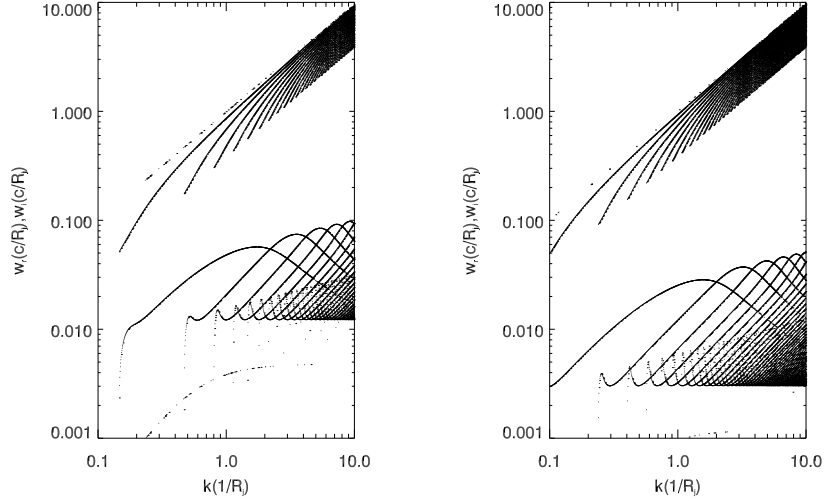


Figure 2.5: Same as Fig. 2.2 for jets with $\gamma = 10$, $\varepsilon = 6.1 c^2$ and $\nu = 0.44$ (left panel) and $\gamma = 20$, $\varepsilon = 6.1 c^2$ and $\nu = 0.44$ (right panel).

in the transverse direction to the flow. In order to understand this, we can compare the jet to a waveguide in the electromagnetic theory. In Kelvin-Helmholtz instabilities, the surface mode is defined as that presenting no nulls perpendicular to the flow, like the fundamental mode in waveguides, and body modes are those which do present nulls, like reflection modes in waveguides. The main difference between them is that in the case of jets, the number of wavelengths in the transverse section is not necessarily an integer, i.e., the mode is called fundamental for all combinations of wavelengths and frequencies which do not present a single null inside the cavity $k_{\perp} < \pi/R_j$, first body mode for all those combinations which give only one null ($\pi/R_j < k_{\perp} < 2\pi/R_j$), second body mode for those giving two nulls ($2\pi/R_j < k_{\perp} < 3\pi/R_j$), etc. We have seen in equation (2.22) that k_{\perp} is a function of k_{\parallel} and ω . This makes that body modes show up as continuous lines starting at a given wavenumber (longest unstable wavelength of that mode), and that the surface mode is the only one which has non-zero solutions when $k_{\parallel} \rightarrow 0$ for it may appear with arbitrarily large transversal wavelengths. These lines represent the combinations of k_{\parallel} and ω for which k_{\perp} is within two multiples of π/R_j .

Summarizing, from $k_{\parallel} = 0$ to larger values, the first mode to appear with

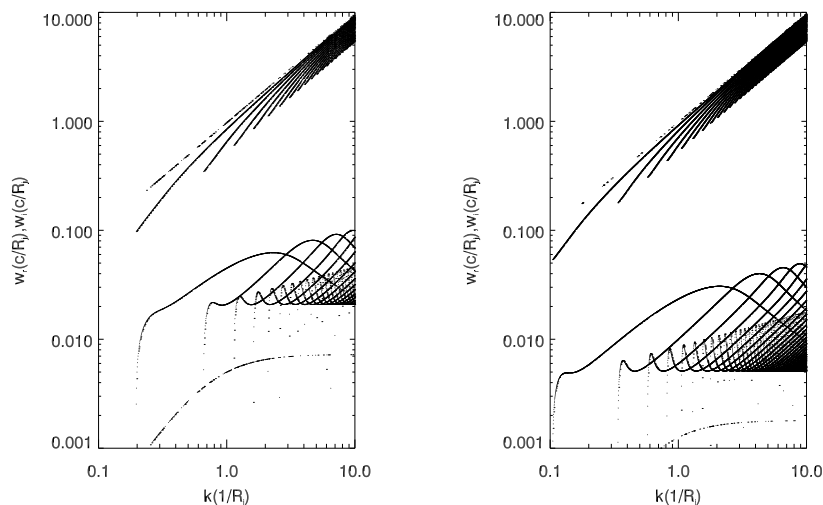


Figure 2.6: Same as Fig. 2.2 for jets with $\gamma = 10$, $\varepsilon = 60 c^2$ and $\nu = 0.87$ (left panel) and $\gamma = 20$, $\varepsilon = 60 c^2$ and $\nu = 0.87$ (right panel).

non-vanishing solutions is the fundamental mode. Then, when a suitable combination of wave-numbers and frequencies allows the presence of a mode with a transversal zero inside the jet, first body mode appears in the solution, followed by second, third, etc. body modes. Body modes have all the same structure determined by the maximum unstable wavelength (minimum wavenumber for which a solution exists) and by a resonant wavenumber (the wavenumber for which we find the highest growth-rate of the mode). We also observe that in symmetric instabilities, the fundamental mode is damped with respect to body modes, due to its lack of transversal structure which makes difficult the interaction of waves with the boundaries and therefore makes it a more *stable* mode.

2.2 Note on temporal versus spatial approach

The main differences between the use of both approaches arises when the design of the numerical simulations has to be undertaken. On one hand, the spatial approach consists on perturbing a jet at the inlet and let the

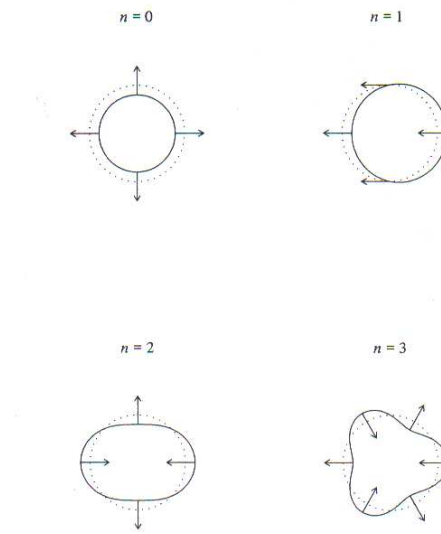


Figure 2.7: Deformations of jets by Kelvin-Helmholtz instability modes (from Birkinshaw 1991b).

perturbations grow downstream; this can be applied to a steady (if we are interested in the growth of specific perturbations; e.g. Agudo et al. 2001) or injected jet in a physically long grid (if we are interested in the stability of the jet against perturbations generated by the interaction with the external medium or the backflow; Hardee et al. 1998). On the other hand, the temporal approach consists on considering a portion of an infinite jet in a grid box with periodic boundary conditions, far from the inlet or the interaction with the ambient medium, and let the perturbation grow with time (Bodo et al. 1994 for the classical case).

Certainly, the spatial approach allows for a more realistic approximation to real jets. However, larger grids are needed, and therefore less numerical resolution is used. In this work, we have used the temporal approach, which, though less realistic, it is maybe more efficient in the process of understanding the evolution and effects of Kelvin-Helmholtz instabilities in relativistic flows, from a theoretical point of view. The latter approach allows for the use of smaller grids (the size of the wavelength of the mode) with higher resolution, what has proven to be crucial in order to follow the linear regime and be confident about our results on the non-linear phases.

The necessity of performing the simulations which we present here is evident from a theoretical point of view, in order to learn as much as possible on the stability properties of jets. This information will allow us to undertake more realistic computations and be able to interpret them in depth.

2.3 Numerical simulations

Once the solutions of the dispersion relation $\omega(k)$ are found, the derivation of eigenstates (each one of the solutions) of the system is straightforward. By utilizing the set of relativistic equations (2.9) - (2.12) one can relate perturbations of gas density and velocity to the perturbation of pressure.

First, we choose the amplitude of the pressure wave in the jet, p_j^+ , as a free constant and then relate the other constants to its value. The corresponding '-' amplitudes are computed by multiplying these values by s in case of pressure and longitudinal velocity and by $-s$ in the case of transversal velocity.

The amplitude of pressure wave in the ambient medium, p_a^+ , is found from the pressure matching condition at $x = 1$:

$$p_a^+ \exp(i k_{a\perp}) = p_j^+ \exp(i k_{j\perp}) + s p_j^- \exp(-i k_{j\perp}). \quad (2.33)$$

The remaining amplitudes of velocity perturbations are

$$v_{ax}^+ = \frac{\eta}{\Gamma_j} \frac{k_{a\perp}}{\omega} p_a^+, \quad (2.34)$$

$$v_{jx}^+ = \frac{k_{j\perp}}{\Gamma_j \gamma \omega'} p_j^+, \quad (2.35)$$

$$v_{az}^+ = \frac{\eta}{\Gamma_j} \frac{k_{\parallel}}{\omega} p_a^+, \quad (2.36)$$

$$v_{jz}^+ = \frac{k'_{\parallel}}{\Gamma_j \gamma^2 \omega'} p_j^+, \quad (2.37)$$

where η is the ratio of enthalpies as defined earlier.

Regarding specific internal energy and rest-mass density, perturbations are calculated as follows:

$$\frac{\varepsilon_{a,j1}}{\varepsilon_{a,j}} = \frac{\Gamma_{a,j} - 1}{\Gamma_{a,j}} p_{a,j1} \quad (2.38)$$

$$\frac{\rho_{a,j1}}{\rho_{a,j} + 1/c^2} = \frac{1}{\Gamma_{a,j}} p_{a,j1}, \quad (2.39)$$

where $\rho_{a,j}$ refer to the relativistic density in ambient and jet media in dimensionless units, respectively, and $\rho_{a,j1}$ is the corresponding perturbation.

In the forthcoming discussion of results of numerical simulations we shall analyze the velocity components in the reference frame comoving with the jet. The standard Lorentz transformation formulae for the velocity components are

$$v'_z = \frac{v_z - v_j}{1 - v_z v_j / c^2}, \quad v'_x = \frac{v_x \sqrt{1 - v_j^2 / c^2}}{1 - v_z v_j / c^2}. \quad (2.40)$$

Assuming that the Lorentz transformation is applied for linear perturbations of sufficiently small amplitude, these transformation rules can be approximated by the following formulae

$$v'_{z1} = \gamma^2 v_{z1}, \quad v'_{x1} = \gamma v_{x1}, \quad (2.41)$$

where v_{x1} , v_{z1} are the velocity perturbations in the reference frame of the ambient medium and v'_{x1} , v'_{z1} are the velocity perturbations in the jet reference frame. These transformation rules tell us that the longitudinal and transversal velocity perturbations in the jet reference frame are larger by factors of γ^2 and γ respectively than the corresponding components in the rest (ambient medium) frame.

We proceed by performing numerical simulations of jet models to study the growth of unstable modes through the linear and non-linear phases. To this aim, we adopt as an equilibrium initial state the one described in the former section. In order to avoid the growth of random perturbations with wavelengths of the order of the cell size, we replace the transverse discontinuous profiles of equilibrium quantities by smooth profiles of the form

$$v_z(x) = \frac{v_j}{\cosh(x^m)} \quad (2.42)$$

$$\rho_0(x) = \rho_{0a} - \frac{\rho_{0a} - \rho_{0j}}{\cosh(x^m)} \quad (2.43)$$

(see Bodo et al. 1994), where m is the steepness parameter for the shear layer. Typically we used $m = 40$, for which the shear layer has a width $\sim 0.1R_j$.

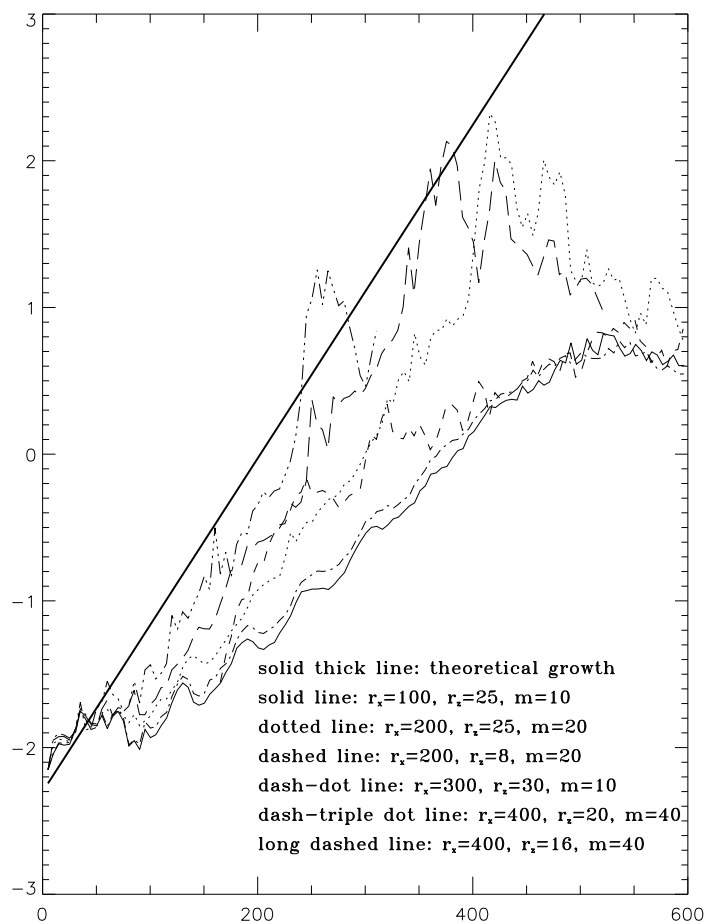


Figure 2.8: Linear growth of the amplitude of the pressure perturbation (in logarithmic scale) versus time (in units of R_j/c) for different resolutions. r_x stands for transversal resolution, r_z for longitudinal resolution, and m is the value which gives the shear layer steepness.

Growth of the instability depends critically on the numerical viscosity of the algorithm. Hence our first aim was to look for suitable numerical resolutions by comparing numerical and analytical results for the linear regime. We performed a number of simulations based on model A05 (see Table 2.1) chang-

ing longitudinal and radial resolution, and also the exponent m for the shear layer steepness (see eqs. 2.42 and 2.43). Figure 2.8 shows results for several of those simulations. If, for given transversal resolution, we introduced a shear layer which was too thin, we found the typical non-steady behavior appearing when a numerical tangential discontinuity is applied. However, in order to reproduce the linear regime, we needed a steep enough shear layer, due to the fact that theory was developed for a discontinuous separation between both media. We can see in figure 2.8 that $m = 10$ models are considerably damped with respect to the theoretical growth, independent of the transversal resolution. Hence resolution perpendicular to the flow appeared to be essential, requiring very high resolutions (400 zones/ R_j) and thin shear layers ($m = 40$) with 40 to 45 zones, i.e., an equilibrium between steepness and number of cells. Lower transversal resolutions and/or thicker shear layers led to non-satisfactory results, with a slow or damped growth. A very low longitudinal resolution results in damping of growth rate, too, as can be seen from comparison of $m = 20$ models, but $r_z = 16$ seems to give a reasonable growth rate compared to theory. This (small) resolution of 16 zones/ R_j along the jet was taken as a compromise between accuracy and computational efficiency.

The linear solutions derived correspond to an idealized case with a contact discontinuity at the jet interface. We decided to implement corresponding smoothed eigenstates obtained for the vortex sheet limit as approximate solutions for the case of sheared boundary. The validity of this procedure is proven *a posteriori* by the convergence of theoretical growth rates and the ones determined for simulated KH modes. Since, in case of the vortex sheet approximation, all first order dynamical variables (except pressure and the transversal displacement of fluid element adjacent to the jet boundary) are discontinuous, we apply the following smoothing of the equilibrium quantities and linear perturbations at the thin layer surrounding the jet boundary

$$\delta_1 = \delta_{a1} - \frac{\delta_{a1} - \delta_{j1}}{\cosh(x^m)}, \quad (2.44)$$

where δ stands for any perturbed variable. Such smoothed eigenstates are subsequently implemented as small-amplitude perturbations in the initial equilibrium model of the simulations.

As we said before, our first aim is to reproduce the linear evolution of unstable modes by means of hydrodynamical simulations. For this reason and in order to make the picture of evolution of the KH instability as clear and simple as possible, we perturb the equilibrium with the most unstable first

reflection mode, which is smoothed at the jet interface according to formula (2.44). The length of the computational grid is, in each simulation, equal to the wavelength of the aforementioned mode. Defining the initial state in such a way, we know precisely which growth rate to expect in numerical simulations. The difference between the expected and computed growth rates is a measure of the performance of the code in describing the linear regime and gives us confidence on the numerical results from the non-linear evolution.

The simulations have been performed using a high-resolution shock capturing code described in Section A to solve the equations of relativistic hydrodynamics in Cartesian planar coordinates.

The parameters of the simulations presented in this Section are listed in Table 2.1. Values of the parameters were chosen to be close to those used in some simulations by Hardee et al. (1998) and Rosen et al. (1999) and are chosen to span a wide range in thermodynamical properties as well as beam flow Lorentz factors. In all simulations, the density in the jet and ambient gases are $\rho_{0j} = 0.1$, $\rho_{0a} = 1$ respectively and the adiabatic exponent $\Gamma_{j,a} = 4/3$.

Since the internal rest mass density is fixed, there are two free parameters characterizing the jet equilibrium: the Lorentz factor and the jet specific internal energy displayed in columns 2 and 3 of Table 2.1. Models whose names start with the same letter have the same thermodynamical properties. Beam (and ambient) specific internal energies grow from models A to D. Three different values of the beam flow Lorentz factor have been considered for models B, C and D. The other dependent parameters mentioned in Section 2.1 are displayed in columns 4-10 of Table 2.1. Note that given our choice of ρ_{0j} , the ambient media associated to hotter models are also hotter due to pressure equilibrium condition. The first three columns in Table 2.2 show the longitudinal wavenumber together with oscillation frequency and the growth rate of the most unstable reflection mode. The following three columns display the same quantities in the jet reference frame. Next two columns show the perpendicular wavenumbers of linear sound waves in jet and ambient medium respectively. The last column in Table 2.2 shows the linear growth rate of KH instability in the jet reference frame expressed in dynamical time units, i.e. in which time is scaled to R_j/c_{sj} . All other quantities in the table, are expressed in units of the ambient density, ρ_{0a} , the speed of light, c , and the jet radius, R_j .

In order to extend our conclusions to a wider region in the initial parameter space, we performed a new set of simulations (F-L), which will be discussed

Model	γ	ρ_{0j}	ε_j	ε_a	c_{sj}	c_{sa}	p	ν	η	M_j
A05	5	0.1	0.08	0.008	0.18	0.059	0.0027	0.11	0.11	5.47
B05	5	0.1	0.42	0.042	0.35	0.133	0.014	0.14	0.15	2.83
C05	5	0.1	6.14	0.614	0.55	0.387	0.205	0.44	0.51	1.80
D05	5	0.1	60.0	6.000	0.57	0.544	2.000	0.87	0.90	1.71
B10	10	0.1	0.42	0.042	0.35	0.133	0.014	0.14	0.15	2.88
C10	10	0.1	6.14	0.614	0.55	0.387	0.205	0.44	0.51	1.83
D10	10	0.1	60.0	6.000	0.57	0.544	2.000	0.87	0.90	1.73
B20	20	0.1	0.42	0.042	0.35	0.133	0.014	0.14	0.15	2.89
C20	20	0.1	6.14	0.614	0.55	0.387	0.205	0.44	0.51	1.83
D20	20	0.1	60.0	6.000	0.57	0.544	2.000	0.87	0.90	1.74
F	5	0.01	0.77	0.008	0.41	0.058	0.0026	0.018	0.02	2.38
G	5	0.001	7.65	0.008	0.55	0.058	0.0026	0.009	0.01	1.78
H	5	0.0001	76.5	0.008	0.57	0.058	0.0026	0.008	0.01	1.71
I	11.7	0.01	0.77	0.008	0.41	0.058	0.0026	0.018	0.02	2.42
J	15.7	0.001	7.65	0.008	0.55	0.058	0.0026	0.009	0.01	1.81
K	15.7	0.01	0.77	0.008	0.41	0.058	0.0026	0.018	0.02	2.43
L	11.7	0.001	7.65	0.008	0.55	0.058	0.0026	0.009	0.01	1.81

Table 2.1: Equilibrium parameters of different simulated jet models. The listed parameters are: γ - jet Lorentz factor, ρ_{0j} - rest mass density, ε_j and ε_a - specific internal energies of jet and ambient medium, c_{sj} , c_{sa} - the sound speeds in jet and ambient medium, p - pressure, ν , η - relativistic density and enthalpy contrasts and M_j - the jet Mach number. All the quantities in the table, except the last column, are expressed in units of the ambient density, ρ_{0a} , the speed of light, c , and the jet radius, R_j . Parameters for the new set of simulations are shown in the lower part of the table.

only in some selected aspects. The initial data for these new simulations are compiled and shown in the lower part of Tables 2.1 and 2.2. The external medium in all cases is that of model A05. From models F to H, internal energy in the jet is increased and rest-mass density decreased in order to keep pressure equilibrium, whereas the jet Lorentz factor is kept equal to its value in model A05. The initial momentum density in the jet decreases along the sequence A05, F, G, H. Simulations I and J have the same thermodynamical values as models F and G, respectively, but have increasing jet Lorentz factors to keep

Model	k_{\parallel}	ω_r	ω_i	k'_{\parallel}	ω'_r	ω'_i	$k_{j\perp}$	$k_{a\perp}$	ω_i^{dyn}
A05	0.30	0.20	0.026	1.32	7.20	0.13	7.08	0.53	0.73
B05	0.69	0.49	0.055	2.62	7.32	0.28	6.84	1.08	0.79
C05	2.00	1.60	0.114	5.73	9.98	0.57	8.17	1.07	1.05
D05	2.63	2.18	0.132	7.02	11.56	0.66	9.18	0.24	1.15
B10	0.50	0.41	0.031	3.59	10.28	0.31	9.64	0.94	0.90
C10	1.91	1.72	0.055	9.77	17.67	0.55	14.72	1.49	1.01
D10	2.00	1.81	0.063	9.67	16.58	0.63	13.47	0.20	1.10
B20	0.46	0.39	0.014	6.51	18.76	0.28	17.60	0.90	0.81
C20	1.44	1.37	0.027	13.89	25.38	0.54	21.24	1.28	0.99
D20	2.00	1.91	0.029	18.11	31.43	0.58	25.68	0.31	1.01
F	0.46	0.53	0.14	1.23	2.83	0.70	2.55	3.72	1.70
G	0.66	0.53	0.15	1.87	3.22	0.75	2.62	4.99	1.36
H	0.66	0.48	0.15	1.95	3.23	0.75	2.57	4.71	1.31
I	0.30	0.50	0.07	1.11	2.66	0.82	2.42	3.52	1.99
J	0.35	0.44	0.058	1.70	3.05	0.91	2.53	4.16	1.65
K	0.30	0.55	0.054	1.17	2.80	0.85	2.55	3.87	2.06
L	0.30	0.31	0.069	1.52	2.72	0.81	2.26	2.93	1.47

Table 2.2: Solutions of the dispersion relation (Eq. 2.26), corresponding to fastest growing first reflection mode, taken as input parameters for numerical simulations. The primes are used to assign wavenumber and complex frequency in the reference frame comoving with jet. All the quantities in the table, except the last column, are expressed in units of the ambient density, ρ_{0a} , the speed of light, c , and the jet radius, R_j . Parameters for the new set of simulations are shown in the lower part of the table.

the same initial momentum density as model A05. Finally, in simulations K and L we exchange the values of the Lorentz factor with respect to those in runs I and J.

As it is apparent in Table 2.2 growth rates tend to increase with the specific internal energy of the beam and to decrease with the beam flow Lorentz factor. Note that, in the jet reference frame, models with the same thermodynamical properties tend to have (within $\approx 10\%$) the same growth rates. Note also that in the jet reference frame and in dynamical time units, all the models have comparable (within a factor 1.5) linear growth rates.

The initial numerical setup consists of a steady two-dimensional slab jet model (see Fig. 2.1). As stated above, a thin shear layer between the ambient medium and the jet is used instead of the vortex sheet. Due to symmetry properties, only half of the jet ($x > 0$) has to be computed. Reflecting boundary conditions are imposed on the symmetry plane of the flow, whereas periodical conditions are settled on both upstream and downstream boundaries. The numerical grid covers a physical domain of one wavelength along the jet (3 to $20 R_j$; see Table 2.2) and $100 R_j$ across ($200 R_j$ in the case of models D). The size of the transversal grid is chosen to prevent losses of mass, momentum and energy through the boundaries. As explained before, due to linear regime convergence, 400 numerical zones per beam radii are used in the transverse direction across the first $3 R_j$. From this point up to the end of the grid, 100 (200, in case of models D) extra numerical zones growing geometrically have been added. The width growth factor between contiguous zones is approximately 1.08 for models A, B and C and 1.04, for models D. Along the jet, a resolution of 16 zones per beam radius has been used.

The steady model is then perturbed according to the selected mode, with an absolute value of the pressure perturbation amplitude inside the beam of $p_j^\pm = 10^{-5}$. This means that those models with the smallest pressure, like model A, have relative perturbations in pressure three orders of magnitude larger than those with the highest pressures, D. This was chosen in order to compensate smaller growth rates in colder models. In any case, this difference seems not to affect the linear and postlinear evolution, as we tested by repeating simulation D05 with an initial relative amplitude equivalent to that of model A05 (see subsection on non-linear results in section 2.4.1, Fig. 2.18).

2.4 Results

2.4.1 Linear phase

Following the behaviour of simulated models we find that the evolution of the perturbations can be divided into a linear phase, a saturation phase and mixing phase. This section is devoted to describing the properties of these phases in our models, focusing on the influence of the basic parameters. Our description shares many points with that of Bodo et al. (1994) for the case of classical jets.

In order to illustrate the growth of perturbations and determine the duration of the linear and saturation phases in our simulations, we plot in Fig. 2.9

the amplitudes of the perturbations of the longitudinal and transversal velocities, inside the jet and in the jet reference frame, together with the pressure oscillation amplitude. We plot also the growth of the imposed eigenmodes resulting from the linear stability analysis. Both the velocity perturbations are transformed from the ambient rest frame to the unperturbed jet rest frame using the Lorentz transformation rules for velocity components, given by Eq. (2.40).

We define the characteristic times in the following way. During the linear phase the ratios of the exponentially growing amplitudes of pressure, longitudinal velocity and transversal velocity remain constant by definition. We define the end of the linear phase (t_{lin}) as the moment at which one of quantities starts to depart from the initial exponential growth. Within the set of our models the first quantity to break the linear behaviour is the longitudinal velocity perturbation.

Later on the transversal velocity saturates, i.e. stops growing at the saturation time (t_{sat}). We call the period between t_{lin} and t_{sat} the saturation phase. We find also that the pressure perturbation amplitude reaches a maximum. This moment is denoted by t_{peak} . We will see that this peak announces the entering of the fully non-linear regime. The choice of t_{lin} , t_{sat} , t_{peak} has been illustrated in Fig. 2.9 (top panel).

Table 2.3 collects times of the linear and saturation phases in the different models (columns 2 and 5). Column 7 shows the saturation time in dynamical units and in the jet reference frame. The change of reference frame eliminates the effects coming from the jet flow Lorentz factor that stretches out the rhythm of evolution in the ambient rest frame. Dynamical time units are adapted to the characteristic time of evolution of each model. Hence this change of units and reference frame allows us to compare the relevant scales of evolution of all the models directly.

In the linear phase the ratios of oscillation amplitudes of different dynamical variables (density, pressure and velocity components) are constant. We have used this property to identify the end of the linear phase with the time t_{lin} at which one of the variables deviates from linear growth in a systematic way. Note that our definition is different from that of Bodo et al. (1994) who associate the end of the linear phase with the formation of the first shocks inside the jet.

We note that in our simulations, during the linear phase, the growth of perturbations of each dynamical variable follows the predictions of the linear

Model	t_{lin}	t_{mex}	t_{mix}	t_{sat}	t_{peak}	$t_{\text{sat}}^{\text{dyn}}$	Δ_{peak}	t_{fmix}	t_{meq}
A05	180	335	335	380	380	13.69	100	380	–
B05	125	175	185	200	205	13.99	70	210	215
C05	100	115	120	125	130	13.74	5	> 595	195
D05	105	115	115	120	130	13.71	5	> 595	185
B10	235	375	335	380	385	13.29	100	445	–
C10	210	245	240	245	250	13.46	10	> 595	–
D10	180	220	215	225	225	12.86	10	350	345
B20	450	775	625	760	780	13.29	100	> 1000	–
C20	270	675	595	645	775	17.72	5	> 1000	> 1000
D20	350	465	450	480	500	13.71	10	> 1000	> 1000

Table 2.3: Times for the different phases in the evolution of the perturbed jet models. t_{lin} : end of linear phase (the amplitudes of the different quantities are not constant any longer). t_{sat} : end of saturation phase (the amplitude of the transverse speed perturbation reaches its maximum). t_{mix} : the tracer starts to spread. t_{peak} : the peak in the amplitude of the pressure perturbation is reached. t_{fmix} : external material reaches the jet axis. t_{mex} : the jet has transferred to the ambient a 1% of its initial momentum. t_{meq} : longitudinal momentum in the jet and the ambient reach equipartition. $t_{\text{sat}}^{\text{dyn}}$: saturation time in dynamical time units and in the jet reference frame. Δ_{peak} : relative value of pressure oscillation amplitude at the peak (see Fig. 2.9). Note that, as a general trend, $t_{\text{lin}} < t_{\text{mex}} \approx t_{\text{mix}} < t_{\text{sat}} < t_{\text{peak}} < t_{\text{fmix}} < t_{\text{meq}}$.

stability analysis with relatively good accuracy. On average the growth rates measured for all our numerical experiments are about 20 % smaller than corresponding growth rate resulting from the linear stability analysis. This small discrepancy may be partially a result of the application of the shearing layer in simulations and the vortex sheet approximation in the linear stability analysis, and also to a lack of transversal resolution in the numerical simulations.

In all cases the amplitude of the longitudinal velocity oscillation is the first quantity to stop growing. The reason for the limitation of the velocity oscillations is obvious: the oscillations of velocity components (corresponding to sound waves propagating in the jet interior) cannot exceed the speed of light. This limitation (specific to relativistic dynamics) is easily noticeable in the jet reference frame, but it is obscured by the Lorentz factor (in the first

and second power) in the reference frame of the ambient medium, as it follows from the formulae (2.41).

As seen in Fig. 2.9, model C20 evolves distinctly from the other models: at $t = 270$, the linear phase ends before the saturation of longitudinal speed. See the middle panels of Fig. 2.14 (especially the pressure panel) where small scale transversal structure is apparent, which could be responsible for the peculiar evolution of model C20. Note also that model C20 is the only one that has a theoretical perturbation growth rate smaller than the numerical one (probably associated with the excited short wavelength mode).

At the end of the linear phase, the values of quantities like density, pressure and flow Lorentz factor are still very close to the corresponding background values (the perturbation in pressure is between 10 % and 50% of the background pressure in all the models). Figure 2.10 shows the distribution of pressure at the end of the linear phase for two representative models B05 and D05.

2.4.2 Saturation phase

As it has been mentioned, the end of the linear phase coincides with the limitation of the longitudinal oscillation velocity. At time t_{lin} the transversal velocity component is smaller than the speed of light, by an order of magnitude approximately, so the transversal velocity perturbation has still room to grow. We defined t_{sat} as the time corresponding to the saturation of the transversal velocity and saturation phase as the period between t_{lin} and t_{sat} .

We find that the longitudinal velocity perturbation amplitude reaches almost the speed of light (more than $0.9c$) while the transversal perturbation amplitude stops its growth at the level of approximately $0.5c$ for all presented simulations. This can be explained in the following way. We remind that the eigenmodes are built of oblique sound waves overreflected at the jet/ambient medium interface. This means that the amplitude of the reflected wave is larger than the amplitude of the incident one. Sound waves are longitudinal waves, so the gas oscillation velocity can be split into the longitudinal and transversal components separately for the incident and reflected waves. Let us consider locally the incident wave and the reflected wave in the jet medium, in a fixed point close to the jet boundary. Then the longitudinal velocity components of the incident and reflected waves sum in phase, while the transversal ones sum in counterphase. This means that while the amplitude of the total longitudinal velocity oscillation component grows and approaches the speed

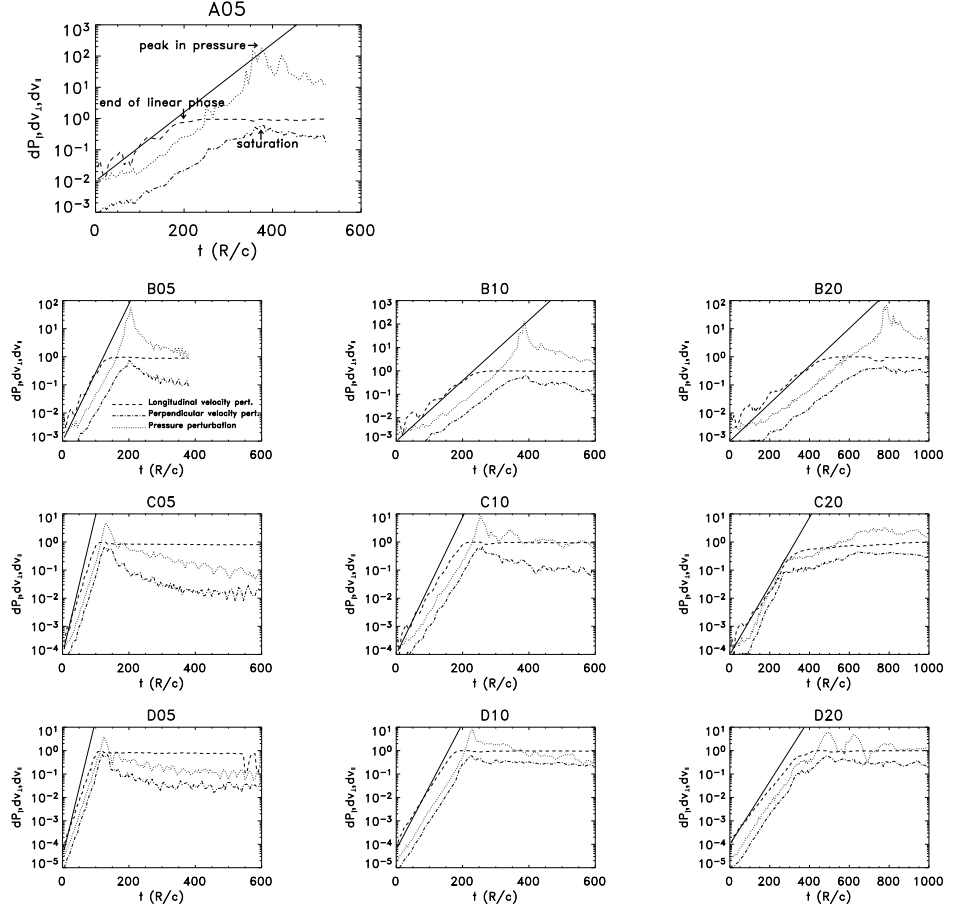


Figure 2.9: Evolution of the relative amplitudes of perturbations. Dotted line: pressure perturbation $((p_{max} - p_0)/p_0)$. Dashed line: longitudinal velocity perturbation in the jet reference frame $(0.5(v'_{z,max} - v'_{z,min}))$. Dash-dotted line: perpendicular velocity perturbation in the jet reference frame $(0.5(v'_{x,max} - v'_{x,min}))$. The search for maximum $((p_{max}, (v'_{x,max}, (v'_{z,max})$ and minimum $(v'_{x,min}, (v'_{z,min}))$ values have been restricted to those numerical zones with jet mass fraction larger than 0.5. Solid line: linear analysis prediction for the growth of perturbation. Note that abscissae in the last column plots extend up to $t = 1000R_j/c$ and that ordinate values adapt to fit the scale of each plot. Arrows in the plot of Model A05 point to specific stages of evolution used to define t_{lin} , t_{sat} and t_{peak} (see text).

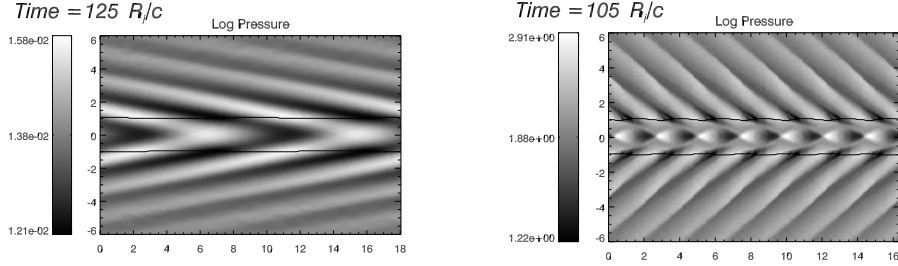


Figure 2.10: Pressure distribution at the end of linear phase for models B05 (left panel) and D05 (right panel). The continuous line corresponds to jet mass fraction equal to 0.5 and serves to distinguish jet and ambient media.

of light, the oscillation amplitude of the total transversal component is a difference of the two velocities, each smaller than the speed of light. Therefore the oscillation amplitude of the total transversal component has to take values significantly smaller than the longitudinal one.

The duration of the saturation phase depends on the Lorentz factor and the specific internal energy with a tendency to increase with the former and to decrease with the latter (exception made of models C10 or D10 and C20). It ranges between a few tens of (absolute) time units to a few hundreds.

We note that the saturation times expressed in dynamical time units and in the jet reference frame (see Table 2.3) are almost equal for all models. This similarity can be explained by the following argument. First, the amplitude of pressure perturbations $p_1^\pm = 10^{-5}$ is the same for all simulations. Second, the amplitudes of pressure and transversal velocity perturbations are related by formula (2.35). The perturbation of perpendicular velocity is then transformed to the jet reference frame following (2.41). Following the results of numerical experiments, the transversal velocity grows with the linear growth rate until the transversal velocity perturbation reaches the upper limit, i.e. $|v_{j\perp}^+| \exp(\omega_i t_{\text{sat}}) \simeq 0.5c$. If we express t_{sat} in dynamical time units then in the jet reference frame

$$t_{\text{sat}}^{\text{dyn}} \simeq \frac{\gamma}{c_{sj}\omega_i} \log \left(\frac{c\Gamma_j}{2p_1^+} \left| \frac{\omega'}{k_{j\perp}} \right| \right). \quad (2.45)$$

Since the term $\omega'/k_{j\perp}$ under the logarithm is close to the jet sound speed and is varying only slightly in between models, while the other factors under the logarithm are constants, the saturation time is proportional to the inverse

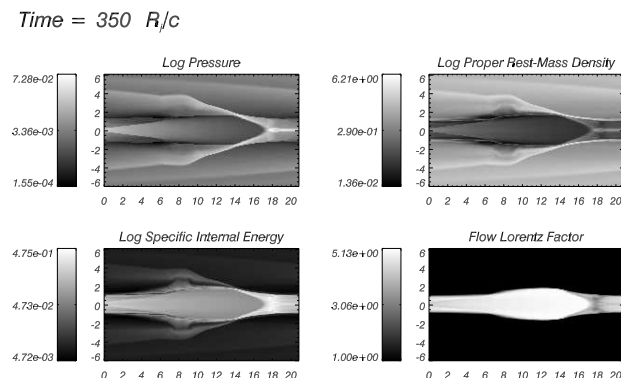


Figure 2.11: Snapshot around saturation of logarithmic maps of pressure, rest-mass density and specific internal energy and non-logarithmic Lorentz factor for model A05.

growth rate. From the linear stability analysis, the latter one measured in the jet reference frame and expressed in dynamical time units is almost equal for all the models (see last column in Table 2.2). Substitution of numbers into the formula (2.45) provides t'_{sat} in the range $10 \div 15$, which is consistent with the value 13.5 in Table 2.3. However, the remarkable convergence of saturation times for all the models is difficult to explain in view of the additional randomness in the evolution of perturbations, which is apparent in Fig. 2.9.

During the saturation phase, the jet inflates (Bodo et al. 1994 called this phase the expansion phase) and deforms due to transversal oscillations. On the other hand, the saturation time t_{sat} coincides (within a few time units) with the appearance of an absolute maximum in the pressure distribution (at t_{peak}) at the jet boundary, and with the start of the mixing phase. Figures 2.11-2.14 display snapshots of several quantities close to the end of the saturation phase before the distortion of the jet boundary.

The structure of perturbations at the end of the saturation phase is quite similar in all models. The longitudinal wavelength of perturbations is given by the linear stability analysis and it is constant because of the fixed length of the computational domain. Along with the longitudinal wavelength, the opening angle of oblique waves, far from the jet symmetry plane, is given by the linear analysis. The opening angle of oblique waves is enlarged in the vicinity of the jet interface. Closer to the jet symmetry plane the perturbations

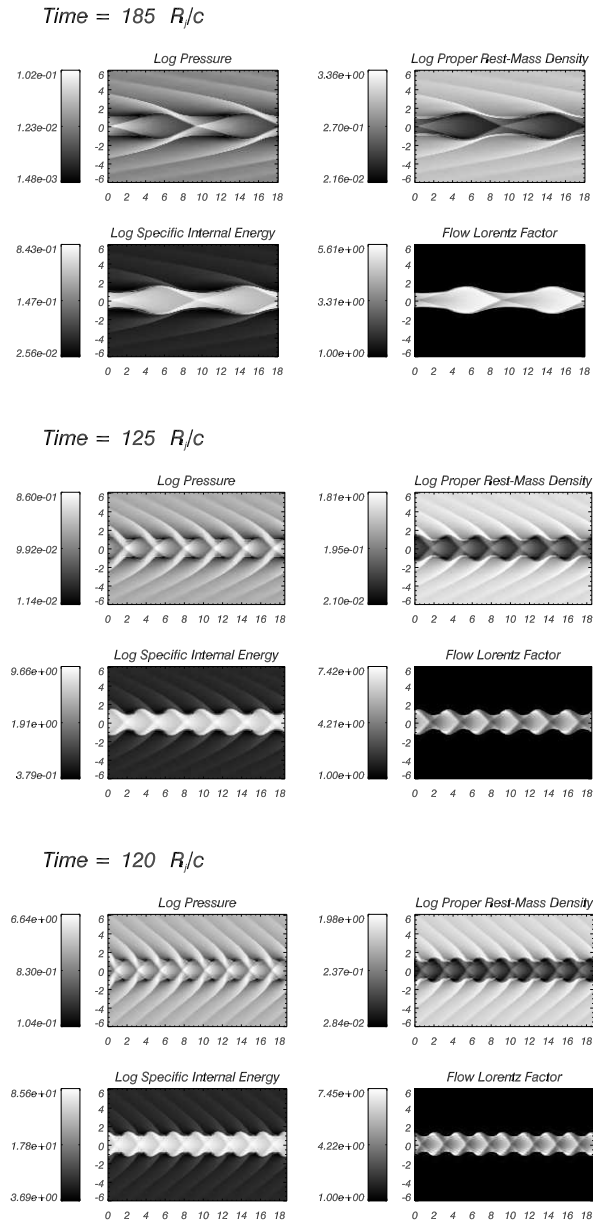


Figure 2.12: Same as Fig. (2.11) for models B05 (upper), C05 (middle) and D05 (lower).

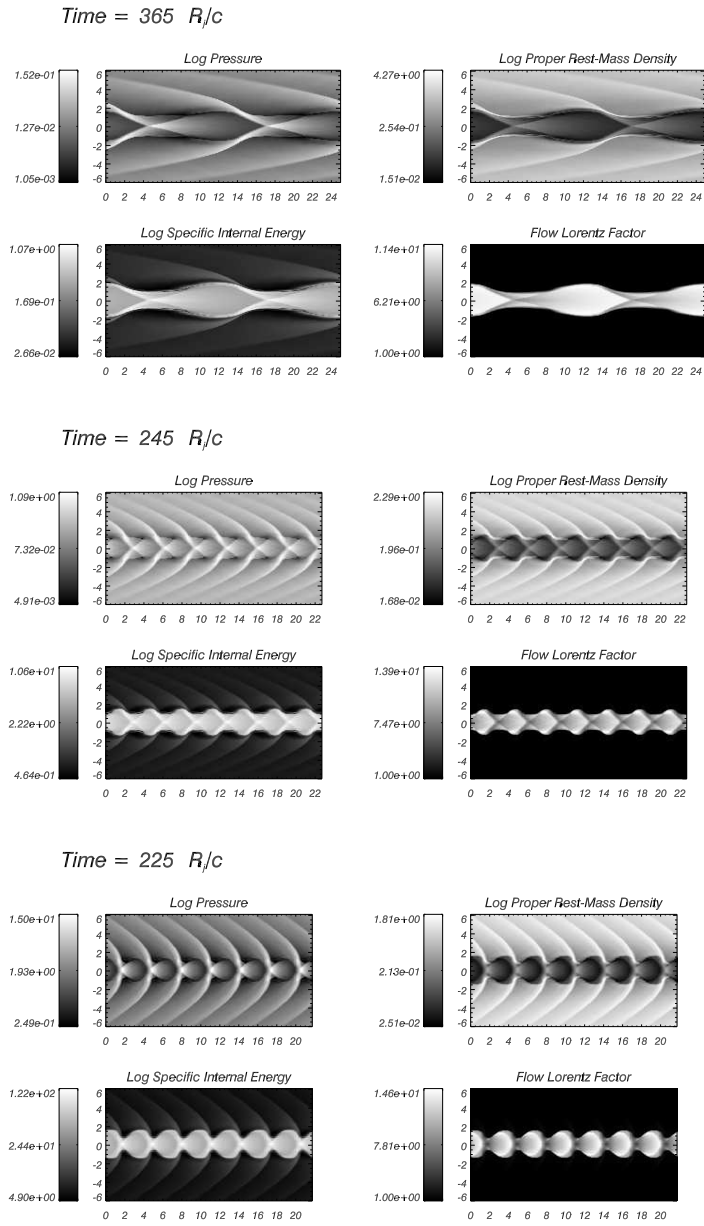


Figure 2.13: Same as Fig. (2.11) for models B10 (upper), C10 (middle) and D10 (lower).

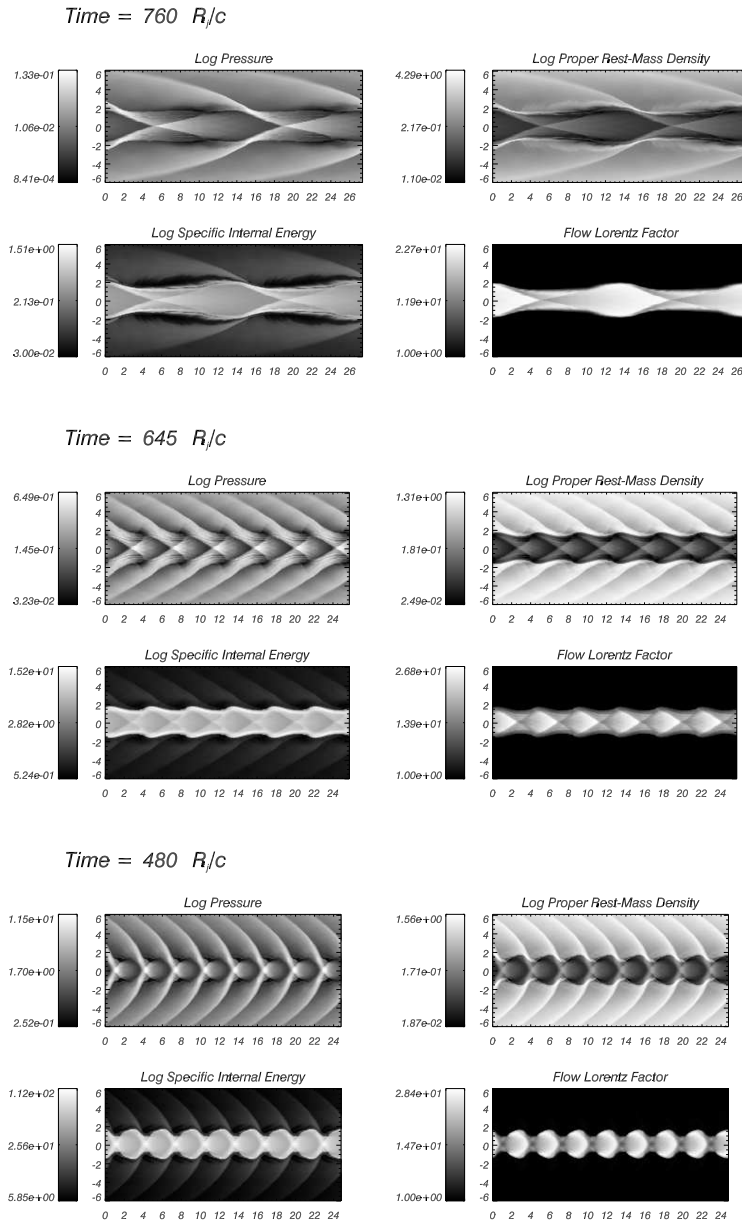


Figure 2.14: Same as Fig. (2.11) for models B20 (upper), C20 (middle) and D20 (lower).

are already in the non-linear phase, which can be recognized by the apparent presence of oblique shock fronts in the jet itself and the ambient medium. These shocks form as a natural consequence of the non-linear steepening of oblique sound waves as their amplitude becomes large. Practically all the four quantities displayed for a given model (i.e. pressure, rest-mass density, Lorentz factor and internal energy) show the same structure, so there is no need to discuss them separately. Therefore we treat the pressure distribution as a representative quantity. The following properties of the flow patterns can be noticed in Figs. 2.11-2.14:

1. The interface between jet and ambient medium forms a regular sinusoidal pattern. The amplitudes are all comparable and have values of the order of $0.5 - 1.0 R_j$. In all cases the departure from a regular sinusoidal shape is rather small.
2. The structure of oblique shocks crosses the jet interface in such a way that the deformed interface is almost parallel to the shock front. One should notice however that the oblique shock moves in the flow direction in the external medium and in the counter-flow direction in the jet medium, as can be deduced from the distribution of hot post-shock and cold pre-shock material. These two oppositely moving shock waves fit together because of the jet background flow.
3. The highest gas pressure is always located on the jet symmetry plane (the brightest spots on pressure plots), where the crossing shocks form the familiar x-pattern, but the pressure enhancement on the jet interface is almost as strong as on the jet symmetry plane.
4. The shocks are much stronger (i.e., the jumps between pre- and post-shock pressure larger) in the cold cases. In the case of hot models the jumps are smoother. This is a straightforward consequence of the larger ratios of the perturbed velocity to the sound speed in the cold cases.
5. There is no significant variation of the structure of non-linear perturbations for different values of the Lorentz factor.
6. Model C20 displays a structure of internal waves, which is absent in other cases. This fine structure is probably connected to the distinct evolution of this model in the postlinear phase (see Sect. 2.4.1 and Fig. 2.9). See also Chapter 3.

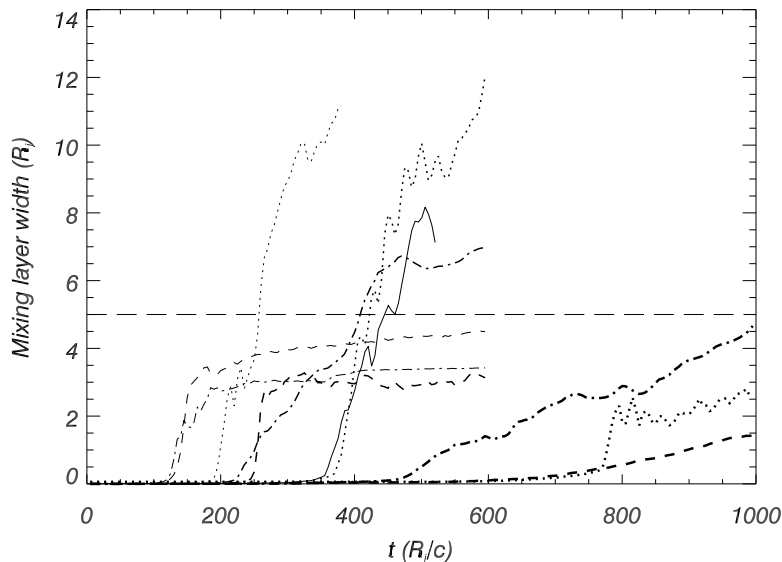


Figure 2.15: Evolution of the mean width of the jet/ambient mixing layer with time for all the simulations. Different types of lines are used for models with different internal energies: Continuous line: model A; dotted line: model B; dashed line: model C; dashed-dotted line: model D. Line thickness increases with Lorentz factor (from 5, thinnest line, to 20 thickest one). A value of 5 R_j for the width of the mixing layer (horizontal dashed line) serves to classify the evolution of the different models.

Therefore the differences between models just before the end of the saturation phase can be considered as minor.

2.4.3 Non-linear phase

The beginning of the mixing phase can be detected by the spreading of the tracer contours in the jet/ambient interface. This can be seen in Fig. 2.15, where the evolution with time of the mean width of the layer with tracer values between 0.05 and 0.95 is shown. The times at which the mixing phase starts (t_{mix}) are shown in Table 2.3. Consistently with the width of the initial shear layer in our simulations (around $0.1 R_j$), we have defined t_{mix} as the time at

which the mixing layer exceeds a width of $0.1 R_j$.

For models with the same thermodynamical properties, those with smaller Lorentz factors start to mix earlier (see Table 2.3). Moreover, according to Fig. 2.15, the models can be sampled in two (or perhaps three) categories. Models A05, B05, B10 and D10 have wide ($> 5R_j$) shear layers which are still in a process of widening at the end of the simulation. The rest of the models have thinner shear layers ($< 5R_j$ wide) which are inflating at smaller speeds ($0.5 - 2 \cdot 10^{-3}c$, in the case of models C05, D05 and C10; $0.5 - 1.2 \cdot 10^{-2}c$, in the case of models B20, C20, and D20). A deeper analysis of the process of widening of the shear layers as a function of time shows that all the models undergo a phase of exponential growth extending from t_{mix} to soon after t_{peak} .

We note that those models developing wider mixing layers are those in which the peak in the maxima of the pressure perturbation as a function of time, Δ_{peak} , reach values of the order of $70 - 100$, with the exception of model B20 that has a thin mixing layer at the end of the simulation but has $\Delta_{\text{peak}} \approx 100$, and model D10, which does develop a wide shear layer but for which Δ_{peak} remains small. We also note that (with the exception of model D10) the models developing wide mixing layers are those with smaller internal energies and also relatively smaller Lorentz factors.

There are two basic mechanisms that contribute to the process of mixing between ambient and jet materials. The first one is the deformation of the jet surface by large amplitude waves during the saturation phase. This deformation favors the transfer of momentum from the jet to the ambient medium and, at the same time, the entrainment of ambient material in the jet. From Table 2.3, it is seen that the process of mixing and momentum exchange overlap during the saturation phase.

The second mechanism of mixing starts during the transition to the full non-linear regime and seems to act mainly in those models with large Δ_{peak} . As we shall see below, this large value of Δ_{peak} is associated with the generation of a shock at the jet/ambient interface at t_{peak} , which appears to be the responsible of the generation of wide mixing layers in those models. Figure 2.16 shows a sequence of models with the evolution of mixing in two characteristic cases, B05 and D05, during the late lapse of the saturation phase. The evolution of model B05 is representative of models A05, B05 and B10. Models B20, C05, C10, C20 and D10 have evolutions closer to model D05. As it is seen in Fig. 2.16, in the case of model B05 (left column panels), the ambient material carves its way through the jet making difficult the advance of the jet material

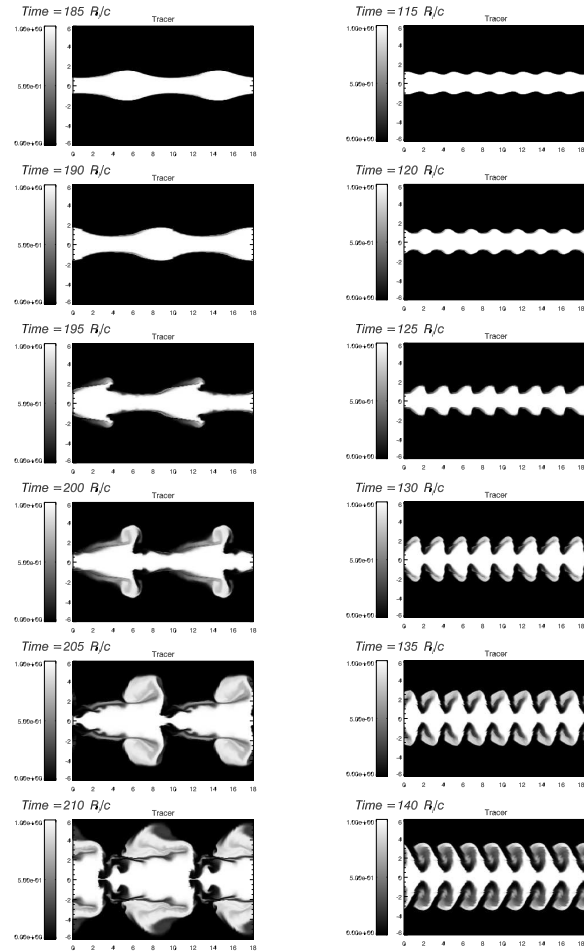


Figure 2.16: Evolution of the jet particle fraction showing the development of mixing in two representative models. Left column (model B05): the ambient material carves its way through the jet making difficult the advance of the jet material which is suddenly stopped. Right column (model D05): the amount of ambient matter hampering the jet material is smaller and matter from the jet at the top of the jet crests is ablated by the ambient wind.

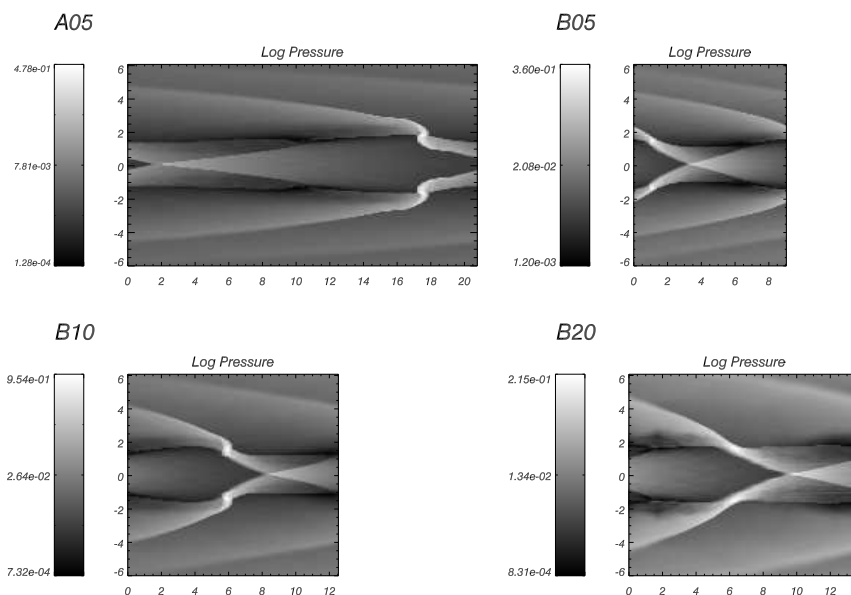


Figure 2.17: Pressure distribution at the onset of the jet/ambient surface distortion at the end of the saturation phase for models A05, B05, B10 and B20. The corresponding times are 355, 190, 370 and 765 R_j/c . In the case of models A05, B05 and B10 this distortion leads to the formation of a shock.

which is suddenly stopped. The result is the break-up of the jet. In model D05, (right column panels), matter from the jet at the top of the jet *crests* is ablated by the ambient wind forming vortices of mixed material filling the *valleys*.

The large amplitude of Δ_{peak} reached in models A05, B05 and B10 is clearly associated with a local effect occurring in the jet/ambient interface (see second panel in the left column of Fig. 2.16 and Fig. 2.17) that leads to the jet disruption. The sequence of events preceding the jet disruption includes the formation of oblique shocks at the end of the linear/saturation phase, the local effect in the jet/ambient interface just mentioned and then a supersonic transversal expansion of the jet that leads to i) a planar contact discontinuity (see last panels in the left column of Fig. 2.16), and ii) the formation of a shock (see below) that propagates transversally. It appears that contrary to the velocity perturbations in the jet reference frame (see Fig.2.9), the maxi-

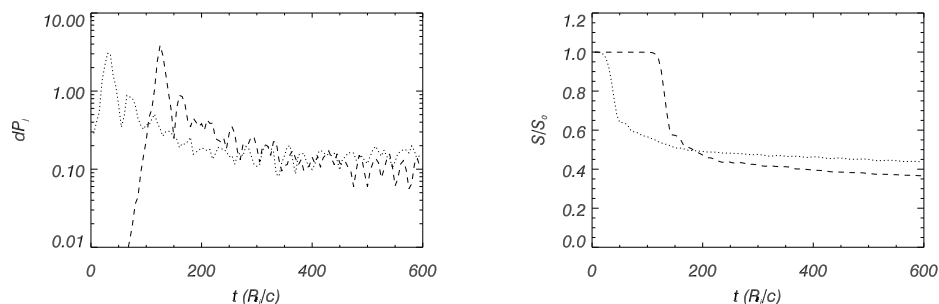


Figure 2.18: Left panel: pressure perturbation amplitude in simulation D05 (dashed line) and D05 with the same initial relative amplitude as model A05 (dotted line); the similarity between pressure peak values can be observed. Right panel: normalized axial momentum in the jet versus time (the lines correspond to the same simulations as in left panel); the final axial momentum is around 40% in both cases.

mum relative amplitudes of pressure perturbation are strongly dependent on physical parameters of simulations.

In order to see how much this peak in relative pressure amplitude was influenced by initial relative amplitude to background values, we repeated the simulation corresponding to model D05 with the same initial relative amplitude as model A05 (i.e., three orders of magnitude larger). Results show that there is not a significant difference in the peak values of the pressure and that the evolution is basically the same as the one of the original model. We can observe this in Figs. 2.18 and 2.19. Comparing the latter with Fig. 2.27, we observe the same structures in the long term mixing phase.

The origin of the shock in models with $\Delta_{\text{peak}} \approx 100$, that enhances the turbulent mixing of the jet and ambient fluids, can be found in the non-linear evolution of Kelvin-Helmholtz instability that leads to significant changes of local flow parameters at the end of saturation phase. For instance, the oblique shock front resulting from the steepening of sound waves, during the linear and saturation phases (see Figs. 2.10-2.14), crosses the initial shear layer at the interface of jet and ambient medium. The formation of such oblique shock implies a sudden and local growth of gradients of all the dynamical quantities at the jet boundary. The local conditions changed by these oblique shocks may

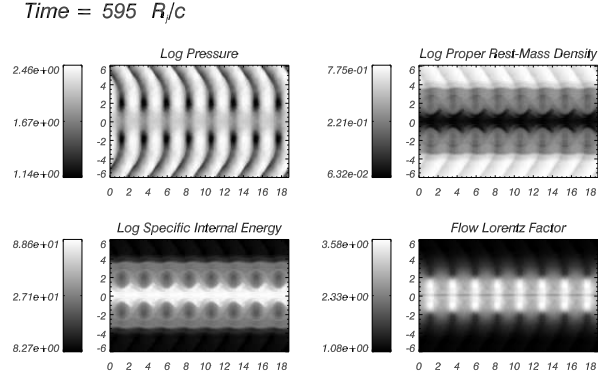


Figure 2.19: Snapshot in the mixing phase of logarithmic maps of pressure, jet mass fraction and specific internal energy and non-logarithmic Lorentz factor for model D05, started with an initial relative amplitude of the pressure perturbation equal to that of model A05. Compare this figure with lower panel in Fig. 2.27.

become favorable for the development of other instabilities like those discussed by Urpin (2002).

The generation of the shock wave at the jet/ambient interface is reflected in the evolution of the maxima of $M_{j,\perp} = \gamma_{j,\perp} v_{j,\perp} / (\gamma_{c_{sa}} c_{sa})$ ($\gamma_{j,\perp}$ and $\gamma_{c_{sa}}$ being the Lorentz factors associated with $v_{j,\perp}$ and c_{sa} , respectively) representing the transversal Mach number of the jet with respect to the unperturbed ambient medium. This quantity becomes larger than 1 around t_{peak} in those models with $\Delta_{\text{peak}} \approx 100$ (see Fig. 2.20) pointing toward a supersonic expansion of these jets at the end of the saturation phase. The fact that in all our simulations the ambient medium surrounding colder models (i.e., A, B) are also colder (see subsection on numerical setup) favors the generation of shocks in the jet/ambient interface in these models. On the other hand, in the case of models with the highest Lorentz factors (B20, C20, D20) the transversal velocity can not grow far enough to generate the strong shock which breaks the slower jets.

As mentioned above, in order to extend our conclusions to a wider region in the initial parameter space, we have performed supplementary simulations (namely F, G, H, I, J, K, L) with the aim of clarifying the effect of the ambient

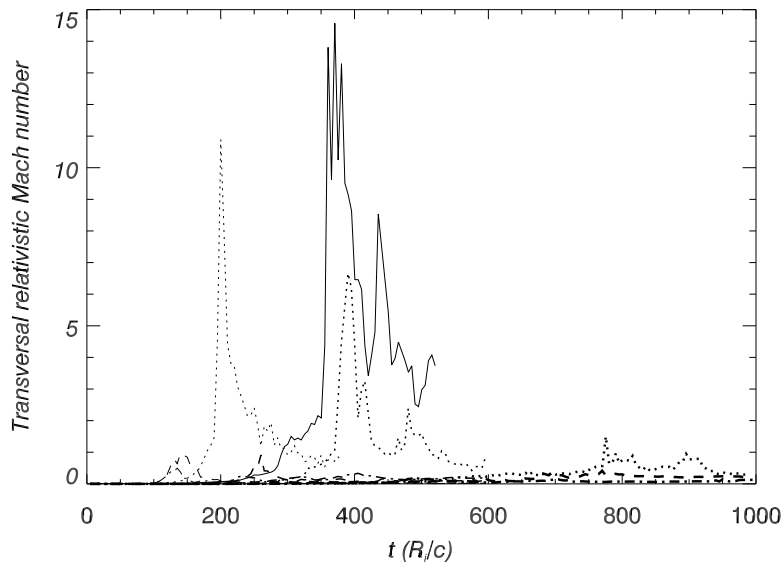


Figure 2.20: Time evolution of the maxima of the transversal Mach number of the jet with respect to the unperturbed ambient medium, $M_{j,\perp}$. See text for further explanations. Lines are as in Figure 2.15.

medium in the development of the disruptive shock appearing after saturation. In all the cases, the external medium is that of model A05.

From models F to H, internal energy in the jet is increased and rest-mass density decreased in order to keep pressure equilibrium, whereas the jet Lorentz factor is kept constant to its value in model A05. The transversal Mach numbers at the peak in these models reach values very similar to that of model A05 ($\gg 1$, see Fig. 2.21). In fact, the formation of a shock at the end of the saturation phase is observed in these models as it is in model A05.

The initial momentum density in the jet has decreased along the sequence A05, F, G, H. Simulations I and J have the same thermodynamical values as models F and G, respectively, but have increasing jet Lorentz factors to keep the same initial momentum density as model A05. In the case of model I we find the same behavior as in previous ones: large transversal Mach number, shock and disruption. On the contrary, model J behaves much more like model B20, with a value of transversal Mach number slightly larger than one, strong

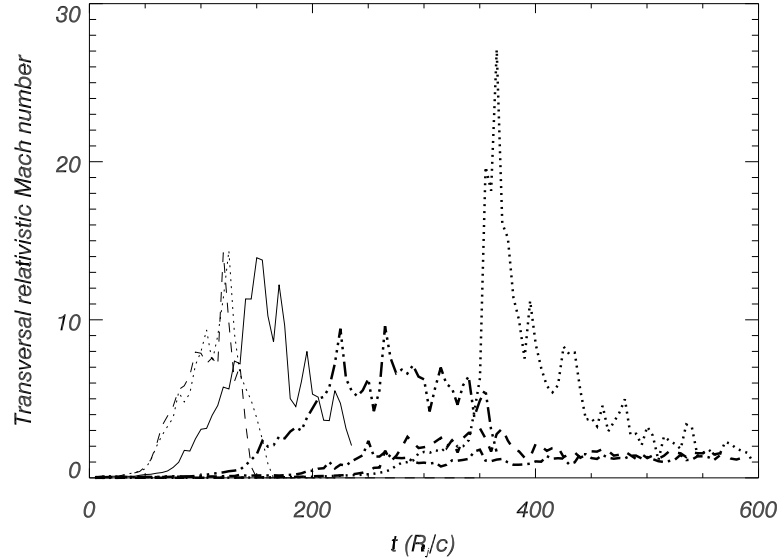


Figure 2.21: Same as Fig. 2.20 for models F, G, H, I, J, K and L. Lines are as in Figure 2.22.

expansion and almost no mixing (Fig. 2.22). Finally, in order to know to which extent this change in behavior was caused by the increase in Lorentz factor or in specific internal energy, in simulations K and L we cross these values with respect to those in I and J. The results from these last simulations show that the evolution of model L is very close to that of model I: the large value of the transversal Mach number at the peak, shock and strong mixing; and that the evolution of model K is close to that of model J: a weaker shock, expansion and no mixing (Fig. 2.21 and Fig. 2.22).

In the models developing a shock, mixing is associated with vorticity generated after the shock formation and, in the case of models A05, B05, B10 as well as F, G, H, I and L matter from the ambient penetrates deep into the jet as to reach the jet axis (jet break-up). The times at which this happens for the different models are displayed in Table 2.3. Note that in models A05 and B05 the entrainment of ambient matter up to the axis occurs just after t_{peak} , whereas in model B10 occurs later, probably because the shock in this model is weaker. The process of mixing can be affected by resolution, as small

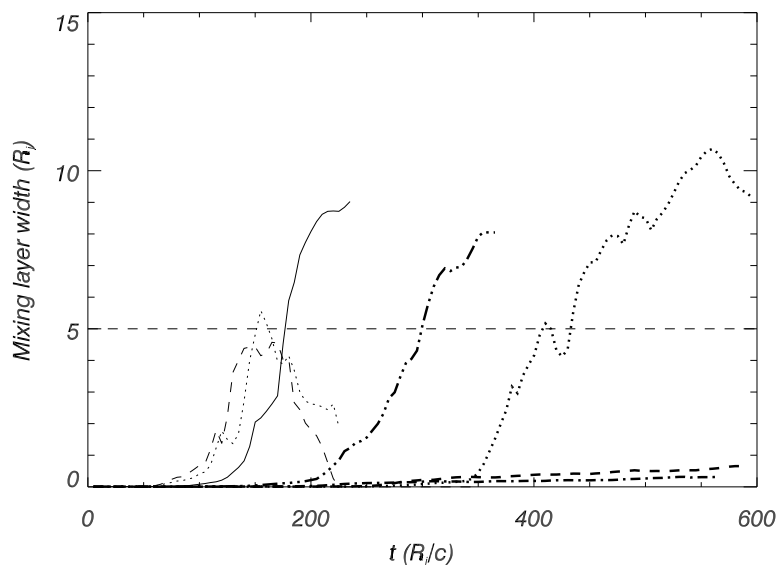


Figure 2.22: Same as Fig. 2.15, for models F, G, H, I, J, K and L. Different types of lines are used for models with different internal energies: Continuous line: model F; dotted line: model G; dashed line: model H; thick dotted line: model I; thick dashed line: model J; thick dashed-dotted line: model K; thick dash-dot-dot line: model L. A value of $5 R_j$ for the width of the mixing layer (horizontal dashed line) serves to classify the evolution of the different models.

resolutions may suppress the development of turbulence. We will analyze this further on (see section 2.4.4), focusing on the influence of longitudinal resolution.

Regarding the evolution of the longitudinal momentum with time, Figure 2.23 shows the evolution of the total longitudinal momentum in the jet for the different models. Jets in models B05, C05, D05 and D10 (also D20) transfer more than 50% of their initial longitudinal momentum to the ambient, whereas models A05, B10 and C10 (also B20) seem to have stopped the process of momentum transfer retaining higher fractions of their respective initial momenta. Models C20 and D20 continue the process of momentum exchange at the end of the simulations but at a remarkable slower rate (specially C20).

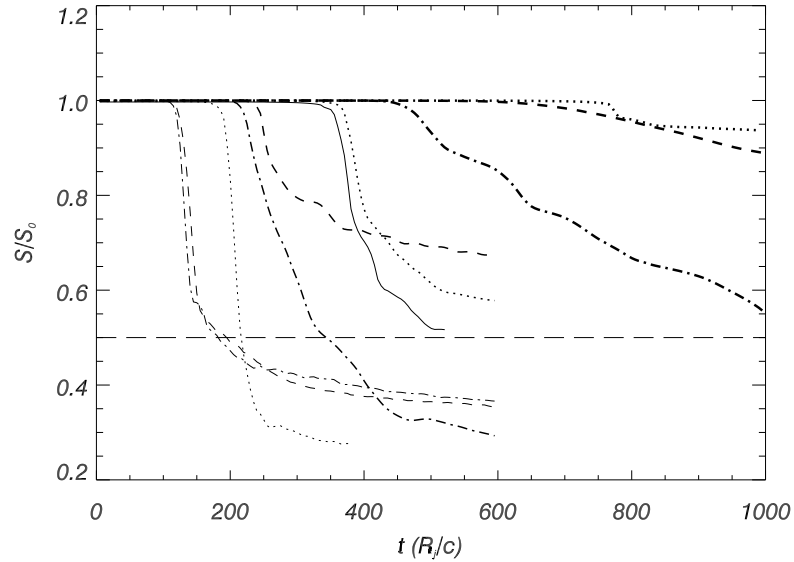


Figure 2.23: Evolution of the total longitudinal momentum in the jet as a function of time for all the simulations. Lines represent the same models than in Fig. 2.15. The long-dashed horizontal line serves us to identify those models transferring more than 50% of the initial jet momentum to the ambient.

In the case of models F, G, H, I and L (Fig. 2.24), the transfer of longitudinal momentum is also very efficient. The reason why these models, as well as A05, B05 and B10, develop wide shear layers and transfer more than 50% of their initial momentum to the ambient could be turbulent mixing triggered by the shock. In the case of models D10 and D20, the processes of mixing and transfer of longitudinal momentum proceed at a slower rate pointing to another mechanism. The plots of the time evolution of the jet's transversal momentum (Fig. 2.25) for the different models give us the answer. Jets disrupted by the shock (as A05, B05, B10) have large relative values of transversal momentum at saturation (> 0.04) that decay very fast afterward (A05 is an exception). The peak in transversal momentum coincides with the shock formation and the fast lateral expansion of the jet at t_{peak} . Contrarily, models D10 and D20 have a sustained value of transversal momentum after saturation which could drive the process of mixing and the transport of longitudinal momentum. In

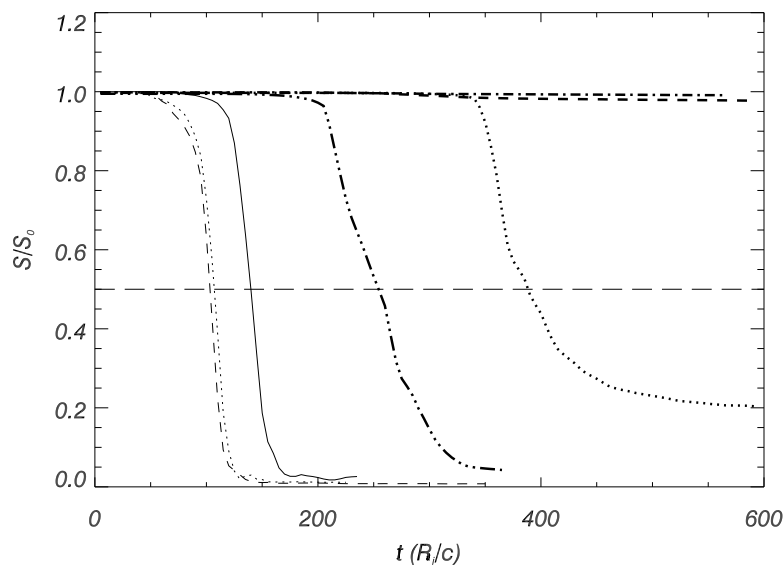


Figure 2.24: Same as Fig. 2.23 for models F, G, H, I, J, K and L. Lines represent the same models than in Fig. 2.22. The long-dashed horizontal line serves us to identify those models transferring more than 50% of the initial jet momentum to the ambient.

these models, the originally high internal energy in the jet and the high jet Lorentz factor (that allows for a steady conversion of jet kinetic energy into internal) make possible the sustained values of transversal momentum. Between these two kinds of behavior are hot, slow models C05, D05 that do not develop a shock having, then, thin mixing layers, but transferring more than 50% of their longitudinal momentum.

Our previous analysis based in the width of the mixing layers and the fraction of longitudinal momentum transferred to the ambient can be used to classify our models:

- Class I (A05, B05, B10, F, G, H, I, L): develop wide shear layers and break up as the result of turbulent mixing driven by a shock.
- Class II (D10, D20): develop wide shear layers and transfer more than 50% of the longitudinal momentum to the ambient, as a result of the

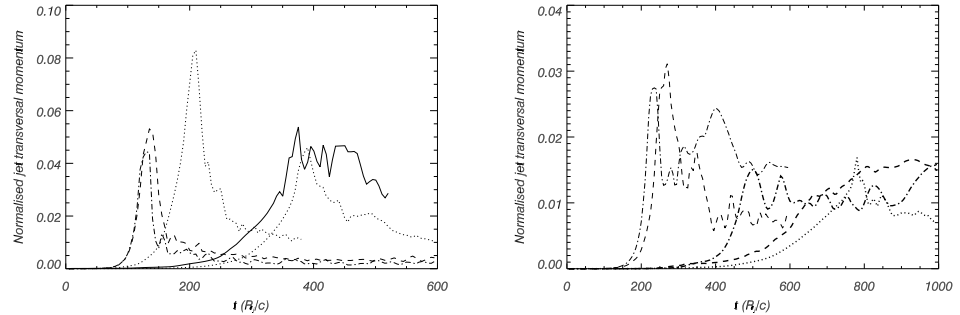


Figure 2.25: Evolution of the total transversal momentum in the jet as a function of time for all the simulations. Lines represent the same models than in Fig. 2.15. Left panel: models A05, B05, B10, C05, D05. Right panel: B20, C10, C20, D10, D20. Note the change in both horizontal and vertical scales between the two panels.

sustained transversal momentum in the jet after saturation.

- Class III (C05, D05): have properties intermediate to models in classes I and II.
- Class IV (B20, C10, C20, J, K): are the most stable.

Figures 2.26-2.32 show the flow structure of the different models at the end of the simulations. The following morphological properties of the members of each class are remarkable:

- Class I: irregular turbulent pattern of the flow, the structure of KH modes still visible on the background of the highly evolved mean flow pattern.
- Class II: a regular pattern of *young* vortices (visible in the tracer and specific internal energy distributions), the structure of KH modes visible. The enhanced transfer of momentum found in the models of this class is probably connected to the presence of these *young* vortices.
- Class III: the flow is well mixed, i.e. tracer, internal energy and Lorentz factor are smoothed along lines parallel to the jet symmetry plane.

Highly evolved vortices visible. A *fossil* of KH modes visible only as pressure waves.

- Class IV: no vortices, no chaotic turbulence, very weak mixing, very regular structure of KH modes.

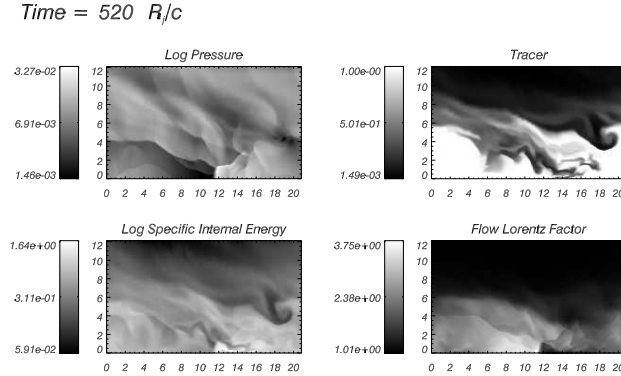


Figure 2.26: Snapshot in the mixing phase of logarithmic maps of pressure, jet mass fraction and specific internal energy and non-logarithmic Lorentz factor for model A05. Only the top half of the jet is shown.

At the end of our simulations, the models continue with the processes of mixing, transfer of momentum and conversion of kinetic to internal energy, however they seem to experience a kind of averaged quasi-steady evolution which can be still associated with the evolution of a jet, i.e., a collimated flux of momentum. This jet is always wider, slower and colder than the original one and is surrounded by a broad shear layer. In the following paragraphs we examine the transition layers in distributions of gas density, jet mass fraction and internal energy as well as shearing layers in velocity, longitudinal momentum and Lorentz factor.

Let us start by analyzing the overall structure of the pressure field for the different models at the end of our simulations. Figure 2.33 shows the transversal, averaged profiles of pressure across the computational grid. Several comments are in order. In the case of models A and B, the shock formed at the end of the saturation phase is seen propagating (at $r \approx 30R_j$ in the case of model A, and at $r \approx 40 - 60R_j$ in the case of models B) pushed by the

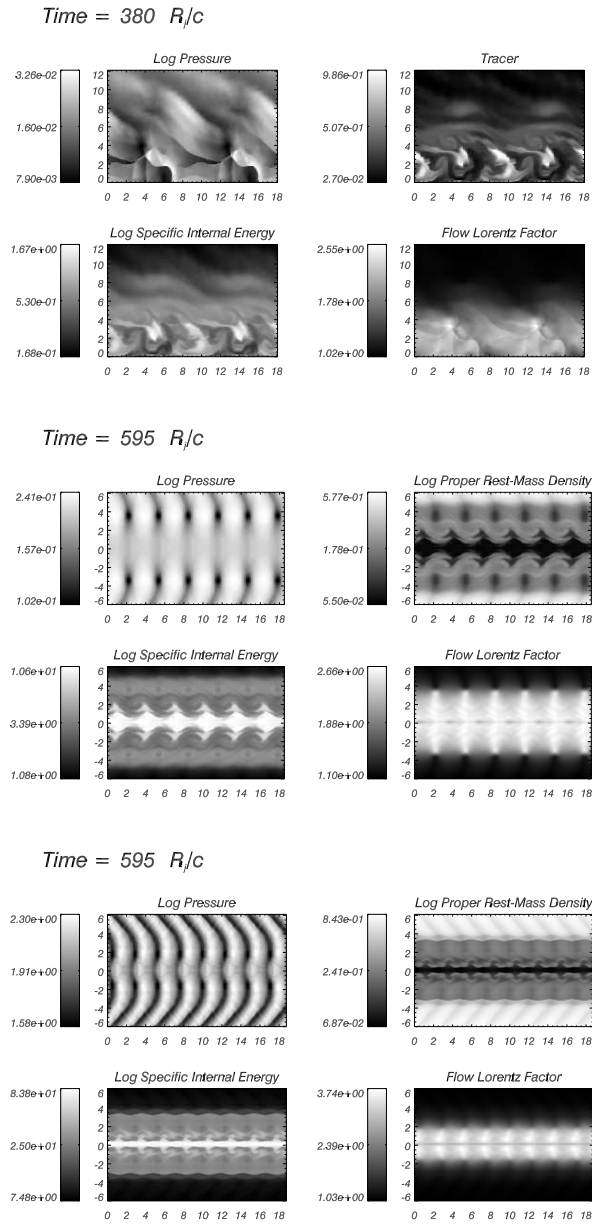


Figure 2.27: Same as Fig. (2.26) for models B05 (upper; only top half of the model shown), C05 (middle) and D05 (lower).

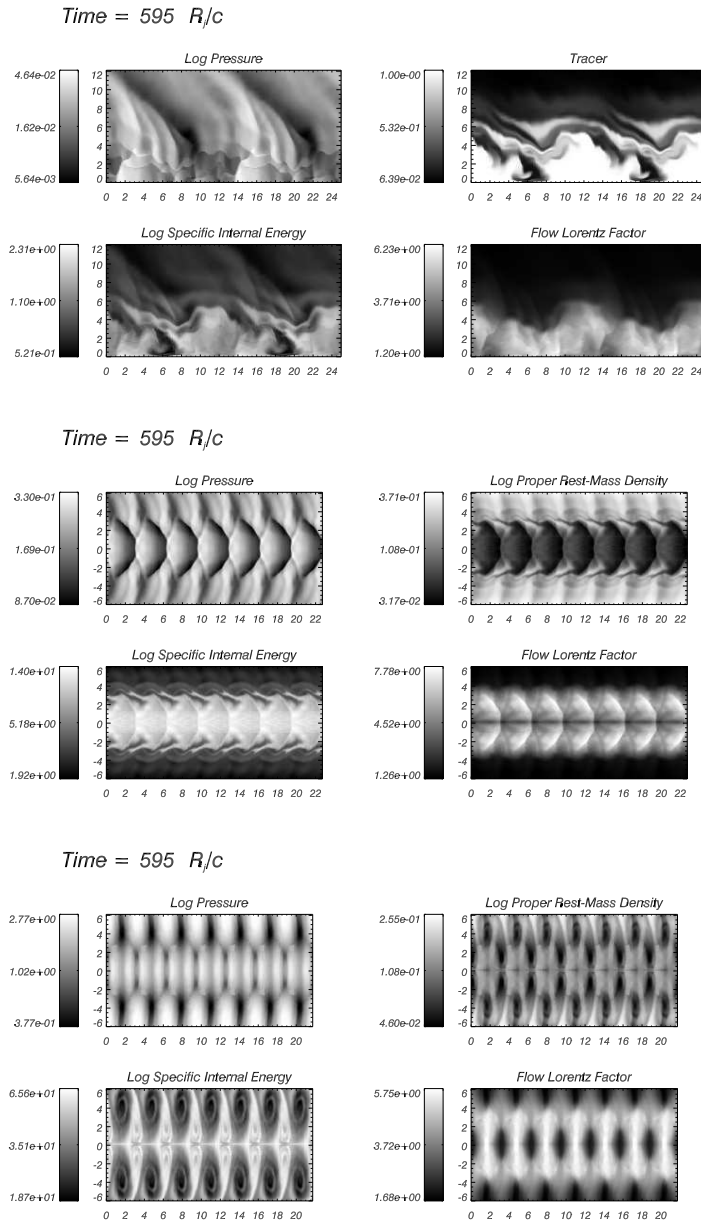


Figure 2.28: Same as Fig. (2.26) for models B10 (upper; only top half), C10 (middle) and D10 (lower; only top half).

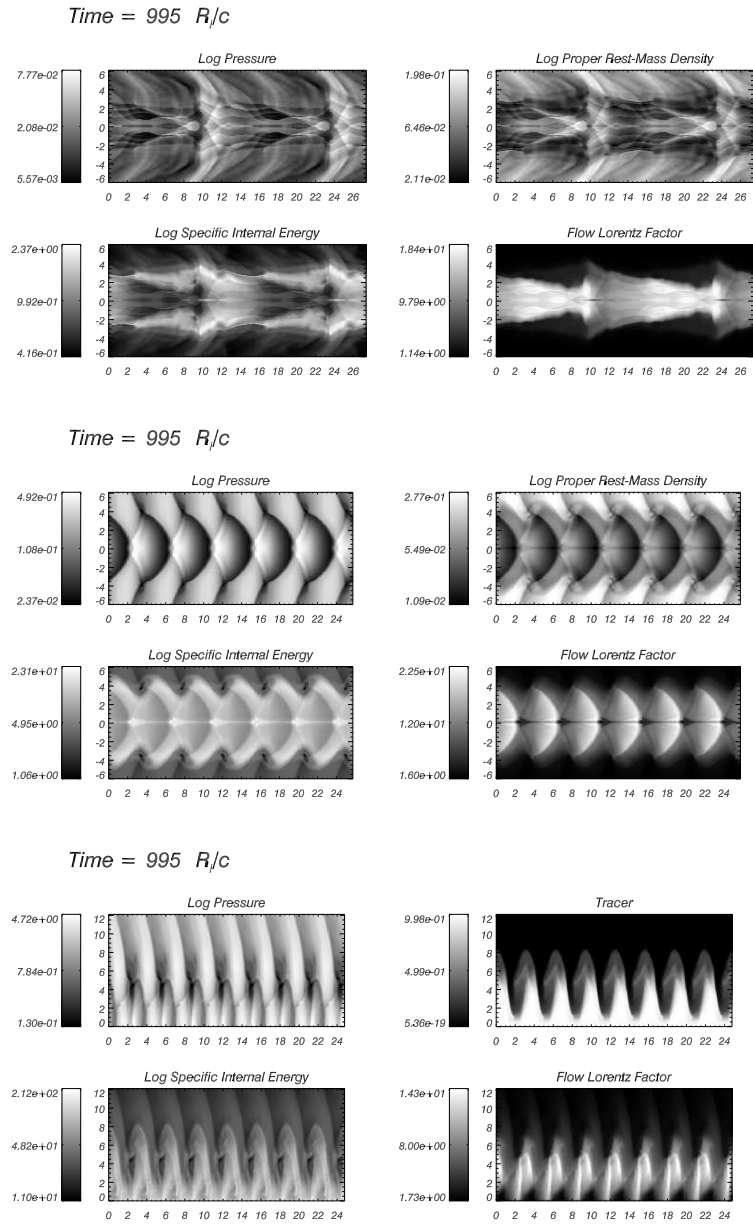


Figure 2.29: Same as Fig. (2.26) for models B20 (upper), C20 (middle) and D20 (lower; only top half of the model shown).

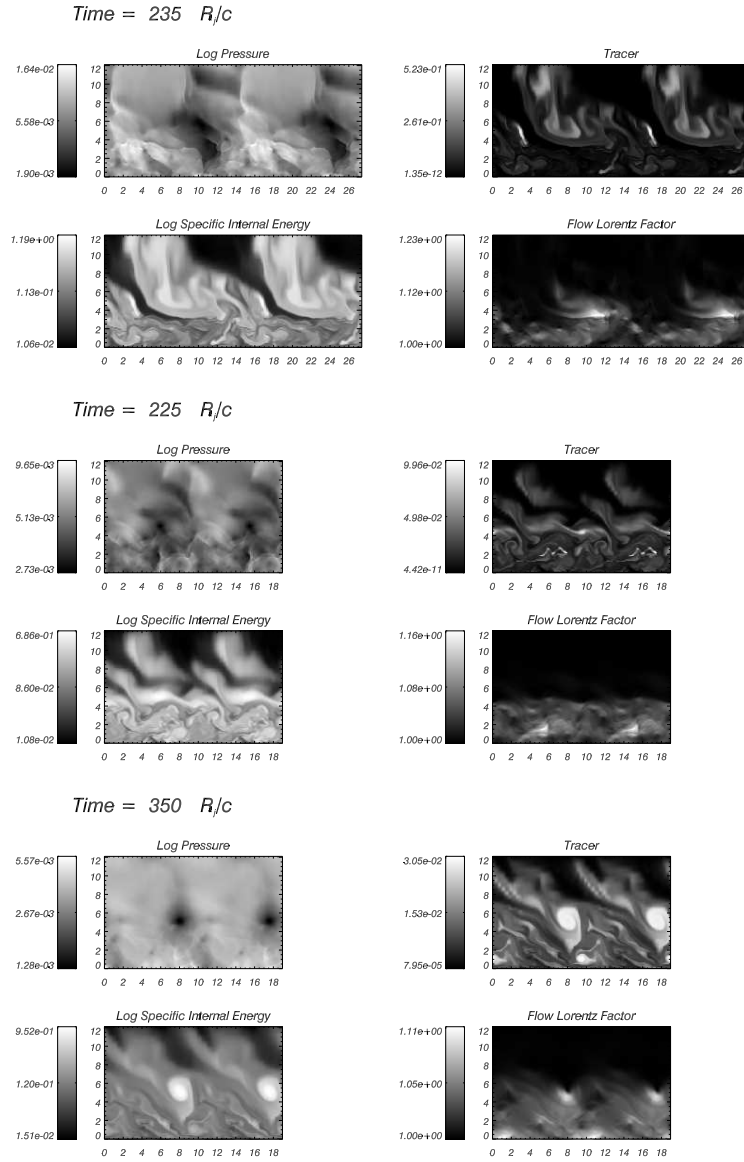


Figure 2.30: Same as Fig. (2.26) for models F (upper), G (middle) and H (lower). Only top half of the model shown.

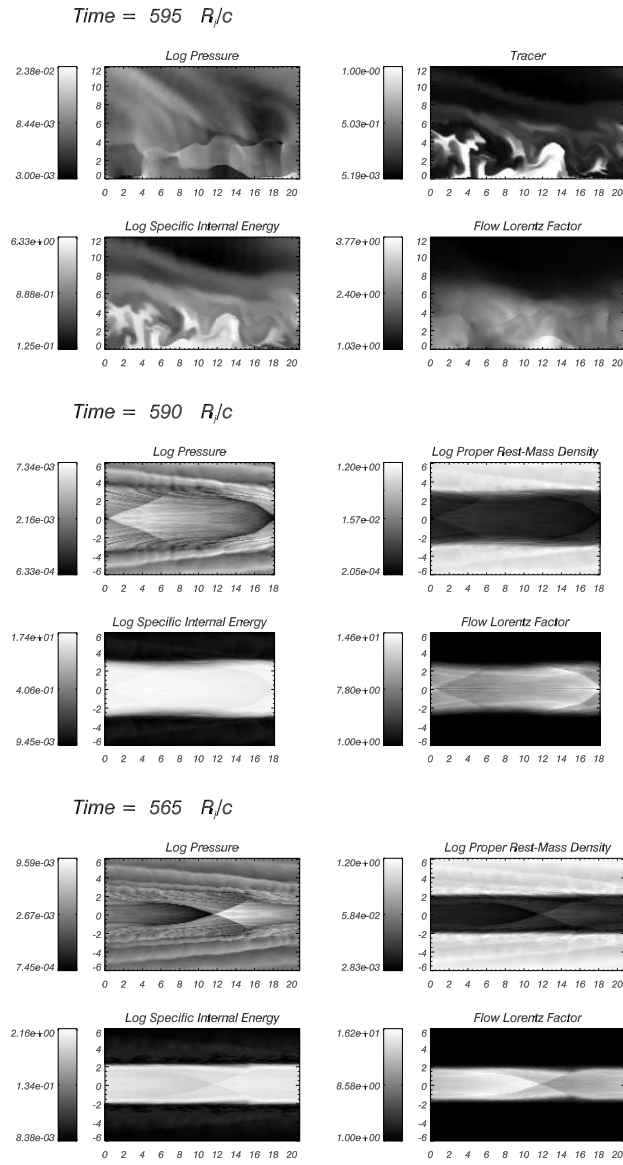


Figure 2.31: Same as Fig. (2.26) for models I (upper), and J (middle) and K (lower); only top half of the model shown for I).

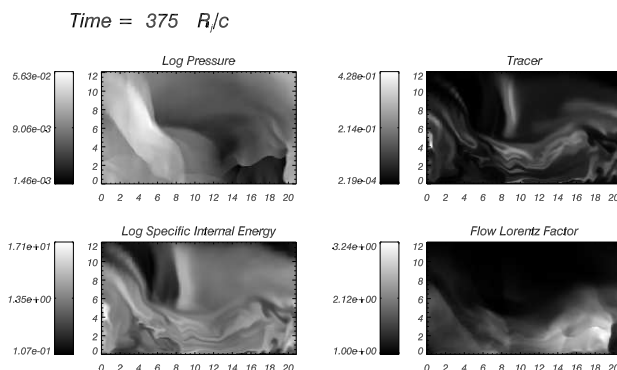


Figure 2.32: Same as Fig. (2.26) for model and L; only top half of the model shown.

overpressure of the post shock state. In the case of models C and D, the wave associated with the peak in the pressure oscillation amplitude seem to have left the grid (remember that in our jet models, hotter jets have also hotter ambient media). The most remarkable feature in the pressure profile is the depression centered at $r \approx 2R_j$ in the case of models C10 and C20 and at $r \approx 3R_j$ in the case of models D10, D20. These pressure minima coincides with the presence of vortices (clearly seen in models C20 and D20 in the corresponding panels of Fig. 2.28 and Fig. 2.29). Also remarkable in these plots is the almost total pressure equilibrium reached by models C05 and D05 and the overpressure of the jet in model D20. As we noted in previous paragraphs the models evolve following four schemes. Jets belonging to the classes I and II disrupt leading to the dispersion of tracer contours for more than five initial jet radii. Model D20 of class II is specific. It has not reached the tracer contour dispersion equal to five jet radii, but it clearly follows from Fig. 2.15 that this should happen around $t = 1100$. The models belonging to the classes III and IV do not exhibit the dispersion of tracer contours for more than 5 jet radii and look different at the end of simulations.

Fig. 2.34 displays, for models B05 and D05 representing classes I/II and III/IV respectively, the profiles of relevant physical quantities averaged along the jet at the end of the simulations. Let us note that different shear (in case of velocity related quantities) or transition layers (in case of material quantities) can be defined depending on the physical variable used.

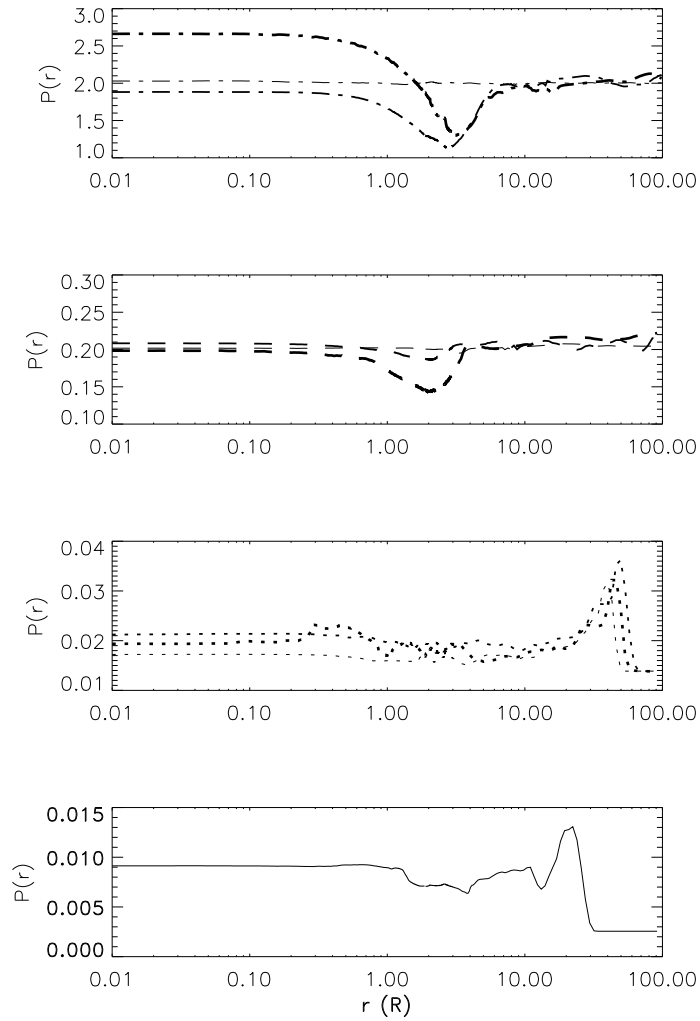


Figure 2.33: Longitudinal averaged profiles of gas pressure for all models. Different types of lines are used for models with different internal energies: Continuous line: model A; dotted line: model B; dashed line: model C; dashed-dotted line: model D. Line thickness increases with Lorentz factor (from 5, thinnest line, to 20 thickest one).

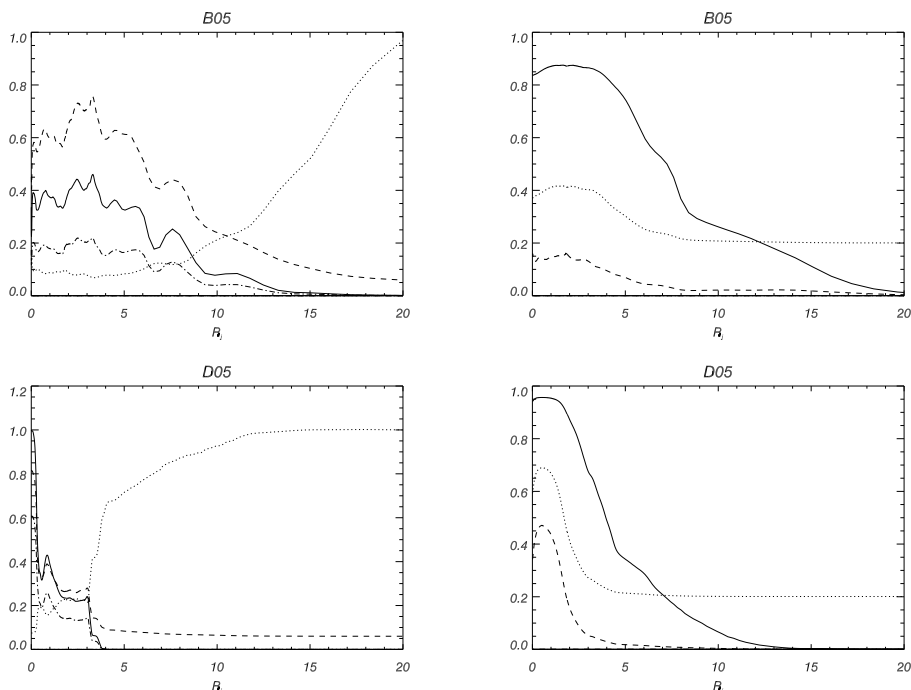


Figure 2.34: Transversal averaged profiles of relevant physical quantities at the end of simulations B05 and D05. Left column: tracer, f (full line), rest mass density, ρ_0 (dotted line), specific internal energy ε (dashed line) and jet internal energy density, $e (= \rho_0 \varepsilon f$; dash-dot line). Right column: longitudinal velocity, v_z (full line), Lorentz factor normalized to its initial value, γ/γ_0 (dotted line) and longitudinal momentum normalized to its initial value, S/S_0 . The upper plots represent the model B05 and the lower plots represent D05. Note that the values of e are multiple by 10 for model B05 and divided by 10 for model D05. The values of ε for the model D05 are divided by 100.

In case of model B05 all the material quantities (tracer, density and internal energy) exhibit a wide broadening in the radial direction. The distribution of tracer extends up to $r = 15R_j$, which means that jet material has been spread up to this radius, with a simultaneous entrainment of the ambient material into the jet interior. The latter effect is indicated by the lowering of the maximum tracer value from 1 down to 0.4. The fine structure of the tracer distribution

displays random variations, which apparently correspond to the turbulent flow pattern well seen in Fig. 2.27 (upper set of panels). The curve of internal energy is very similar to the one corresponding to tracer, however variations are seen up to $r = 20R_j$. The profile of density is wider than the profile of the tracer (the density is growing up to $r \sim 40R_j$, which can be explained by the heating of external medium, in the jet neighborhood, by shocks associated with outgoing large amplitude sound waves and by transversal momentum transmitted to the ambient medium via sound waves. Finally, the profile of the specific internal energy is consistent with the density profile and the fact of the jet being in almost pressure equilibrium.

The dash-dot curve in Fig. 2.34 (top left panel) represents the (internal) energy per unit volume held in jet matter. Such a quantity, like the mean Lorentz factors in both inner jet and shear layer are of special importance as they are directly related to the emission properties of the model. Internal energy density in jet particles is related to the fluid rest frame synchrotron emissivity, whereas the fluid Lorentz factor governs the Doppler boosting of the emitted radiation. As seen in the top right panel of Fig. 2.34, the final mean profile of velocity is similar in shape to the profile of internal energy, despite the fact that it is smoother. Similarly to internal energy, the longitudinal velocity variations extend up to $r = 20R_j$. This can be understood in terms of large amplitude, non-linear sound waves, which contribute to the transport of internal and kinetic energies in the direction perpendicular to the jet axis. The profiles of Lorentz factor and longitudinal momentum are significantly narrower. Therefore in case of models similar to B05 only the the most internal part, up to $r \leq 8R_j$ of the wide sheared jet, will be Doppler boosted, even though the jet material quantities extend behind $r \simeq 15R_j$.

A similar discussion can be performed for the model D05 representing the other group of jets, which form a shear layer without experiencing the phase of rapid disruption. As seen in the bottom panels of Fig. 2.34, the jet of model D05 preserves sharp boundaries between their interior and the ambient medium, although both media are modified by the dynamical evolution at earlier phases. The sharp boundary (transition layer) at $r \simeq 3.2R_j$ is apparent in the plots of all material quantities, i.e. tracer, density, internal energy. The thickness of the transition layer for all the quantities is comparable to one initial jet radius, 10 times narrower than in case of B05. We note, however a smooth change of ambient gas density in the range of $r \sim 3.2R_j \div 12R_j$.

It is apparent also that a narrow core of almost unmixed ($f = 1$) jet

material remains at the center in the currently discussed case. The radius of the core is about one half of the original jet radius. The core sticks out from a partially mixed, relatively uniform sheath and is well seen in the plots of tracer and internal energy for that model, however it disappears when increasing the resolution in the longitudinal direction, as we will see in the next subsection.

Concerning the dynamical quantities, we note that there is no sharp jump in the profiles of longitudinal velocity, Lorentz factor and longitudinal momentum and the central core does not appear in profiles of these quantities. Significant longitudinal velocities extend up to $r \simeq 12R_j$ as in case of density, in contrast to tracer and internal energy. As noted previously, the averaged pressure distribution for model D05 is practically uniform in the whole presented range of the transversal coordinate. Therefore as in case B05 we can conclude that the variations of density in the ambient medium are due to the heat deposited by non-linear sound waves. On the other hand the widths of the profiles of the Lorentz factor and longitudinal momentum are comparable to those of jet mass fraction and specific internal energy. Then the emission of the whole jet volume will be Doppler boosted.

Models B05 and D05 were considered as representative cases of models developing shear layers wider (group 1; classes I and II) and narrower (group 2; classes III and IV), respectively, than $5R_j$. Now the question is up to which extent the characteristics of the shearing flow of these two models are common to the models in the corresponding groups. We note that given the large differences between the initial parameters of models in classes I and II, on one hand, and III and IV, on the other, we do not expect a perfect match among the properties of the transversal structure in models within the same group. For example, whereas models in class I develop wide shear layers due to the action of a strong shock formed at the end of the saturation phase, models in class II develop shear layers through a continuous injection of transversal momentum and the generation of large vortices at the jet ambient interface.

We now investigate relations among the following averaged quantities in the whole set of models at the final state: the dispersion of tracer contours, the typical widths of profiles of density, internal energy density in jet matter (r_e), velocity, Lorentz factor (r_γ) and longitudinal momentum (r_S) and the peak values of Lorentz factor and the longitudinal momentum (S_{\max}). In all cases the peak values were measured directly, whereas the typical width of the profiles were taken as their width at the mean value between the maximum and minimum ones. We find that for all models of group 1, $r_\gamma > 4R_j$, $r_S > 3.5R_j$,

$r_e > 7R_j$ and $S/S_0 < 0.2$. In case of all models of group 2, $r_\gamma < 4R_j$, $r_S < 3.5R_j$, $r_e < 7R_j$ and $S_{\max}/S_0 > 0.2$.

2.4.4 Influence of numerical resolution in the non-linear evolution

In order to be aware of the limitations of the resolution used in the results for the non-linear regime, we repeated model C05 (C16 here) with the same transversal resolution (400 cells/ R_j) and changing the longitudinal resolution. First we double it (32 cells/ R_j , C32) and then multiply it by four (64 cells/ R_j , C64), and finally, in order to have similar resolutions in both transversal and longitudinal directions, we performed this simulation using 256×128 cells/ R_j (C128). Models C16, C32 and C64 were evolved up to a time larger than 600 R_j/c , whereas model C128 was stopped at $t = 375R_j/c$.

Table 2.4 displays the data corresponding to Table 2.3 for models C16, C32, C64, C128. Differences in the duration of the phases are apparent but not significant. Regarding the linear regime, perturbations in models C32 and C64 grow closer to linear predictions (growth rate 0.093 c/R_j) in both cases; to be compared with the analytical value 0.114 c/R_j rather than C16 (0.085 c/R_j). C128 has a slower growth rate (0.073 c/R_j) due to its smaller transversal resolution (see subsection on numerical setup). Values of pressure perturbation at the peak range from 3 to 8, increasing generally from smaller to larger longitudinal resolution. Moreover, transversal relativistic Mach numbers are also increasing with resolution (from a value of about unity to two), so that we observe a stronger, although still weak, shock in C64 and C128 than in C16 or C32. This is maybe due either to the instability giving rise to the shock (see previous subsection on non-linear regime) being better captured with increasing resolution or as the result of a smaller numerical viscosity.

Model	t_{lin}	t_{mix}	t_{sat}	t_{peak}	Δ_{peak}	t_{fmix}	t_{meq}
C16	100	120	125	130	5.0	> 595	195
C32	85	100	105	105	3.5	500	150
C64	80	100	110	115	6.5	125	150
C128	100	125	110	125	8.0	135	160

Table 2.4: Times for different phases in the evolution of simulations C16, C32, C64 and C128. See Table 2.3 for the meaning of the times at the table entries.

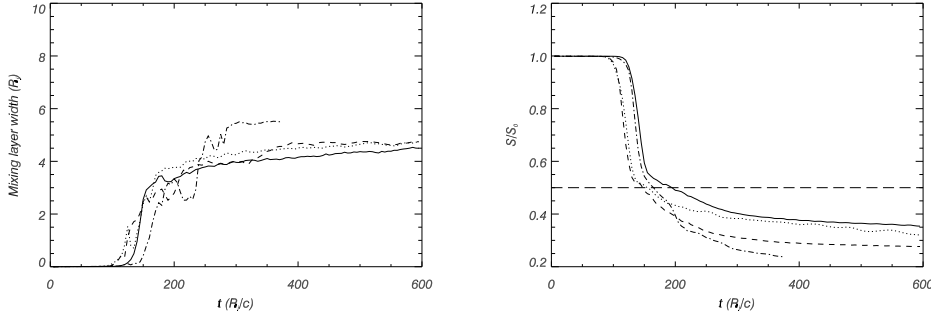


Figure 2.35: Same plots as 2.15 (left) and 2.23 (right) for models C16 (solid line), C32 (dotted line), C64 (dashed line) and C128 (dash-dotted line).

Figure 2.35 shows the time evolution of the mean width of the jet/ambient mixing layer and the total longitudinal momentum in the jet for model C05 as a function of resolution. No noticeable differences are found in the evolution of the different numerical simulations within the linear phase (up to $t \approx 100R_j/c$). However, there is a clear tendency to develop wider mixing layers and enhance momentum transfer in those simulations with higher numerical resolutions as a result of the reduction of numerical viscosity. In the case of model C128 the processes of jet/ambient mixing and momentum exchange are further enhanced by the ratio of longitudinal to transversal resolution close to unity which favors the generation of vortices in the jet/ambient boundary. The enhancement of mixing with numerical resolution and the generation of vortices in model C128 is seen in the sequence of Figs. 2.36-2.37 displaying several jet properties (pressure, specific internal energy, flow Lorentz factor and tracer) at $t = 375R_j/c$, the last computed time for model C128. Models C16 and C32 are very similar, whereas models C64 and C128 are totally mixed (see the maxima of the tracer values in the scales) and colder (as a result of the enhanced mixing with the cold ambient medium).

Finally, Fig. 2.38 shows mean transversal profiles of relevant physical quantities at $t = 375R_j/c$ for models C16 and C128. The thin, hot core in model C16 disappears in model C128 due to the enhanced mixing. In model C32 mixing down to the axis occurs after a long process. Models C64 and C128 develop weak shocks after saturation and suffer sudden mixing, which goes on in time, cooling down the remaining relativistic flow. Transition layers in rest

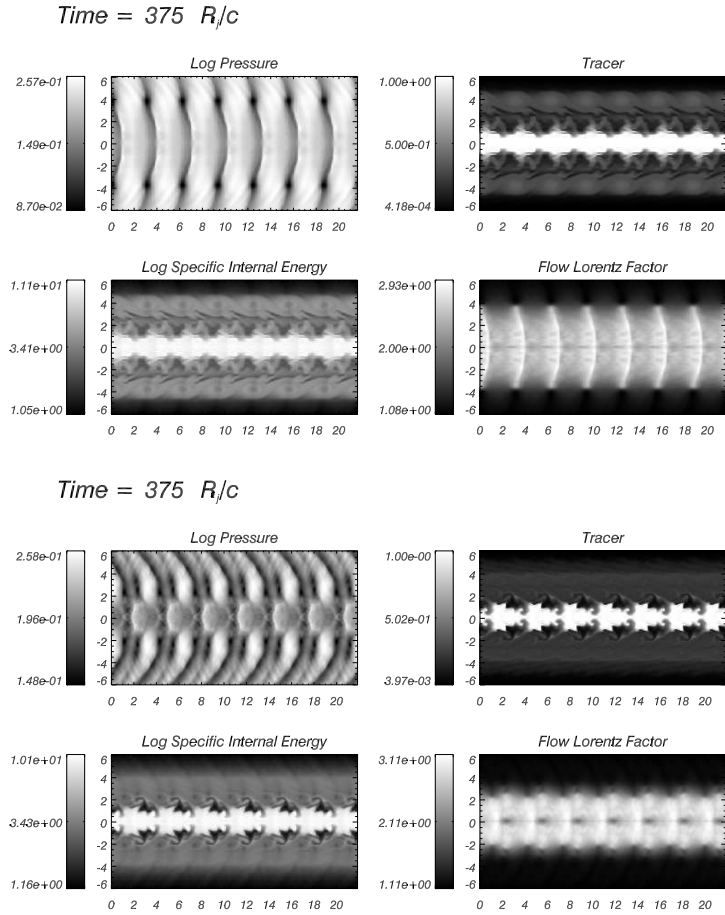


Figure 2.36: Snapshots at $t = 375R_j/c$ of logarithmic maps of pressure, jet mass fraction and specific internal energy and non-logarithmic Lorentz factor for models for for models C16 (upper) and C32 (lower).

mass density, jet mass fraction and specific internal energy are wider in model C128 due to the enhanced mixing. Longitudinal velocity and momentum and Lorentz factor profiles are more similar in all the cases although the relativistic core is thinner in model C128. Main conclusion from this study tells us that we need higher resolution in order to be sure that turbulent mixing is not stopped by numerical viscosity. Nevertheless, global dynamical quantities

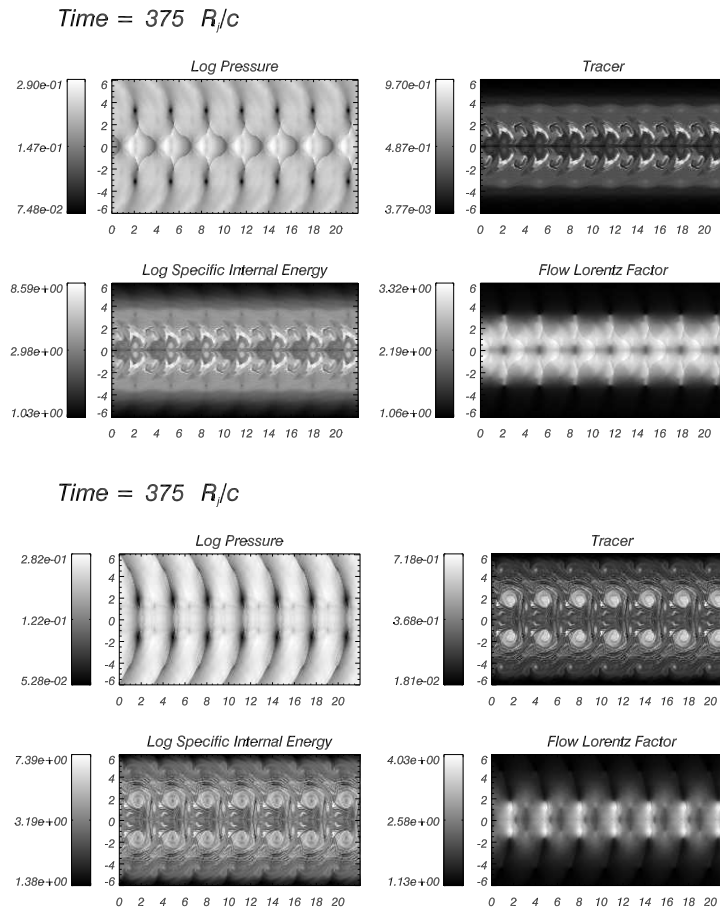


Figure 2.37: Same as Fig. 2.36 for models C64 (upper) and C128 (lower).

are well described with the resolution used in the simulations presented in this Chapter, with respect to the largest resolutions used in the tests. Therefore, main conclusions from our work remain unchanged.

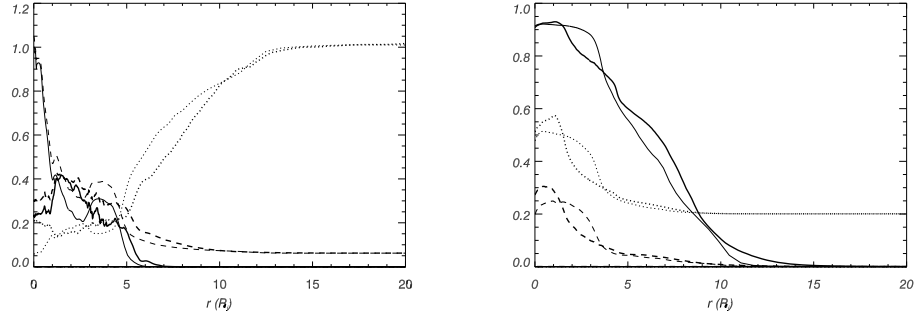


Figure 2.38: Longitudinal averaged profiles of relevant physical quantities for models C16 (thin lines) and C128 (thick lines) in the last snapshot of simulation C128 ($t = 375R_j/c$). Left panel: tracer (full line), rest mass density (dotted line) and internal energy divided by 10 (dashed line). Mixing produces a denser and colder jet in model C128. Right panel: longitudinal velocity (full line), Lorentz factor normalized to its initial value (dotted line) and longitudinal momentum normalized to its initial value (dashed line).

2.5 Conclusions

We have performed a linear stability analysis and high-resolution numerical simulations for the most unstable first reflection modes in the temporal approach, for three different values of the jet Lorentz factor γ (5, 10 and 20) and a few different values of specific internal energy of the jet matter (from 0.08 to $60.0c^2$).

Our simulations describe the linear regime of evolution of the excited eigenmodes of the different models with high accuracy. The growth rates of the perturbed modes in the vortex sheet approximation were determined with an average relative error of 20%.

In all the examined cases the longitudinal velocity perturbation is the first quantity that departs from linear growth when it reaches a value close to the speed of light in the jet reference frame. The reason for this saturation, specific to relativistic dynamics, is not so obvious in the reference frame of the external medium where it saturates at a smaller value ($\approx c/\gamma$, where γ is the bulk flow Lorentz factor in the jet).

The saturation phase extends from the end of the linear phase up to the

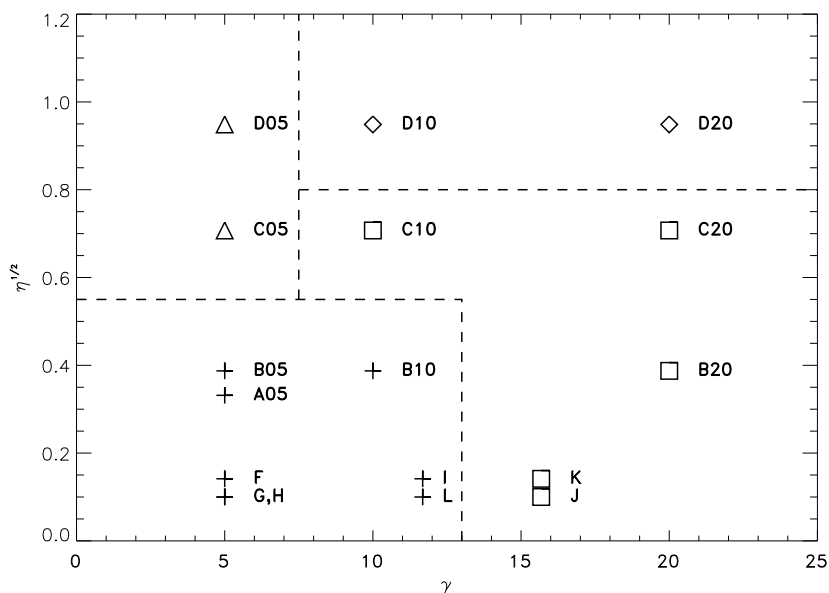


Figure 2.39: Square root of the jet-to-ambient enthalpy ratio versus jet Lorentz factor. Symbols represent different non-linear behaviors: crosses stand for shock disrupted jets (cold, slow jets, along with tenuous, hot, moderately fast or slow ones); diamonds for unstable, hot, fast jets; triangles for relatively stable hot, slow, and squares for stable, warm, fast, along with hot, tenuous, faster jets.

saturation of the transversal velocity perturbation (at approximately $0.5c$ in the jet reference frame). The saturation times for the different numerical models have been explained from elementary considerations, i.e. from properties of linear modes provided by the linear stability analysis and from the limitation of the transversal perturbation velocity.

The limitation of the components of the velocity perturbation at the end of the linear and saturation phases allows us to conclude that the relativistic nature of the flow appears to be responsible for the departure of the system from linear evolution. This behaviour is consistent with the one deduced by Hanasz (1995, 1997) with the aid of analytical methods.

At the saturation time the perturbation structure is close to the structure of the initial perturbation (the one corresponding to the most unstable first re-

flection mode), except that the oblique sound waves forming the perturbation became steep due to their large amplitude. It is interesting to note that the oblique shocks are stronger (i.e., the pressure jumps are larger) in the colder cases.

Our simulations, performed for the most unstable first reflection modes, confirm the general trends resulting from the linear stability analysis: the faster (larger Lorentz factor) and colder jets have smaller growth rates. As we mentioned in the Introduction, Hardee et al. (1998) and Rosen et al. (1999) note an exception which occurs for the hottest jets. These jets appear to be the most stable in their simulations (see also the simulations in Martí et al. 1997). They suggest that this behaviour is caused by the lack of appropriate perturbations to couple to the unstable modes. This could be partially true as fast, hot jets do not generate overpressured cocoons that let the jet run directly into the non-linear regime. However, from the point of view of our results, the high stability of hot jets may have been caused by the lack of radial resolution that leads to a damping in the perturbation growth rates. We note that the agreement between the linear stability analysis and numerical simulations of KH instability in the linear range has been achieved for a very high radial resolution of 400 zones/ R_j , which appears to be especially relevant for hot jets. Finally, one should keep in mind that the simulations performed in the aforementioned papers only covered about one hundred time units, well inside the linear regime of the corresponding models for small perturbations.

The high accuracy of our simulations in describing the early stages of evolution of the KH instability (as derived from the agreement between the computed and expected linear growth rates and the consistency of the saturation times) establishes a solid basis to study the fully non-linear regime. We show that the similarities found in the evolution of all the models across the linear and saturation phases is lost and very different non-linear evolution is found depending on the initial jet parameters.

We have also studied the non-linear evolution of the relativistic planar jet models. The models have been classified into four classes (I to IV) with regard to their evolution in the non-linear phase, characterized by the process of mixing and momentum transfer. Cold, slow jets (Class I) develop a strong shock in the jet/ambient interface at the end of the saturation phase leading to the development of wide, mixed, shear layers. Hot fast models (Class II) develop wide shear layers formed by distinct vortices and transfer more than 50% of the longitudinal momentum to the ambient medium. In models within

this class, the high Lorentz factor in the original jet and its high internal energy act as a source of transversal momentum that drives the process of mixing and momentum transfer. Between these classes we find hot, slow models (Class III) that have intermediate properties. Finally we have found cold/warm and fast models (Class IV) as the most stable. Whether a jet is going to develop a strong shock and be suddenly disrupted seems to be encoded in the peak of the pressure oscillation amplitude at the end of the saturation phase and the related transversal Mach number.

The above picture is clarifying but is subject to the limitations of our choice of initial parameters that was restricted to values with $\rho_{0j} = 0.1$. This restriction together with the initial pressure equilibrium lead to a constant jet-to-ambient ratio of specific internal energies for all the models, i.e., hotter jets are surrounded by hotter ambient media. In order to extend our conclusions to a wider region in the initial parameter space, we have performed a supplementary set of simulations (F-L) with the aim of disentangling the effect of the ambient medium in the development of the disruptive shock appearing after saturation. Thus, hot, tenuous, slow/moderately fast jets (F, G, H, I, L) behave like cold, dense ones in a cold environment (A05, B05, B10). However, if these hot, tenuous jets are faster (J, K), they behave as warm, fast models (e.g., C10, C20, B20). The fact that the initial Lorentz factor is high seems to prevent the transversal velocity from growing enough to generate the strong shock which breaks the slower jets.

Models undergoing qualitatively different non-linear evolution are clearly grouped in well-separated regions in a jet Lorentz factor/jet-to-ambient enthalpy diagram (see Fig. 2.39). Models in the lower, left corner (low Lorentz factor and small enthalpy ratio) are those disrupted by a strong shock after saturation. Those models in the upper, left corner (small Lorentz factor and hot) represent a relatively stable region. Those in the upper right corner (large Lorentz factor and enthalpy ratio) are unstable although the process of mixing and momentum exchange proceeds on a longer time scale due to a steady conversion of kinetic to internal energy in the jet. Finally, those in the lower, right region (cold/warm, tenuous, fast) are stable in the non-linear regime.

Our results differ from those of Martí et al. (1997), Hardee et al. (1998) and Rosen et al. (1999) who found fast, hot jets as the more stable. The explanation given by Hardee et al. (1998) invoking the lack of appropriate perturbations to couple to the unstable modes could be partially true as fast, hot jets do not generate overpressured cocoons that let the jet run directly into

the non-linear regime. However, as pointed out before, the high stability of hot jets may have been caused by the lack of radial resolution, that leads to a damping in the perturbation growth rates. Finally, the simulations performed in the aforementioned papers only covered about one hundred time units, well inside the linear regime of the corresponding models for small perturbations. Here, the problem of the stability of relativistic jets is analyzed on the basis of long-term simulations that extend over the fully non-linear evolution of KH instabilities.

At the end of our simulations, the models continue with the processes of mixing, transfer of momentum and conversion of kinetic to internal energy, however they seem to experience a kind of averaged quasisteady evolution which can be still associated with the evolution of a jet, i.e., a collimated flux of momentum. This jet is always wider, slower and colder than the original one and is surrounded by a distinct shear layer. Hence transversal jet structure naturally appears as a consequence of KH perturbation growth. The widths of these shear (in case of velocity related quantities) or transition layers (in case of material quantities) depend on the specific parameters of the original jet model as well as the physical variable considered. However, models in classes III and IV develop thin shear layers, whereas the shear layers of models in classes I and II are wider.

2.6 Single antisymmetric mode simulations

We performed simulations, following the same perturbation setup as in the symmetric case, but using the first antisymmetric reflection mode of slab jets, instead, for models B05, B20, D05 and D20, representing the four stability regions found (see Fig. 2.39). First aim was to check symmetry properties of the numerical code (see Section A) in order to perform more general models, including both symmetric and antisymmetric modes.

Numerical setup in these simulations is in general, very similar to that in the symmetric case. Main differences are the following: we simulate the whole jet, so we have outflow boundary conditions far from the axis in both directions; the resolution was changed, using 256 cells/ R_j in the transversal direction and 32 cells / R_j in the axial direction, following results from the study on the influence of axial resolution in the non-linear regime; due to the decrease in transversal resolution, we also decreased the value of m , giving the steepness of the shear layer, and $m = 25$ in these simulations, so the thickness

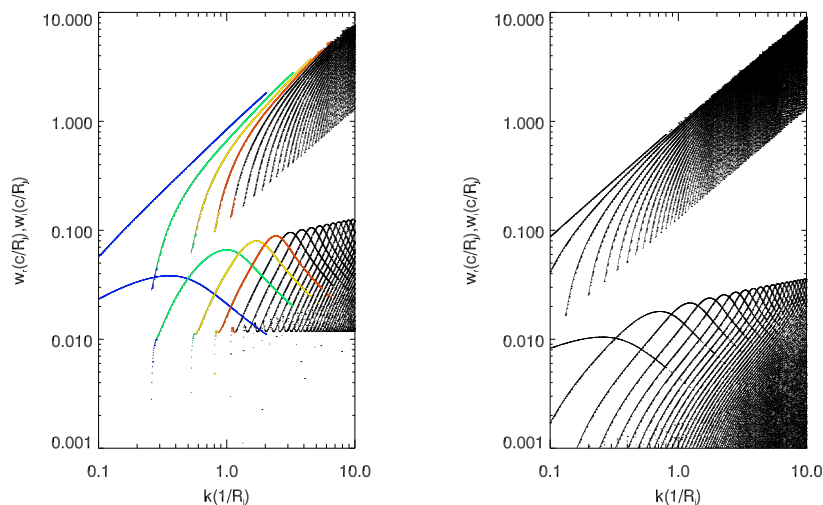


Figure 2.40: Antisymmetric solutions of Equation 2.26 for slab jets B05 (left panel) and B20 (right panel). In left panel colors identify real and imaginary parts of single modes as an example for the reader.

of the shear layer is $0.18 R_j$, i.e., thicker than used in the symmetric case. The box size was also adapted to the wavelength of the first reflection eigenmode ($\sim 7 R_j$ for model B05, $\sim 1.8 R_j$ for D05, $\sim 9 R_j$ for B20 and $\sim 3 R_j$ for D20) at its maximum growth rate (see Figs. 2.40 and 2.41).

The first noticeable fact in the linear regime is the breaking of the slope of perturbations in models B20 and D20 (see Figs. 2.42 and 2.43). Fourier analysis showed that this fast growing modes which dominate the growth of the instabilities are generated as harmonics of the excited mode. They represent very short longitudinal ($\sim 1 R_j$) and transversal (high order reflection modes) wavelength modes which do not appear in the dispersion relation solution for the antisymmetric case. In right panels of Figs. 2.40 and 2.41 we see that at the corresponding wavenumbers, only low order reflection modes have the largest growth rates (up to 10th reflection mode in B20), whereas found fast growing modes in the simulations are around the 30th body mode, what can be simply seen by counting zeros in transversal cuts of pressure perturbation (see the section on the linear regime at the beginning of this chapter). Therefore, there is a clear inconsistency in this result. The origin of these new modes

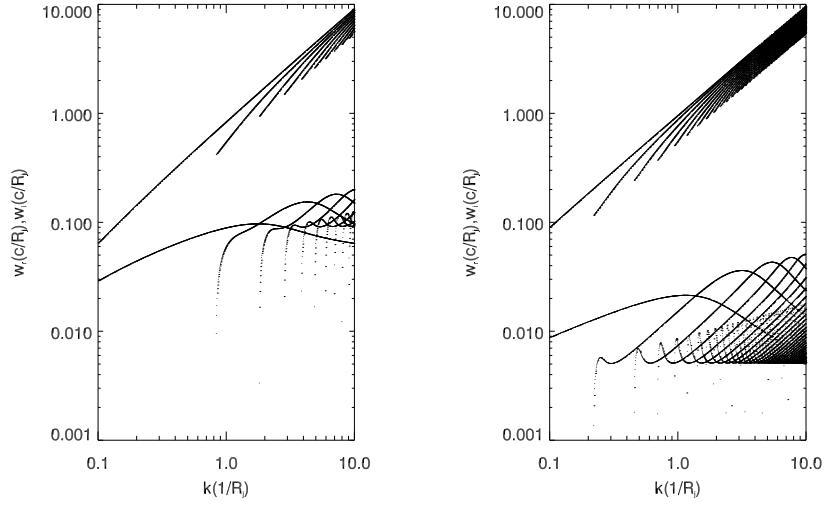


Figure 2.41: Same as Fig. 2.40 for models D05 (left panel) and D20 (right panel)

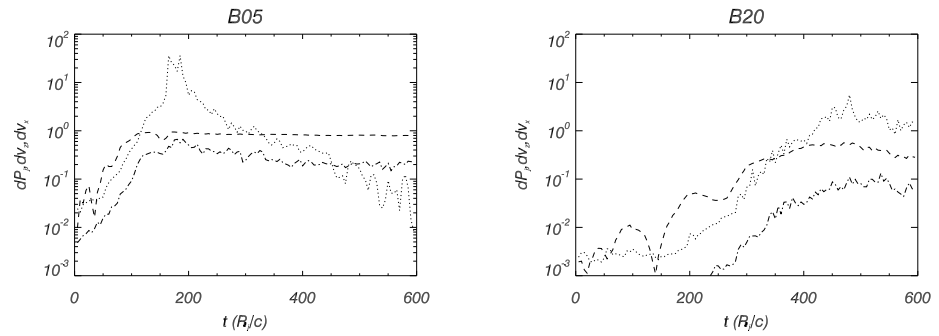


Figure 2.42: Evolution of the relative amplitudes of perturbations for models B05 (left panel) and B20 (right panel). Dotted line: pressure perturbation. Dashed line: longitudinal velocity perturbation in the jet reference frame. Dash-dotted line: perpendicular velocity perturbation in the jet reference frame. Definitions are like those in Fig 2.9.

represented a problem which was only solved when we took into account the

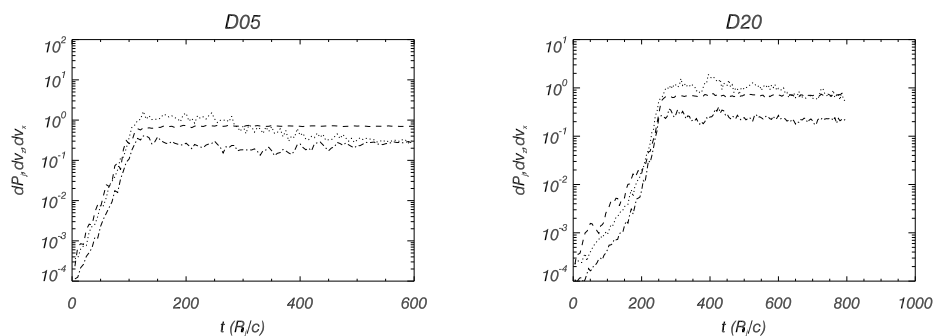


Figure 2.43: Same as Fig 2.42 for models D05 (left panel) and D20 (right panel).

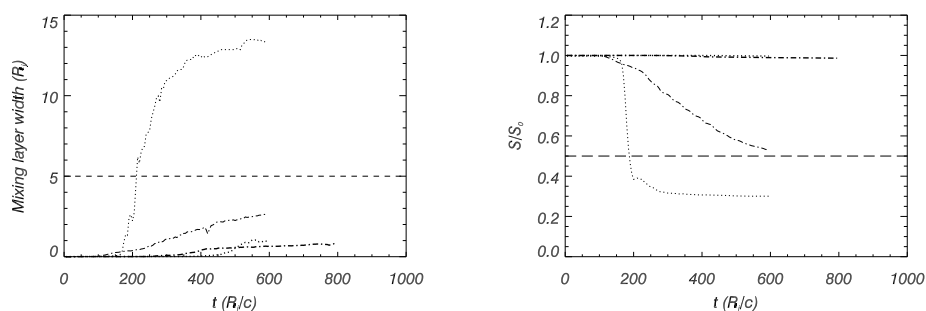


Figure 2.44: Upper left panel shows mixing layer width, upper right panel is for relative axial momentum. Dotted thin line stands for model B05, dotted thick for B20, dash-dot thin for D05 and dash-dot thick for D20.

effects of the presence of the shear layer (used in the numerical simulations) in the linear evolution of perturbations (see Chapter 3).

Regarding the non linear regime, model B05 presents a similar evolution to that in the symmetric case, whereas model D05 presents a slow disruption, contrary to the symmetric one, what may be due to the longest wavelength of the first body antisymmetric mode, to the more disruptive character of antisymmetric modes or to the numerical resolution in the axial direction, as shown before. Models B20 and D20 are conditioned by the appearance of short wavelength, fast growing modes, no shock appear after saturation

and the transition to the non-linear, mixing phase is smooth, with almost no transfer of longitudinal momentum to the ambient and no mixing (see Fig. 2.44).

In Figs. 2.45-2.46 we show panels at the last frame of the simulations, for pressure, jet mass fraction, internal energy density and Lorentz factor. First remarkable fact is that the symmetry properties of the flow are kept by the code. Regarding physical properties, in Lorentz factor 20 models we can see the long term stability generated due to the appearance of the fast modes, mostly in model D20 with respect to the symmetric case, along with the presence of a wide and hot shear layer, protecting a faster and colder core.

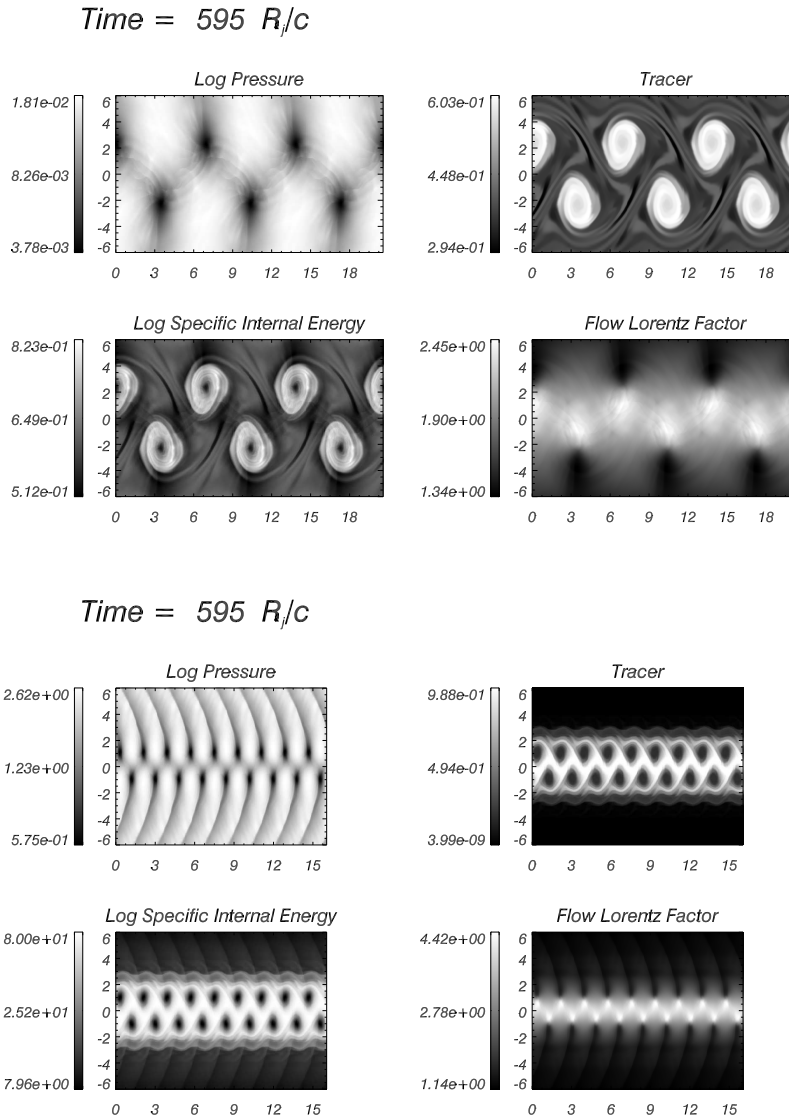
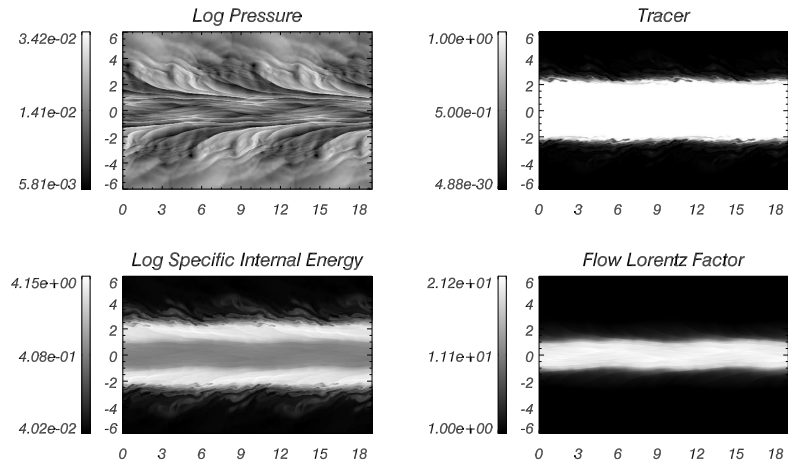


Figure 2.45: Same as Fig. (2.26) for models B05 (upper) and D05 (lower) perturbed with first body antisymmetric mode, at the end of simulations.

Time = 595 R/c



Time = 795 R/c

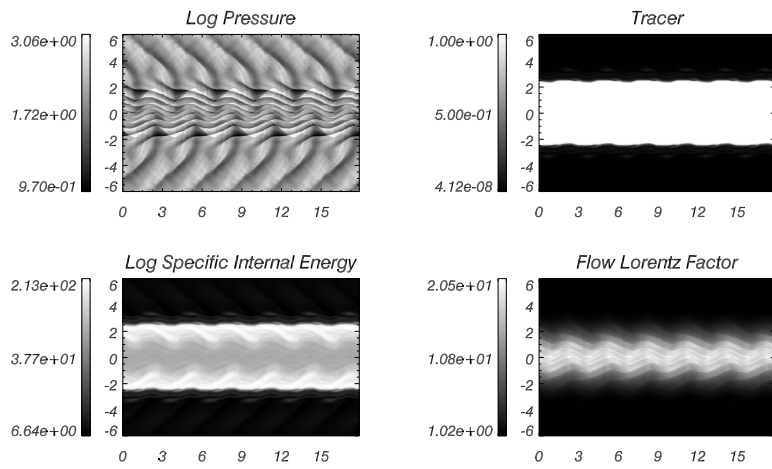


Figure 2.46: Same as Fig. 2.45 for models B20 (upper) and D20(lower).

Chapter 3

STABILITY OF SHEARED FLOWS

Transversal structure in extragalactic jets could be the natural consequence of current formation mechanisms (see, e.g., Sol et al. 1989; Celotti and Blandford 2001), in which an ultrarelativistic presumably electron/positron outflow from the high latitude region close to the spinning black hole (and powered by, e.g., the extraction of energy from the hole) is surrounded by a mildly relativistic, electron/proton, hydromagnetic outflow launched from the outer parts of the accretion disk. Recent numerical simulations of jet formation from black hole magnetospheres (Koide et al. 1998) also lead to outflows with *two-layered shell structure* consisting of inner, fast gas pressure driven jets surrounded by slower, magnetically dominated winds. At larger scales, shear layers (with distinct kinematical properties and magnetic field configurations) have been invoked in the past by several authors (Komissarov 1990a,b, Laing 1996, Laing and Bridle 2002a,b) in order to account for a number of observational characteristics of FR I radio sources. The model of De Young (1993) to explain the FRI/FRII morphological dichotomy is based on the deceleration of the jet flow at the inner galactic core and the subsequent formation of turbulent shear layers in FRIs. Recently, Swain et al. (1998) have found evidence of shear layers in FR II radio galaxies (3C353), and Attridge et al. (1999) have inferred a two-component structure in the parsec-scale jet of the source 1055+018. On the other hand, first simulations of radio emission from three-dimensional relativistic jets with shear layers (Aloy et al. 2000) allowed to interpret several observational trends in parsec and kiloparsec jets: inho-

mogeneous distributions of apparent speeds within radio knots (Biretta et al. 1995); rails of low polarization along jets (as in 3C353; Swain et al. 1998); top/down jet emission asymmetries in the blazar 1055+018 (Attridge et al. 1999). Stawarz and Ostrowski (2002) have studied the contribution to the radiative jet output from turbulent shear layers in large-scale jets.

In this chapter we present the results obtained from the study of the stability of relativistic, sheared slab and cylindrical jets. These results, in the linear and non-linear regimes, have been submitted (Perucho et al. 2005a and Perucho et al. 2005b).

3.1 Linear analysis

A general treatment of compressible shear layers in the case of infinite plane boundary (non-relativistic) problems was first proposed in Blumen et al. (1975) and Drazin and Davey (1977). In Ferrari et al. (1982) the study on the effects of shear layers was extended to the case of infinite slab jets, concentrating on the wave number range $0.1/R_j \leq k \leq 10/R_j$ for ordinary ($n_x = 0$) and the first reflection ($n_x = 1, 2, 3$) symmetric and antisymmetric modes (n_x represents the number of nodes between the axis and the surface across the planar jet).

An attempt to investigate the growth of the KH instability in some particular class of sheared, cylindrical relativistic jets was pursued in Birkinshaw (1991a). However, the study is limited to the ordinary ($n_r = 0$) and first two reflection modes ($n_r = 1, 2$), and the domain of jet parameters considered involves only marginally relativistic flows (beam flow velocities $\leq 0.1c$; c is the speed of light) and non-relativistic (jet, ambient) sound speeds ($\leq 0.01c$). The main conclusion extracted from Ferrari et al. (1982) and Birkinshaw (1991) was that shear layers reduce the growth rates of body modes and prohibit the growth of modes with wavelengths smaller than the width of the layer. Other approaches to the linear analysis of the stability of relativistic stratified jets (Hanasz and Sol 1996, Hardee and Hughes 2003) and sheared, ultrarelativistic jets (Urpin 2002) have also been performed. Several recent works have combined linear analysis and hydrodynamical simulations in the context of both relativistic jets (Rosen et al. 1999, Hardee 2000, 2001) and GRBs (Aloy et al. 2002).

In this Chapter, we show new results on the linear analysis of sheared relativistic flows, along with numerical simulations which support them and

allow us to obtain information on the non-linear regime.

In Appendix D we present the development of the differential equation for the evolution of pressure perturbations. We give here a summary of this work. In Appendix D we also present the development of the differential equations for the linear problem of relativistic rotating and expanding jets.

Like in Chapter 2, the initial equilibrium configuration is that of a steady slab jet in Cartesian coordinates flowing along the z -coordinate, surrounded by a denser and colder ambient medium. A single-component ideal gas equation of state with adiabatic exponent $\Gamma = 4/3$ has been used to describe both jet and ambient media. Both media are in pressure equilibrium and are separated by a smooth shear layer of the form described in Eqs. (2.42) and (2.43) (Ferrari et al. 1982). Again, the integer m controls the shear layer steepness. In the limit $m \rightarrow \infty$ the configuration tends to the vortex-sheet case.

We introduce an adiabatic perturbation of the form $\propto A(x) \exp(i(k_z z - \omega t))$ in the flow equations, ω and k_z being the frequency and wavenumber of the perturbation along the jet flow, and $A(x)$ giving the transversal structure of the perturbation. We shall follow the *temporal approach*, in which perturbations grow in time having real wavenumbers and complex frequencies (the imaginary part being the *growth rate*). By linearizing the equations and eliminating the perturbations of rest mass density and flow velocity, a second order ordinary differential equation for the pressure perturbation, P_1 , is obtained (Birkinshaw 1984)

$$P_1'' + \left(\frac{2\gamma^2 v_z' (k_z - \omega v_z)}{\omega - v_z k_z} - \frac{\rho'}{\rho + P} \right) P_1' + \gamma^2 \left(\frac{(\omega - v_z k_z)^2}{c_s^2} - (k_z - \omega v_z)^2 \right) P_1 = 0 \quad (3.1)$$

where ρ is the energy-density of the unperturbed model, P the pressure, v_z the unperturbed three-velocity component, $\gamma = 1/\sqrt{1 - v_z^2}$ is the Lorentz factor and c_s is the relativistic sound speed. The prime denotes the x -derivative. Unlike the vortex sheet case, in the case of a continuous velocity profile, a dispersion relation can not be written explicitly. The equation (3.1) is integrated from the jet axis, where boundary conditions on the amplitude of pressure perturbation and its first derivative are imposed

$$\begin{aligned} P_1(x=0) = 1, \quad P_1'(x=0) = 0 & \quad (\text{sym. modes}), \\ P_1(x=0) = 0, \quad P_1'(x=0) = 1 & \quad (\text{antisym. modes}). \end{aligned} \quad (3.2)$$

Solutions satisfying the Sommerfeld radiation conditions (no incoming waves from infinity and wave amplitudes decaying towards infinity) are found with the aid of the method, based on the shooting method (Press et al. 1992), proposed in Roy Choudhury and Lovelace (1984).

We have solved the linear problem for more than 20 models with different specific internal energies of the jet, Lorentz factors and shear layer widths, fixing jet/ambient rest-mass density contrast ($= 0.1$). We used $m = 8, 25, 2000$ (shear layer width, $d \approx 0.6, 0.18, 5 \cdot 10^{-3} R_j$) and vortex sheet for jets having specific internal energies $\varepsilon_j = 0.4c^2$ (models B) and $60c^2$ (models D) and Lorentz factors $\gamma_j = 5$ (B05, D05) and 20 (B20, D20). Solutions with $m = 2000$ were considered in order to test convergence to vortex sheet in the case of narrow shear layers, with positive results. Also, fixing the width of the shear layer $m = 25$ we solved for $\varepsilon_j = 0.08c^2$ (models A), along with models B and D, using $\gamma_j = 2.5$ and 10, in order to span a wide range of parameters.

The basic effect of the shear layer in the stability is seen in Figs. 3.3-3.18 where we show the solutions of the equation (3.1) together with the boundary conditions (3.2) for considered models. The corresponding solution for the vortex sheet case is also shown in the case of B05 and D20 for comparison and as a test of convergence of our solutions to vortex sheet, when $m \rightarrow \infty$. We note that the reflection mode solutions of the shear problem are more stable for most wavenumbers, especially in the large wavenumber limit, than the corresponding solutions in the vortex sheet case. This behaviour was reported for the first time in Ferrari et al. (1982), for the first and second reflection modes in the non-relativistic limit. The growth rate curves corresponding to a single n_x -th reflection mode consists on a broad maximum at larger wavenumbers and a local peak which is placed in the small wavenumber limit, near the marginal stability point of the mode. While in the vortex-sheet, relativistic case the small wavenumber peaks are relatively unimportant (since the maximum growth rates at these peaks are lower than the growth rates of other unstable modes), in the presence of the shear layer they significantly dominate over other modes. Therefore we shall call these peaks *the shear layer resonances* (these resonances have been discovered during the development of the work, and this fact is reported in the paper Perucho et al. 2005a). The dependence of the properties of the growth rates associated to the shear layer resonances on the jet specific internal energy, jet Lorentz factor and shear layer parameter m are summarized in Fig. 3.1 for $0.1 < k < 100$. In that plot, we find that (see also Figs. 3.3-3.18): i) A decrease of the jet Lorentz factor

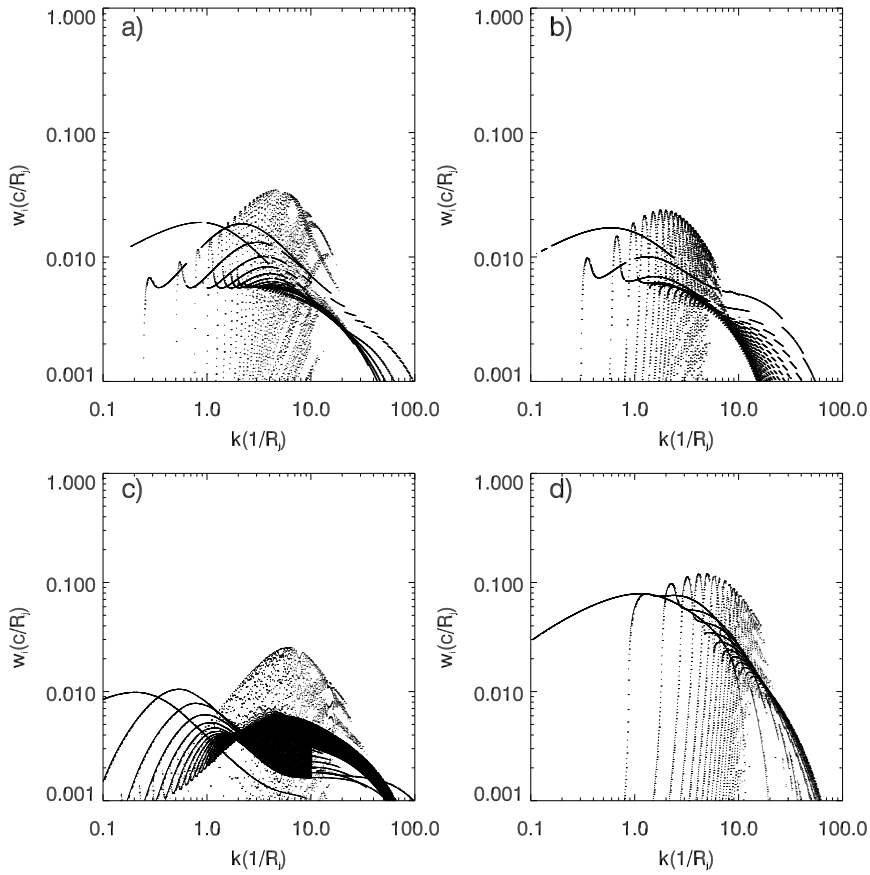


Figure 3.1: Dependence of mode growth rates with jet specific internal energy, jet Lorentz factor and shear-layer parameter m . Top panels correspond to Model D20 with $m = 25$ (panel a) and $m = 8$ (panel b). Panel c: Model B20 with $m = 25$. Panel d: Model D05 with $m = 25$.

reduces the dominance of resonant modes with respect to ordinary and low order reflection modes; ii) a decrease in the specific internal energy of the jet causes resonances to appear at longer wavelengths; iii) a further widening of the shear layer reduces the growth rates¹ and the dominance of the shear-layer

¹Models D05 and D20 were computed using a wide shear layer ($m = 1$) and results showed the disappearance of all body modes, and a slight increase in the growth rates of the fundamental mode.

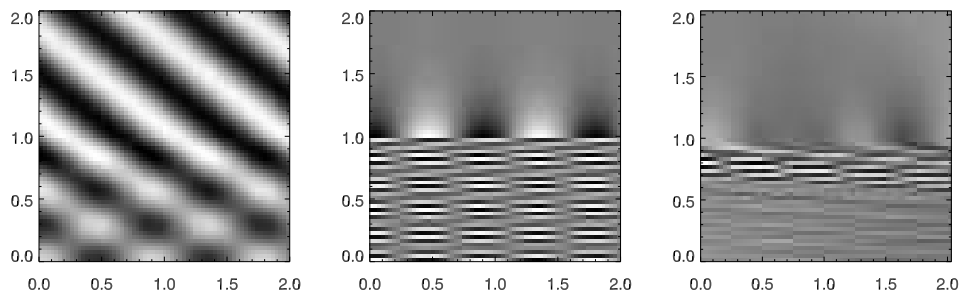


Figure 3.2: Two-dimensional panels of different pressure perturbation structures for a detail of Model D20. Left panel: vortex sheet dominant mode (low order reflection mode) at a given wavelength (from linear solution). Central panel: Dominant mode (high order reflection mode) at the same wavelength when $m = 25$ shear layer is included (also from linear solution). Right panel: Pressure perturbation map from numerical simulation.

resonances, suggesting that there is an optimal width of the shear layer that maximizes the effect, for a given set of jet parameters; the largest growth rate of resonant modes moves to smaller wavenumbers and lower order reflection modes; iv) modes with wavenumber larger than some limiting value that decreases with the shear layer width are damped significantly (short-wavelength cut-off), consistently with previous non-relativistic results (Ferrari et al. 1982).

The shear layer resonances correspond to very distinct spatial structures of eigenmodes, as it is seen in Fig. 3.2 for Model D20. The structure of maximally unstable eigenmodes in the vortex sheet case (left panel) represents a superposition of oblique sound waves in both the jet interior and the ambient medium. Contrarily, in the shear layer case, the most unstable resonant modes (central panel) have a very large transversal wavenumber in the jet interior and display a monotonic dependence on the radial coordinate (no oblique waves) in the ambient medium. This property is related to the fact that the resonant modes possess a very small phase speed in the ambient medium. In order to demonstrate the relevance of the resonant modes we display in the right panel of Fig. 3.2 an analogous pressure map resulting from a numerical hydrodynamical simulation. In this simulation an equilibrium jet with shear layer corresponding to $m = 25$ has been perturbed with a superposition of many sinusoidal perturbations which are not eigenmodes. Therefore such a perturbation can be considered as *general*, containing a contribution of

virtually all eigenmodes. As we can see the resonant mode appears in numerical simulations and its spatial structure is very similar to the most unstable resonant eigenmode obtained from the linearized equations. Fourier analysis of the results of numerical simulation shows that the fastest growing mode corresponds to the one expected from the linear analysis.

The importance of the shear-layer resonant modes relies not only on their dominance among solutions of the linearized problem, but also on their effects on the non-linear evolution of jets. In the next sections we analyze their effects on the non-linear regime in those models where they appear.

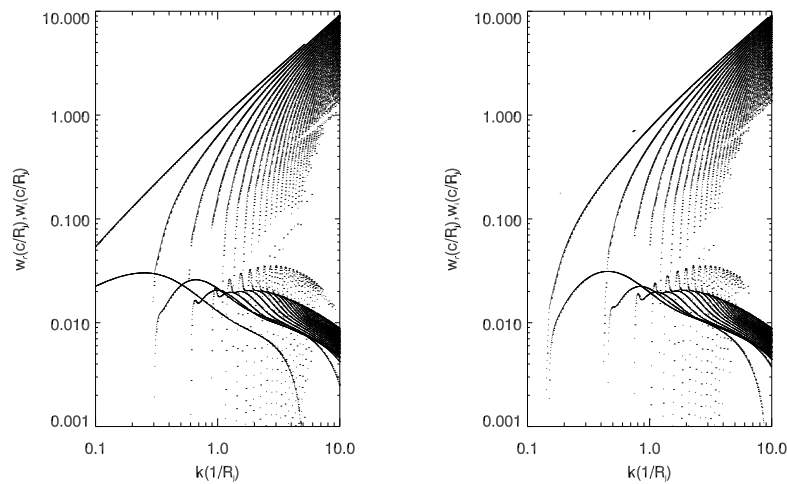


Figure 3.3: Solution for the shear layer stability problem of a slab jet with the parameters of B05 and $m = 8$. Left panel: antisymmetric; right panel: symmetric.

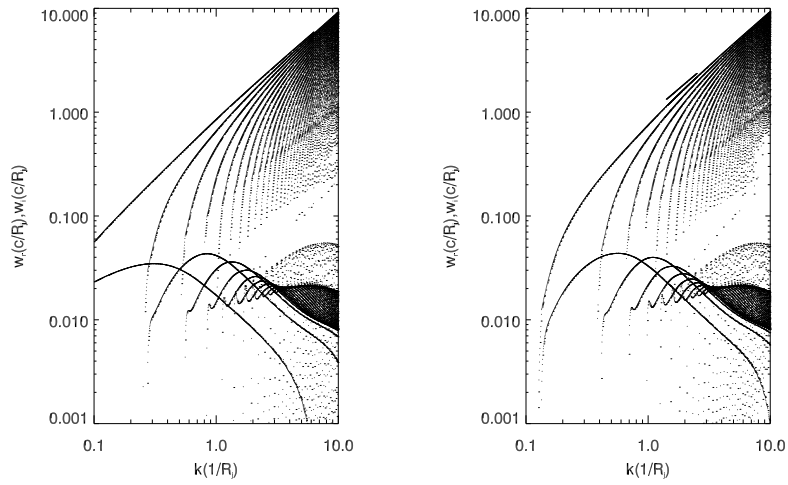


Figure 3.4: Same as Fig. 3.3 for B05 and $m = 25$. Left panel: antisymmetric; right panel: symmetric.

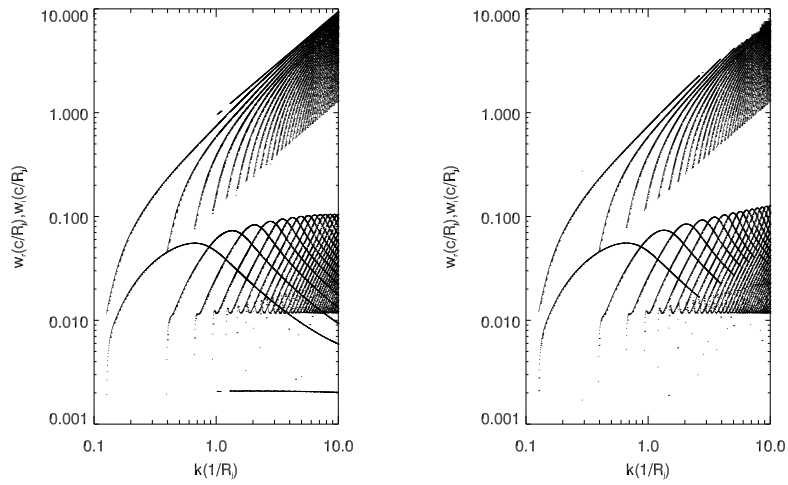


Figure 3.5: Same as Fig. 3.3 for the symmetric case of B05 and $m = 2000$ (left panel) compared to the vortex sheet solution (right panel)

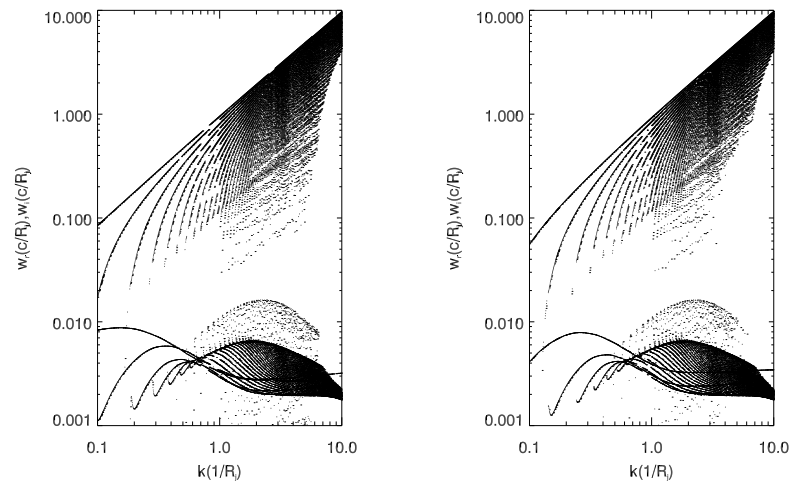


Figure 3.6: Same as Fig. 3.3 for B20 and $m = 8$. Left panel: antisymmetric; right panel: symmetric.

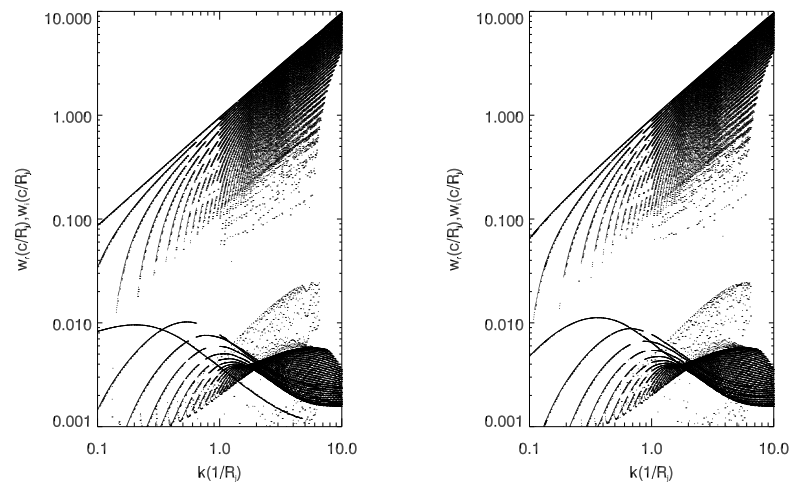


Figure 3.7: Same as Fig. 3.3 for B20 and $m = 25$. Left panel: antisymmetric; right panel: symmetric.

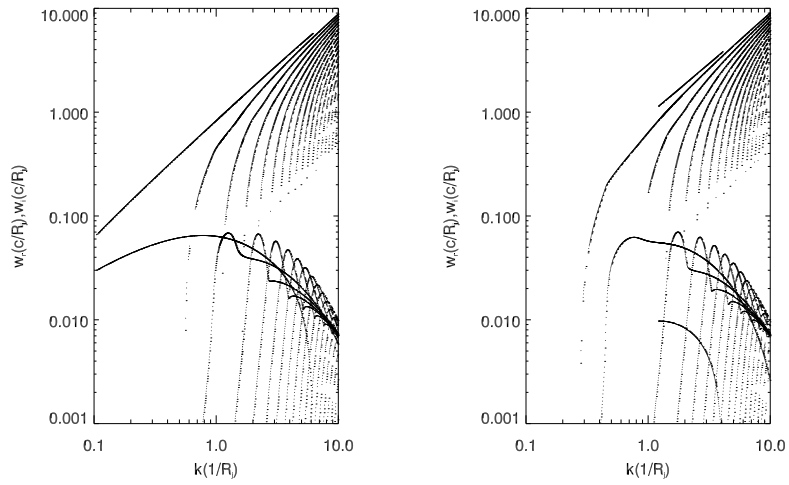


Figure 3.8: Same as Fig. 3.3 for D05 and $m = 8$. Left panel: antisymmetric; right panel: symmetric.

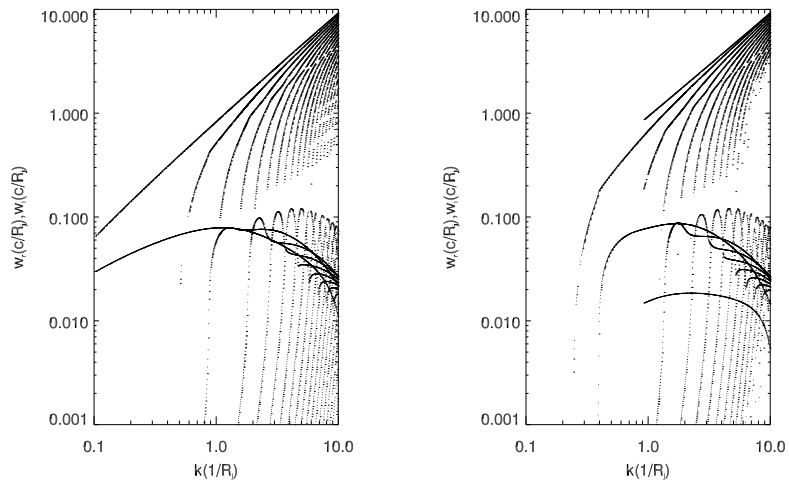


Figure 3.9: Same as Fig. 3.3 for D05 and $m = 25$. Left panel: antisymmetric; right panel: symmetric.

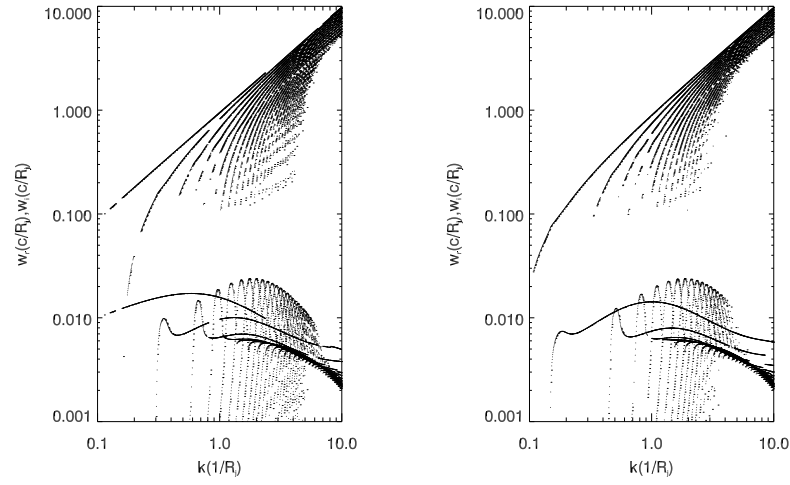


Figure 3.10: Same as Fig. 3.3 for D20 and $m = 8$. Left panel: antisymmetric; right panel: symmetric.

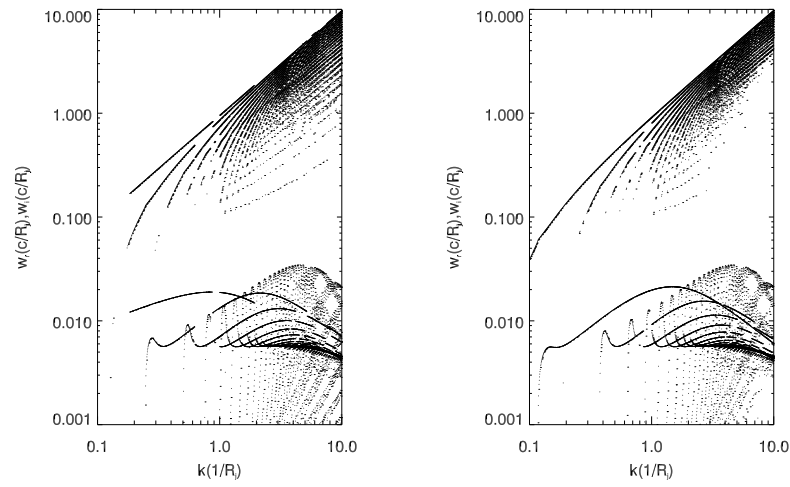


Figure 3.11: Same as Fig. 3.3 for D20 and $m = 25$. Left panel: antisymmetric; right panel: symmetric.

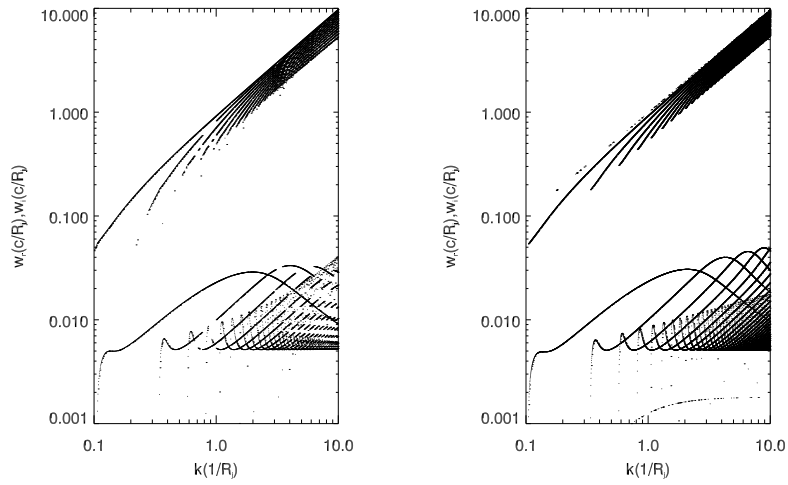


Figure 3.12: Same as Fig. 3.3 for the symmetric case of D20 and $m = 200$ (left panel) compared to the vortex sheet solution (right panel).

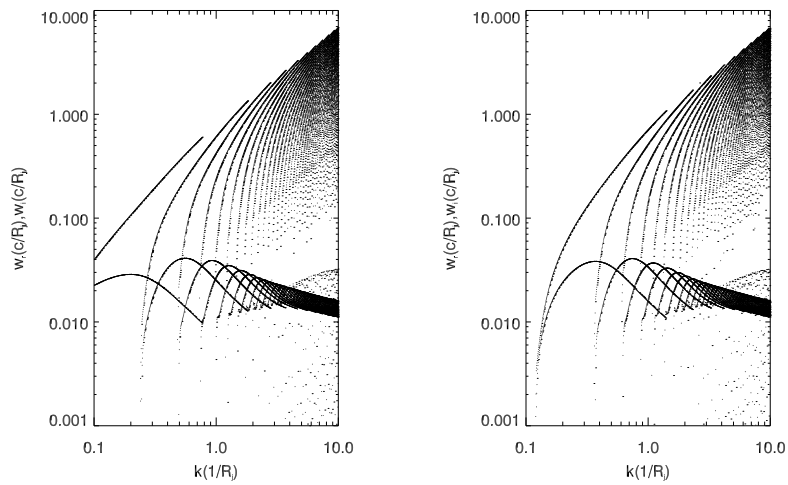


Figure 3.13: Same as Fig. 3.3 for A2.5 (see Table 3.1) and $m = 25$. Left panel: antisymmetric; right panel: symmetric.

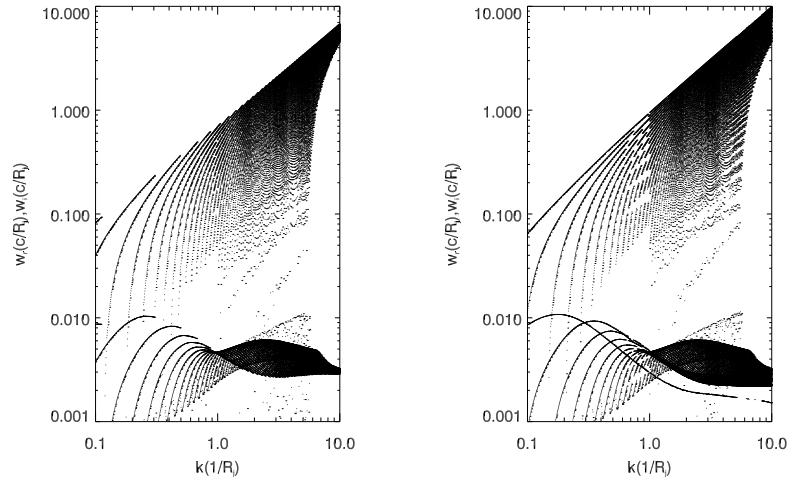


Figure 3.14: Same as Fig. 3.3 for A10 (see Table 3.1) and $m = 25$. Left panel: antisymmetric; right panel: symmetric.

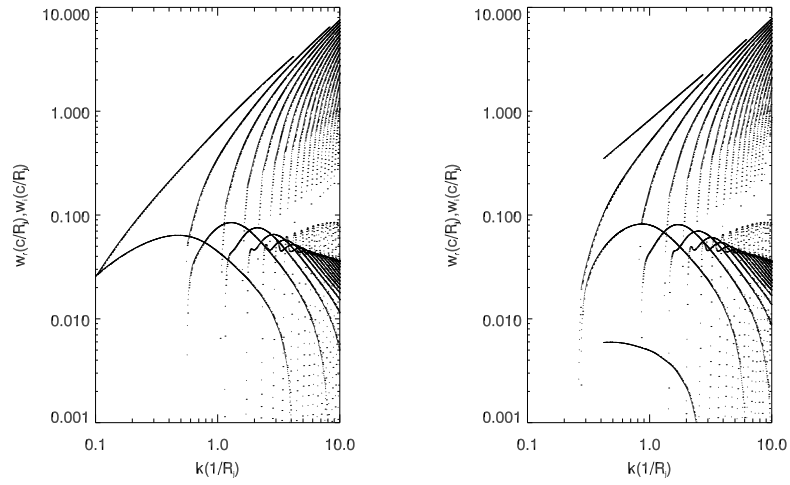


Figure 3.15: Same as Fig. 3.3 for B2.5 (see Table 3.1) and $m = 25$. Left panel: antisymmetric; right panel: symmetric.

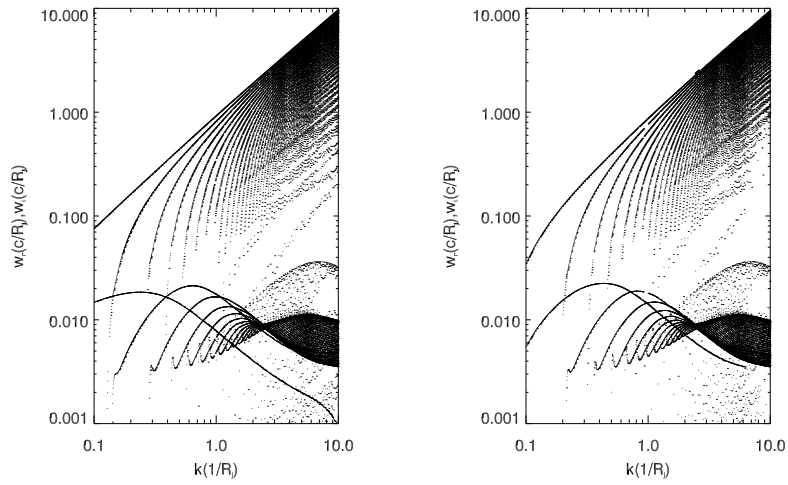


Figure 3.16: Same as Fig. 3.3 for B10 (see Table 3.1) and $m = 25$. Left panel: antisymmetric; right panel: symmetric.

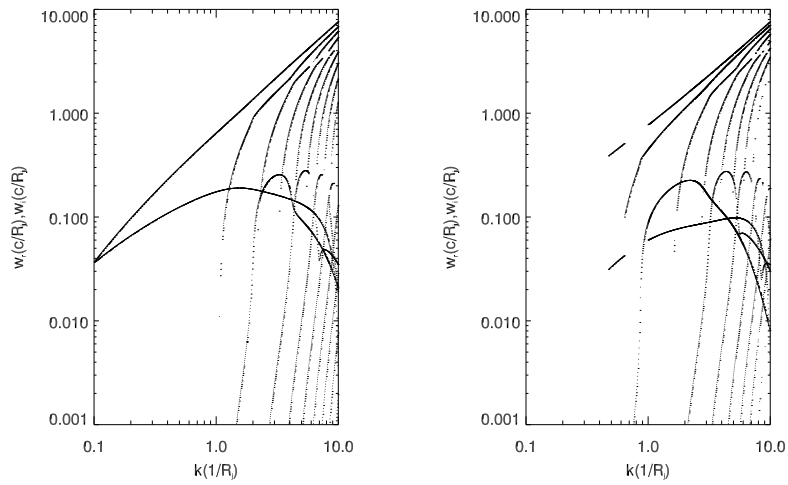


Figure 3.17: Same as Fig. 3.3 for D2.5 (see Table 3.1) and $m = 25$. Left panel: antisymmetric; right panel: symmetric.

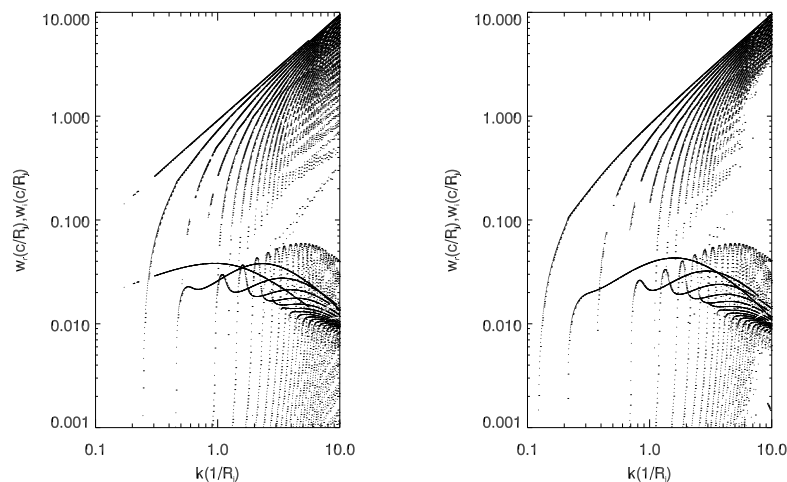


Figure 3.18: Same as Fig. 3.3 for D10 (see Table 3.1) and $m = 25$. Left panel: antisymmetric; right panel: symmetric.

3.2 Numerical simulations

Previous to performing the simulations, several improvements were done in the numerical code (see Appendix A and Section 2.6). Simulations were performed in 4 processors in SGI 2000 and SGI Altix 3000 machines.

Our simulations are performed following the temporal view, as in Chapter 2, i.e., a periodical box representing an infinite jet in which perturbations grow in time. We have tried to use a scenario as general as possible, from the point of view of what we know from previous results, by including a thicker shear layer ($0.17 R_j$):

$$v_z(x) = \frac{v_{z,j}}{\cosh x^m}, \quad (3.3)$$

$$\rho(x) = \rho_a - \frac{\rho_a - \rho_j}{\cosh x^m}, \quad (3.4)$$

where x is the transversal coordinate to the direction of the flow (z) and m is a measure of the shear layer steepness (in the limit $m \rightarrow \infty$ the configuration tends to the vortex-sheet case, here $m = 25$), and by perturbing the jet with several symmetric and antisymmetric modes in boxes of a given size, which is not determined by any specific mode wavelength as in simulations from

Model	γ	ε_j	ε_a	c_{sj}	c_{sa}	p	ν	η	M_j
A2.5	2.5	0.08	0.008	0.18	0.059	0.0027	0.11	0.11	12.5
B2.5	2.5	0.42	0.042	0.35	0.133	0.014	0.14	0.15	6.12
D2.5	2.5	60.0	6.000	0.57	0.544	2.000	0.87	0.90	3.29
B05	5	0.42	0.042	0.35	0.133	0.014	0.14	0.15	13.2
D05	5	60.0	6.000	0.57	0.544	2.000	0.87	0.90	7.01
A10	10	0.08	0.008	0.18	0.059	0.0027	0.11	0.11	54.2
B10	10	0.42	0.042	0.35	0.133	0.014	0.14	0.15	26.9
D10	10	60.0	6.000	0.57	0.544	2.000	0.87	0.90	14.2
B20	20	0.42	0.042	0.35	0.133	0.014	0.14	0.15	54.0
D20	20	60.0	6.000	0.57	0.544	2.000	0.87	0.90	28.5

Table 3.1: Equilibrium parameters of different simulated jet models. The meaning of the symbols is as follows: γ : jet flow Lorentz factor; ε : specific internal energy; c_s : sound speed; p : pressure; ν : jet-to-ambient relativistic rest mass density contrast; η : jet-to-ambient enthalpy contrast; M_j : jet relativistic Mach number. Labels a and j refer to ambient medium and jet, respectively. All the quantities in the table are expressed in units of the ambient density, ρ_{0a} , the speed of light, c , and the jet radius, R_j .

Chapter 2. Following conclusions regarding effects of resolution in linear and non-linear regimes studied before, the resolution used in this work was 256 cells/ R_j in the transversal direction to the flow, times 32 cells/ R_j in the axial direction. We reduced the transverse resolution due to mainly two reasons: we are not trying to mimic vortex sheet evolution, so we do not need such a steep shear layer, and therefore, we do not need such a large resolution, and our grids are now twice as large in the transversal direction as in the axis-symmetric case, as we are combining symmetric and antisymmetric structures, so we need to reduce resolution for computational time reasons.

This allowed us to double axial resolution, which affects non-linear results. Physical size of grids is $8 R_j$ axially times $6 R_j$ transversally for hot jets (D models, see Tables 3.1 and 3.2) and $16 R_j$ axially times $6 R_j$ transversally for cold jets (A and B in Tables 3.1 and 3.2). The jet is a steady flow in the z direction, in the interval $-R_j \leq x \leq R_j$. The different size is due to hot models having shorter unstable modes (in Figs. 3.3-3.18).

Tests were performed in order to assess the difference in the evolution

Model	k_0	k_1	k_2	k_3
A2.5	0.39	0.78	1.18	1.57
B2.5	0.39	0.78	1.18	1.57
D2.5	0.78	1.57	2.36	3.14
B05	0.39	0.78	1.18	1.57
D05	0.78	1.57	2.36	3.14
A10	0.39	0.78	1.18	1.57
B10	0.39	0.78	1.18	1.57
D10	0.78	1.57	2.36	3.14
B20	0.39	0.78	1.18	1.57
D20	0.78	1.57	2.36	3.14

Table 3.2: $k_{0,1,2,3}$: excited longitudinal wavenumbers for each model (R_j^{-1}).

of linear and non-linear regimes using a general sinusoidal perturbation and the specific wavelengths and structure of several eigenmodes; results showed that structures and qualitative properties of the resulting flow were basically the same. See Figs. 3.19, 3.20, 3.21 and 3.22 for direct comparison of both simulations. This fact confirms that general perturbation excite eigenmodes of the system.

The parameters used in the simulations are shown in Table 3.1. We sweep a wide range in Lorentz factors (from 2.5 to 20) and internal energies (from $0.08c^2$ to $60c^2$) in order to obtain a global view of the response of different initial data sets to perturbations. These parameters were chosen in order to study the stability regions found in Chapter 2. We have performed simulations for models **B05**², **B10**, **B20**, **D05**, **D10** and **D20** from Chapter 2, and have added **A2.5** (same thermodynamical properties as A05), **A10**, **B2.5** and **D2.5**. Models **A2.5**, **B2.5**, and **B05** correspond to region of class I jets, which include cold and slow flows. Models **D10** and **D20** correspond to class II (including hot and fast flows), **D2.5** and **D05** to class III (including hot and slow flows), and **A10**, **B10** and **B20** belong to class IV (including cold-warm and fast flows).

Perturbations are applied adding the following sinusoidal form to transver-

²Boldface will be used for new simulations in order to differentiate them from those in Chapter 2 with the same name.

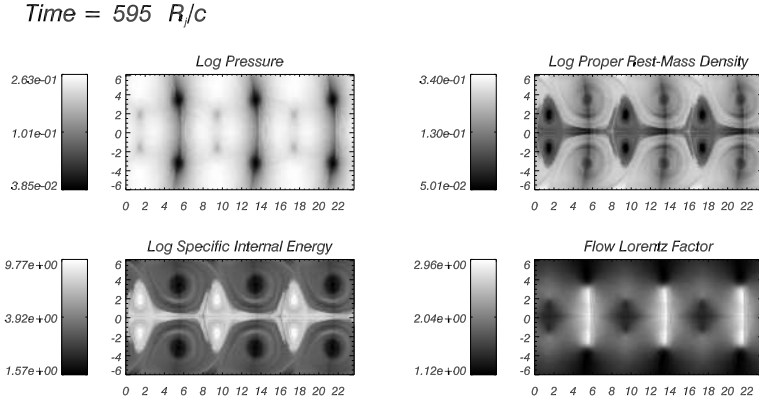


Figure 3.19: Snapshot in the mixing phase of logarithmic maps of pressure, jet mass fraction and specific internal energy and non-logarithmic Lorentz factor for model C05 (see Chapter 2) with four symmetric eigenmodes excited.

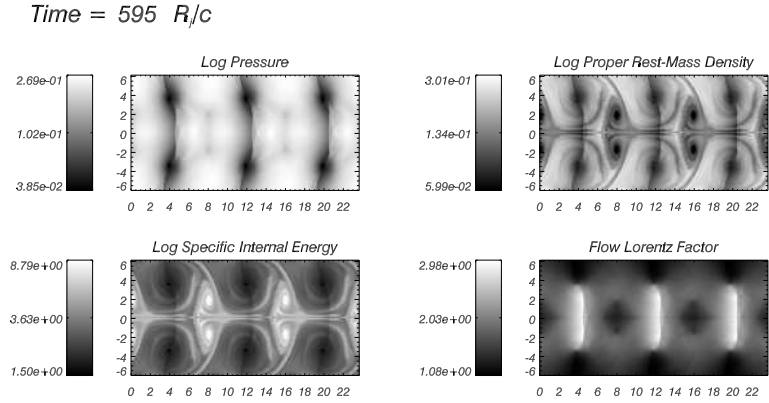


Figure 3.20: Same as Fig. 3.19 but for the case four sinusoidal perturbations with the same wavelengths as eigenmodes excited there.

sal velocity, $v_x(x, z)$:

$$v_x = \frac{V_{x1}}{N} \left(\sum_{n=0}^{N-1} \sin((n+1)k_n z + \varphi_n) \sin^2((n+1)\pi x) \frac{x}{|x|} \right) + \frac{V_{x1}}{M} \left(\sum_{m=0}^{M-1} \sin((m+1)k_m z + \varphi_m) \sin^2((m+1)\pi x) \right), \quad (3.5)$$

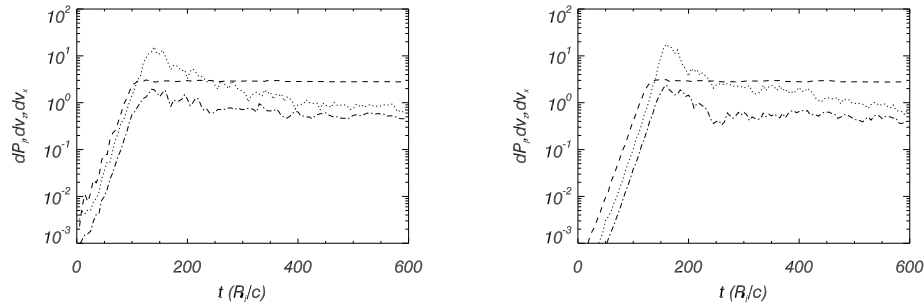


Figure 3.21: Evolution of the relative amplitudes of perturbations. Dotted line: pressure perturbation. Dashed line: longitudinal velocity perturbation in the jet reference frame. Dash-dotted line: perpendicular velocity perturbation in the jet reference frame. Definitions are like those in Fig 2.9. Left panel is for perturbed eigenmodes simulation and right panel is for that with sinusoidal perturbations.

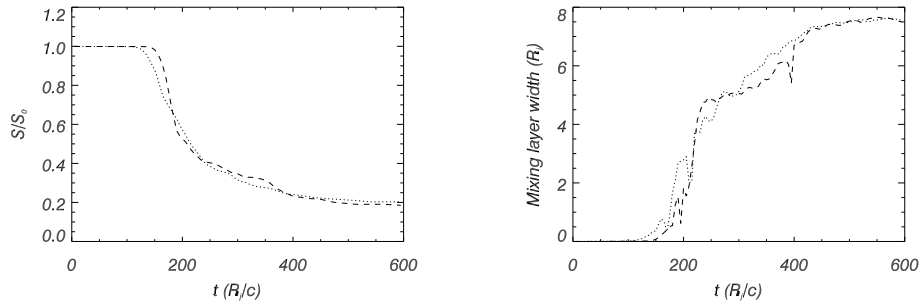


Figure 3.22: Left panel: evolution of total longitudinal momentum in the jet versus time. Right panel: evolution of the mean width of the jet/ambient mixing layer with time. Dotted line: eigenmodes. Dashed line: sinusoidal perturbation.

where $V_{x1} (\sim 10^{-4})$ is the amplitude given to the perturbation, $k_{m,n}$ are the wave numbers of the grid box (so that $n k_n$ and $m k_m$ stand for the harmonics of the symmetric (pinching) and antisymmetric (helical) modes, respectively), and φ_n and φ_m are random phases given to each mode. In our simulations,

Model	w_{i,k_0}		w_{i,k_1}		w_{i,k_2}		w_{i,k_3}	
	Symm.	Antis.	Symm.	Antis.	Symm.	Antis.	Symm.	Antis.
A2.5	0.036	0.032	0.038	0.037	0.034	0.036	0.031	0.034
B2.5	0.042	0.056	0.070	0.052	0.066	0.084	0.073	0.080
D2.5	0.046	0.160	0.131	0.182	0.210	0.194	0.142	0.256
B05	0.037	0.035	0.037	0.044	0.036	0.038	0.034	0.035
D05	0.068	0.063	0.085	0.063	0.100	0.068	0.068	0.110
A10	0.009	0.009	0.006	0.006	0.005	0.006	0.006	0.006
B10	0.022	0.018	0.019	0.021	0.018	0.017	0.013	0.013
D10	0.034	0.038	0.041	0.037	0.044	0.034	0.051	0.035
B20	0.011	0.010	0.009	0.010	0.007	0.007	0.009	0.010
D20	0.018	0.018	0.020	0.017	0.022	0.017	0.027	0.028

Table 3.3: Dominant modes in the linear phase of the numerical simulations. w_{i,k_j} : maximum growth rate for the j -th wavenumber excited in the simulation (see Table 3.1). Left columns: symmetric mode; right columns: antisymmetric one. Growth rate values are in c/R_j units.

four symmetric ($M = 4$) plus four antisymmetric modes ($N = 4$) were excited, i.e., the fundamental mode of the box and the first three harmonics.

3.3 Results

3.3.1 Linear phase

Tables 3.3, 3.4, 3.5 and 3.6 summarize the properties of linear regime in our simulations. Table 3.4 gives the values of the growth rates corresponding to the dominant wavelength as deduced from Fourier analysis of the transversal profiles of the rest mass density distribution in the jet. We use Table 3.3 along with that Fourier analysis of simulations in order to identify dominant wavelengths and modes. Note however that Fourier analysis can only give us information about wavelengths, but can not distinguish between symmetric and antisymmetric modes. The growths of pressure, axial and transversal velocity perturbations along the simulations are shown in Figs. 3.23-3.27.

- **A2.5:** modes with longer wavelengths are faster growing, and their Fourier amplitudes are consistently larger than those for modes with shorter wavelengths in the simulation. Growth rate found in the simulation is close to that found using linear stability analysis.

Model	Dominant	w_i
A2.5	k_0	0.030
B2.5	k_1, k_2	0.070
D2.5	k_2, k_1	0.200
B05	k_0, k_1	0.035
D05	k_1, k_2, k_1	0.080
A10	k_0^*	0.004 (0.005)
B10	k_0	0.020
D10	k_1, k_2	0.040
B20	k_0^*	0.006 (0.008)
D20	k_1, k_0	0.016

Table 3.4: The dominant mode refers to the mode with the largest amplitude in rest mass density as derived from Fourier analysis of the box; they are written from larger to smaller amplitude when more than one is present. w_i : fitted pressure perturbation growth rate for the linear regime in the simulation. Growth rate values are in c/R_j units. *: Models where non regular growth affects the evolution (see text).

- **B2.5**: first (k_1) and second (k_2) harmonics of the box have larger amplitudes in the Fourier analysis, and therefore, dominate the linear regime. Linear stability analysis gives k_1 , k_2 and k_3 as the fastest growing modes, with same growth rate as found in the simulation. However, k_3 modes have smaller amplitudes.
- **D2.5**: found growth rate for the simulation is close to that of k_1 and k_2 modes, which is confirmed by Fourier analysis. Antisymmetric k_3 mode might grow with slower rates than theory predicts due to numerical viscosity affecting shorter modes more than longer ones.
- **B05**: Fourier analysis shows competition between fundamental and first harmonics of the box (k_0 and k_1 , respectively). This, as well as the mean growth rate, is confirmed by the linear stability analysis. Second harmonic of the box (k_2) is damped.
- **D05**: from Fourier analysis we see that k_1 and k_2 modes dominate evolution in the linear regime. The growth rate is close to that of the symmetric k_1 mode, despite the fact that symmetric k_2 and antisymmetric

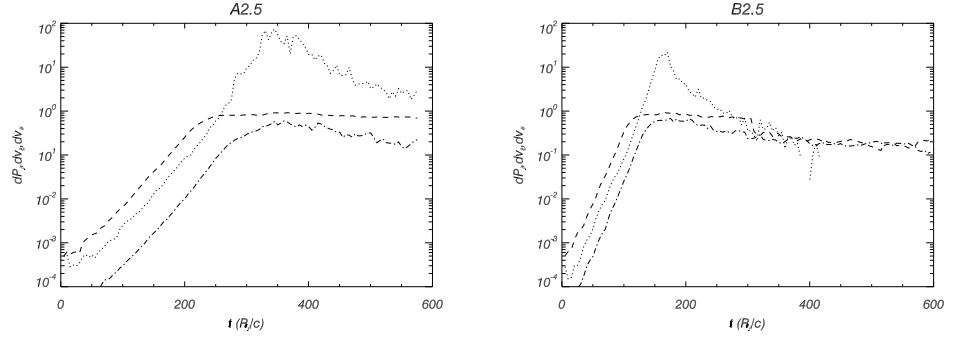


Figure 3.23: Evolution of the relative amplitudes of perturbations (models **A2.5** and **B2.5**). Dotted line: pressure perturbation $((p_{max} - p_0)/p_0)$. Dashed line: longitudinal velocity perturbation in the jet reference frame $(0.5(v'_{z,max} - v'_{z,min}))$. Dash-dotted line: perpendicular velocity perturbation in the jet reference frame $(0.5(v'_{x,max} - v'_{x,min}))$. The search for maximum $(p_{max}, v'_{x,max}, v'_{z,max})$ and minimum $(v'_{x,min}, v'_{z,min})$ values have been restricted to those numerical zones with jet mass fraction larger than 0.5.

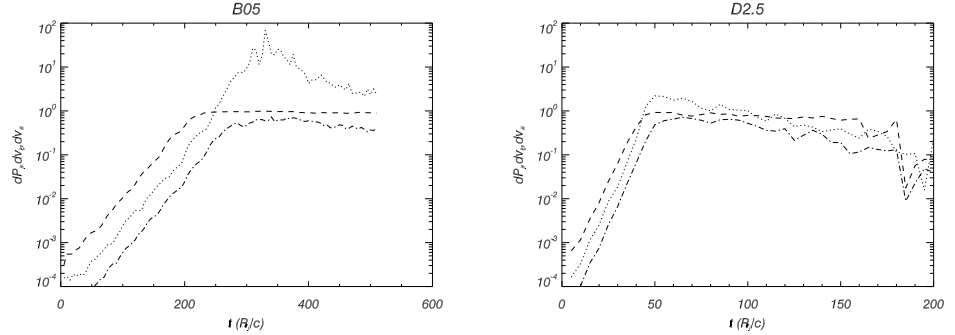
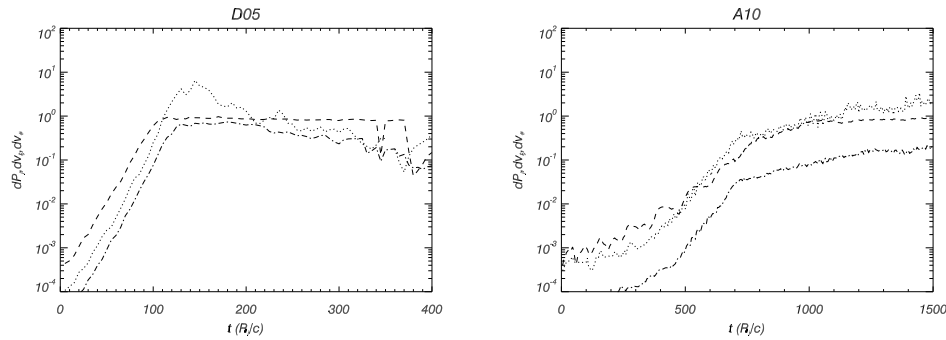
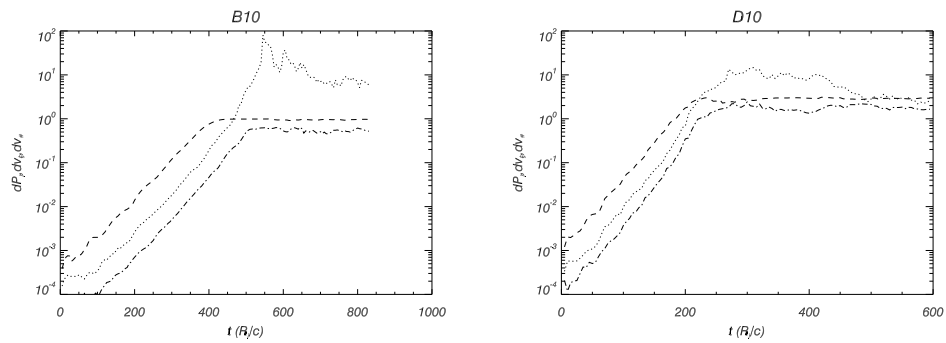


Figure 3.24: Same as Fig. 3.23 for models **D2.5** and **B05**.

k_3 present faster growth rates, so they must be damped.

- **A10**: Fourier analysis shows that longer modes dominate, in agreement with linear stability analysis. However, growth rate is not coincident, being two times smaller in the numerical simulation than predicted. We also observe in Fourier analysis that resonant modes, excited as harmon-

Figure 3.25: Same as Fig. 3.23 for models **D05** and **A10**.Figure 3.26: Same as Fig. 3.23 for models **B10** and **D10**.

ics of perturbed wavelengths, become important by the end of the linear regime.

- **B10**: in this case, the fundamental mode (k_0) dominates, as predicted by linear stability analysis.
- **D10**: as in models **D2.5** and **D05**, k_1 and k_2 have larger amplitudes in Fourier analysis, but the smaller wavelength modes (k_3) are damped with respect to the predictions of linear stability analysis.
- **B20**: longer modes dominate linear evolution, in agreement with linear analysis but growth rate in the numerical simulation is 1.5 times smaller than predicted. After some time, resonant modes, as those in model

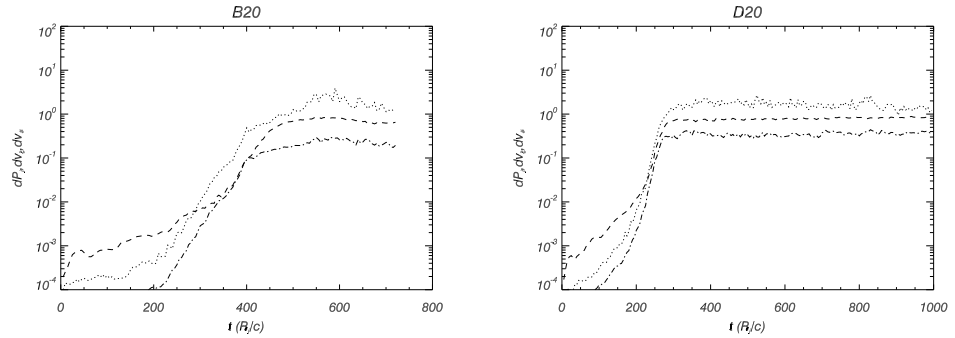


Figure 3.27: Same as Fig. 3.23 for models **B20** and **D20**.

A10, become dominant and lead to a smooth transition to the non-linear regime.

- **D20**: long modes present larger amplitudes with predicted growth rates up to the moment when resonant modes reach larger amplitudes, the same effect found in models **A10** and **B20**.

It is observed in several simulations (e.g., **B2.5**, **B05**, **D2.5**, **D05**, **D10**) that modes with similar or even slightly larger growth rates to those dominating in simulations present lower amplitudes in the linear regime. It happens usually for shorter modes (typically k_2 , k_3), so it may be caused by numerical viscosity, for less cells are involved in one wavelength. However, the way in which we perturb the jet may also favor the dominating growth of certain modes starting with a larger amplitude. We add a general sinusoidal perturbation, so the input amplitude of the perturbation at a given wavelength is shared in a random way among all the modes present at that wavelength. This makes some modes start their growths with smaller amplitudes, as we could see in the Fourier analysis of different models. Initial low amplitudes are more probable for short wavelength modes, as more eigenmodes are present at a given wavenumber in this range (see Figs. 3.3-3.18). From an initial lower amplitude, and taking into account that they have similar growth rates to other modes, they grow with smaller amplitudes for the rest of the linear phase.

Models **A10** and **B20**, marked with an asterisk in Table 3.4, have fitted growth rates in the first part of the linear regime below the predicted values. Note that these models have the smaller growth rates. After this initial phase,

Model	$w_{i,max}$	$w_{i,p,v_{\perp}}$	$w_{i,v_{\parallel}}$
B05	0.052	-	-
D05	0.11	-	-
A10	0.013	0.017	0.009
B10	0.035	-	-
D10	0.057	-	-
B20	0.026	0.036	0.036
D20	0.035	0.070	0.047

Table 3.5: Growth of resonant modes. Models with maximum growth rate (according to the linear analysis) for all resonant modes (i.e., at any wavelength) above the growth rates of the perturbed modes are listed. $w_{i,max}$: maximum growth rate for all resonant modes from linear analysis; $w_{i,p,v_{\perp}}$: fitted growth rates of pressure and perpendicular velocity perturbations for the fast growth linear regime in the simulation, only for those simulations where it occurs; $w_{i,v_{\parallel}}$: same as $w_{i,p,v_{\perp}}$ for axial velocity. All values are in c/R_j units.

short harmonics start dominating the linear growth.

We have observed the appearance of fast growing, very short modes in models **A10**, **B20** and **D20** which are clearly associated to the resonant modes presented above in the previous section and that could have been excited as harmonics of the initially perturbed wavelengths. The same kind of resonant mode might have developed in model C20 of Chapter 2 and caused the irregular linear growth found with respect to the rest of models. These modes generate a rich internal structure in the jet due to their large perpendicular wavenumber (characteristic of high order modes). A direct comparison between the structure generated by these resonant modes in the numerical simulations and that coming from linear stability analysis can be seen in Fig. 3.28. In this figure, we display one snapshot from model **D20** and the theoretical counterpart using one of those modes. According to the linear stability analysis, resonant modes dominate over long wavelength modes in high Lorentz factor jets and, among them, in colder jets. This could be the reason why they only appear in models **A10**, **B20** and **D20**. Table 3.5 collects the models with maximum growth rate (according to the linear analysis) for all resonant modes (i.e., at any wavelength) above the growth rates of the perturbed modes. Maximum growth rates for resonant modes in those models where they have been found,

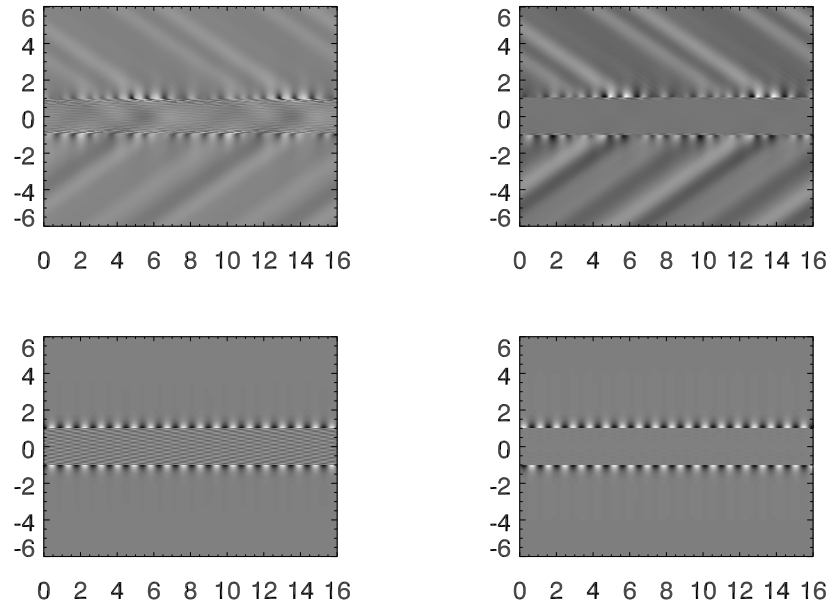


Figure 3.28: Upper panels: pressure and perpendicular velocity perturbation at late stages of linear phase (model D20). Lower panels: Generic perturbation distribution extracted from one resonant mode from linear stability analysis (pressure perturbation and perpendicular velocity perturbation). Oblique waves in upper panels are the result of longer wavelength modes, whereas in bottom panel, only the resonant mode has been plotted, so no oblique waves appear. See also 3.2.

along with the fitted growth rates in the simulation, are listed. Typically, the growth rates from the numerical simulations are about 1.4 – 2.0 times larger. This difference remains unexplained, but it could be caused by second order effects, like interaction between modes.

Summarizing, two kinds of linear growth are found in these simulations, one dominated by longer modes, typical of slower jets, and another one where resonant modes appear (Fig. 3.29). This difference is important, for the transition to the non-linear evolution depends critically on the dominant modes at the end of the linear regime.

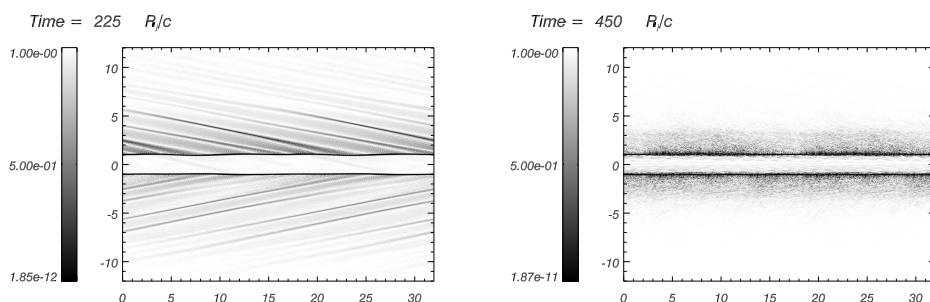


Figure 3.29: Schlieren plots showing waves in the linear regime in models **B05** (left) and **B20** (right). Long wavelength structures in **B05** are apparent, contrary to small structures in **B20**. These plots represent a negative exponential of the density gradient times an arbitrary factor chosen for the sake of clarity ($\exp(-k|\nabla\rho|)$, with $k = 30$). Thus 1.0 means no density gradient and the lowest value stands for maximum density gradient.

Table 3.6 shows the times at which linear phase ends. We see that colder jets have longer linear phases than hot ones, due to smaller typical growth rates in the former. t_{lin} times are larger than those in Chapter 2, as growth rates are reduced by the presence of the shear layer. Model **A10** presents the longest linear phase. In general, we observe that conclusions derived in Chapter 2 regarding different phases of evolution are fulfilled here.

3.3.2 Saturation and transition to non-linear phase

Saturation of perturbations is reached when perpendicular velocity cannot grow further in the jet reference frame due to the speed of light limit (see Chapter 2). Transition to non-linear regime depends mainly on the way linear regime has developed. Saturation times, t_{sat} , for the different models are listed in Table 3.6. In this phase structures generated by dominating modes become visible in the deformations of the jet. In Fig. 3.30 we show snapshots of three models (**B2.5**, **D05** and **D10**) at saturation time where mode competition derived from Fourier analysis is clearly observed. Asymmetric structures appear as a result of several symmetric and antisymmetric modes having large amplitudes.

Saturation is followed in some models by a peak in pressure due to the de-

Model	t_{lin}	t_{mex}	t_{mix}	t_{sat}	t_{peak}	Δ_{peak}
A25	225	250	300	340	340	100
B25	110	125	140	150	165	20
D25	40	45	50	50	50	2
B05	220	275	300	280	330	70
D05	105	125	110	130	140	2
A10	725	—	—	—	—	3
B10	400	520	500	500	540	100
D10	205	260	220	290	300	4
B20	475	—	520	550	590	4
D20	275	510	300	275	320	2

Table 3.6: Times for the different phases in the evolution of the perturbed jet models. t_{lin} : end of linear phase (the amplitudes of the different quantities are not constant any longer). t_{sat} : end of saturation phase (the amplitude of the transverse speed perturbation reaches its maximum). t_{mix} : the tracer starts to spread. t_{peak} : the peak in the amplitude of the pressure perturbation is reached. t_{mex} : the jet has transferred to the ambient a 1% of its initial momentum. Δ_{peak} : relative value of pressure oscillation amplitude at the peak (see Figs. 3.23-3.27).

veloping of a shock in the shear layer, and jet disruption. The relative values of pressure oscillation amplitude at the peak, Δ_{peak} , and the corresponding times, t_{peak} , appear listed in Table 3.6. The values of Δ_{peak} are connected with the non-linear evolution of the flow. Those cases in which $\Delta_{\text{peak}} > 70$ develop a shock in the jet/ambient interface followed by the sudden disruption of the jet. From Table 3.6, we see that peak values in the present simulations are in general qualitatively the same as the corresponding ones in Chapter 2. Colder and slower jets have larger peaks and hence suffer stronger shocks after saturation. The main difference between the values given here and those presented in Chapter 2 appears for models **B20** and **D20**, where shock strength is much smaller due to the appearance of resonant, stabilizing modes, as we shall discuss next.

The parallel and perpendicular wavelengths of the shear-layer resonant modes, λ_z and λ_x , respectively, are both small ($\lambda_z \leq R_j$) with $\lambda_x \ll \lambda_z$. Therefore their wavevectors are almost perpendicular to the jet axis and thus

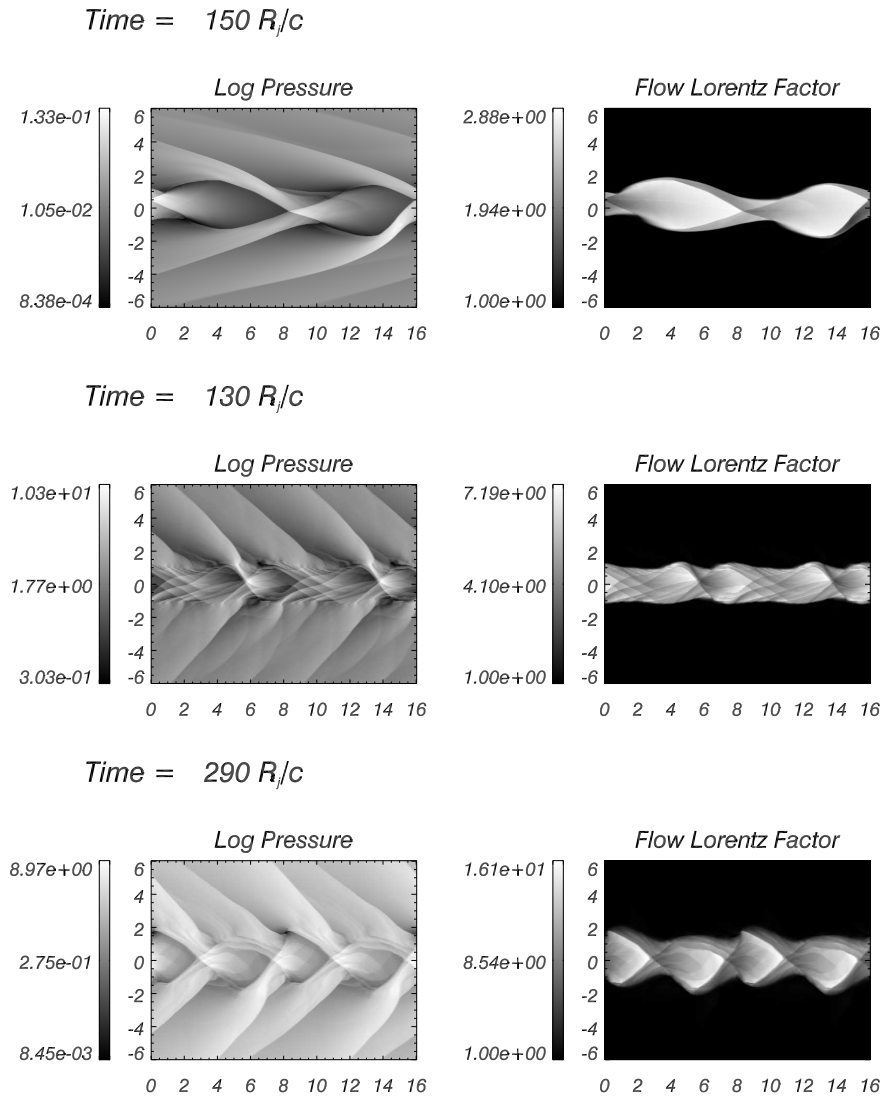


Figure 3.30: Snapshots of logarithm of pressure (left) and Lorentz factor (right) for **B25** (upper panels), **D05** (center panels) and **D10** (bottom panels) at t_{sat} , where irregular structures caused by mode competition are observed.

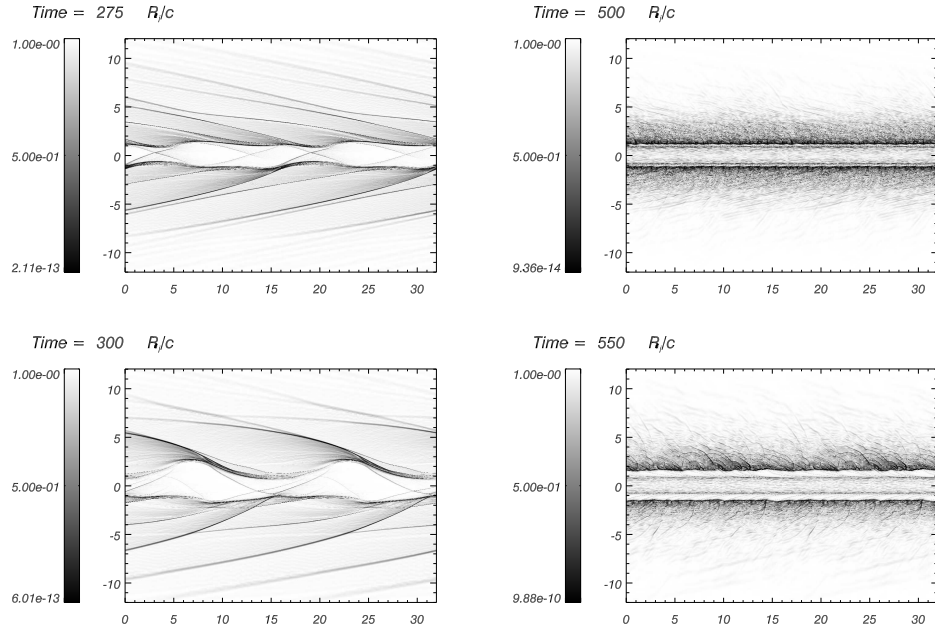


Figure 3.31: Schlieren plots showing waves in the saturation phase and transition to non-linear regime for models **B05** (left panels) and **B20** (right panels).

the waves propagate from the shear layer towards the jet axis. On the other hand the resonant modes have large growth rates, exceeding the growth rate of other modes, so they start to dominate in numerical simulations. Subsequently the resonant modes saturate as soon as the flow velocity oscillation amplitude approaches the speed of light. As the maximum amplitude is reached the sound waves steepen while travelling towards the jet axis and form shock fronts on the leading edges of wave profiles. The dissipation of oscillation energy in shocks leads to a sudden drop of the resonant wave amplitude that tends to reduce the value of Δ_{peak} . In Fig. 3.28 we show a comparison between simulation results and the linear mode structure.

In Fig. 3.31, we show schlieren plots, where the different morphology and structures observed in a jet where resonant modes are not present (**B05**), and one where these modes dominate the saturation phase (**B20**), is clear.

Finally, as it was found in Chapter 2, the generation of the shock wave at the jet/ambient interface is imprinted in the evolution of the maxima of the

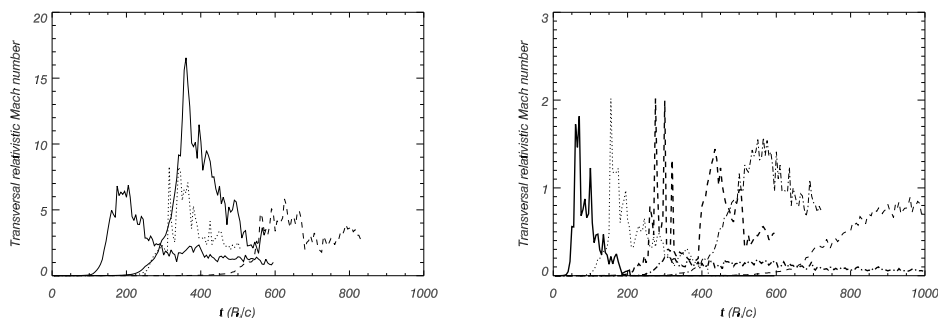


Figure 3.32: Transversal Mach number in simulations (see text for definition). Solid line $\gamma = 2.5$; dotted line $\gamma = 5.0$; dashed line $\gamma = 10.0$; dash-dot line $\gamma = 20.0$. Thinner line is for models A and thickest is for models D, with B in between. Left panel shows models **A2.5**, **B2.5**, **B05** and **B10**, and right panel shows models **A10**, **B20**, **D2.5**, **D05**, **D10** and **D20**.

transversal Mach number of the jet with respect to the unperturbed ambient medium. This quantity is defined as $M_{j,\perp} = \gamma_{j,\perp} v_{j,\perp} / (\gamma_{c_{sa}} c_{sa})$, being $\gamma_{j,\perp}$ and $\gamma_{c_{sa}}$ the Lorentz factors associated to $v_{j,\perp}$ and c_{sa} , respectively. A value significantly larger than 1 around t_{peak} points towards a supersonic expansion of the jet at the end of the saturation phase. This magnitude is shown in Fig. 3.32. We observe a clear inverse tendency of the peak value of this magnitude from colder to hotter and from slower to faster jets, with the exception of **A10** with respect to **B10** and **D10**, due to the presence of the resonant stabilizing modes preventing the formation of a shock. It is important to note that models with $\Delta_{\text{peak}} > 10$ (**A2.5**, **B2.5**, **B05** and **B10**) coincide with those developing larger transversal Mach numbers.

3.3.3 Non-linear regime

In Chapter 2, the non-linear evolution of the instability in the different models has been characterized through the processes of jet/ambient mixing and momentum transfer. The models were then classified into four classes (I to IV) according to the particular nature of these processes in each of the models. In Fig. 3.33 we show the mixing layer width as a function of time for all the models. Wider mixing layers imply more mixing as material from the jet is moving out at the same time that the jet is entrained by ambient

material. We observe that those models with larger values of Δ_{peak} (lower Lorentz factor and colder jets) develop, rapidly after saturation, wider layers ($> 5R_j$) due to the turbulent mixing induced by the shock, while those models where resonant modes appear do not show strong mixing with the ambient. Models **B10** and **D10** undergo a mixing process, however slower than the former (dashed lines in Fig. 3.33).

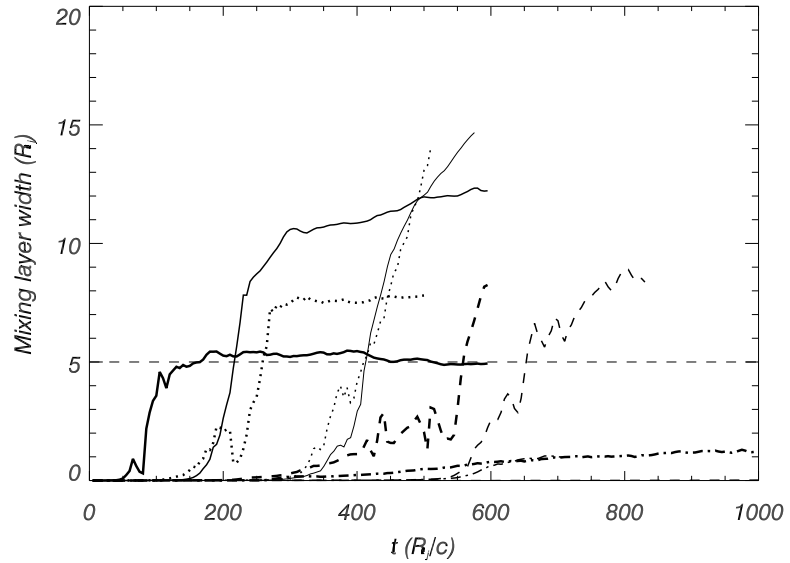


Figure 3.33: Evolution of the mean width of the jet/ambient medium layer (for tracer values between 0.05 and 0.95) with time for all simulations. Lines represent the same models as in Fig. 3.32. A value of $5R_j$ for the width of the mixing layer (horizontal dashed line) serves to classify the evolution of the different models.

Fig. 3.34 shows the fraction of initial axial momentum which is kept by the jet versus time. Axial momentum is lost first through sound waves generated by linear perturbations, which result from conversion of kinetic energy in the flow into thermal energy, and second, but more important, through shocks themselves and by subsequent mixing, which implies sharing of momentum with the ambient medium. Correlation with Fig. 3.33 is remarkable. Models developing wide mixing layers coincide with those losing more than 50% of

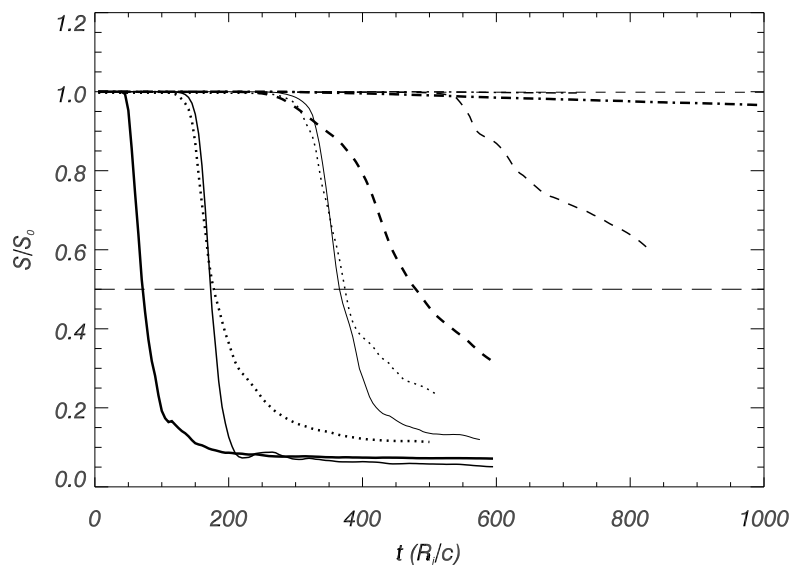


Figure 3.34: Evolution of the normalized total longitudinal momentum in the jet as a function of time. Lines represent the same models as in Fig. 3.32. The long-dashed horizontal line serves us to identify those models transferring more than 50 % of the initial jet momentum to the ambient.

their initial axial momentum just after saturation, models **B10** and **D10** share their momentum with the ambient medium continuously in the non-linear regime, and models where resonant modes dominate saturation keep almost all their initial momentum by the end of the simulations. Results derived from Fig. 3.34 are completed by Fig. 3.35. In the latter we plot the total transversal momentum in the jets normalized to the corresponding initial longitudinal momentum. Transversal momentum in the jet (initially zero) is generated through turbulent motions and continuous conversion of kinetic into internal energy. The value of the normalized transversal momentum at a given time is an indication about how far from equilibrium the jet is. We observe that colder and lower Lorentz factor models present strong peaks at t_{sat} , coincident with the triggering of the shock and the sudden transfer of longitudinal momentum seen in the previous plot; those models where resonant modes appear, barely generate any transversal momentum, and models **B10** and **D10** do not present

strong peaks at saturation but show sustained transversal momentum through the non-linear regime.

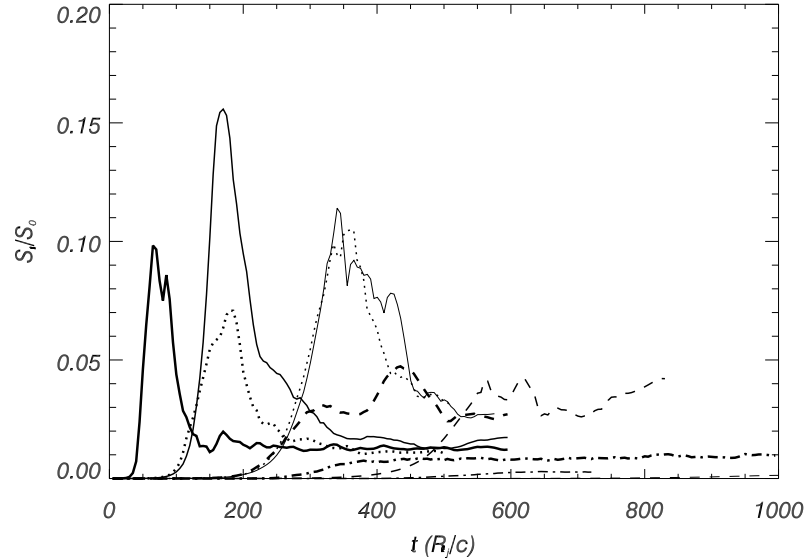


Figure 3.35: Evolution of the total transversal momentum in the jet as a function of time for all the simulations. Lines represent the same models than in Fig. 3.32.

In Fig. 3.36, we show mean pressure profiles for all models at the end of the simulations. All jets are close to pressure equilibrium with the ambient medium, excepting **B10**, **D2.5**, **D05** and **D10** which are slightly underpressured. At this time, shocks have moved out from the plotted region in cases where they occur.

Panels showing several physical magnitudes for all models at the end of simulations are presented in Figs. 3.37-3.41. In these former panels we can see that colder and slower models (**A2.5**, **B2.5** and **B05**) show turbulent mixing in a wide region, and that they are barely relativistic by the end of the simulations. Models **D2.5** and **D05**, have mixed completely but keep larger Lorentz factors. Moreover, these models seem to have stopped the process of widening of the mixing layer as it is deduced from the flattening of the mixing layer width as a function of time in Fig. 3.33. Models **B10** and **D10** are also un-

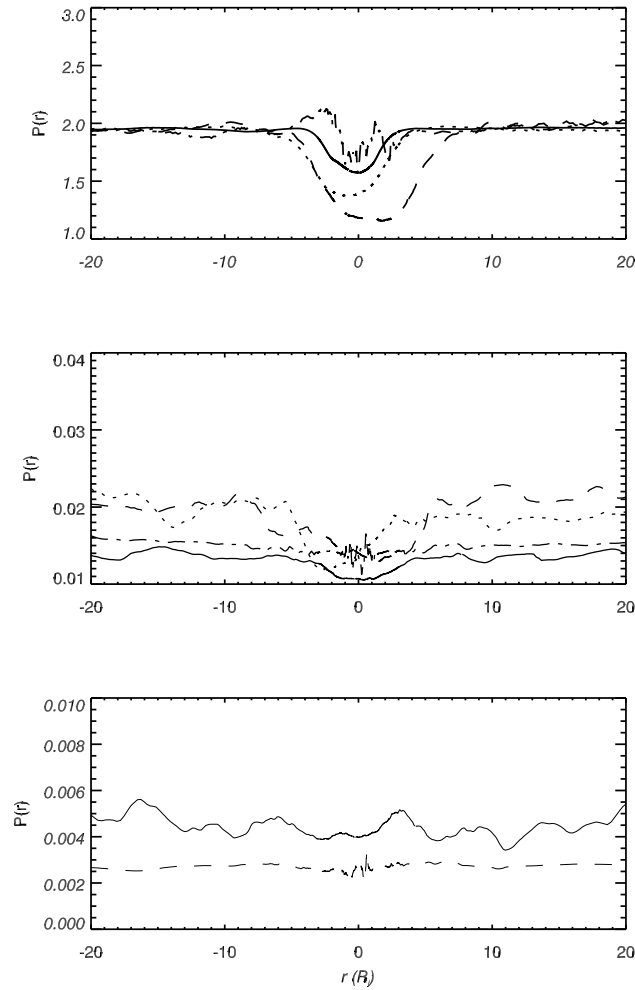


Figure 3.36: Longitudinal averaged profiles of gas pressure for all models. Different types of lines are used for models with different internal energies: Continuous line is used for Lorentz factor 2.5; dotted line for Lorentz factor 5; dashed line for Lorentz factor 10; dashed-dotted line for Lorentz factor 20. Line thickness increases with internal energy (from model A, thinnest line, to D thickest one).

dergoing turbulent mixing and show smaller Lorentz factors. From Figs. 3.33 and 3.34 it is deduced that **B10** and **D10** are still mixing and transferring momentum by the end of simulations. These models will eventually lose a large amount of their initial longitudinal momentum becoming colder and denser due to mass entrainment from the ambient medium. Finally, models **A10**, **B20** and **D20** present a fast core $\sim 1 R_j$ wide with rich internal structure as a consequence of the resonant modes (see subsection on the linear regime) which is surrounded by a hot and slow shear layer which extends up to $\sim 2 R_j$ in models **A10** and **B20** or $\sim 4 R_j$ in model **D20**.

In Fig. 3.42 we show schlieren plots which remark all the aspects discussed here, in terms of the structures generated in models with very different non-linear behaviours (**B05** and **B20**). Turbulent mixing is observed in **B05**, whereas small scale, very rich structure is seen outside the shear layer surrounding the unmixed core in **B20**, with both transitions (core/shear layer and shear layer/ambient) very well resolved in the plots.

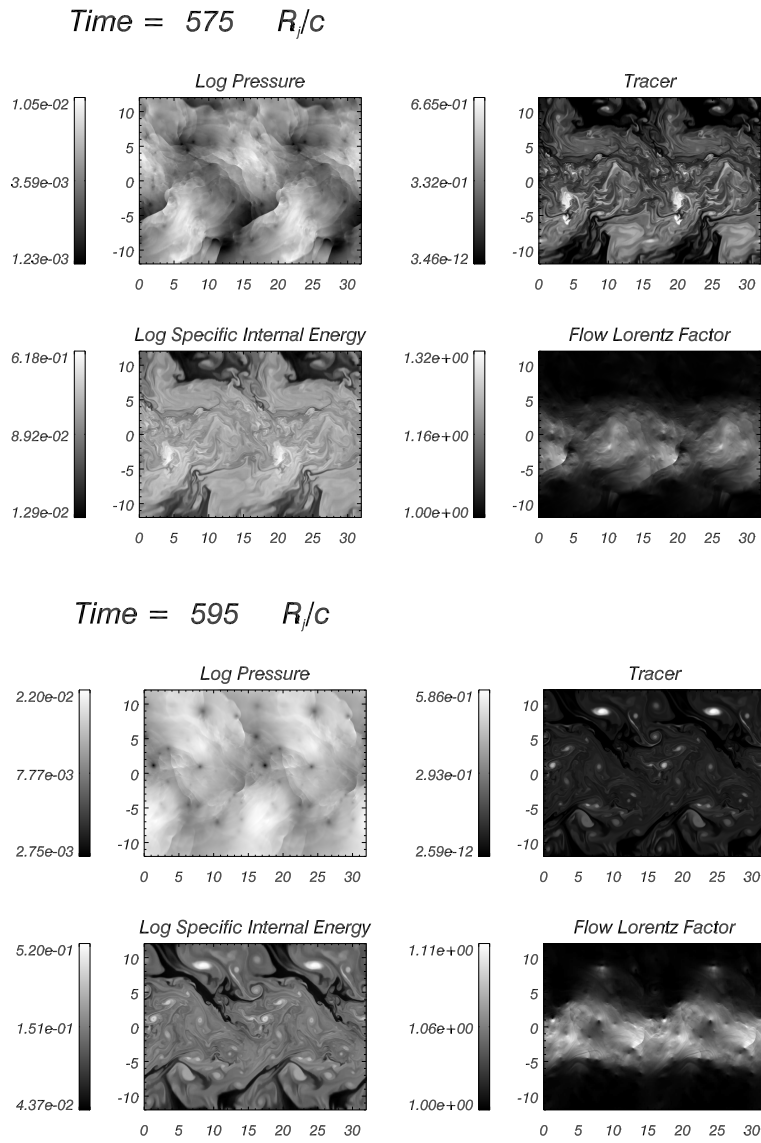


Figure 3.37: Snapshot at the last frame of the simulation of logarithmic maps of pressure, jet mass fraction and specific internal energy and non-logarithmic Lorentz factor for model **A2.5** (upper) and **B2.5** (lower).

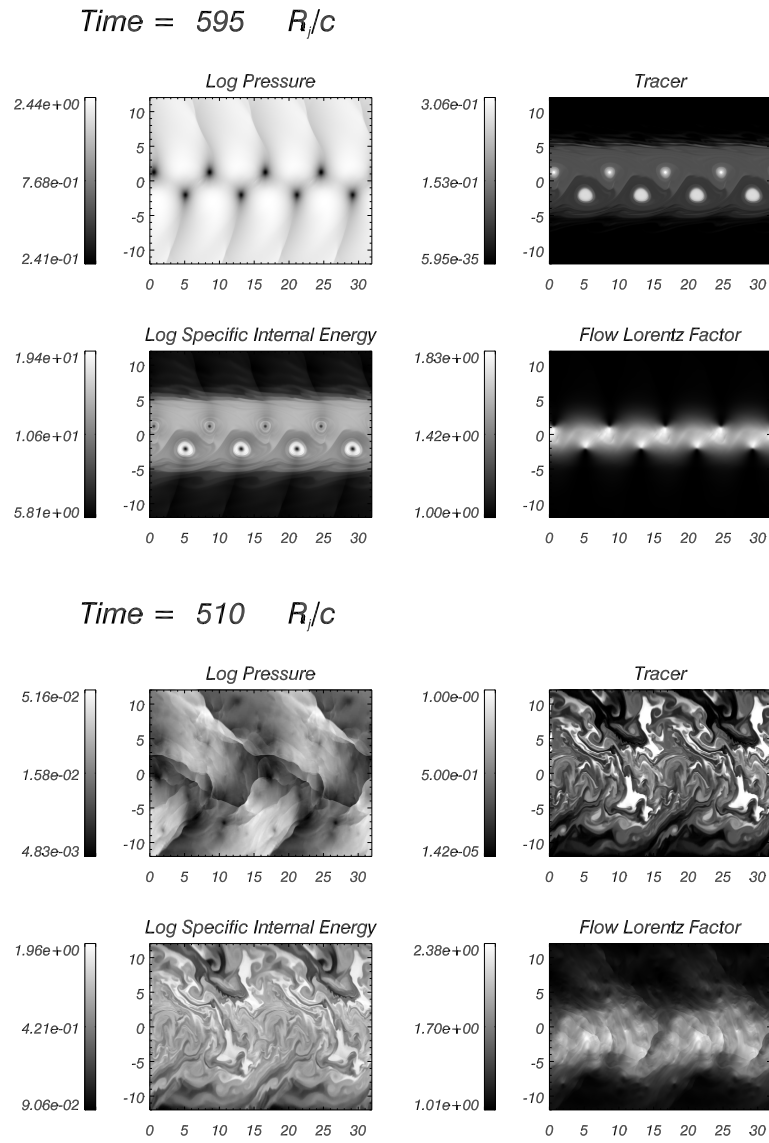


Figure 3.38: Snapshot at the last frame of the simulation of logarithmic maps of pressure, jet mass fraction and specific internal energy and non-logarithmic Lorentz factor for models **D2.5** (upper) and **B05** (lower).

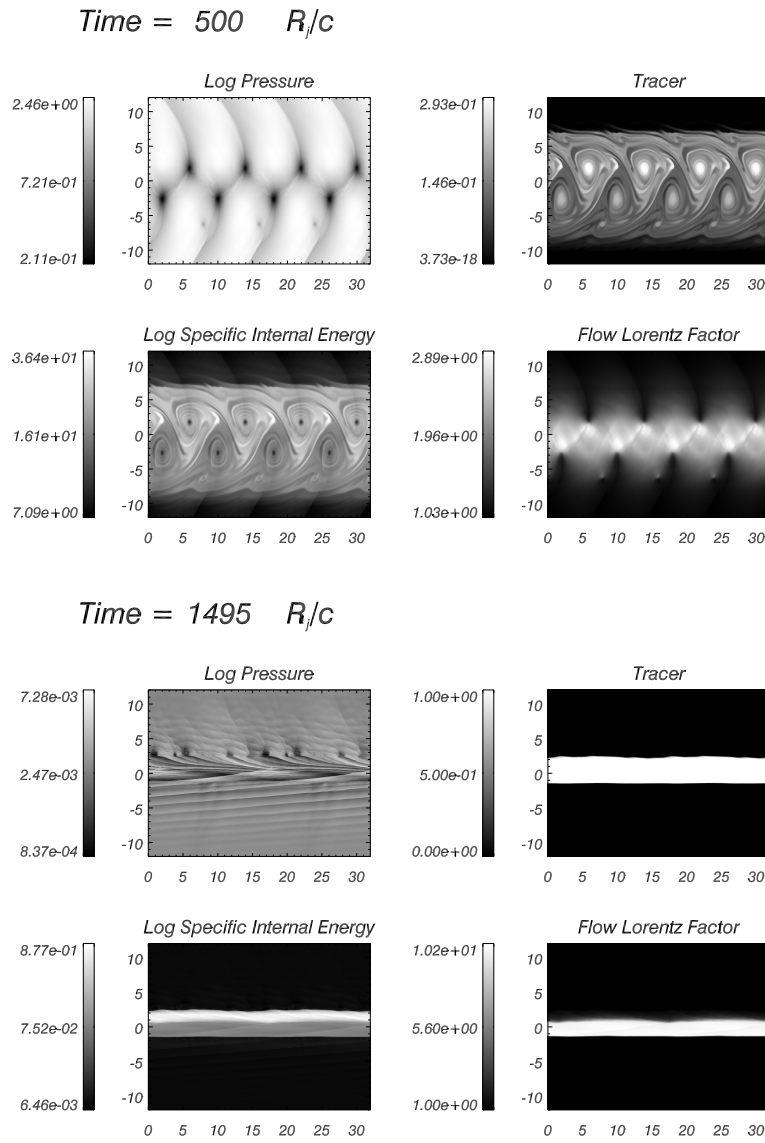


Figure 3.39: Snapshot at the last frame of the simulation of logarithmic maps of pressure, jet mass fraction and specific internal energy and non-logarithmic Lorentz factor for models **D05** (upper) and **A10** (lower).

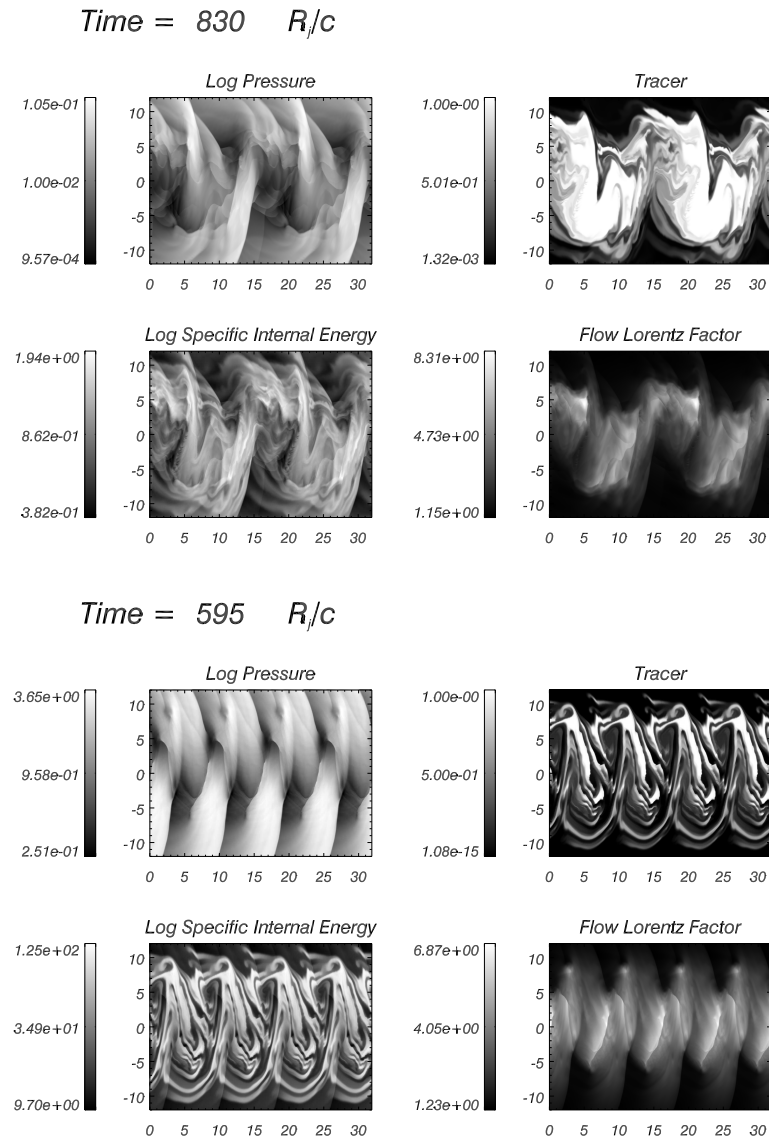


Figure 3.40: Snapshot at the last frame of the simulation of logarithmic maps of pressure, jet mass fraction and specific internal energy and non-logarithmic Lorentz factor for models **B10** (upper) and **D10** (lower).

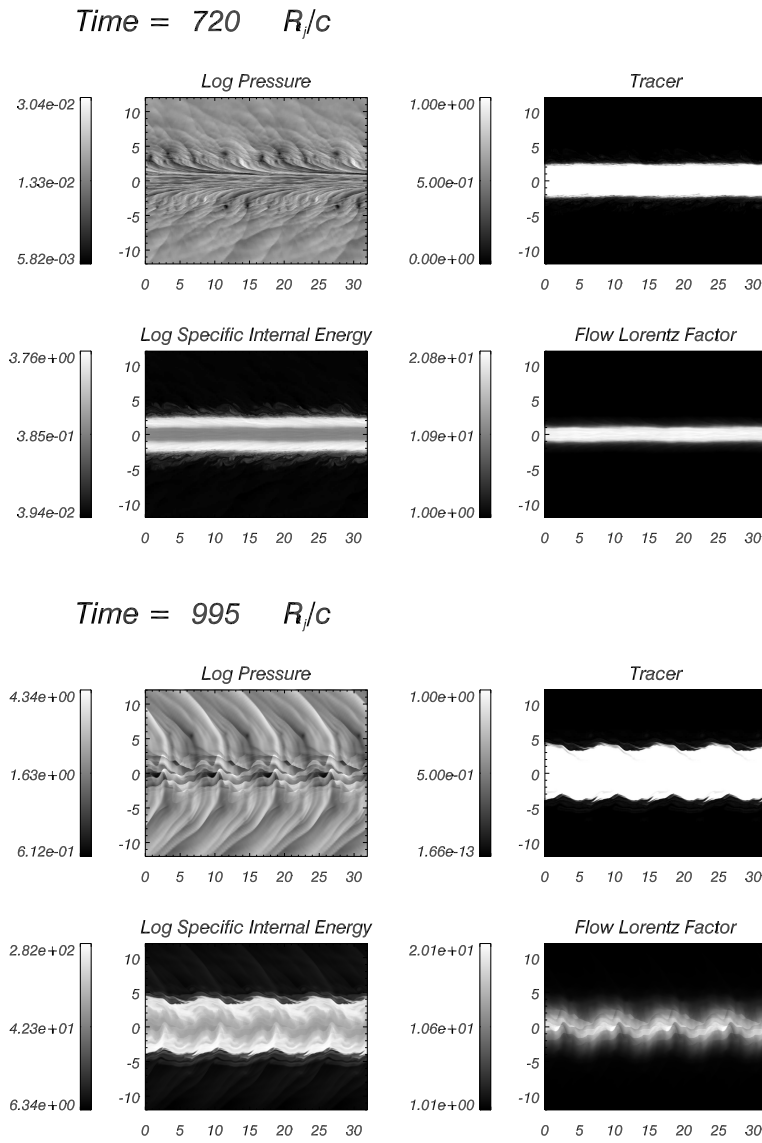


Figure 3.41: Snapshot at the last frame of the simulation of logarithmic maps of pressure, jet mass fraction and specific internal energy and non-logarithmic Lorentz factor for models **B20** (upper) and **D20** (lower).

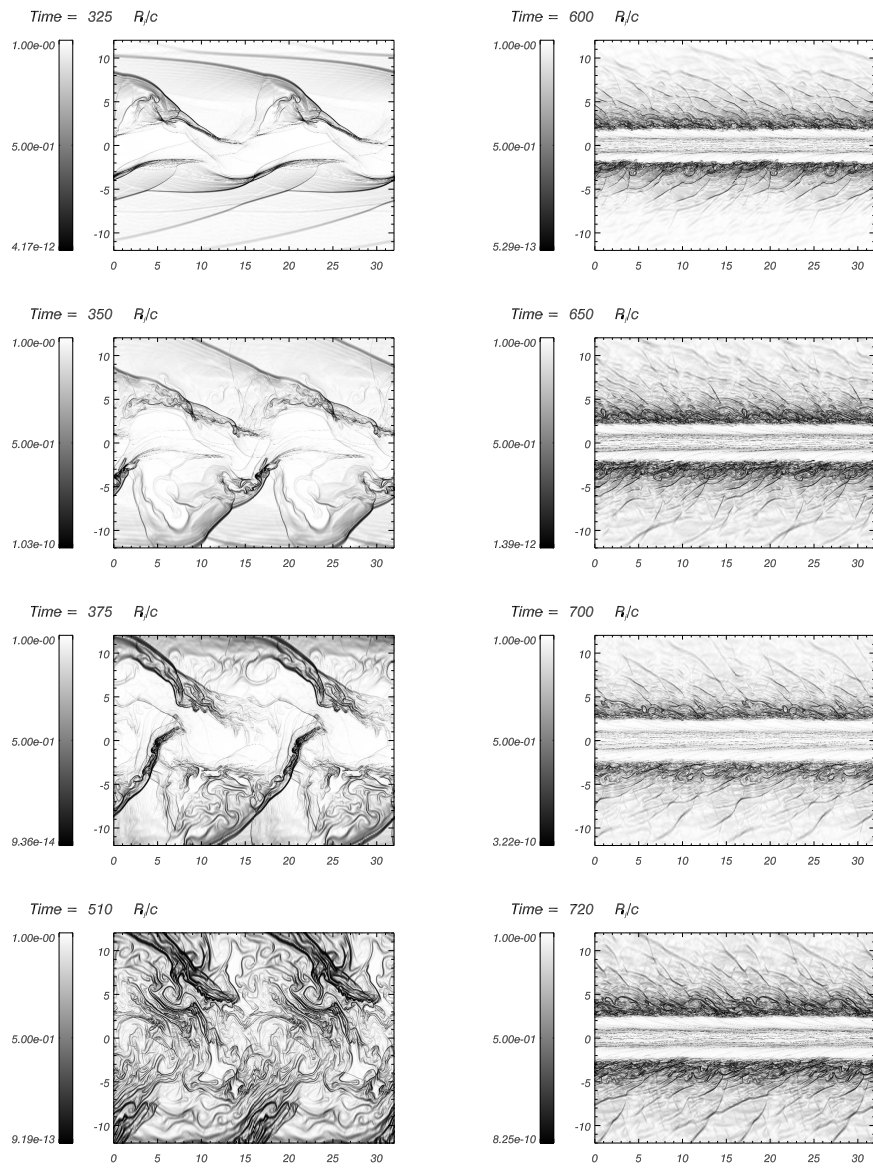


Figure 3.42: Schlieren plots showing waves in the non-linear regime for models **B05** (left panels) and **B20** (right panels).

3.4 Cylindrical jet simulations

Solving the differential equation for linear perturbations in cylindrical coordinates as shown in Appendix D we find solutions plotted in Figs. 3.43 and 3.44. We chose models B05, D05, B20 and D20 as representative of different non linear evolutions in order to perform linear analysis and numerical simulations and check similarities and differences with the slab jet case, thus generalizing our results. First simulations in cylindrical coordinates were performed perturbing only one mode. The numerical set up consisted on a grid with transversal size of $3 R_j$, with resolution of $256 \text{ cells}/R_j$, and an extended region up to $100 R_j$ with a 2.5% of relative growth, $32 \text{ cells}/R_j$ were used in the axial direction, with a size of $15.71 R_j$ for model B05, $10.47 R_j$ for B20, $2.5 R_j$ for D05 and $3 R_j$ for D20. Periodical boundary conditions were used longitudinally, reflection in the axis and outflow far from the jet.

In Figs. 3.45, 3.46 and 3.47, we see the same typical behaviours found in Chapter 2. Models B05 and D05 disrupt after saturation, D20 undergoes a slightly slower non-linear mixing and B20 seems to be the most stable, however mixing slowly with the ambient.

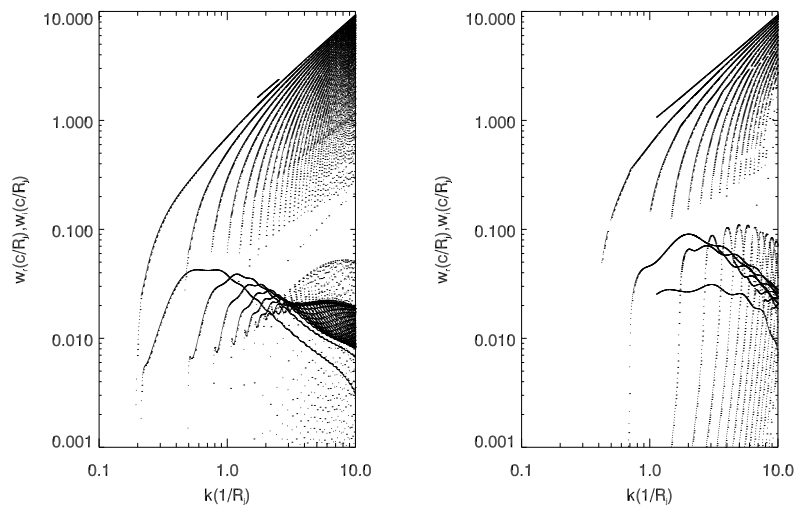


Figure 3.43: Solutions for the temporal stability problem of the pinching mode in cylindrical coordinates. Left panel: model B05. Right panel: model D05.

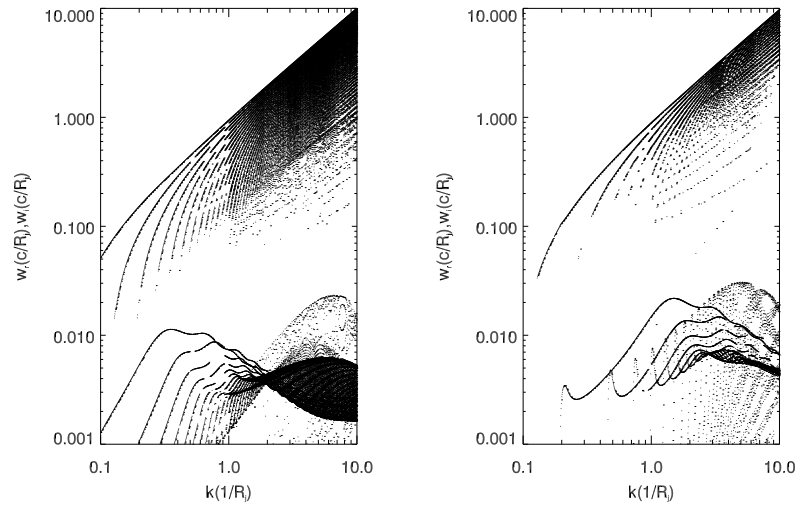


Figure 3.44: Same as Fig. 3.43. Left panel: model B20. Right panel: model D20.

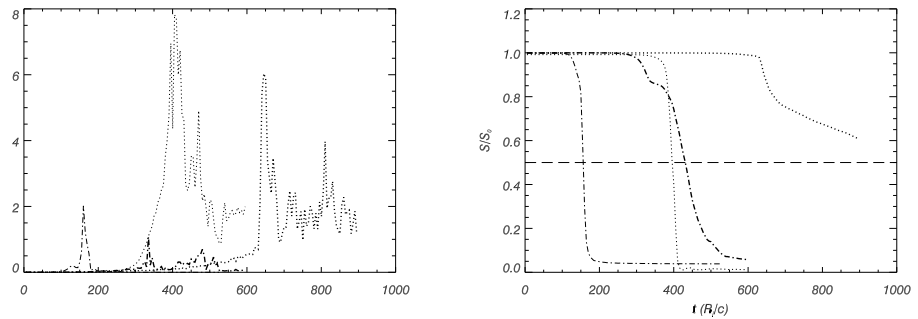


Figure 3.45: Left panel shows transversal relativistic Mach number as defined in Chapter 2 and right panel shows evolution of axial momentum in the jet and right panel stands for transversal momentum for one mode simulations. Dotted thin line stands for model B05, dotted thick for B20, dash-dot thin for D05 and dash-dot thick for D20.

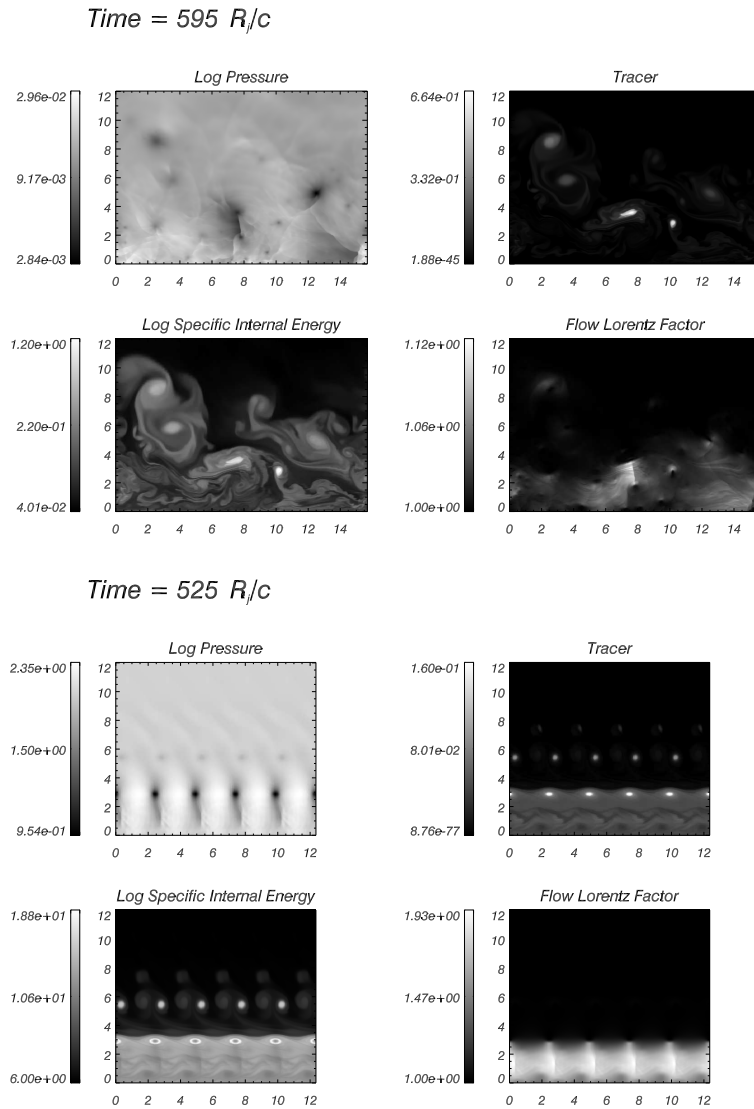


Figure 3.46: Snapshot at the last frame of the simulation of logarithmic maps of pressure, jet mass fraction and specific internal energy and non-logarithmic Lorentz factor for one mode cylindrical models B05 (upper) and D05 (lower).

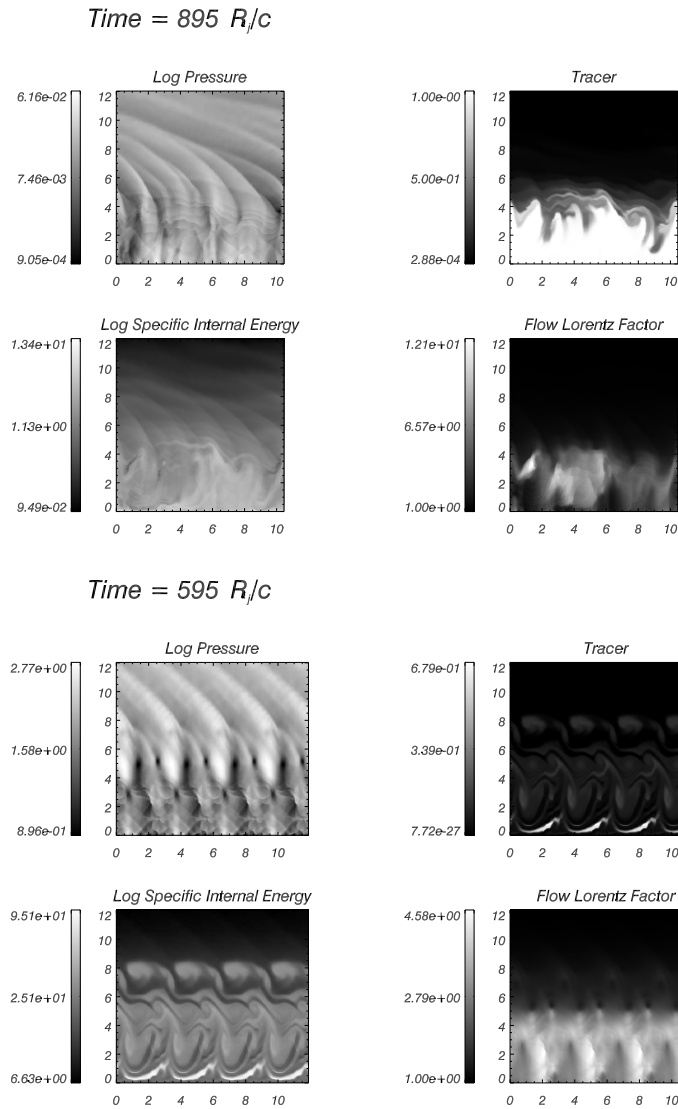


Figure 3.47: Snapshot at the last frame of the simulation of logarithmic maps of pressure, jet mass fraction and specific internal energy and non-logarithmic Lorentz factor for one mode cylindrical models B20 (upper) and D20 (lower).

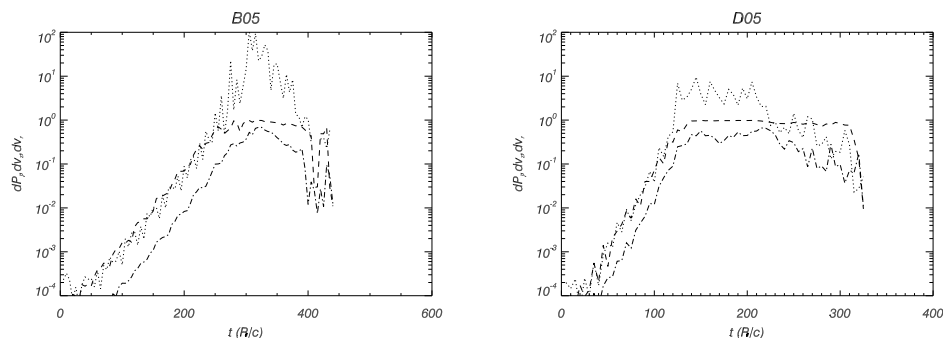


Figure 3.48: Pressure and axial and radial velocity perturbation evolution for several modes simulations. Left panel: model B05. Right panel: model D05.

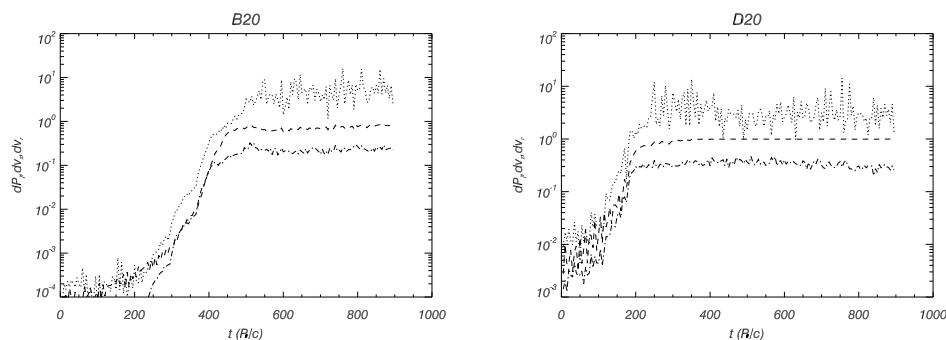


Figure 3.49: Same as Fig. 3.48. Left panel: model B20. Right panel: model D20.

These simulations were also performed applying several symmetric (pinching) sinusoidal perturbations. In this case, resolution is 128 cells/ R_j axially and 256 cells/ R_j radially, shear layer width is the same as in planar coordinates. Reflection boundary conditions were applied in the jet axis. In Figs. 3.48 and 3.49 we show the evolution of perturbation with time for all four models. Fitted growth rates for models B05 and D05, $0.04 c/R_j$ and $0.08 c/R_j$ respectively, fall well within the values plotted in Fig. 3.43. In models B20 and D20, resonant modes appear as in their slab counterparts, giving rise to larger numerical growth rates than those found in Fig. 3.44 (0.04 and 0.05 respectively). The same non linear evolutionary patterns as those observed for

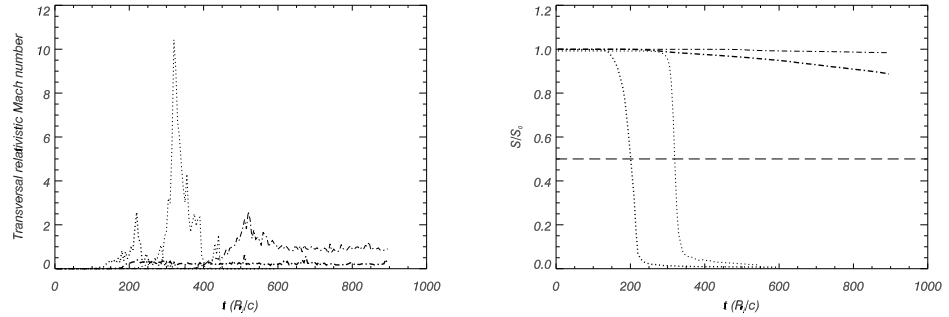


Figure 3.50: Left panel shows transversal relativistic Mach number as defined in Chapter 2 and right panel is for relative axial momentum (several mode simulations). Dotted thin line stands for model B05, dotted thick for B20, dash-dot thin for D05 and dash-dot thick for D20.

sheared slab jets counterparts are found: models B05 and D05 are disrupted after saturation, whereas models B20 and D20 are stabilized by resonant modes. The latter fact represents also a difference with one mode simulations, where resonant modes did not appear. Most remarkable features in the cylindrical simulations are the very low axial momentum kept by the jet in models B05 and D05, and their stronger mixing and mass loading (see Fig. 3.50). This may be due to geometric effects, as the surface of the interface grows radially in cylindrical coordinates, resulting in a more efficient transference of momentum to the ambient medium. In any case, results show the generalized character of conclusions presented here. In Figs. 3.51-3.52 we show panels at the last frame of the simulations, for jets mass fraction and Lorentz factor. These results show the generalized character of those presented in this Chapter and discussed in next Section.

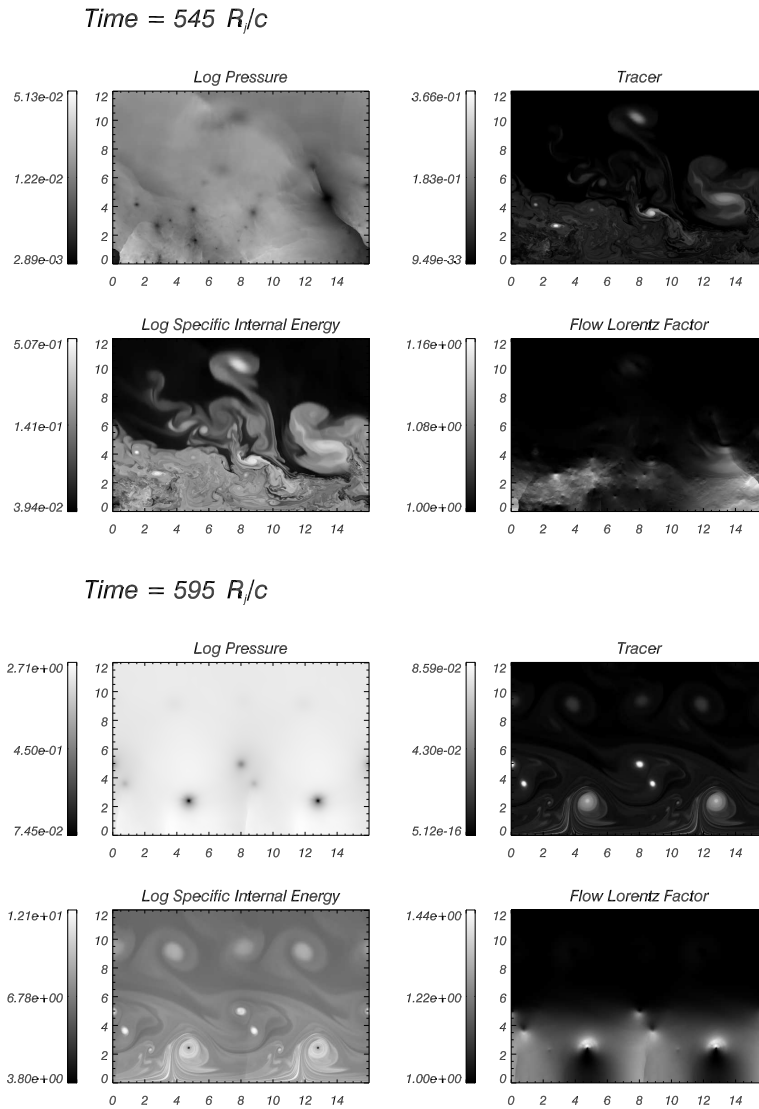


Figure 3.51: Snapshot at the last frame of the simulation of logarithmic maps of pressure, jet mass fraction and specific internal energy and non-logarithmic Lorentz factor for cylindrical models B05 (upper) and D05 (lower).

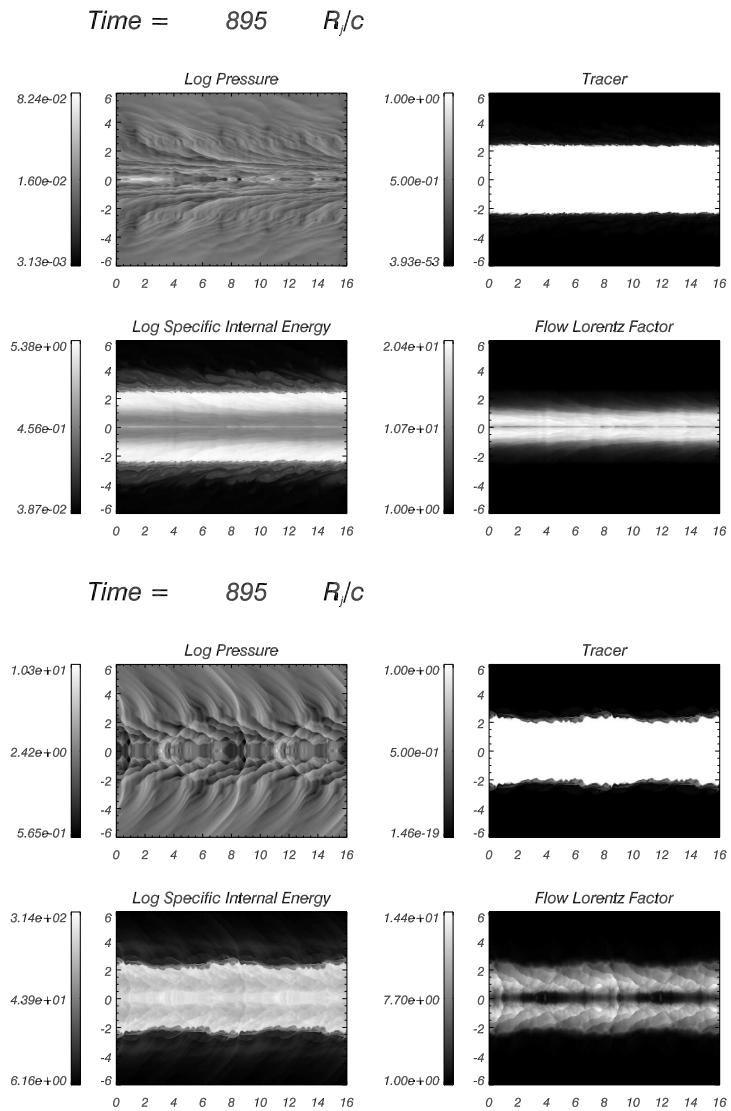


Figure 3.52: Snapshot at the last frame of the simulation of logarithmic maps of pressure, jet mass fraction and specific internal energy and non-logarithmic Lorentz factor for cylindrical models B20 (upper) and D20 (lower).

3.5 Discussion

3.5.1 Non-linear stability

Simulations presented in Chapter 2, performed for the most unstable first reflection mode of the corresponding models, confirmed the general trends resulting from the linear stability analysis: the faster (larger Lorentz factor) and colder jets have smaller growth rates in the linear regime. In Chapter 2, the non-linear evolution of the instability in the different models was characterized through the processes of jet/ambient mixing and momentum transfer. The models were then classified into four classes (I to IV) according to the particular nature of these processes in each of the models. Class I models (corresponding to cold and slow jets) were deeply mixed and mass loaded by the end of the simulation. Models in Class II (hot and fast jets) were slowly mixed in the non-linear regime, losing progressively their longitudinal momentum. Models in Class III (hot and slow jets) have properties between Classes I and II. Finally, Class IV (containing cold/warm and fast models) appeared as the most stable in the non-linear regime. Shear layers formed in all the models as a result of the non-linear evolution. Models in Classes I/II have broad shear layers, appear totally mixed, cooled and slowed down. Oppositely, models in Classes III/IV have an inner core surrounded by thinner layers and keep a larger amount of their initial longitudinal momentum. We performed a number of additional simulations keeping fixed the properties of the ambient medium and changing the rest-mass density of the jet and the Lorentz factor. Results confirmed that these models behave like previous simulations, and are naturally placed in the classification already defined.

The stability classes considered in Chapter 2 were defined according to the jet response to single modes. In this Chapter we revisit this classification scheme on the light of the present results based on more general perturbations. Following results in this Chapter (see Figs. 3.33, 3.34 and 3.35), we have classified jets depending on their non-linear behaviour in three different groups

- Unstable 1 (UST1) models: Jets which are disrupted after a strong shock is formed after the linear regime, enhancing turbulent mixing with ambient medium. It includes models **A2.5**, **B2.5**, **D2.5**, **B05**, and **D05**, i.e., lower Lorentz factor jets. The mixing layer width becomes larger than $5R_j$ (Fig. 3.33) and they share more than 50% of their initial momentum with the ambient medium (Fig. 3.34).

- Unstable 2 (UST2) models: Jets which are disrupted in the non-linear phase by a continuous process of momentum transfer to the external medium, like **B10** and **D10**. This is observed in Fig. 3.35 as a non-decreasing transversal momentum in the non-linear regime. These models end up, eventually, sharing a large fraction of initial momentum and developing a wide mixing layer.
- Stable (ST): Jets which develop resonant modes, and remain collimated for long time, **A10**, **B20**, and **D20**. These models have a thin mixing layer and share a very small fraction of their axial momentum with the ambient medium. They expand, but remain collimated.

In the course of the evolution, the jets develop a rich transversal structure in all the physical variables. This structure is different depending on the non-linear evolution of the jets. Figure 3.53 displays the transversal profiles of relevant physical quantities averaged along the jet at the end of the simulations for models **A2.5**, representative of models in UST1, **D10**, of UST2, and **B20**, of ST.

Model **A2.5** shows a totally mixed, mass-loaded flow with averaged maximum speed $0.4c$, i.e., barely relativistic, as these jets are efficiently slowed down by mass entrainment after the disruption. The mass loading is inferred from the low values in the tracer profile ($f < 0.3$), which imply large fraction of ambient medium material inside the jet. The efficient conversion of kinetic energy into internal energy enhanced by the shock triggered in the early post-linear phase causes the jet to increase its specific internal energy.

UST2 jets undergo a slower process of mixing so they still keep a larger fraction of axial velocity and Lorentz factor by the end of the simulation, even though they appear to be totally mixed ($f < 0.7$ everywhere). However, as we have mentioned in previous section, the mixing and slowing process is still going on in **B10** and **D10** so it is clear that if the simulation had continued, the longitudinal velocity and Lorentz factor values would be smaller than those found. We also observe that the more mass-loaded parts of the jet (i.e., the region with $-10 R_j < x < 0$) are consistently colder.

Finally, the jet in model **B20** remains very thin. The velocity profile of model has widened by $2 - 3 R_j$ by the end of the simulation, coinciding with the generation of a hot shear layer. This layer is seen in the Figure as an overheated and underdense ($\rho < 0.1$) region shielding the unmixed core ($f = 1$), which keeps almost all its initial axial momentum and Lorentz factor.

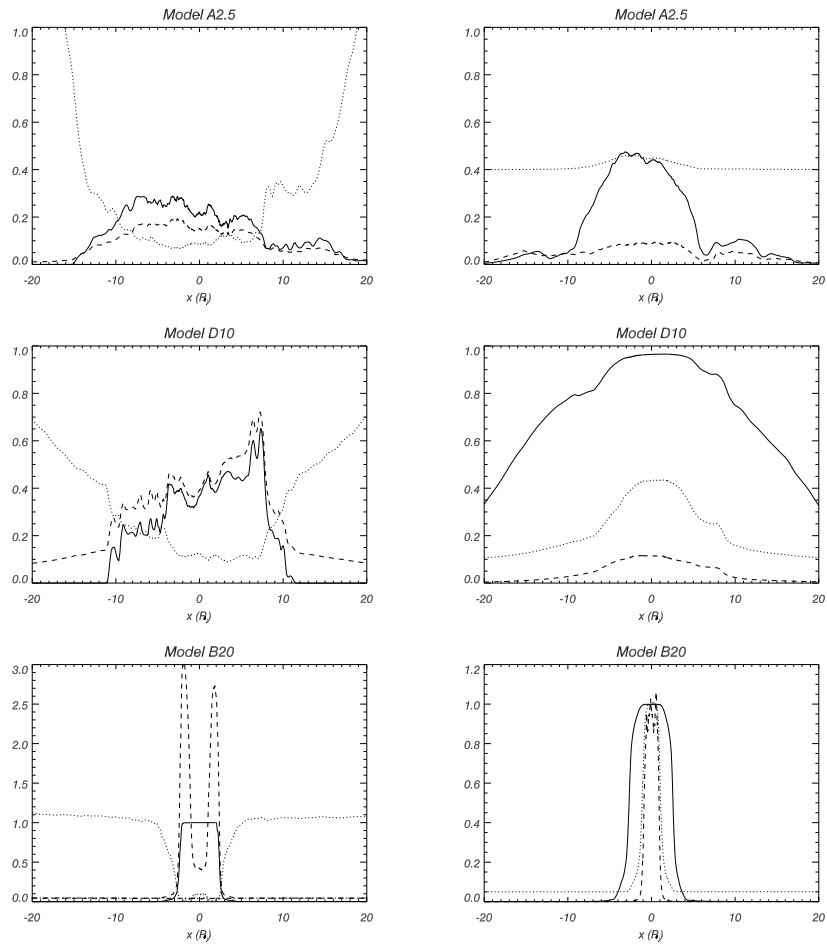


Figure 3.53: Averaged transversal structure in the final state of the jets corresponding to models **A2.5** (upper panels), **D10** (middle) and **B20** (bottom). Left panels (thermodynamical quantities): solid line, tracer; dotted line, rest mass density; dashed line, specific internal energy. Right panels (dynamical quantities): solid line, longitudinal velocity; dotted line, lorentz factor normalized to the initial value in the jet; dashed line, longitudinal momentum normalized to the initial value in the jet. Specific internal energy for model **D10** has been divided by 100 to fit in the scale.

The core has a rich internal structure (see the pressure panels in Fig. 3.41) that also manifests in the spiky structure of the shows longitudinal momentum profile.

A comparison of the present non-linear evolution classification scheme and that of Chapter 2 (classes I-IV) allows to conclude that, in general, models in classes I and III fall into UST1, whereas models in Class II corresponds to UST2 and those in Class IV to ST. The reason why models **D2.5** and **D05** (belonging formerly to Class III) move to UST1 may be the inclusion of longer wavelength perturbations, along with antisymmetric modes, which are more disruptive than the symmetric first reflection mode used in the previous work. This can be seen by comparing structures and evolution of model **D05** here and in Chapter 2, in particular the evolution of the mixing and the momentum transfer.

Regarding UST2 here compared to former class II, **B10** and **D10** undergo a very similar slow process of momentum transfer to the external medium as that observed for D10 and D20 in Chapter 2, although their temperatures are very different and the shock in **B10** is much stronger than that in **D10** (see Table 2.3). The reason for this process of slow momentum exchange may be the same as that proposed in Chapter 2 for D10 and D20, i.e., a continuous conversion of kinetic into internal energy due to the large initial Lorentz factor, that acts as a source of transversal momentum favoring the process of mixing and mass-loading (see Fig. 3.35), and contrary to the rest of models. **B10** changes from class I to UST2, meaning that disruption occurs by slow mixing in the new simulation, compared to sudden disruption in previous one.

Models in Class IV were characterized by a rich internal structure jet preserving a large fraction of initial momentum and Lorentz factor. ST models share those features, but now we are able to clearly associate them to the growth of resonant modes, which could be the reason of the breaking of the linear slope in model C20 (see Fig. 2.9 in Chapter 2). Steepening of short wavelength modes at the shear layer generates small shocks which favor local mixing and an efficient conversion of kinetic into thermal energy. As a result of this process, the shear layer heats up and the jet expands, forming a hot and underdense layer around the jet core (see Fig 3.53). It is remarkable that A10 is largely asymmetric by the end of the simulation (see bottom panels Fig. 3.39). This is a consequence of the resonant modes only growing on one side of the jet during the linear regime, and it is understood from the basis of asymmetry resulting from mixture of symmetric and antisymmetric modes.

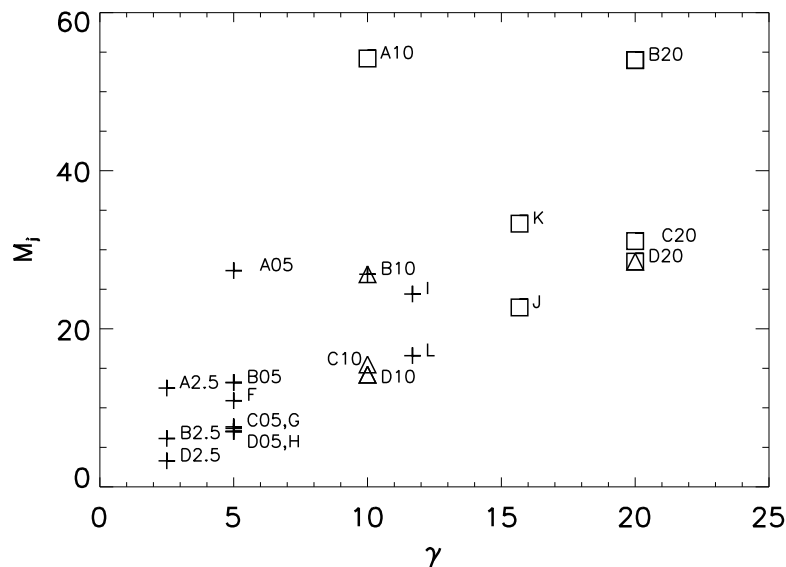


Figure 3.54: Relativistic Mach number (M_j) versus Lorentz factor (γ) of the simulated models here and in Chapter 2. Symbols represent different non-linear behaviors: crosses stand for UST1 disrupted jets (low relativistic Mach number and low Lorentz factor); triangles for UST2 jets (moderately fast and supersonic), and squares for ST jets (highly supersonic and fast jets). Models where two different points have been used are those with a different evolution in simulations presented here and those from Chapter 2 (see text).

This effect, though much less evident, is also observed in model **B20** (see Fig 3.53). Finally, model **D20** has moved from class II to ST, clearly due to the appearance of resonant modes. This fact allows us to conclude that the fate of ST models would be exactly the same as those in UST2 if it was not for the growth of resonant modes. Hence, their importance in the long term stability of these jets.

We have classified jets depending on their non-linear behaviour in three different groups, which are clearly separated in a relativistic internal jet Mach number-jet Lorentz factor plot (Fig. 3.54). In this plot, we also include models from Chapter 2. We do this in order to show the general character of our

results, and remark that this division of the stability properties of jets is more accurate than that used in Chapter 2 (with the jet-to-ambient enthalpy ratio instead of the relativistic Mach number). A clear correlation between the two plotted parameters and the non-linear stability properties of the jets is observed. Models **B10** and **D20** show two different types of point in order to remark the change of non-linear behaviour from Chapter 2. These are placed in transition regions of the plot, either in Lorentz factor (**B10**) or in relativistic Mach number (**D20**). This fact could explain differences in the non-linear behaviour as caused by changes in the initial conditions, what is quite evident in the case of **D20** (for resonant modes appear due to the presence of the shear layer). Consistently with previous discussion, we have given to models in Class III the same symbols (crosses) as for UST1 jets, as we do not consider that they have different non-linear behaviour in both simulations. Figure 3.54 can be considered as the relativistic counterpart of the $M - \nu$ (Mach number-density ratio) diagram presented in Bodo et al. (1994) (note that their density ratio ($\nu = \rho_a/\rho_j$) is inverted with respect to ours). In our case the Mach number is relativistic, and the density ratio, which stands for the inertia of the flow, is substituted by the Lorentz factor here, as relativistic momentum is $\propto \gamma^2$, so it dominates the inertia of relativistic jets. Our conclusions are similar to theirs, for denser (higher Lorentz factor) and highly supersonic jets (high relativistic Mach number) are the most stable. However, in our case, we have found a higher degree of stability due to the growth of resonant, stabilizing modes.

3.5.2 Astrophysical implications

One of the current open problems in extragalactic jet research is to understand the morphological dichotomy between FRI and FRII jets. Several possible explanations have been proposed which mainly fall in one of these two general possibilities: either FRI and FRII sources are intrinsically the same, and morphology and jet evolution depend mainly on the ISM in which they are embedded in the first kiloparsecs, or they depend on intrinsic differences stemming on the jet formation process (black hole rotation, Blandford 1994; accretion rate, Baum et al. 1995; black hole mass, Ghisellini and Celotti 2001; the so called magnetic switch, Meier et al. 1998), or a combination of both (e.g., Snellen and Best 2003). Of course, all these mechanisms could be at action with different importance depending on the source.

Leaving aside the basis of the morphological dichotomy, current models (Laing and Bridle 2002a,b and references therein) interpret FRI morphologies

as the result of a smooth deceleration from relativistic ($\gamma \leq 3$, Pearson 1996) to non-relativistic, transonic speeds ($\sim 0.1 c$) on kpc scales. On the contrary, flux asymmetries between jets and counter-jets in the most powerful radio galaxies and quasars indicate that relativistic motion ($\gamma \sim 2 - 10$) extends up to kpc scales in these sources, although with smaller values of the overall bulk speeds ($\gamma \sim 2 - 4$, Bridle et al. 1994). Current models for high energy emission from powerful jets at kpc scales (e.g., Celotti et al. 2001) bears additional support to the hypothesis of relativistic bulk speeds on these scales.

The results concerning the long term evolution of relativistic jets presented in this chapter, and summarized in Fig. 3.54, confirm that slower and smaller Mach number jets (UST1) are entrained by ambient material and slowed down to $v < 0.5 c$ after becoming overpressured (due to conversion of kinetic into internal energy) and being disrupted by non-linear instabilities effects which cause flaring and rapid expansion of the mixing flow. UST2 jets undergo a smooth slowing down, and though by the end of the simulation jet velocity is $\sim 0.9 c$, this process is continuous and eventual loss of velocity to mildly relativistic values is to be expected. Finally, ST jets keep their initial highly relativistic velocities, and their steadiness by the end of simulations makes them firm candidates to remain collimated through long distances. Hence our results would point to high Lorentz factor, highly supersonic jets as forming FRII Class, whereas FRI jets would be found in the opposite corner of the diagram (slow, small Mach number jets). The validity of our results extends to models with different jet-to-ambient density ratios and specific internal energies as it was seen in Chapter 2 (models F-L).

Our conclusions point to an important contribution of intrinsic properties of the source in the morphological dichotomy. Nevertheless, the importance of the ambient medium cannot be ruled out on the basis of our simulations since we consider an infinite jet in pressure equilibrium flowing in an already open funnel and surrounded by an homogeneous ambient medium. Thus our approach does not take into account the consequences of the interaction of the jet with the ambient in order to penetrate it or the effects of a spatially varying atmosphere. Simulations following the spatial approach (in which perturbations grow with distance) for jets propagating in different ISM profiles and using a more realistic microphysics (allowing for a local mixture of electron, positron and proton Boltzmann gases) will be performed in order to clarify these points (see Section 4.2 for first results in this direction).

As discussed in the introduction of this chapter, there are plenty of ar-

guments indicating the existence of transversal structure in extragalactic jets at all scales. In the simulations presented here, the initial states were defined with a continuous transition layer of thickness $\approx 0.2R_j$. As discussed in the previous paragraphs, this shear layer has played an important role in the long-term stability of the jet flow. Besides this, thicker shear layers have been generated in the course of the non-linear evolution. Relatively thin ($\approx 2R_j$), hot shear layers are found in present ST models (the physically meaningful counterparts of the layers found in the three-dimensional, low resolution simulations of Aloy et al. 1999a, 2000) which could explain several observational trends in powerful jets at both parsec and kiloparsec scales (see Aloy et al. 2000 and references therein). Conversely and according to our simulations, these transition layers could be the responsible of the stability of fast, highly supersonic jets, preventing the mass-loading and subsequent disruption. Finally, the type of shear layers developed by models UST1/2 could mimic the transition layers invoked in models of FRIs (Laing and Bridle 2002a,b).

3.6 Conclusions

We have performed a number of simulations spanning a wide range of parameters such as Lorentz factor and specific internal energy, for a general setup where a slab sheared jet is perturbed with a set of symmetric and antisymmetric sinusoidal perturbations, in order to characterize the stability properties of relativistic jets.

The most remarkable feature regarding the linear evolution of instabilities is the finding of resonant modes in our simulations, which were later confirmed on the basis of linear stability theory applied to sheared flows. These modes are important for the long term stability properties of some jets (ST), for they remain collimated and unmixed, keeping a large amount of initial axial momentum. Jets in which these modes do not grow fast enough with respect to longer modes, are disrupted, either after a shock, or by slow momentum transfer and mixing.

We have classified jets depending on their non-linear behaviour in three different classes which are clearly separated in a relativistic Mach number-Lorentz factor plot (Fig. 3.54). UST1 models are disrupted after a shock forms after saturation, and ambient gas penetrates deep into the jet stream, decelerating and cooling down the initial flow. UST2 models are slowly decelerated by an efficient conversion of kinetic energy into internal energy which

causes momentum transfer and mixing. Finally, ST models present small expansion, but remain collimated and isolated from the ambient by a hot shear layer. ST models would fall into UST2 if resonant modes would not be present, as it occurs for model D20 in Chapter 2.

Our simulations admit a clear interpretation in the context of the morphological dichotomy of radio jets. Our results would point to high Lorentz factor, highly supersonic jets as forming FRII Class, whereas FRI jets would be related to slow, small Mach number jets. In the former, the generation of a hot shear layer surrounding a stable core could be related to the transversal structure observed in several powerful jets.

Chapter 4

ASTROPHYSICAL APPLICATIONS

4.1 Pc scale jets. Numerical simulations on 3C 273

4.1.1 Introduction

3C 273 is the brightest quasar known; it was the second to be discovered by Hazard, MacKey and Shimmins (1963), and the first for which the emission lines were identified with red-shifted hydrogen lines by Schmidt (1963). Due to its closeness (its red-shift is $z = 0.158$), it has become a paradigmatic object to be studied in all the spectral range in order to try to understand the AGN phenomena.

Schmidt (1963) pointed out the presence of a jet-like structure in 3C 273, so it has also become an excellent laboratory for AGN astrophysicists to study jet-physics. This jet is observed on parsec scales using VLBI (Pearson et al. 1981, Krichbaum et al. 2000, Abraham et al. 1996) and VSOP (Lobanov and Zensus 2001, Asada et al. 2002), and in kiloparsec scales up to a deprojected distance of about 60 kpc (Stawarz 2004), depending on the cosmological parameters.

Main observational features tell us that is a highly collimated and beamed one-sided relativistic jet, presenting superluminal motion $5 - 8h^{-1}c$ (h being the normalized Hubble constant), with a periodicity of $\simeq 15$ yrs (Abraham et al. 1996), on the VLBI scales. Beaming angle is constrained between $\theta = 10^\circ$ and 15° and Lorentz factor has been computed to be between $\gamma = 5$ and $\gamma = 10$ in order to explain those measured superluminal velocities. No counter-jet has

been detected on dynamic ranges up to 16000:1. Observed helical structures are explained by means of Kelvin-Helmholtz instabilities (Lobanov and Zensus 2001) or a helical magnetic field (Asada et al. 2002). Variability in emission from submillimetre to radio wavelengths is explained by Türler et al. (2000) in terms of a Marscher and Gear (1985) like shock model, using observations taken along 20 years. Correlation between UV and radio light curves was found by Courvoisier et al. (1990), where the former leads the latter by a few months, suggesting that UV radiation could be a signature of the energy release from accretion processes, which after manifests in the synchrotron radiation from the jet. Also a large optical/infrared outburst was observed to be followed by a superluminal component (Krichbaum et al. 1990).

Abraham et al. (1996) and Abraham and Romero (1999) argued that precession of the inner jet, due to precession of a binary black hole in the central engine with a period of 16 yrs, may account for the periodicity in superluminal velocities. They assume constant speed injection, and derive bulk Lorentz factor $\gamma = 10.8$, precession cone opening angle $\simeq 4^\circ$ and Doppler factor between 2.8 and 9.4. Qian et al. (2001a) also model the source ejection, taking into account that from VLBI observations it is found a decrease in the apparent speeds of superluminal components from $7.5c$ to $2.5c$ from 1963 to 1997 (Krichbaum et al. 2000), in contradiction with constant ejection suggested by Abraham and Romero (1999), a short-term oscillation of the ejection Lorentz factor with a $\simeq 4$ yrs period, and a quasi periodical rate of ejection of superluminal components with a period of $\simeq 0.8 - 1.7$ yrs. Qian et al. (2001a) confirm the precession period and find a very similar precession cone half-opening angle to that of Abraham and Romero (1999), by using the position angles of components ejected during these years, which vary from 225° to 265° . Babadzhanyants and Belokon (1993) found variability in the optical with periods of 1 yr and 13.4 yrs, coincident with superluminal component ejection and precession, respectively. Qian et al. (2001a) also suggest a periodicity of 50 – 70 yrs for ejection Lorentz factor, which has decreased from $\gamma \simeq 8$ in 1963 to $\gamma \simeq 3$, and for which we would be now observing the minimum value. Also, Krichbaum et al. (2001) found that apparent velocity increases outwards for several superluminal components.

VSOP observations at 5 GHz (Lobanov et al. 2000) allowed for larger resolution and resolving rich transversal structure of the parsec-scale jet in 3C 273, which presented three different components. The central, dominating component is interpreted as shocked plasma embedded in an underlying flow with

Kelvin-Helmholtz instabilities revealed in the weaker components surrounding the central one, and in the curvature of the jet. They observe that the central components are not following the curved path, but drift closer to the northern edge of the jet with increasing distance, and suggest that this may reflect the ballistic trajectories reported for fast components by Abraham et al. (1996). Qian et al. (2001b) point out stationary spectral reversals along the VLBI jet, from 22 to 86 GHz, a phenomenon also observed in Cygnus A parsec-scale jet associated to acceleration, suggesting that a pinch in an overpressured, stratified jet (a fast spine surrounded by a slower component), could cause this flattening of the spectrum in the widening region. They claim that emission at 22 and 86 GHz are produced in different regions, as Krichbaum et al. (2001) noticed that maps at larger frequencies show that emission is more concentrated to the jet axis than at lower frequencies, result which is confirmed when comparing optical and radio emission in the jet of M87 (Biretta 1996), suggesting that higher energy electrons and/or stronger magnetic fields may be closer to the axis.

On the large scale, a 10° misalignment with the VLBI jet is observed. The jet is observed from $13''$ ($\simeq 35$ kpc), where the first knot appears, to $23''$ ($\simeq 60$ kpc) from the core. The bridge between parsec and kiloparsec scales is very faint, but there is little doubt about the connection between both scales. The kiloparsec scale jet is very bright in a large range of wavelengths (from radio to X rays). Bahcall et al. (1995) identified the optical and radio jet, suggesting also transversal structure on these scales, and helical movement to explain the coincidence of the optical and radio knots. Absence of counter-jet is difficult to explain on the basis of Doppler beaming alone, requiring some degree of asymmetry in the system. There is debate about the origin of the lack of cooling and X-ray emission: re-acceleration either by magnetic reconnection (Lesch and Birk 1998), or due to turbulence (Manolakou et al. 1999), intermittent activity (Stawarz 2004), a second high-energy electron population (Röser et al. 2000, Marshall et al. 2001), inverse Compton scattering of the cosmic microwave background, requiring the jet material to be relativistic and moving at a small angle to the line of sight (Marshall et al. 2001, Sambruna et al. 2001). The latter mechanism has been considered not to be sufficient in order to explain the lack of cooling by Jester et al. (2001), who also claim that particle acceleration at a few localized sites is also not sufficient for this purpose. Other mechanisms as Synchrotron Self Compton (SSC) and thermal bremsstrahlung (Röser et al. 2000, Marshall et al. 2001, Sambruna et al.

2001) have also been discarded. Moreover, Kataoka et al. (2002) claim that the *visible* kinetic energy of the jet is $\simeq 100$ times smaller at the bottom of the VLBI jet than in the first knot of the kpc-scale jet, suggesting that a process of acceleration of non relativistic electrons to relativistic regime, taking the energy from that carried by protons (thermal component), should be taking place in order to explain this difference.

As we see, many questions remain open about the nature of 3C 273 jet: helical and transversal structure of the VLBI jet, different periods in ejection, X-ray emission and lack of cooling of the kiloparsec scale jet along with the absence of counter-jet and jet composition.

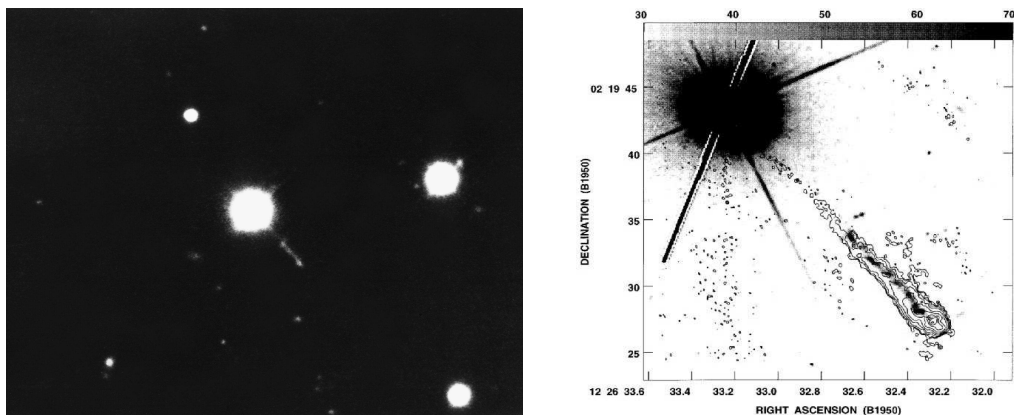


Figure 4.1: Optical image of quasar 3C273 (left), where the jet is also seen, and composition of optical and radio images (right).

Here, we are going to focus on the parsec scale jet physics. VSOP observations allowed Lobanov and Zensus (2001) (LZ01 from now on) to interpret structures in the parsec scale jet of 3C 273 as a double helix. Using approximate equations derived by Hardee (see, eg., Hardee 2000), they could infer, very accurately, the bulk parameters of the flow. This result, if confirmed, would make out of linear stability theory in combination with observations a really powerful tool in order to probe the physical conditions in jets and also to understand their physics. A different interpretation (Asada et al. 2002) suggests that a helical magnetic field could generate such a structure. We will study the first possibility. LZ01 obtain a bulk Lorentz factor $\gamma = 2.1$, well below those measured for superluminal components ($\gamma = 5 - 10$, Abraham et al. 1996), but suggest that instabilities develop in the slower underlying flow,

interpreting those fast components as shock waves inside the jet.

The question which arises from LZ01 is: Is really linear theory able to explain observable structures? Are there fingerprints of linear modes even when the flow has gone into the non-linear regime? A possibility for trying to answer to this question is by performing numerical simulations, which allow us to follow evolution from linearity to non-linearity (Chapter 2 and Perucho et al. 2004a). We will also keep in mind that numerical codes, although they have proven able to reproduce observed VLBI structures (Agudo et al. 2001), have limitations and will point out those which could affect the interpretation of our results.

Our aim is to compare structures generated in a numerical simulation of a steady jet, with the initial conditions of the underlying flow given in LZ01 and perturbed with several helical and elliptical modes, with those observed by LZ01. In Chapter 2 (see also Perucho et al. 2004a and 2004b) we have shown that numerical simulations allow for studies of the transition from the linear to the non-linear regime.

4.1.2 Linear Analysis

LZ01 obtained 240 profiles of the brightness distribution across the jet. Profiles were centered on a previously fixed ridge line, and orthogonal to it at each point. They fitted a double gaussian to each profile and identified two components which were interpreted as a double helix. Then, they fitted the positions of those gaussians to a number of sinusoidal modes, giving wavelengths, phases and amplitudes. In Table 4.1 we give the values found for wavelengths of fitted waves, their amplitudes, relative phases and identification.

Approximations by Hardee (1987, 1998, 2000) to the characteristic wavelengths of a perturbed system, relate those wavelengths to the speed of the jet (β_j), its Mach number (M_j) and the density ratio ($\eta = \rho_j/\rho_a$). Starting from the dispersion relation of a cylindrical, relativistic and supersonic jet, derived approximations for the perturbations in the long (low frequency) and the short wavelength (high frequency) limit.

$$\lambda_{nm}^l = \frac{4\gamma_j R_j (M_j^2 - 1)^{1/2}}{n + 2m - 1/2}, \quad (4.1)$$

$$\lambda_{nm}^* = \frac{2\pi}{\beta_{s,a}/\beta_j (n + m + 1/2) (M_a^2 - \beta_j^2)^{1/2} + \gamma_j (M_j^2 - \beta_j^2)^{1/2}}, \quad (4.2)$$

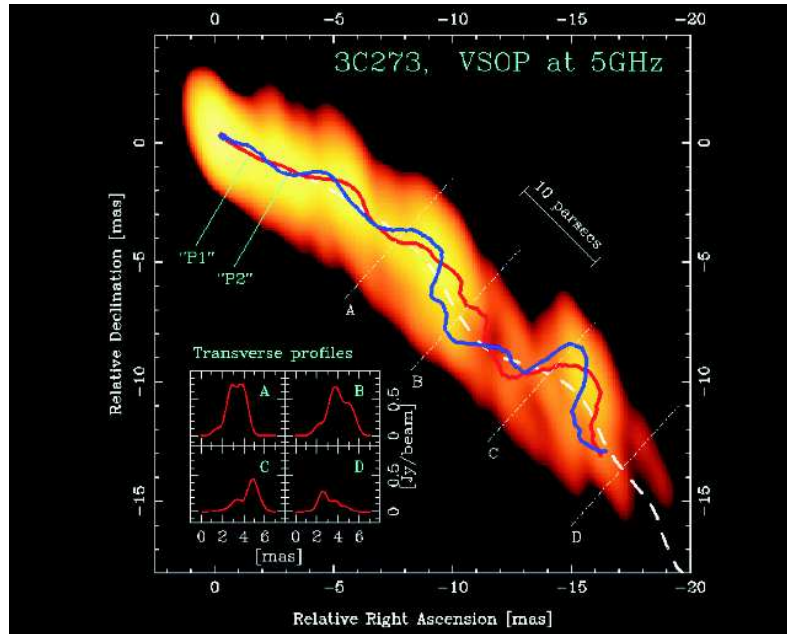


Figure 4.2: VSOP image of parsec scale jet in 3C 273 (from LZ01). In the left corner, we can see some transversal cuts to which the double gaussians are fitted.

where $\beta_{s,a}$ is the sound speed of the external medium in units of the speed of light, γ_j is the Lorentz factor of the jet, $M_a = \beta_j/\beta_{s,a}$, R_j is the jet radius, and n, m are the azimuthal numbers which give the number of nodes around the jet surface and the number of nodes between the axis and the surface, respectively. The first equation gives the longest unstable wavelength for a body mode ($m > 0$) and the zero frequency limit for a surface mode ($m = 0$), and the second stands for the most unstable wavelength of a given mode. Relating these equations to fitted sinusoidal waves, the physical parameters of the jet were obtained. Identification of modes is in the last column of Table 4.1, and derived parameters are displayed in Table 4.2.

We observe that the derived Lorentz factor is below those given by other authors in order to explain superluminal motion. However, this could possibly be caused by the fact that Kelvin-Helmholtz instability acts on the underlying, slower flow, and not on the ballistic, superluminal components (LZ01).

This represents a very powerful tool for deriving physical parameters in

λ (mas)		Amplitude (mas)		φ (deg)		Mode
P1	P2	P1	P2	P1	P2	
	18		1.5		180	H_s
	12		1.4		260	E_s
3.9	4.1	2.2	1.5	315	135	H_{b1}
	3.8		1.2	135	315	E_{b1}
	1.9		0.25	175	355	H_{b2}

Table 4.1: Identified wavelengths, modes and their amplitudes and relative phases from observations (LZ01). φ stands for the relative phase, and P1 P2 stand for both found helices (see text). H stands for helical, E for elliptical modes, and subscripts refer to surface (s , fundamental) or body modes (b , reflection). The latter are followed by the index identifying the exact body mode.

γ_j	M_j	η	$R_j(\text{pc})$	ϕ_j	θ_j	$c_{s,j}$ (c)	$c_{s,a}$ (c)	pc/mas
2.1	3.5	0.023	0.8	1.5	15	0.53	0.08	2.43

Table 4.2: Jet parameters from the fit. γ_j is Lorentz factor, M_j is Mach number, η is rest mass density ratio, ϕ_j is jet half opening angle, θ_j is jet viewing angle, $c_{s,j,a}$ are sound speeds, and pc/mas is the projected linear scale.

relativistic jets, as they become directly related to observable features of jets as their structure and observed wavelengths, as shown by LZ01. Of course, these observable features may be caused by other physical processes than Kelvin-Helmholtz instabilities, but the general nature of this kind of instabilities appearing in sheared flows, makes them firm candidates to be responsible for those structures.

4.1.3 Simulation 3C273-A

Initial setup

We start with a steady jet with Lorentz factor $\gamma = 2.1$, density contrast with the external medium $\eta = 0.023$, sound speed $c_{s,j} = 0.53c$ in the jet and $c_{s,a} = 0.08c$ in the external medium and perfect gas equation of state

(with adiabatic exponent $\Gamma = 4/3$). Assuming an angle to the line of sight of 15° and redshift $z = 0.158$ ($1 \text{ mas} = 2.43 \text{ pc}$), the observed jet is 169 pc long. Considering the jet radius given in LZ01 (0.8 pc), the numerical grid is $211 R_j$ (axial) times $8 R_j$ (transversal), i.e., $169 \text{ pc} \times 6.4 \text{ pc}$.

Resolution is $16 \text{ cells}/R_j$ in the transversal direction and $4 \text{ cells}/R_j$ in the direction of the flow. A shear layer of $2 R_j$ width ($m = 2$ in equations (2.42) and (2.43)) is included in the initial rest mass density and axial velocity profiles to keep numerical stability of the initial jet. An extended grid with 24 cells and extending up to $30 R_j$ on each side of the jet, with 20% increasing size, and also in the axial direction, with $105.5 R_j$ size and 168 cells. Boundary conditions are injection at the inlet, and outflow far from the axis and in the axial direction. Elliptical and helical modes are induced at the inlet using the following expression:

$$P' = \frac{A_0}{\cosh^2 |r|} \cos(\omega t + n \arctan \theta + \phi) \sin^2(\pi r), \quad (4.3)$$

where A_0 is the initial amplitude, r is the radius, ω is the frequency of the mode, $n = 1$ for helical modes and $n = 2$ for elliptical ones, θ is the polar angle in cylindrical coordinates, ϕ is the phase given to the perturbations, and $\sin^2(\pi r)$ is used in order to give an initial transversal structure to the modes. In Fig. 4.3 we show the typical structures induced by equation (4.3). The addition of all the input modes gives the total perturbation.

Frequencies of the excited modes are computed from the observed wavelengths of modes, λ^{obs} , corrected for projection effects and relativistic motion and wave speed, v_w according to $\omega = 2\pi v_w / \lambda^{theor}$, where

$$\lambda^{theor} = \frac{\lambda^{obs}(1 - v_w/c \cos \theta)}{\sin \theta}, \quad (4.4)$$

θ being the angle to the line of sight. We have used $v_w = 0.23 c$ excepting for the 12 mas mode, which, being a surface mode, it moves with a speed close to that of the jet (e.g., Hardee 2000). The 18 mas mode in LZ01, which is not identified with any Kelvin-Helmholtz mode, was not included in this simulation. We list excited modes in Table 1. Simulation lasted for a time $1097 R_j/c$ (i.e., $\simeq 2852 \text{ yrs}$), and it used $\simeq 11 \text{ Gb}$ RAM Memory and 8 processors during around 30 days in a SGI Altix 3000 computer.

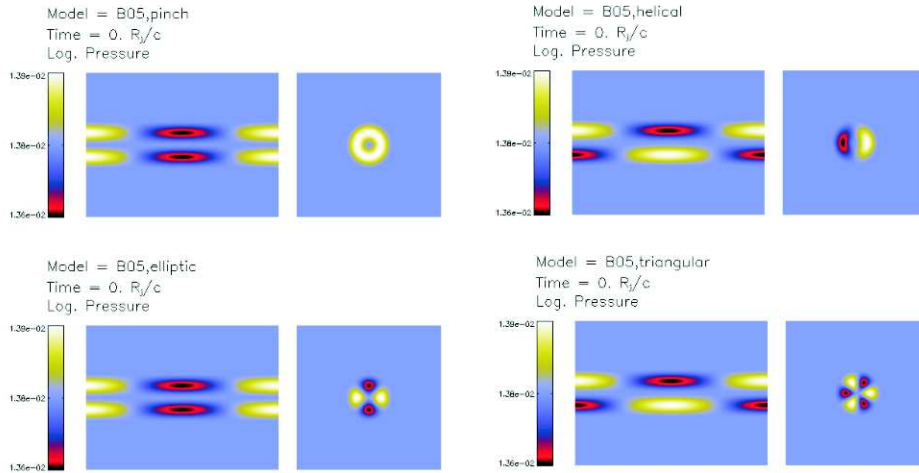


Figure 4.3: Structure of perturbations (axial and transversal cuts) in a generic 3D jet, induced by eq (4.3). Top left: pinching mode ($n = 0$). Top right: helical mode ($n = 1$). Bottom left: elliptic mode ($n = 2$). Bottom right: triangular mode ($n = 3$).

Discussion

The simulation can be divided in two parts, a first one, where modes grow linearly up to disruption of the jet, and a second part where disruption dominates evolution. In Figs. 4.4 and 4.6 we display several transversal cuts of the jet that show mode competition, and axial cuts at two different times of the simulation, respectively. In the former, we can see how excited modes dominate at different positions and times in the jet. Plots of transversal structure of the jet and Fourier transforms tell us that short helical modes ($\simeq 4 R_j$) modulated by longer helical (antisymmetric, $\simeq 20 R_j$) and elliptical (symmetric, $\simeq 50 R_j$) wavelengths as can be seen in Fig. 4.5, dominate during the linear phase of the simulation. Linear regime ends up with the disruption of the jet, due to one of the longest helical modes ($\simeq 20 R_j$), at time $t = 350 R_j/c$. After disruption, evolution of the jet is totally influenced by it, and induced perturbations propagate slowly backwards as a backflow in the ambient medium. Also, the disruption point moves outwards due to the constant injection of momentum at the inlet and the change of conditions around the jet, which

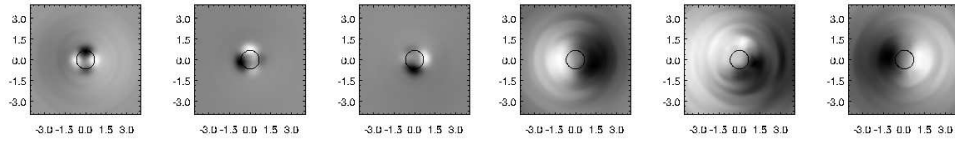


Figure 4.4: Map of pressure perturbation transversal cuts in arbitrary units, values increasing from dark to lighter colors (to be compared with Fig. 4.3). Solid line indicates $v_z = 0.8c$ contour. Three left panels: Cuts at $35 R_j$, $t = 70, 140, 200 R_j/c$ where elliptical mode rotation is apparent. Three right panels: Cuts at $105 R_j$, $t = 210, 220, 240 R_j/c$ where helical mode rotation is apparent.

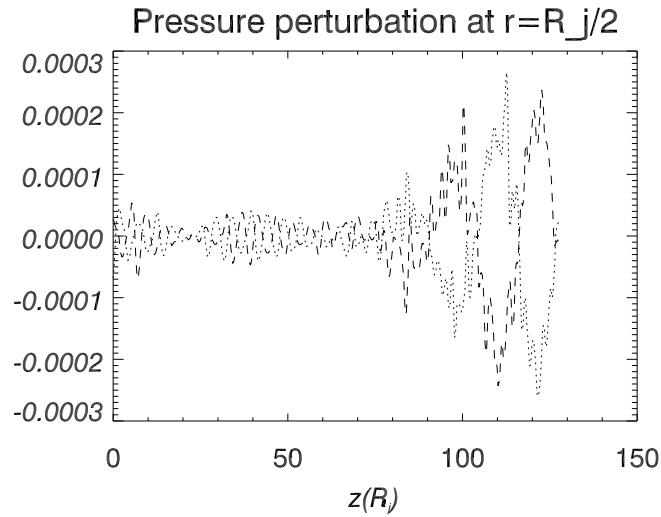


Figure 4.5: Longitudinal cut of pressure perturbation at $R_j/2$ in symmetric positions with respect to the jet axis at $t = 250 R_j/c$. Helical (antisymmetric) structures of 4 and $25 R_j$ and an elliptic (symmetric) one of $50 R_j$ are apparent.

seem to make it more stable. This point moves from $160 R_j$ to $180 R_j$ by the end of the simulation (see Fig. 4.6).

In order to check the consistency of the results obtained for the linear regime of the simulation with observed structures, we need to measure the propagation speeds of the perturbations. Our data frames are too separate to

λ^{obs} (mas)	Mode	λ^{theor} (R_j)	λ^{sim} (R_j)	$\lambda_{v_w=0.23c}^{sim}$ (mas)	$\lambda_{v_w=0.38c}^{sim}$ (mas)	$\lambda_{v_w=0.88c}^{sim}$ (mas)
2	H_{b2}	18.7	4	0.44	0.54	2.27
4	E_{b1}, H_{b1}	37.4	25	2.7	3.37	14.3
12	E_s	21.2 ^a	50	5.5	6.7	28.5

Table 4.3: First two columns give identified wavelengths and modes in LZ01 (H stands for helical, E for elliptical, s for surface mode and $b1$ and $b2$ for first and second body modes, respectively), third column gives the intrinsic wavelengths (see text), in the fourth column we have written observed wavelengths in the simulation, and the last three columns give the fourth column wavelengths as observed depending on the wave speed. ^a Computed assuming it propagates with the flow speed.

allow for the measurement of those speeds directly from the simulation, so we use other means to estimate them. From pressure perturbation plots (like Fig. 4.5), we estimate the velocity of propagation of the fastest modes by measuring the position of the perturbation front in each frame. In this way, we find perturbations which travel with a velocity close to that of the flow ($v_w \simeq 0.88c$ as an upper limit). We can also derive the wave speed of the disruptive mode following the motion of the large amplitude wave (see Fig. 4.6) from frame to frame, and we find $v_w \simeq 0.38c$. We can associate the former, faster perturbation, with the longer wavelength and longer exponential growth length elliptical surface mode (see Fig. 4.5), and the latter with a shorter wavelength and shorter exponential growth length body mode (see Hardee 2000). Both measured speeds are different to that given by LZ01 ($0.23c$). It is difficult to assess the reason for that difference, which may be caused by an accumulation of errors in different assumptions, or just by a different wavelength (implying different velocity) having been excited. Expected observed wavelengths for the different speeds are given in Table 4.3.

Results differ morphologically from the observed source mainly due to the disruption of the jet. These differences may be a consequence of one or several factors. We point as possible reasons the difficulty of simulating these objects, the errors introduced by numerical methods, lack of resolution due to memory limitations in 3D simulations, arbitrary selection of initial amplitudes of perturbation and the point where the jet is perturbed. Regarding the linear

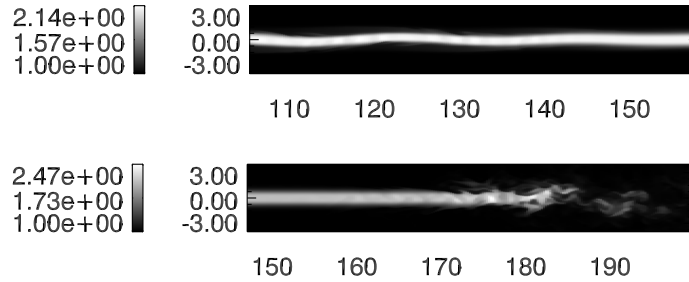


Figure 4.6: Map of Lorentz factor distribution of a portion of the jet at a time before disruption, where a large amplitude wave is apparent (top panel, $t = 320 R_j/c$) and at the last frame (bottom panel, $t = 1097 R_j/c$). Coordinates are in jet radii. Note that the vertical scale size is increased by a factor of 4 for the sake of clarity.

analysis, uncertainties in the calculation of the physical parameters from the characteristic wavelengths (see below) are also to be considered as a source of error.

In the following paragraph we study possible sources of inaccuracy in the approximations of linear analysis. Hardee et al. (1998) and Hardee (2000) present a stability analysis using parameters from simulations by Duncan and Hughes (1994). They solve the dispersion relation for the models and compare results with found wavelengths in the simulations. Using the parameters they give, and in order to check the validity of the method, we compared wavelengths obtained from equations (4.1) and (4.2) with those given by the solved dispersion relation. We give those values in Tables 4.5 and 4.6. Relevant parameters from those simulations are given in Table 4.4. Simulations A, B and C present different parameters from Hardee et al. (1998) to Hardee (2000), which was pointed out in Rosen et al. (1999) as an error. In the case of simulation A, the change was very small (from $\gamma = 2.55$ to $\gamma = 2.5$), but in cases B and C we used the changed values in order to compare with Hardee (2000) for figures in Table 4.6. In the case of Hardee et al. (1998) we use the *wrong* values due to the fact that their analysis was done for those parameters. There are differences between values predicted by the approximations and those computed by solving the dispersion relation. They are larger for longest unstable wavelength and also tend to grow for larger Lorentz factors.

Simulation	β_j	γ_j	M_j	M_a
A	0.3	1.05	5.77	3.
E	0.92	2.55	3.34	3.
B	0.9835	5.52	1.88	1.8
C	0.9976	14.35	1.3	1.3
D	0.9950	10.00	1.8	1.8
B (H00)	0.9798	5.00	1.88	1.5
C (H00)	0.9950	10.0	1.3	1.3

Table 4.4: Relevant parameters (to be used in equations (4.1) and (4.2)) from Hardee et al. (1998) and Harde (2000). (H00) stands for the parameters of simulations B and C in Hardee (2000).

Simulation	$\lambda_{0,1}^l$	$\lambda_{0,1}^*$	$\lambda_{0,2}^l$	$\lambda_{0,2}^*$	$\lambda_{0,3}^l$	$\lambda_{0,3}^*$
A	15.9/11.5	5.0/3.3	6.8/4.8	2.8/1.7	4.3/3.0	1.9/1.2
E	21.7/15.5	5.7/3.9	9.3/6.6	3.2/2.0	5.9/4.1	2.2/1.3
B	23.4/11.2	3.8/2.3	10.0/4.6	2.1/1.2	6.4/2.9	1.5/0.8
C	31.8/7.7	3.0/1.2	13.6/3.2	1.7/0.6	8.7/-	1.2/-
D	39.9/18.7	4.1/2.4	17.1/8.0	2.3/1.3	10.9/-	1.6/-

Table 4.5: Comparison of characteristic wavelengths of pinching surface and first three body modes, computed from equations (4.1) and (4.2) (first number), and those taken from the dispersion relation solution (second number) in Hardee et al. (1998). All wavelengths are in R_j units.

We observe that in the case of larger Mach number jet (A), the error is smaller, and this points towards the large Mach number approximation used in order to derive equations (4.1) and (4.2) as a source of error in the case of jets with smaller values of M_j .

Another limitation of this method is the fact that magnetic fields may influence the dynamics of the parsec scale jet (Asada et al. 2002), and they have not been considered neither in the linear analysis, nor in the simulations.

Disruption of the jet in the simulation is in contradiction with the fact that we can observe it in much larger scales, which we could not if it was mass-loaded as we observe in the simulation. Therefore, a stabilizing factor is needed in order to explain the jet in 3C273. A thicker shear layer, the

Simulation	$\lambda_{1,0}^*$	$\lambda_{1,1}^l$	$\lambda_{1,1}^*$	$\lambda_{2,0}^*$	$\lambda_{2,1}^l$	$\lambda_{2,1}^*$
A	8.4/7.2	9.6/6.7	3.6/2.3	5.0/5.9	6.8/4.9	2.8/1.9
B	5.7/3.9	12.7/4.9	2.4/1.6	3.4/2.7	9.1/3.5	1.9/1.4
C	5.0/1.9	12.7/3.4	2.2/0.6	3.0/1.7	9.1/2.3	1.7/0.5

Table 4.6: Comparison of characteristic wavelengths of helical and elliptic surface and first body modes, computed from equations (4.1) and (4.2) (first number), and those taken from the dispersion relation solution (second number) in Hardee et al. (2000). All wavelengths are in R_j units.

inclusion of the superluminal components in the simulations, as faster jets are much more stable against Kelvin-Helmholtz instabilities (see Perucho et al. 2004b), a decreasing density atmosphere, which must be the case as can be derived from the outward dimming of the jet in the parsec scale, or a stabilizing configuration of magnetic field should be taken into account if the observations of the jet in 3C273 are to be understood.

4.1.4 Simulation 3C273-B

Initial setup

Basing on results of Simulation 3C273-A, we have set up a new simulation, which includes fast (*superluminal*) components and a precession at the inlet. Again, we start with a steady jet with the Lorentz factor $\gamma = 2.1$, the density contrast $\eta = 0.023$, the perfect gas equation of state (with the adiabatic exponent $\Gamma = 4/3$), and the sound speeds $c_{s,j} = 0.53c$ in the jet and $c_{s,a} = 0.08c$ in the external medium. We have demonstrated before that we do not need a large grid, if patterns move fast and relativistic effects *elongate* structures. Therefore, the numerical grid for this simulation covers $30 R_j$ (axial, see below for explanation) times $6 R_j$ (transversal).

The resolution of the grid is 16 cells/ R_j in the transversal direction and 32 cells/ R_j in the direction of the flow. A shear with $m = 8$ ($\sim 0.6 R_j$ thick) in equations (2.42) and (2.43) is included in the initial rest mass density and axial velocity profiles to keep the numerical stability of the initial jet. An extended grid is introduced in the transverse direction, with 36 cells reaching out to $15 R_j$ on each side of the jet (increasing the cell size by 7.7% from one cell to the next), and also in the axial direction, $15 R_j$ long, and using 192

cells. Boundary conditions are formulated for the injection at the inlet, and for the outflow far (transversally) from the axis and in the (axial) end of the grid. The precession of the jet is included in transversal velocities as follows:

$$v_{\perp} = A_0 v_z \sin(\omega t) \quad (4.5)$$

where v_{\perp} is the transversal speed, v_z the injection axial velocity, t is time, $A_0 = 6.83 \cdot 10^{-3} c$ is the initial amplitude, calculated from the opening angle given by LZ01 (1.5° , which has to be deprojected from the viewing angle $\sin(15^{\circ})$, giving the true opening angle of 0.4°), and $\omega \sim 1.01 c/R_j$ is the frequency calculated from the precession period of ~ 15 yrs estimated by Abraham et al. (1996).

We have also included a periodic injection of faster components with Lorentz factor $\gamma_c = 5$ and a periodicity of $1 \text{ yr} = 0.4 c/R_j$ as measured by Babadzhanyants and Belokon (1993), and associated with ballistic components reported by Abraham et al. (1996) and Lobanov et al. (2000). These components are treated as shells of diameter $0.5 R_j$ ejected, in a centered position with respect to the axis, during the estimated duration of the disk activity $0.066 c/R_j \sim 2$ months. The axial size of the grid is also related with these components. We take into account that the wavelength induced by the precession of the faster components is $\lambda_c \sim P v_c$, being P the period and v_c is the injection velocity of the components. This gives $\lambda_c \sim 6 R_j$, and we have chosen the grid of $5 \lambda_c$ to allow the wave to become apparent. The simulation has lasted for a time of $70 R_j/c$ (i.e., more than two light crossing times of the grid).

Discussion

In Figures 4.7 and 4.8, we show longitudinal cuts of pressure perturbation, where we can see the effect of precession and injected components. Close to the injection point, we observe that, at $r \sim 0.0625 R_j$ (Fig. 4.7), the symmetric structure of fast components dominates the structures. It has a wavelength $\sim 0.4 R_j$, similar to the period of ejection of ballistic components ($0.4 R_j/c$) moving at a speed v_c . In the jet boundary (Fig. 4.8) the most pronounced structure is the typical antisymmetric pattern of helical motion induced by the precession ($\lambda \sim 4 R_j$). After $3 - 4 R_j$, the effect of the presence of the fast components is also visible in the jet boundaries. Further downstream,

$\lambda^{sim} (R_j)$	$\lambda_{v_w=0.88c}^{sim}(\text{mas})$	$\lambda_{v_w=0.94c}^{sim}(\text{mas})$	$\lambda_{v_w=0.98c}^{sim}(\text{mas})$
0.4 (symmetric)	0.23	0.37	0.62
4 (antisymmetric)	2.27	3.7	6.2

Table 4.7: First column gives the observed wavelengths in the simulation, and the last three columns give this wavelengths as observed depending on the wave speed. We have used, for the wave speed, the underlying flow speed (second column), the maximum speed from the components (third column), and the corresponding speed to injection Lorentz factor ($\gamma = 5.$, fourth column).

longer structures are apparent which can be associated with the precession¹. This effect is modulated by short wavelengths close to the axis. Amplitudes of the short waves induced by fast components decrease outwards (Fig. 4.7), as the components slow down gradually (see also Fig. 4.10). This slowing down of the components may be caused either by the interaction with the background flow, or by a sideways and longitudinal expansion. It can also be a result of numerical diffusion due to the limited resolution of the simulation run. Contrary to the behavior of the shorter wavelength modes, the helical waves increase their amplitude as they move outwards.

The downstream evolution of the jet structure is also visible in Fig. 4.9 showing a surface plot for the Lorentz factor 2.5. At smaller distances (up to $z \sim 10 - 15 R_j$), the periodicity induced by the symmetric components dominates the jet structure, but further downstream the components begin to interact with each other, generating a semi-continuous structure that is dominated by the helical motion induced by the precession. The consequence of the deceleration of the fast components is illustrated in Fig. 4.10, where the components slowing down from the initial Lorentz factor of 3 are observed to disappear downstream.

In Table 4.7 we show the observed wavelengths depending on the pattern speed. We note that the simulated wavelength obtained from the precession is smaller than the one calculated theoretically from the advance speed of components ($4 R_j$ versus $6 R_j$). One of the reasons for this could be that the advance speed is overestimated, as indicated by the fact that injected

¹We know that the structure of antisymmetric waves is such that the values of the perturbations on both sides, but close to the axis, are very similar. This is the reason for dotted and dashed lines in Figure 4.7 being close despite it is the helical mode which dominates the pressure perturbations.

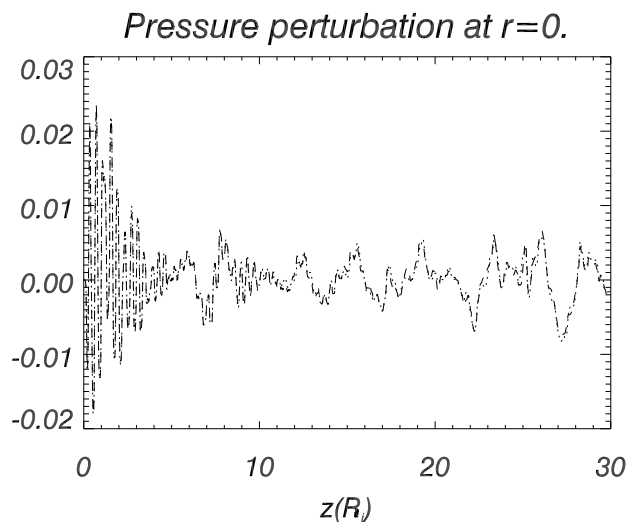


Figure 4.7: Longitudinal cuts of pressure perturbation at $r \sim 0.0625 R_j$ in symmetric positions (dashed and dotted lines) with respect to the jet axis at $t = 40 R_j/c$.

components do not propagate at $\gamma = 5$, but at $\gamma \leq 3$. However, this difference in velocity does not cover completely the difference found in the wavelengths. We may also have overestimated the wavelength by considering the ballistic motion of components and ignoring, to some extent, the observed dissipation of the faster components in the flow that suggests that the components are likely to move non-ballistically. This fact favors the conclusion from LZ01 that the observed structure is generated in the slower, underlying flow. This is evident, if we take into account that slower flows generate longer wavelengths. An alternative to this explanation requires the components to remain ballistic throughout the entire observed region.

The latter explanation can be tested against the observed wavelengths calculated in Table 4.7. It is clear that the observed wavelength of precession ($18 \text{ mas} \sim 54 R_j$) cannot be recovered even by extremely fast components ($v_w = c$ gives 10 mas at this viewing angle). The key here is the relativistic/projection factor $\sin \theta / (1 - v_w \cos \theta)$ ($= \beta_{app} / \beta$, the apparent speed divided by the intrinsic speed) in the transformation from λ^{sim} to λ^{obs} , see Eq. (4.4).

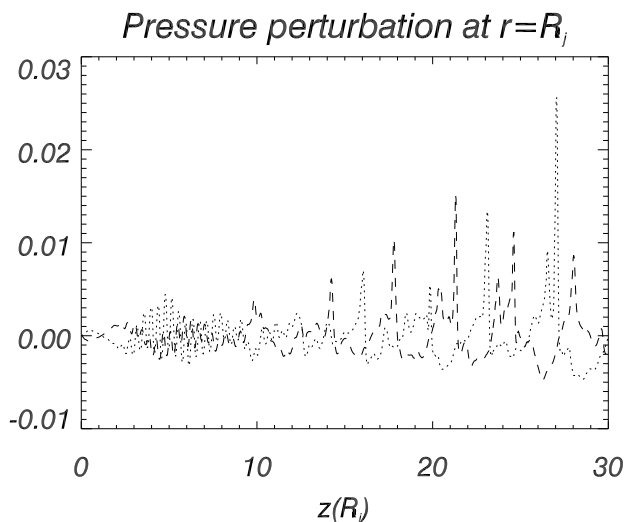
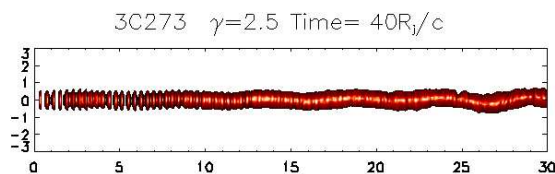
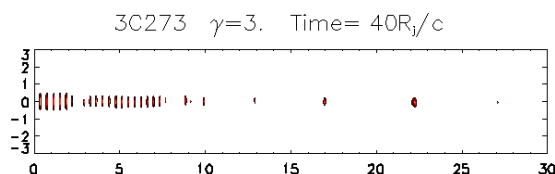


Figure 4.8: Longitudinal cuts of pressure perturbation at $r \sim R_j$ in symmetric positions (dashed and dotted lines) with respect to the jet axis at $t = 40 R_j/c$.

This term is always smaller than the Lorentz factor of the flow ($\leq \gamma$, see e.g. Körding and Falcke 2001 and Fig. C.1 in Appendix C). If we consider the mean angular velocity of $0.93 h^{-1} \text{mas/yr}$ (Abraham et al. 1996), with $h = 0.7$, the apparent speed is $\beta_{app} \sim 10$. This apparent speed cannot be reconciled with a viewing angle of 15° , and it requires the Lorentz factor of $\gamma = 10$ if the viewing angle is 10° . With the relativistic and geometric effects implied by these angle and velocity, we could convert our measured $4 R_j$ wavelength in the simulation into the observed 18 mas one.

On the other hand, considering that the helical pattern is generated by $\gamma = 5$ flow observed at 15° , we would need to measure $\lambda \sim 11 R_j$ in the simulation in order to recover the observed wavelength. This wavelength contradicts the wavelength computed for the ballistic motion ($6 R_j$). Thus, either the period is longer (almost twice than that given in previous works), or components are faster and the angle to the line of sight is slightly smaller than the commonly assumed ones.

Another question addressed by this simulation is whether the periodic injection of fast components could generate smaller structures observed by LZ01

Figure 4.9: Surface plot of Lorentz factor $\gamma = 2.5$ at $t = 40 R_j/c$.Figure 4.10: Surface plot of Lorentz factor $\gamma = 3.0$ at $t = 40 R_j/c$.

(2 and 4 mas modes), where these wavelengths are identified with the elliptical modes of Kelvin-Helmholtz instability. In our simulation, the fast components generate pinching modes, although this is simply due to their symmetric nature. Again, we find that the structures generated in the simulation are smaller compared to those observed. However, in this case, the simulated components move slower ($\gamma \leq 3$, see Fig. 4.10) than the observed ones ($\gamma \sim 5 - 10$). Moreover, the simulated components here have the same density as the background flow (what could be a cause for slowing down), whereas if we understand them as the result of a strong accretion activity, they should be mass loaded, and thus be denser than the underlying flow. Fine tuning of these ingredients, together with varying the injection period, could give the correct wavelengths. We find that, in order to produce a 4 mas mode, we need the Lorentz factor $\gamma \sim 30$, whereas $\gamma \sim 15$ is required to explain the 2 mas structure, if we keep the 1 yr period. Adopting the longest measured period of the ejections of 1.7 yrs (Abraham and Romero 1999), these values would be reduced to $\gamma \sim 17$ and $\gamma \sim 8.5$, respectively. The same authors gave a periodicity in the injection Lorentz factor of about 4 yrs; if we consider this period as the generator of short modes, $\gamma \sim 7.5$ and $\gamma \sim 4.0$ could explain those structures. The latter values agree well with the Lorentz factors inferred from the observed kinematics of the jet. This means that the wavelengths should be associated only with the ejections of the strongest, and fastest, components occurring

roughly once every 4 years.

4.1.5 Conclusions

We have performed two simulations with different initial setups in order to study the physical processes generating the observed structures in the parsec-scale radio jet in the quasar 3C 273. In the Simulation 3C273-A, we have included a general set of helical and elliptic perturbations in a long jet with the basic physical parameters adopted from LZ01. In the Simulation 3C273-B, we have used a shorter jet with the same physical parameters and have included a precession and an injection of fast components. 3C273-A was aimed to generate structures with wavelengths similar to those measured by LZ01 from the growth of Kelvin-Helmholtz perturbations. 3C273-B was thought to generate the same structures by combining the ejection of *superluminal* components and the inclusion of a precession with relativistic effects, with the periodicities reported in Babadzhanyants and Belokon (1993).

We have proven that the structures found in a jet with the physical properties of the underlying flow given in LZ01, and perturbed with elliptical and helical modes (3C273-A), are of the same order in size as those observed, if the relativistic propagation effects of the waves are taken into account. We find that the wave speeds found in this work differ from those derived from the linear analysis, and we do not find a unique combination of parameters which explain observed structures. We show however that wavelengths similar to the observed ones are found for given combinations of the simulated wavelengths and the wave speeds (see Table 4.3). Regarding the long-term stability of the flow, the jet in simulation 3C273-A is disrupted, contrary to the observations tracing the jet in 3C273 up to 60 kpc away from the source (compared with 170 pc in this simulation). The reasons for this difference may be found in the conjunction of several factors. 1) Magnetic fields have not been taken into account either in the linear analysis, or in the numerical simulation - and it should be noted that the magnetic fields may be dynamically important at parsec scales. 2) We only simulate the underlying flow, without considering the superluminal components. 3) inaccuracies in the linear analysis approximations can lead to differences in physical parameters derived. 4) Differential rotation of the jet, shear layer thickness, and a decreasing density external medium (along with jet expansion; see Hardee 1982, 1987, and Hardee et al. 2005) could also play a central role. 5) Arbitrary initial amplitudes of perturbations were chosen for the simulation, so we could have included too large

perturbations. The combination of these factors could well change the picture of the evolution of the jet in terms of its stability properties. The effects of the rotation and magnetic fields on the stability of jets remain unclear, since no systematic study has been performed up to now.

In the simulation 3C273-B, we have shown that, in order to explain the 18 mas wavelength in terms of precession, either different periodicities would be needed (unless this mode is induced by very fast components observed at an angle $\theta < 15^\circ$), or the modes observed are acting on the slower, underlying flow, as concluded in LZ01. In the latter picture, the superluminal components would just move ballistically through the helical pattern drawn by the underlying flow. We have also seen that fast components could generate the shorter wavelengths observed in LZ01 (2 mas and 4 mas) if a proper combination of the velocities and injection periodicities is used. In this sense, numerical simulations of this kind may be used to constrain the basic parameters of the flow such as the viewing angle and the component speed. The inclusion of magnetic fields, differential rotation and an atmosphere with a decreasing density could help reconciling the simulations with the observed structures. In this way, for example, an increase of the jet radius due to decreasing external pressure could cause a downstream enlargement of wavelengths.

4.2 Kpc scale jets. Numerical simulations on 3C 31

4.2.1 Introduction

Laing and Bridle (2002a,b; LB02a,b from now on) presented a model which accurately described kinematic and dynamically the jets in the FRI radio-galaxy 3C 31, mapping the emission and magnetic fields of the jets. In this section, we present the results from a simulation in which input is taken from those models. Our aim is to compare the results from the simulation with those from observations and modelling.

In LB02a, the authors fit observed brightness and polarization distributions by modelling the velocity, synchrotron emissivity and ordering of the magnetic field. They assume that jet and counter-jet are identical, antiparallel, axisymmetric and stationary, and that the differences between them result from relativistic aberration. Thus, they use Doppler boosting as a constraint for their model, along with the rotation of the line of sight relative to the magnetic field structure between emitted and observed frames. They focus on the inner part of jets and split it in three parts (see Fig. 4.11): the inner

(from 0 to 1.1 kpc, or from 0 to 2.5 arcsec), the flaring (from 1.1 to 3.5 kpc, or from 2.5 to 8.3 arcsec) and the outer (from 3.5 to 12 kpc, or from 8.3 to 28.3 arcsec) regions. The linear distances are calculated considering Hubble constant $H_0 = 70 \text{ km s}^{-1} \text{ Mpc}^{-1}$ and taking the redshift of the parent galaxy of 3C 31 (NGC 383, $z = 0.0169$).

In LB02b, they present a dynamical model based on the results of LB02a and estimates from external pressure and density profiles from *Chandra* (Hardcastle et al. 2002), applying conservation laws and assuming that the jets are in pressure equilibrium with the external medium at large distances from the nucleus, and that the momentum flux is $\Pi = \Phi/c$, where Φ is the momentum flux and a velocity profile. The model is *quasi-one-dimensional*, as, although they consider the widening of the jet, they only take the axial velocities for their analysis.

They conclude that the jets are overpressured at the beginning of the flaring region; in this part of the jet they find local minima in the pressure and density and maxima in the Mach number and entrainment rate. At the end of the flaring region the jets are slightly underpressured with respect to the ambient medium and recollimate. Changes in the outer region are smooth, with almost constant density and monotonically increasing entrainment rate, and Mach numbers are always $\sim 1 - 2$ in the outer region. They derive a pair plasma ($e^- - e^+$) composition, and require barionic mass load from the galactic medium in order to explain the deceleration of the flow, though in this point they suggest that stellar mass is the most important source of loaded material at the flaring region. In order to perform the simulation,

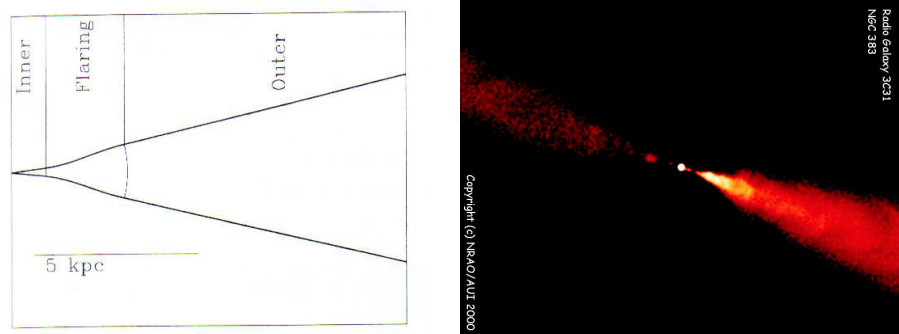


Figure 4.11: Schematic plot of the jet 3C31 as shown in Laing and Bridle (2002a), compared with an image of the inner part of the source.

we have implemented Sygne's equation of state for relativistic gases, with the routines used in the simulations of Scheck et al. (2002) and have introduced the appropriate changes in the code in order to include the new variables needed by this approach (e.g., leptonic and barionic density, which have to be evolved along with total density) and a stationary decreasing density atmosphere. The latter is accomplished by introducing source terms in the momentum equations which compensate initial pressure gradients in the radial and axial directions.

The equation of state

The equation of state of a relativistic perfect gas can be written in the form (Synge 1957, see also Falle and Komissarov 1996):

$$w = \sum_{I=1}^N n_I m_I G(\xi_I), \quad (4.6)$$

$$p = \sum_{I=1}^N n_I m_I \xi_I^{-1}, \quad (4.7)$$

where, $w = \rho h$, n_I is the number density of a given family of particles with mass m_I ,

$$\xi_I = \frac{m_I}{k_B T}, \quad (4.8)$$

$$G(\xi) = \frac{K_2(\xi)}{K_3(\xi)} = \frac{K_1(\xi)}{K_2(\xi)} + \frac{4}{\xi}. \quad (4.9)$$

In the latter equations k_B is the Boltzmann constant, T the temperature and $K_\nu(\xi)$ are the modified Bessel functions:

$$K_\nu(\xi) = \int_0^\infty \exp(-\xi \cosh \theta) \cosh \nu \theta d\theta. \quad (4.10)$$

The adiabatic exponent is derived from the definition of sound speed:

$$a^2 = \left(\frac{\partial p}{\partial \varepsilon} \right)_s, \quad (4.11)$$

and turns out to be:

$$\Gamma = \frac{\sum_{I=1}^N n_I G'(\xi_I) \xi_I^2}{\sum_{I=1}^N n_I (G'(\xi_I) \xi_I^2 + 1)}. \quad (4.12)$$

In our case, we deal with two species of particles: leptons (electrons and positrons) and barions (protons). We define the leptonic number as:

$$X_l = \frac{\rho_{e^-} + \rho_{e^+}}{\rho}, \quad (4.13)$$

so the number of protons will be $X_p = 1 - X_l$, e.g., in a neutral gas composed by hydrogen $X_l = m_e/(m_e + m_p) \sim 1/1837$. The pressure of a mixture of these species is

$$P = \frac{\rho}{m_{eff}} k_B T, \quad (4.14)$$

where

$$m_{eff} = \left[\frac{X_l}{m_e} + \frac{X_p}{m_p} \right]^{-1}. \quad (4.15)$$

In order to obtain the adiabatic exponent, we have to take

$$\xi_l = \frac{m_e}{k_B T}, \quad \xi_p = \frac{m_p}{k_B T}, \quad \xi_{eff} = \frac{m_{eff}}{k_B T}, \quad (4.16)$$

and then, from Eq. (4.12):

$$\Gamma = 1 - \frac{1}{(X_l G'(\xi_l) \xi_l^2 / m_e + X_p G'(\xi_p) \xi_p^2 / m_p) m_{eff} + 1}, \quad (4.17)$$

The temperature of the gas is a function of internal energy, density and leptonic number (X_l): $T = T(\varepsilon, \rho, X_l)$. The Newton-Raphson method is used in each cell in order to look for the physical roots of a function $f(T) = \varepsilon(\rho, X_l, T) - \varepsilon_0$, where ε_0 is the internal energy, derived directly from the conserved variables as explained in Appendix A, in particular in equations A.21 and A.22. Also, from Eq. 4.6, we know that $\varepsilon = X_l G(\xi_l) + X_p G(\xi_p) - P/\rho - 1$. Thus:

$$f(T) = X_l G(\xi_l) + X_p G(\xi_p) - P/\rho - 1 - \varepsilon_0, \quad (4.18)$$

and its derivative:

$$f'(T) = k_B [X_l G'(\xi_l) \xi_l^2 / m_e + X_p G'(\xi_p) \xi_p^2 / m_p + 1/m_{eff}]. \quad (4.19)$$

Once we have the temperature in the cell, we can compute the adiabatic exponent, from Eq. 4.17, and the sound speed. Scheck et al. (2002) estimated that the iterative process takes 50 % more computational time than if the one component, ideal gas equation of state was used, due to the presence of Bessel functions in the equation of state.

Component	Central density	Form factor	Core radius	Temperature
Galaxy	$n_c = 1.8 \cdot 10^5 \text{m}^{-3}$	$\beta_{atm,c} = 0.73$	$r_c = 1.2 \text{ kpc}$	$T_c = 4.9 \cdot 10^6 \text{ K}$
Group	$n_g = 1.9 \cdot 10^3 \text{m}^{-3}$	$\beta_{atm,g} = 0.38$	$r_g = 52 \text{ kpc}$	$T_g = 1.7 \cdot 10^7 \text{ K}$

Table 4.8: Table 1 in LB02b, where the ambient parameters are given (see text).

4.2.2 Setup for the numerical simulation

The medium in which the jet is injected consists on a decreasing density atmosphere composed by hydrogen; LB02b suggest a composition with 74% hydrogen, but this treatment would require the inclusion of new populations of particles (in order to account for the remaining 26%) in the code, involving longer computational time, so that we discarded this option. The profile for the number density of such a medium is (Hardcastle et al. 2002):

$$n_{ext}(r) = n_c \left(1 + \frac{r^2}{r_c^2}\right)^{-3\beta_{atm,c}/2} + n_g \left(1 + \frac{r^2}{r_g^2}\right)^{-3\beta_{atm,g}/2}, \quad (4.20)$$

where r is the spherical radial coordinate, n_c and n_g are the core densities of the galaxy and the surrounding group, with r_c and r_g the radii of those cores, and $\beta_{atm,c}$ and $\beta_{atm,g}$ are the exponents giving the profile for each media. Temperature profile is:

$$\begin{aligned} T &= T_c + (T_g - T_c) \frac{r}{r_m} & (r < r_m) \\ T &= T_g & (r \geq r_m), \end{aligned} \quad (4.21)$$

with $r_m = 7.8 \text{ kpc}$. Pressure is derived from the following equation of state:

$$P_{ext} = \frac{k_B T}{\mu X} n_{ext}(r), \quad (4.22)$$

where μ is the mass per particle in a.m.u. ($\mu = 0.5$ in our case, versus 0.6 in LB02b), and X is the abundance of hydrogen by mass ($X = 1$ here, versus 0.74 in LB02b). In Table 4.8 we reproduce Table 1 in LB02b, where the parameters for the equations above are listed. The atmosphere is kept in equilibrium with the inclusion of source terms which compensate pressure gradients among cells.

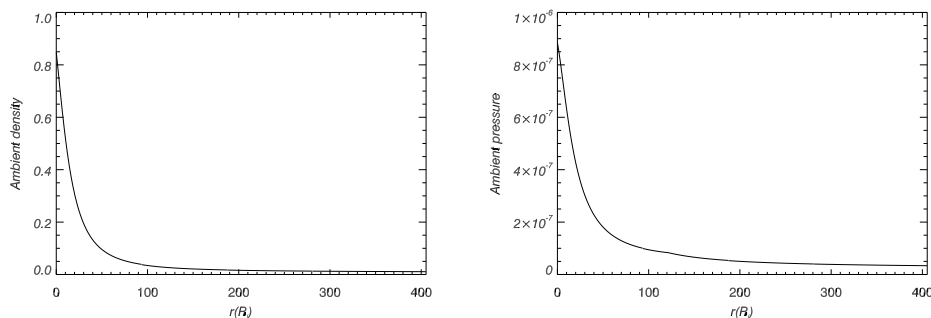


Figure 4.12: Initial profiles of atmospheric rest mass density (left) and pressure (right).

In the simulation, the appropriate unit transformations are performed, as the parameters are given in *cgs* units, but the code works with the same units as in the rest of simulations presented in this thesis: R_j , c and $\rho_{a,c}$.

The simulation was performed in two dimensions and cylindrical coordinates. The grid is 2880×1800 cells, with an axial resolution of $8 \text{ cells}/R_j$ in the axial direction up to $300 R_j$ and an extended grid (up to $450 R_j$) with outflow boundary conditions in the same direction, and $16 \text{ cells}/R_j$ in the radial direction up to $100 R_j$, with an extended grid with increasing cell size (with factor ~ 1.017) and outflow conditions far from the jet ($200 R_j$). We consider a symmetric jet in cylindrical coordinates, so reflection boundary conditions are taken at the jet axis.

Injection of the jet in the atmosphere is done at $r = 500 \text{ pc}$, the point where LB02b start their analysis. The radius of the jet at that point is calculated from the opening angle 6.7° given for the jet in LB02a ($R_j = 60 \text{ pc}$). The uniform grid is then $17.5 \text{ kpc} \times 6 \text{ kpc}$, and, with the extended grid, $26.25 \text{ kpc} \times 12 \text{ kpc}$.

The jet is injected with a speed $v_j = 0.87 c$ ($\gamma_j \sim 2$), internal relativistic Mach number $M_j = 2.5$, temperature $T_j = 4.1 \cdot 10^9 \text{ K}$, density ratio with the external medium $\eta = 1 \cdot 10^{-5}$, purely leptonic composition ($X_l = 1.0$), and overpressured by a factor ~ 8 with respect to the ambient medium. In Table 4.9 we give the complete list of parameters. The parameters given for the ambient medium in the injection are calculated for $r = 500 \text{ pc}$ (this is the reason for differences between Tables 4.8 and 4.9). The numbers in this table

give an energy flux of $\Phi \sim 10^{37}$ W, calculated as given in LB02b, which is very close to the value given in that paper ($\Phi = 1.1 \cdot 10^{37}$ W), the difference being due to slight changes in variables considered.

Our purpose is to inject the jet and analyze its evolution through the atmosphere, but, most importantly, to compare the last frames, when the head of the jet has crossed the whole grid and is thus far from the modelled region in LB02b, with results in that paper and observations of 3C 31 (e.g., those in LB02a).

Velocity (v_j)	$0.87 c$
Mach number (M_j)	2.5
Temperature (T_j , jet)	$4.1 \cdot 10^9 \text{K}$
Temperature (T_c , ambient ¹)	$5.7 \cdot 10^6 \text{K}$
Temperature (T_g , ambient ²)	$1.7 \cdot 10^7 \text{K}$
Density (ρ_j , jet)	$3 \cdot 10^{-30} \text{g/cm}^3$
Density ($\rho_{a,c}$, ambient ¹)	$3 \cdot 10^{-25} \text{g/cm}^3$
Density ratio (η)	10^{-5}
Leptonic number (X_l , jet)	1.0
Specific int. energy (ε_j , jet)	$1.54 c^2$
Specific int. energy ($\varepsilon_{a,c}$, ambient ¹)	$1.57 \cdot 10^{-6} c^2$
Specific int. energy ($\varepsilon_{a,g}$, ambient ²)	$4.69 \cdot 10^{-6} c^2$
Pressure (P_j , jet)	$6.91 \cdot 10^{-6} \rho_{a,c} c^2$
Pressure ($P_{a,c}$, ambient ¹)	$8.84 \cdot 10^{-7} \rho_{a,c} c^2$
Pressure ($P_{a,g}$, ambient ²)	$3.07 \cdot 10^{-8} \rho_{a,c} c^2$
Pressure ratio ($P_j/P_{a,c}$)	7.8
Adiabatic exponent (Γ_j , jet)	1.38
Adiabatic exponent (Γ_a , ambient)	1.66
1D velocity estimation (v_h^{1d})	$9.9 \cdot 10^{-3} c$
Time unit ($1 R_j/c$)	$60 \text{ pc}/c \sim 195 \text{ yrs}$

Table 4.9: Parameters in the simulation. Different units are used in order to make comparisons with other works easier (see text). ¹ and ² stand for values at the injection and most external points in the grid, respectively, for the ambient medium.

In relation with the long term stability properties of the jet, its Mach number and Lorentz factor place it in the UST1 (see Chapter 3) region, coinciding with our prediction of FRI morphology for this kind of jet.

Regarding the parameters taken in simulations presented in Scheck et al. (2002), with which ours shares many similarities, their definition of L_{kin} (kinetic luminosity), coincides with that given for energy flux in LB02b, so we can compare both values. In our case, $L_{kin} \sim 10^{44}$ erg/s, typical of a FRI source, with $L_{kin} \sim 10^{46}$ erg/s fixed by them as that of an FRII.

The one-dimensional velocity estimation given in Table 4.9 stands for the theoretical advance velocity of the jet, computed using the equation derived in Martí et al. (1997) for a pressure-matched jet propagating in one dimension, i.e., without sideways expansion:

$$v_h^{1d} = \frac{\sqrt{\eta_R}}{\sqrt{\eta_R + 1}} v_j, \quad (4.23)$$

where $\eta_R = \rho_j h_j \gamma_j^2 / (\rho_a h_a)$.

4.2.3 Results

At the time of writing this section, the simulation has still not finished. We expect that reaching the final results would take an extra time of about one month. However, we think that interesting partial conclusions can be extracted and we present them here. At this point, the simulation has been running for a time ~ 1130 hours ~ 47 days on eight processors in the SGI Altix computer CERCA, at the *Universitat de València*.

Evolution

In Figures 4.13-4.15 we present the evolution with time of several magnitudes up to time $\sim 19900 R_j/c \sim 3.9 \cdot 10^6$ yrs.

A jet propagating supersonically in an external medium generates a supersonic *bow shock*, which propagates through the ambient and encloses a *cavity* of shocked material. The jet propagates inside this cavity, its head forming a shock called *Mach disk*, and surrounded by a mixture of shocked ambient medium and *backflow* of jet material deflected at the Mach disk, which form the *cocoon*.

Bow shock position is selected at the point where the speed is larger than $10^{-4} c$ and jet radius is calculated using different tracers (see the caption of Fig. 4.15) as indicators. The pressure of the head of the bow-shock is taken as the first maximum in pressure, and the hot-spot pressure is computed with the mean of pressure in 10 cells behind the jet position. The velocity of the bow

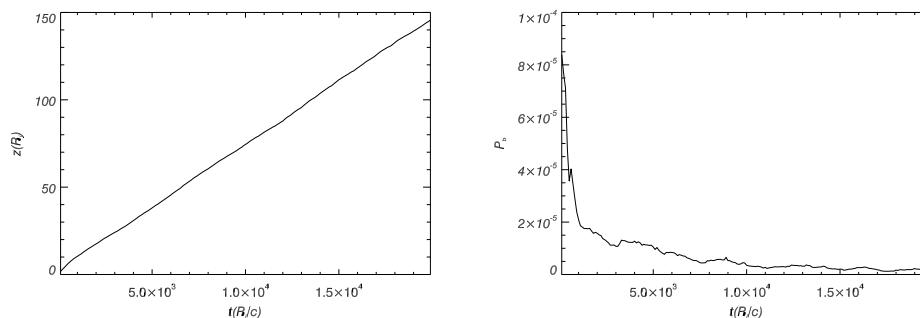


Figure 4.13: Left panel stands for bow shock position, and right panel for bow shock head pressure. See text.

shock is computed with the discretized derivative of position with respect to time at each instant, and Mach number is computed with that advance speed and the mean value of the sound speed in 16 cells ahead of the bow shock position. Bow shock pressure, velocity and Mach number have been smoothed using an IDL routine in order to avoid the peaked shape of rapid variations in those parameters.

In Figs. 4.13 and 4.14 we can see that the advance speed of the bow-shock is basically constant ($\sim 0.007c$), excepting for the initial acceleration and slight slowing down in the last part of the simulation. Advance velocity is close to the one-dimensional prediction in the origin, but it is smaller further downstream, as the jet starts spreading its momentum in a wider region and the one-dimensional approximation gets worse. The pressure behind the bow-shock presents a fast drop and then oscillates until the last frame presented here. Calculations performed for the jet head give very similar results to these found for the bow-shock, so we do not present them here. The Mach number of the shock decreases as it moves outwards due to the increase in the sound speed of the atmosphere and slight slowing down.

From bottom left panel in Figure 4.14 we can derive that the growth of the cavity is basically self-similar. This is confirmed in the bottom panels of Figure 4.15, where almost constant factor for the $L_{c,j}/R_{c,j}$ ratio (for cavity and jet) is observed in the last part of the simulation. Before reaching this plateau, the latter ratio is growing, which means that the cavity and the jet grow faster longitudinally than radially. This is due to propagation in a decreasing density

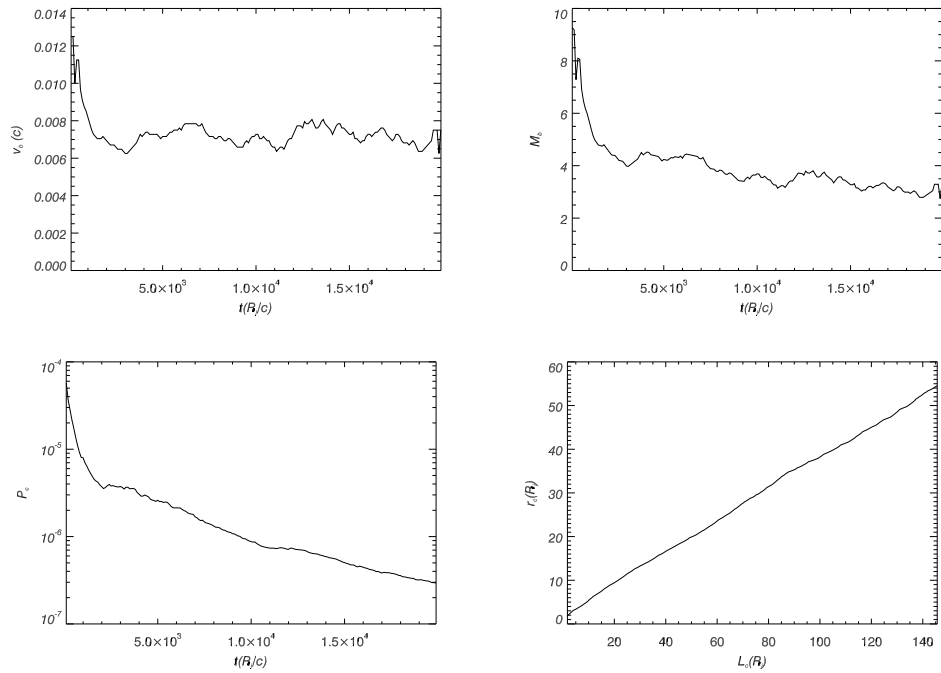


Figure 4.14: Top left panel stands for bow shock velocity, and top right panel for bow shock Mach number. Bottom panels stand for mean cavity pressure (left) and cavity radius versus its length (right). See text.

atmosphere, along with the fact that the jet is injected 500 pc from the origin along its axis (we remind the reader that the decrease in density is spherical and that we work in cylindrical coordinates).

In the case of the jet shape factor, we have plotted only values for two different tracers ($f = 0.5$ and $f = 0.9$), as smaller values have oscillatory behaviors. The plot of jet radius for different tracers (top right panel in Figure 4.15) illustrates the spreading of the jet and the formation of a thick shear layer. This shear layer is similar to that developed by UST1 models of Chapter 3, which were associated to FRI jets.

At the point in which we analyze the simulations, structures in the first part of the jet, which will be discussed in next paragraphs, have become quasi-stationary, so we can expect that they undergo only little changes until the

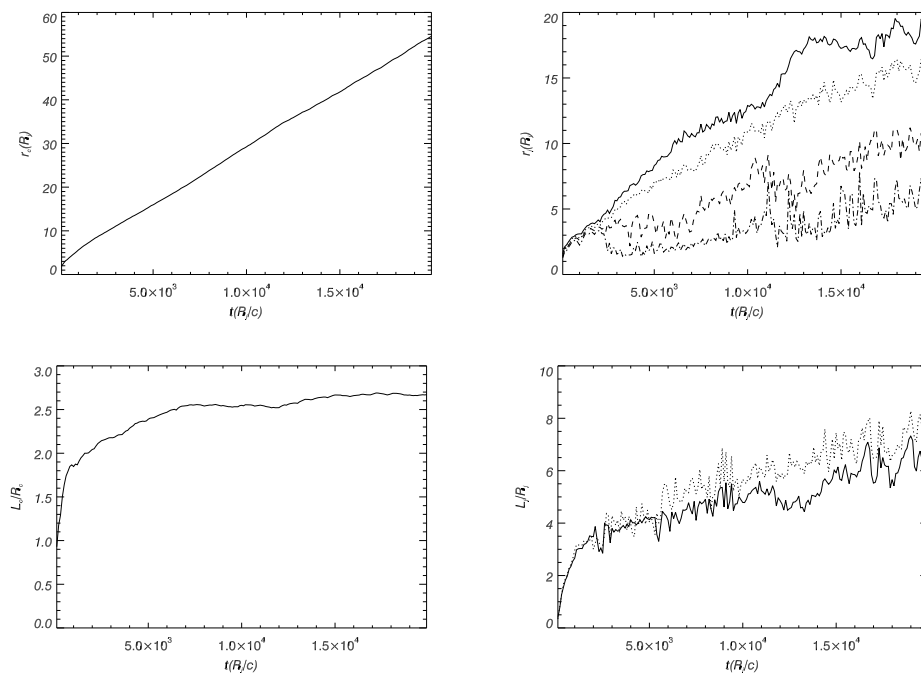


Figure 4.15: Top left panel stands for the mean cavity radius, and top right panel for the mean jet radius (different lines stand for the different criteria used to fix the jet head position: solid line is for tracer $f = 0.01$, dotted line for $f = 0.1$, dashed line for $f = 0.5$ and dash-dotted line for $f = 0.9$). Bottom panels stand for cavity shape (left) and jet shape (right). See text.

proper end of the simulation. We consider that the most important effects in the evolution of the jet will appear when the bow-shock becomes transonic ($M \sim 1$), as this will favor entrainment and slowing down of the flow.

Latest results

In Figures 4.16 and 4.17 we present panels for the logarithm of rest mass density, jet mass fraction (tracer), Lorentz factor and a variable we call *emission*, from the expression used in Hardee et al. (2005):

$$\epsilon_\nu \propto n_j^{1-2\alpha} p_j^{2\alpha} (B \sin \theta)^{1+\alpha} D^{2+\alpha}, \quad (4.24)$$

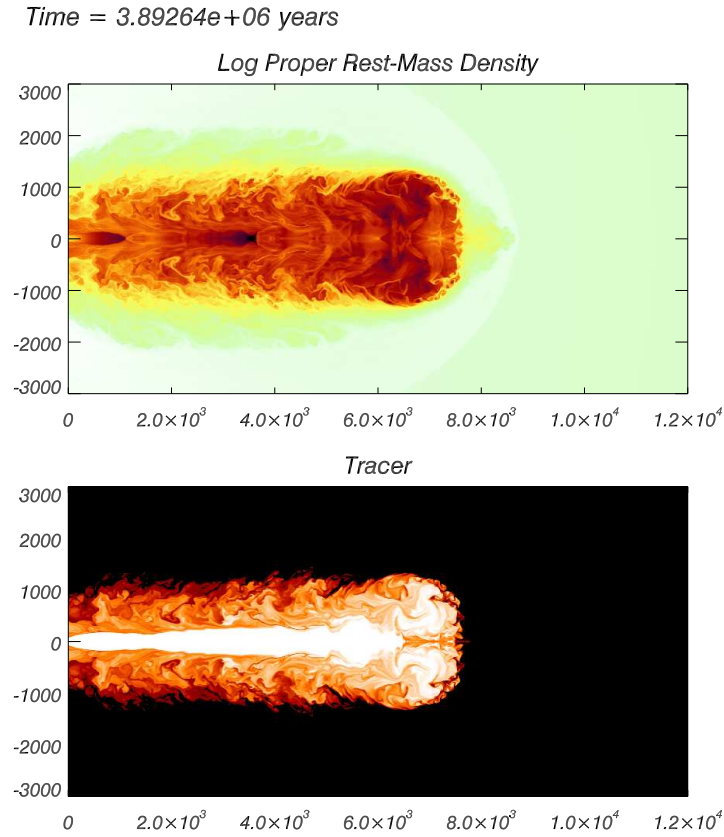


Figure 4.16: Logarithm of rest mass density (upper panel) and jet mass fraction (tracer, lower panel) at the last frame of the simulation in this work. Coordinates are in parsecs (from injection in the grid), rest mass density ranges from $\rho = 3.1 \cdot 10^{-8}$ to $\rho = 0.38$ in the units specified in the text, and jet mass fraction ranges between $f = 0$ and $f = 1$.

where n_j is the particle number density of the jet, p_j is the pressure, B is the magnetic field, θ is the viewing angle (52° , following LB02a), D is the Doppler factor and α is the spectral index (0.55, following LB02a). Hardee et al. (2005) assume that the magnetic field depends on the particle number density as $B \propto n_j^{2/3}$, considering a disordered field. From these assumptions,

our *emission* is:

$$\epsilon_\nu \propto f \rho^{5/3-2.2/3} P^{1.1} (\sin \theta)^{1.55} / (\gamma(1 - v_z \cos \theta))^{2.55}, \quad (4.25)$$

where we include the tracer f in order to account only for the jet material.

The morphological features observed in the panels are those of a typical jet (see, e.g., Martí et al. 1997): a bow-shock surrounding a cavity of shocked ambient gas, a cocoon composed by mixed jet and ambient matter, and the jet itself propagating inside.

In the upper panel of Figure 4.16 we can see the bow-shock which surrounds a cavity of shocked ambient material and the cocoon. In the lower panel we observe the cocoon, formed by mixed jet and ambient material, surrounding the jet. It is remarkable that tracer values different from one are not observed to reach the axis until distances close to the head of the jet. However, from previous snapshots at different times we have detected strong mass entrainment at about $z \sim 3.5 - 4.0 \text{ kpc}^2$, i.e., at $z' \sim 4.0 - 4.5 \text{ kpc}$ from the source. This suggests that the jet is pulsating due to the close presence of the head and is influenced by its accelerations and decelerations, clearly observed in the plot of bow-shock velocity versus time (Figure 4.14). We have thus to wait until the head has moved further away to extract some definite conclusions about the mass loading of the jet in this region.

In Figure 4.17 we can check that the jet keeps being relativistic up to $z \sim 3.5 - 4.0 \text{ kpc}$, where it undergoes a sudden slowing down, and only filaments of relativistic flow are present further downstream. Regarding the lower panel in Figure 4.17, we want to stress the high value of the variable *emission* at the injection, followed by dimming, sudden increase at $z' \sim 1.5 \text{ kpc}$, and a second dimming. Still, the morphology of the simulated jet is not close to the observed one, but, as pointed out before, the head of our computation is still not sufficiently far so as to extract any final conclusions in this aspect.

In Figures 4.18 and 4.19, we plot the profiles of variables on the jet axis. In Fig. 4.18 we see how, after a short distance where the variables remain constant, a strong adiabatic expansion motivates a fast decrease in all of them, up to $z' = 1.5 \text{ kpc}$ from the source. At the same time, in the plots for Lorentz factor and axial velocity of Fig. 4.19 (panels *b* and *c*), we observe a strong acceleration. When the jet becomes underpressured (see panel *b* in Fig. 4.18),

²Along this section and discussion of results we will use z as the coordinate referring to distances to the injection point in the grid and z' will stand for distances to the galactic source ($z' = z + 500 \text{ pc}$).

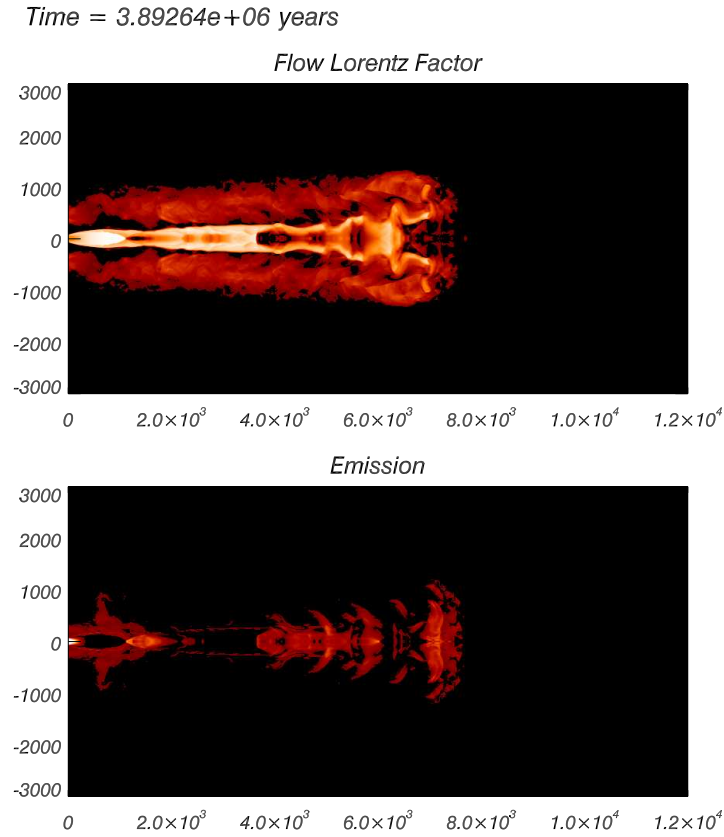


Figure 4.17: Lorentz factor (upper panel), and *emission* in arbitrary units (see text, lower panel) at the last frame of the simulation in this work. Coordinates are in parsecs (from injection in the grid), maximum Lorentz factor is $\gamma = 5.31$.

it recollimates, causing a sudden increase in the thermodynamical variables and emission and a strong slowing down of the jet. Again, the jet becomes overpressured and a slower expansion phase starts, with the consequent acceleration and decrease in pressure, density and emission. This process is not as fast and violent as the first, and it results in a second recollimation at $z' \sim 4.0 - 4.5$ kpc. This point coincides with the observed slowing of the jet in top panel of Figure 4.17, and with the place where we detect pulsation of

the jet, as strong mass entrainment, indicated by tracers significantly smaller than one, are observed at different times (not shown). Mass loading starting at that distance is also confirmed by panel *a* in Fig. 4.18, where a progressive increase in the rest mass density is apparent (see that the scale is logarithmic in that panel). We can understand the second expansion and recollimation of the jet as an oscillation around pressure equilibrium.

In Figure 4.20, we plot radially averaged variables, which have been weighted with the tracer, for those cells where matter is moving forwards, i.e., with axial velocity larger than zero, in order to have mean values for direct comparison with LB02b. From those plots we can extract the same conclusions as from axial profiles: adiabatic expansion causes acceleration and the jet becomes finally underpressured, what is followed by recollimation, slowing down and increase of rest mass density and pressure; the jet becomes again overpressured, so pressure oscillates around equilibrium. It seems that this equilibrium has almost been reached behind the head of the jet. Close to the bow-shock, the jet is overpressured due to the presence of the shock.

Successive expansions and recollimations discussed in the previous paragraphs produce the pinching of the jet, which is visible in Fig. 4.16. This pinching causes mass entrainment, as occurred in simulations of Chapter 2, although here the perturbation is already non-linear (e.g., the jet is highly overpressured with respect to the ambient in the injection). Linear analysis is, in this case, difficult, as the jet expands in a decreasing pressure/density atmosphere, so that the differential equation for the development of perturbations becomes very complex. We have derived this equation, which should be solved in order to obtain the growing perturbations (see Appendix D).

4.2.4 Discussion and Conclusions

In this section, we have presented the status on a simulation of the jets in the radiogalaxy 3C 31, based on the models in LB02a,b. Several implementations have been performed in the code in order to perform this simulation. Our aim is to compare the final result of this simulation with those models.

The head of the bow-shock has reached a distance close to 9 kpc from the injection position, so still no definite conclusions can be extracted. The evolution of the jet in the grid occurs at quasi-constant speed ($\sim 0.007c$), with a slight slowing down with time, and in a self-similar way. We have also shown that the jet spreads, forming a wide shear layer as it evolves. Compared to simulations in Scheck et al (2002), this jet is 100 times less powerful, however

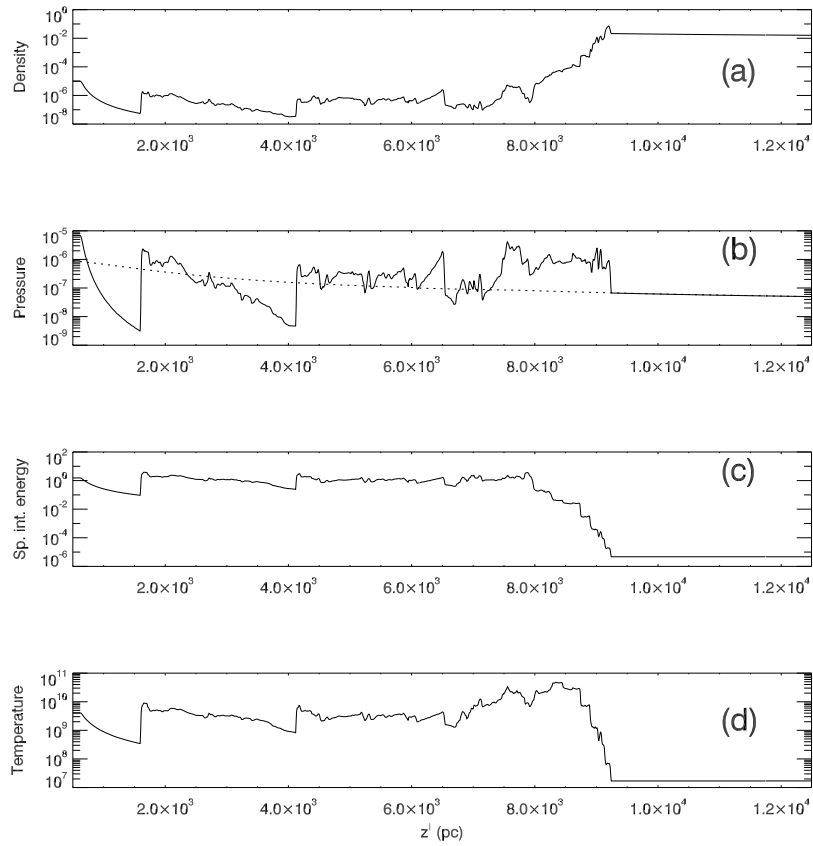


Figure 4.18: Different profiles of variables on the jet axis at the last frame. (a) Rest mass density ($\rho_{a,c}$), (b) pressure ($\rho_{a,c} c^2$, dotted line is the original atmospheric pressure on the axis), (c) specific internal energy (c^2), (d) temperature (K). z' stands for the distance to the source ($z + 500$ pc).

it propagates at a mean velocity which is slightly larger. This is due to the fact that the jet in our simulation is overpressured and propagates through a decreasing density atmosphere. The morphology of our jet is close to that of the LH model in Scheck et al. (2002), but in our case, the jet is much more pinched and presents entrainment behind the head (see last panel in Fig. 4.19).

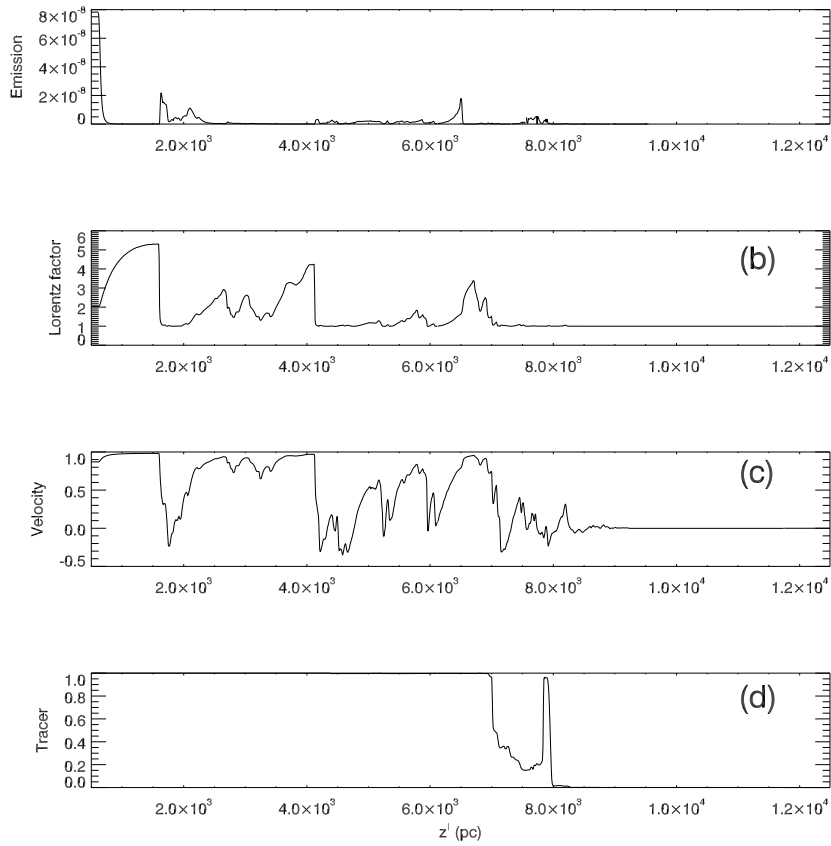


Figure 4.19: Different profiles of variables on the jet axis at the last frame. (a) Emission (code units, see text), (b) Lorentz factor, (c) axial velocity (c), (d) tracer. z' stands for the distance to the source ($z + 500$ pc).

The structures in the inner part of the jet have become quasi-stationary by the time when we analyze these results. We observe a fast adiabatic expansion in the exit from the galactic core, as the jet propagates through the steep density gradient of the galaxy. This expansion ends at $z' \sim 1.5$ kpc with a sudden recollimation and slowing down of the flow. This recollimation generates a new overpressuring of the jet, which starts to expand again, though slower than before, as it is embedded now in a much smoother density gra-

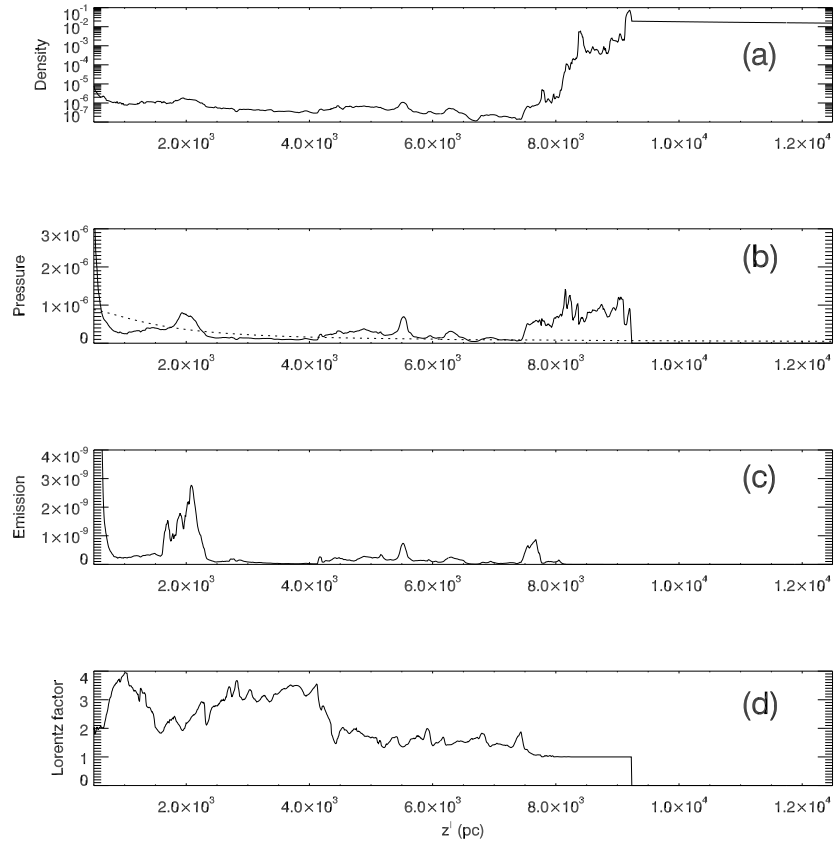


Figure 4.20: Profiles of radially averaged variables, weighted with the tracer and counting only those cells where the axial velocity is greater than zero. (a) rest mass density ($\rho_{a,c}$, in this plot, due to the logarithmic scale, material ahead of the shock -ambient material only- is not weighted with the tracer in order to avoid zeros), (b) pressure ($\rho_{a,c} c^2$, dotted line is the original atmospheric pressure on the axis), (c) emission (the inner part is omitted in order to stress the emission downstream), (d) Lorentz factor. z' stands for the distance to the source ($z + 500$ pc).

dient atmosphere. This process ends, as before in recollimation, this time at $z' \sim 4.0 - 4.5$ kpc, the place where we have detected the stronger slowing down

in the Lorentz factor map (see Fig. 4.17).

As we have mentioned in the previous section, connection of this simulation with linear analysis is difficult, due to the complexity of the linear problem, and to the fact that perturbations are already non-linear in the simulation. In any case, we observe pinching of the mode, associated to expansion and recollimation of the jet, which causes mass entrainment, and we also observe the formation of a thick shear/mixing layer, which make this simulation comparable to UST1 models in Chapter 3.

LB02b suggest that the boundary between the inner and flaring regions (at 1.1 kpc from the source) consists on a discontinuity in velocity, density and pressure which is behind the sudden increase of radio emission. Their results say that, in the flaring region the jet undergoes a rapid expansion followed by collimation, and ends at 3.5 kpc from the source, where the outer region starts. The outer region is characterized by slow decrease in velocity, and continuous mass-load. We identify the first discontinuity, boundary between inner and flaring regions, with the recollimation at $z' \sim 1.5$ kpc. Then, the flaring region would be reproduced by the sudden increase in emission from that point, followed by expansion of the jet and recollimation before going into the outer region, the boundary between which is identified with the second recollimation at $z' \sim 4$ kpc. However, the head of the jet is still too close to have a proper final morphology analysis of the outer region.

In Fig. 4.21, we plot the jet radius versus distance. The three regions are clearly observed. Fitted opening angles (from fits shown by dotted lines in the plot) are 9° in the inner region, 5° in the flaring region and 11.8° in the outer one. We want to stress the similarities of the opening angles given here for the flaring and outer regions with those given in LB02a,b (6.7° for the flaring and 13.1° for the outer).

The main discrepancy between our results and those modelled by Laing and Bridle is that emission in the inner region appears to be strong in our simulation and that the Lorentz factor at the boundary between the inner and the flaring regions is ~ 5 in the simulation versus ~ 2 in their analysis. Both facts could be due to the large pressure ratio given at the injection, which makes the jet to be very bright at that point. Also, we inject the jet with the velocity given by LB02b at 1.1 kpc (boundary between inner and flaring), and assumed by them to be constant form the origin. We observe in the simulation that this velocity at the beginning of the strong density gradient results in larger velocities at the boundary between inner and flaring

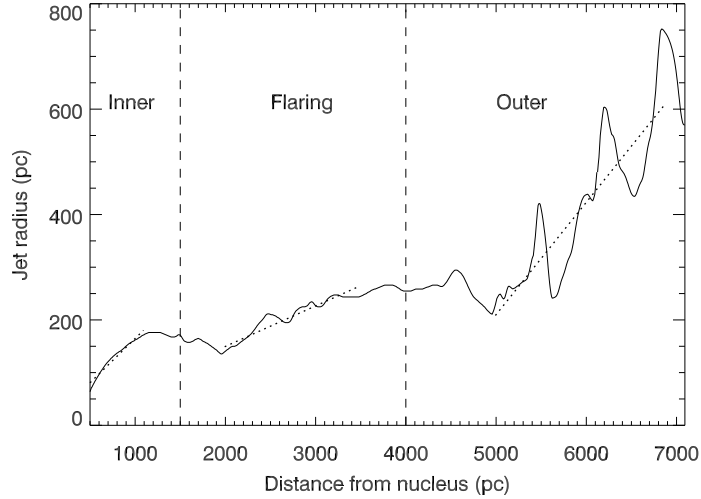


Figure 4.21: Jet radius versus distance in the last frame. Jet radius is computed taking the outermost position where the axial velocity is larger than $0.3c$. The boundaries between regions are marked with dashed vertical lines; dotted lines indicate fitted parts in order to obtain opening angles.

regions. Slightly smaller injection velocities and pressure ratios could result in values in the simulation closer to those fitted in LB02a for velocity at the aforementioned first boundary. The shift in the position of boundaries between regions could also be due to the large value of initial pressure ratio: a smaller value of this ratio could bring the boundaries closer to the observed values, as less time/space would be needed to reach jet underpressure and recollimation.

Regarding mass entrainment, we have detected strong, but intermittent, loading of external material at $z' \sim 4\text{kpc}$. Intermittence in this process is due to jet pulsation because of the close presence of the head of the jet. This place coincides with the boundary between the flaring and the outer regions, which is exactly the place where LB02b compute strong entrainment rate (at 3.5 kpc in their case). Again, since the head is too close, no definitive conclusions can be derived, though it seems that the strong pinching caused by the recollimation occurring at this point could be responsible of the entrainment, as we have seen in Chapter 2.

The lack of appropriate resolution in the simulation causes that entrainment is damped by numerical viscosity. Although, as we have mentioned, entrainment occurs in the simulation during jet pulsation, we will have to wait until the proper end of the simulation to compare it with computations in LB02b and check if the mass loading will be enough to explain the jet deceleration pointed out in LB02a,b and the observed morphology of the radio-galaxy 3C 31. Comparison with other FRI models like those from Komissarov (1990a,b, 1994), Falle (1991) or Bicknell (1984, 1994) will be undertaken.

Chapter 5

CONCLUSIONS

This work represents an important step in the understanding of linear and non-linear stability of relativistic flows. We present linear analysis and numerical simulations for jets spanning a wide range of specific internal energies, Lorentz factors and relativistic Mach numbers in the vortex sheet and shear layer cases. We present our first attempt to apply stability theory to numerical simulations of parsec and kiloparsec scale extragalactic jets.

Many different ingredients have been worked out with that aim. From a theoretical point of view, we have implemented a robust numerical solver for the stability problem which can be applied in many general conditions, and we have developed the stability problem for sheared rotating relativistic jets; both achievements set the basis for further steps in the solving of more realistic situations as will be, for example, the inclusion of magnetic fields. From a numerical point of view, several major improvements in the original hydrodynamical code have been implemented, as the perfect symmetrization of the code, implementation of left eigenvectors and analytic expressions for numerical viscosity, full parallelization and optimization, implementation of a fully 3D relativistic hydrodynamics code, implementation of a general equation of state for relativistic gases and the necessary set up for galactic atmospheres in equilibrium.

Our main results and conclusions are:

- Our numerical code is able to reproduce accurately the linear growth of Kelvin-Helmholtz instabilities in both vortex sheet and shear layer cases, if we use the appropriate numerical resolution (which minimizes the effects of numerical viscosity) for the problem.

- We have confirmed Hanasz's hypothesis (1995, 1997), who predicted that instabilities in relativistic fluids saturate when the amplitude of the velocity perturbation reaches the speed of light in the jet reference frame.
- We have separated the evolution of Kelvin-Helmholtz instabilities in relativistic jets in three phases: linear phase, saturation phase and non-linear phase. We have studied the influence of numerical resolution in the linear/saturation and non-linear phases.
- We have studied and classified the non linear evolution of Kelvin-Helmholtz instabilities in a quantitative way, by means of mean variables like longitudinal momentum in the jet and the width of the mixing region.
- We have discovered the existence of resonant modes in sheared jets, which have a great importance in the stability properties of jets. Their fast growth in high Lorentz factor/relativistic Mach number models results in a smooth transition to the non linear regime, avoiding the generation of shocks, and favor the generation of a hot shear layer which surrounds the jet core. Those models in which these modes do not appear are disrupted, with important loss of momentum and internal energy, either suddenly after the shock generation at the end of the saturation phase, or in a slow non-linear mixing process.
- We have derived a stability map for relativistic flows, depending on their relativistic Mach number and on their Lorentz factor, and we show that jets with high values of both variables tend to be more stable than the rest.
- We have started a series of numerical simulations of the parsec scale jet in 3C 273 with the aim of testing results by Lobanov and Zensus (2001), who, using linear theory (e.g., Hardee 2000), explained observed structures in the jet as a consequence of the development of instabilities, and trying to find an accurate method which allows for derivation of jet parameters. We have concluded that observed structures are identifiable with perturbations induced, either by precession and superluminal components (simulation B) or by any other mechanism which induces the development of Kelvin-Helmholtz instabilities (simulation A). Fine tuning of the velocity of propagation of perturbations and viewing angle must be done in order to clearly identify observed structures. In this

sense, numerical simulations of this kind may be used in order to constrain those parameters. We have found that the jet is disrupted close to injection (simulation A), contrary to observations and suggest mechanisms which could avoid this breaking of the flow which will be tested in the future.

- We are performing a long term evolution simulation of the jets in 3C31, focusing on its evolution through the galaxy and entrance in the intergalactic medium. We have used the parameters given in Laing and Bridle (2002 a,b), with the purpose of testing the model and performing a stability study of jets evolving in a profiled medium. We reproduce in a qualitative way their modelling of the inner part of the jets, with discrepancies regarding the velocities and emission in the innermost region, which are partially understood. We have to wait until the end of the simulation in order to give a deeper analysis of the simulation in comparison with the models in the aforementioned papers and other FRI evolution models. This kind of simulations will open the way towards the understanding of the FRI/FRII dichotomy.

Several aspects like the physical origin of the resonant modes and the reason for their faster growth in simulations than that predicted by theory, or the disruption of the jet in simulation A of 3C 273, which are not understood will be addressed in the continuation of this research.

Future prospects of the work include the continuation of this line of research, by studying effects like jet differential rotation or expansion on the instabilities, and trying to understand the mechanisms which make some jets to keep their collimation and stability through many decades in distance. The development of the stability problem in the case of relativistic magnetohydrodynamics (RMHD), along with the use of the RMHD code developed in a collaboration between the Relativistic Astrophysics group in the *Universitat de València* and the Hydro group in the *Max Planck Institut für Astrophysik* in Garching (Germany) (Leismann et al. 2005), and the possible inclusion of radiation transport in our computations, will generate results which could be directly comparable with observations. In this direction, continuation of direct collaborations with radio astronomers will allow to work out a robust method for the derivation of the parameters and physical conditions in relativistic jets and their environments.

Appendix A

Numerical code

Our aim is to solve the equations for the relativistic fluid dynamics of a perfect gas. These are non-linear equations that cannot be solved analytically. For a review on this topic, see Taub (1978). Using Einstein's summing convention, we can write them as follows:

$$(\rho u^\mu)_{;\mu} = 0 \quad , \quad (\text{A.1})$$

$$(T^{\mu\nu})_{;\nu} = 0 \quad , \quad (\text{A.2})$$

where $\mu, \nu = 0, 1, 2, 3$ and $;\mu$ denotes the covariant derivative with respect to coordinate x^μ . ρ is the proper rest mass density of the fluid, u^μ are the four-velocity components, and $T^{\mu\nu}$ is the stress-energy tensor, which, for a perfect fluid (that assumed in our code) can be written as:

$$T^{\mu\nu} = \rho h u^\mu u^\nu + p g^{\mu\nu} \quad , \quad (\text{A.3})$$

where p is pressure of the fluid, $g^{\mu\nu}$ is the metric tensor and h is the specific enthalpy defined as

$$h = 1 + \varepsilon/c^2 + p/(\rho c^2) \quad , \quad (\text{A.4})$$

with ε the specific internal energy and c the speed of light, which we will take as one ($c = 1$).

In Minkowski space-time and Cartesian coordinates (t, x^1, x^2, x^3) , the conservation equations (A.1) and (A.2) can be written in conservation, vectorial form:

$$\frac{\partial \mathbf{u}}{\partial t} + \frac{\partial \mathbf{F}^i(\mathbf{u})}{\partial x^i} = 0 \quad , \quad (\text{A.5})$$

with $i = 1, 2, 3$. The state vector \mathbf{u} is defined as

$$\mathbf{u} = (D, S^1, S^2, S^3, \tau)^T, \quad (\text{A.6})$$

and the flux vectors $\mathbf{F}^i(\mathbf{u})$ are given by

$$\mathbf{F}^i(\mathbf{u}) = (D v^i, S^1 v^i + p \delta^{1i}, S^2 v^i + p \delta^{2i}, S^3 v^i + p \delta^{3i}, S^i - D v^i)^T. \quad (\text{A.7})$$

The five conserved quantities D, S^1, S^2, S^3 and τ are rest mass density, the three components of the momentum density, and energy density (excluding rest mass density). They are all measured in the laboratory frame, and relations with the corresponding quantities in the local rest frame of the fluid (primitive variables) are

$$D = \rho W, \quad (\text{A.8})$$

$$S^i = \rho h W^2 v^i, \quad i = 1, 2, 3, \quad (\text{A.9})$$

$$\tau = \rho h W^2 - p - D, \quad (\text{A.10})$$

with v^i the components of the three-velocity of the fluid

$$v^i = u^i / u^0, \quad (\text{A.11})$$

and W the Lorentz factor

$$W = u^0 = \frac{1}{\sqrt{1 - v^i v_i}}. \quad (\text{A.12})$$

In order to recover the equivalent conserved magnitudes in the newtonian regime, we consider $v \ll c$ and $h \rightarrow 1$ (see Eq. A.4). We obtain $D \rightarrow \rho$, $S^i \rightarrow \rho v^i$, and $\tau \rightarrow \rho E = \rho \epsilon + \rho v^2/2$, and equations A.5 become the non-relativistic conservation equations.

System (A.5) is closed by an equation of state (EOS), which we assume of the form:

$$p = p(\rho, \epsilon) \quad (\text{A.13})$$

As mentioned above, this system (A.5) cannot be solved by analytic means, so that numerical codes are required. Our code was developed by Dr. J.M. Martí and first results were presented in Martí et al. (1995).

In order to solve system (A.5), we discretize the state vector \mathbf{U} within computational cells. Temporal evolution of quantities in this vector is determined

by the flux balance across the boundaries between separating cells. Using a method of lines (see, LeVeque 1992), discretization leads to:

$$\begin{aligned} \frac{d\mathbf{U}_{i,j,k}}{dt} = & -\frac{1}{\Delta x} \left(\tilde{\mathbf{F}}_{i+\frac{1}{2},j,k}^x - \tilde{\mathbf{F}}_{i-\frac{1}{2},j,k}^x \right) - \frac{1}{\Delta y} \left(\tilde{\mathbf{F}}_{i,j+\frac{1}{2},k}^y - \tilde{\mathbf{F}}_{i,j-\frac{1}{2},k}^y \right) - \\ & \frac{1}{\Delta z} \left(\tilde{\mathbf{F}}_{i,j,k+\frac{1}{2}}^z - \tilde{\mathbf{F}}_{i,j,k-\frac{1}{2}}^z \right) + \mathbf{S}_{i,j,k} \equiv \mathbf{L}(\mathbf{U}), \end{aligned} \quad (\text{A.14})$$

where the Latin indices i , j , and k refer to the x , y and z coordinate directions, respectively. $\mathbf{U}_{i,j,k}$ and $\mathbf{S}_{i,j,k}$ are the mean values of the state and source (any forces acting on the system or geometrical terms, if any) vectors in the corresponding cell, while $\tilde{\mathbf{F}}_{i\pm\frac{1}{2},j,k}^x$, $\tilde{\mathbf{F}}_{i,j\pm\frac{1}{2},k}^y$, and $\tilde{\mathbf{F}}_{i,j,k\pm\frac{1}{2}}^z$ are the numerical fluxes at the respective cell interface. Finally, $\mathbf{L}(\mathbf{U})$ is a short hand notation of the spatial operator in our method.

Next, we need to compute numerical fluxes. Fluxes are calculated with an approximate Riemann solver that uses the complete characteristic information contained in the Riemann problems between adjacent cells (Donat and Marquina 1996). It is based on the spectral decomposition of the Jacobian matrices of the relativistic system of equations derived in Font et al. (1994) and uses analytical expressions for the left eigenvectors (Donat et al. 1998). The spatial accuracy of the algorithm is improved up to third order by means of a conservative monotonic parabolic reconstruction of the pressure, proper rest-mass density and the spatial components of the fluid four-velocity (PPM, see Colella and Woodward 1984, and Martí and Müller 1996).

Besides relativistic density, momentum and energy, the code also evolves a passive scalar representing the jet mass fraction. This allows us to distinguish between ambient and jet matter helping us to characterize processes like jet/ambient mixing or momentum exchange.

Integration in time is done simultaneously in both spatial directions using a multi-step total-variation-diminishing (TVD) Runge-Kutta (RK) method developed by Shu and Osher (1988), which can provide second (RK2) and third (RK3) order in time. The explicit form of the algorithm is (subindexes (i,j,k) are omitted):

1. Prediction step

$$\mathbf{U}^{(1)} = \mathbf{U}^n + \Delta t \mathbf{L}(\mathbf{U}), \quad (\text{A.15})$$

with n the time step.

2. Depending on the order:

- **RK2:**

$$\mathbf{U}^{n+1} = \frac{1}{\alpha} \left(\beta \mathbf{U}^n + \mathbf{U}^{(1)} + \Delta t \mathbf{L}(\mathbf{U}^{(1)}) \right), \quad (\text{A.16})$$

with $\alpha = 2$ and $\beta = 1$.

- **RK3:**

$$\mathbf{U}^{(2)} = \frac{1}{\alpha} \left(\beta \mathbf{U}^n + \mathbf{U}^{(1)} + \Delta t \mathbf{L}(\mathbf{U}^{(1)}) \right) \quad (\text{A.17})$$

$$\mathbf{U}^{n+1} = \frac{1}{\beta} \left(\beta \mathbf{U}^n + 2\mathbf{U}^{(2)} + 2\Delta t \mathbf{L}(\mathbf{U}^{(2)}) \right), \quad (\text{A.18})$$

with $\alpha = 4$ and $\beta = 3$.

Recovery of velocity vector components is more difficult in the relativistic case than in the classical one. In the latter case conserved variables are ρ and ρv^i , so that deriving v^i is straightforward. On the other hand, in the former case, conserved quantities are coupled through Lorentz factor, which makes recovery of velocity components a difficult task solved by numerical techniques. As our code works using conservative schemes which evolve conserved quantities, we need to compute primitive variables from those conserved quantities several times per numerical cell and time step, making this problem a crucial part of the algorithm. This is done by using a Newton-Raphson algorithm (see Appendix B). The function for which we have to find roots is (see Aloy 1999):

$$f(p) = (\gamma - 1)\rho_*\varepsilon_* - p, \quad (\text{A.19})$$

where ρ_* and ε_* are given by:

$$\rho_* = \frac{D}{W_*} \quad (\text{A.20})$$

and

$$\varepsilon_* = \frac{\tau + D(1 - W_*) + p(1 - W_*^2)}{DW_*}, \quad (\text{A.21})$$

with W_* the corresponding Lorentz factor for

$$\mathbf{v}_* = \frac{\mathbf{S}}{\tau + D + p}. \quad (\text{A.22})$$

If we take into account that $|\mathbf{v}| \leq 1$, we obtain, from last equation, a minimum value for the pressure:

$$p_{min} = |\mathbf{S}| - \tau - D, \quad (\text{A.23})$$

so the root must be found in the domain $p \in]p_{min}, \infty[$. Newton-Raphson iteration is done approximating the derivative of function f , f' as:

$$f' = |\mathbf{v}_*|^2 c_{s*}^2 - 1, \quad (\text{A.24})$$

where c_{s*} is the sound speed

$$c_{s*} = \sqrt{\frac{(\gamma - 1)\gamma\varepsilon_*}{1 + \gamma\varepsilon_*}}. \quad (\text{A.25})$$

Summarizing, steps followed by the code are: first, the code builds the grid and gives initial conditions to the problem. After that, evolution starts. Every time step is divided into two or three Runge-Kutta steps. During a Runge-Kutta step the code performs:

- for each spatial direction:
 - vectorization of physical variables,
 - computation of geometrical variables for the cells in the vector and geometric effects as source terms appearing in cylindrical coordinates,
 - computation of source terms, if any,
 - computation of boundary conditions,
 - interpolation of physical variables to find the values in cell interfaces,
 - computation of numerical fluxes in cell boundaries,
- conserved variables advance in time using previous time step values and numerical fluxes,
- and recovery of physical variables using Newton-Raphson.

After the Runge-Kutta steps, next time step value is computed using CFL condition, and output is done if requested.

Several main improvements were applied to the code during the development of this PhD. work:

- In order to solve the system of equations (A.5) we need to derive the left and right eigenvectors from the spectral decomposition of the Jacobian matrix $\partial\mathbf{F}(\mathbf{U})/\partial\mathbf{U}$. The expression for both was given in Donat et al. (1998). Previous to this work, the code computed the left eigenvectors from the inversion of the right eigenvector matrix. Now, left eigenvectors have been explicitly implemented.

High-resolution shock-capturing methods generate numerical viscosity terms which were formulated in Aloy et al. (1999b) (see also Aloy 1999), what allows for reduction of computational time and damping of rounding-off errors. These expressions for the numerical viscosity terms were also added to the code.

- Symmetrization of the code was done by locating the source of asymmetry in the rounding-off errors of PPM reconstruction. PPM method was therefore symmetrized around the axis: each side of the grid around the axis is reconstructed from opposite sides. In the case of antisymmetric flows, we had to take into account that diagonal symmetry forces the axis (it coincides with a cell interface) to be reconstructed from a different side on each longitudinal half of the grid; if this is not considered, the differences are not apparent in the linear regime, but the rounding-off difference in the axis interface in both halves of the grid ends up by generating non symmetric structures in the non-linear regime. This has been tested in a series of simulations for single antisymmetric perturbations.
- The code was parallelized using OMP directives. In particular, the outermost loop of each sweep in all Runge-Kutta steps, the recovery of physical variables, and the computation of the Courant condition for the time step were parallelized. This represented a major achievement, as the saving of computational time has allowed for the use of larger grids and for the performing of more numerical simulations which have been crucial in the final conclusions reached in this work.
- The implementation of a 3D RHD code was achieved, as an extension of the 2D one used in the first part of the work and based on the code GENESIS (Aloy 1999). This code was optimized in order to reduce the number of variables used in the computation, thus decreasing the amount of RAM memory required. This new code was used in simulations on the jet in 3C 273 (see Section 4.1).

- Implementation of a realistic equation of state (Synge, 1957), from routines programmed by L. Scheck (see Scheck et al. 2002). This equation of state allows for the use of different particles in simulations, differentiating electrons (and positrons) from protons. This equation of state was used in simulations on the evolution of the jets in 3C 31 (see Section 4.2).

Appendix B

Numerical methods

B.1 Newton-Raphson method

We use Newton-Raphson method for non-linear systems of equations (Press et al. 1992) to solve equations like (2.26) or inside the numerical code, in the recovery of physical variables and in the Synge equation of state computation. Our system of two equations is formed by the real and imaginary parts of equation (2.26). Unknowns are real and imaginary part of frequency (w) for a given wave-number (k). Let us express a general system in the following form:

$$f_i(x_1, x_2, \dots, x_N) = 0 \quad i = 1, 2, \dots, N \quad (\text{B.1})$$

If we write the vector of values (x_1, x_2, \dots, x_N) as \mathbf{X} , we can expand each f_i close to \mathbf{X} in Taylor series:

$$f_i(\mathbf{X} + \delta \mathbf{X}) = f_i(\mathbf{X}) + \sum_{j=1}^N \frac{\partial f_i}{\partial x_j} \delta x_j + O(\delta \mathbf{X}^2) \quad (\text{B.2})$$

Neglecting terms of order $\delta \mathbf{X}^2$, we obtain a set of linear equations for $\delta \mathbf{X}$, which approach the functions to zero simultaneously. These equations have the following form:

$$\sum_{j=1}^N \alpha_{ij} \delta x_j = \beta_i, \quad (\text{B.3})$$

where

$$\alpha_{ij} = \frac{\partial f_i}{\partial x_j} \quad \beta_i = -f_i \quad (\text{B.4})$$

Equation (B.3) can be solved by LU decomposition (see below). New vector of values \mathbf{X} will be:

$$x_i^{n+1} = x_i^n + \delta x_i \quad i = 1, \dots, N, \quad (\text{B.5})$$

where n is the number of iterations. This process has to be repeated until convergence is reached.

LU decomposition consists on writing a matrix \mathbf{A} as the product of two matrices, one of which presents only elements on the diagonal and below (\mathbf{L}) and the other presents them on the diagonal and above (\mathbf{U}). In this way, $\mathbf{L} \cdot \mathbf{U} = \mathbf{A}$. We can use this to re-write a linear set of equations:

$$\mathbf{A} \cdot \mathbf{x} = \mathbf{b} \implies (\mathbf{L} \cdot \mathbf{U}) \cdot \mathbf{x} = \mathbf{b} \implies \mathbf{L} \cdot (\mathbf{U} \cdot \mathbf{x}) = \mathbf{b} \quad (\text{B.6})$$

Now, we can easily solve for a vector $\mathbf{y} = \mathbf{L} \cdot \mathbf{x}$,

$$\mathbf{L} \cdot \mathbf{y} = \mathbf{b}, \quad (\text{B.7})$$

and then,

$$\mathbf{U} \cdot \mathbf{x} = \mathbf{y} \quad (\text{B.8})$$

B.2 Muller's method

Muller's method (Amat et al. 2002) is used in order to solve for zeros of the dispersion relation for cylindrical coordinates or in the numerical solver of the sheared jet problem. It consists in an extension of secant method, and the fact that it does not use derivatives makes it very stable in discontinuities.

The idea is to use three initial approximations $(x_i, f(x_i))$, $i = k-2, k-1, k$, where k is the step), to build a parabola, $q(x)$, and then to find the closest root for this parabola to the first guess. This root will be next guess, and so on, until we find convergence. The initial x_{-2} and x_{-1} are produced automatically by the routine. Parabola $q(x)$ is defined as:

$$q(x) = b_0 + b_1(x - x_k) + b_2(x - x_k)(x - x_{k-1}), \quad (\text{B.9})$$

if we impose that $q(x_i) = f(x_i)$ for $i = k-2, k-1, k$, we have:

$$b_0 = f(x_k) \quad (\text{B.10})$$

$$b_1 = \frac{b_0 - f(x_{k-1})}{x_k - x_{k-1}} \quad (\text{B.11})$$

$$b_2 = \frac{b_1 - \frac{f(x_{k-1}) - f(x_{k-2})}{x_{k-1} - x_{k-2}}}{x_k - x_{k-2}} \quad (\text{B.12})$$

We see that $q(x)$ is nothing but Newton's polynomial interpolation formula. This way of building the parabola makes the method useful for any function with numerical values for all x . Now we change variable in order to work with differences and look for the closest solution to x_k for the parabola. We define:

$$h_k = x_k - x_{k-1} \quad \lambda h_k = x - x_k, \quad (\text{B.13})$$

and therefore $x - x_{k-1} = (1 + \lambda)h_{k-1}$, so we can write:

$$q(\lambda) = b_0 + b_1 h_k \lambda + b_2 h_k h_{k-1} \lambda(1 + \lambda) \quad (\text{B.14})$$

Next step is to write this polynomial as $q(\lambda) = A_0 + A_1 \lambda + A_2 \lambda^2$, so the solution with the minor modulus for λ is,

$$\lambda^* = \frac{2A_0}{A_1 \pm \sqrt{A_1^2 - 4A_0A_2}}, \quad (\text{B.15})$$

where we have to choose sign \pm for the denominator to have maximum modulus. Finally, next guess will be $x_{k+1} = x_k + \lambda^* h_k$.

B.3 Shooting method

The shooting method (Press et al. 1992) is used in order to solve differential equations. It consists on giving boundary conditions to the problem on two points (one dimensional), integrating the equation from the first to the second, and look for solutions which accomplish the conditions at this last point. It requires the use of two numerical methods, a variable stepsize Runge-Kutta method (see section A for an example of Runge-Kutta integration and Press et al. 1992 for variable stepsize integration) and Muller method for root finding.

We use this method in order to solve equation (3.1). This equation stands for the dynamics of a pressure perturbation, P_1 , wave in a sheared slab jet. As in the vortex sheet case, we can solve it for the symmetric or the antisymmetric case. The former requires that the value of the pressure perturbation in the axis is a maximum (the value of the amplitude), and the first derivative is thus zero, opposite to the antisymmetric problem:

$$\begin{aligned} P_1(x=0) = 1, \quad P_1'(x=0) = 0 & \quad (\text{sym. modes}), \\ P_1(x=0) = 0, \quad P_1'(x=0) = 1 & \quad (\text{antisym. modes}). \end{aligned} \quad (\text{B.16})$$

Given amplitudes in the jet axis have been proved not to influence the result (excepting if too small amplitudes are considered, where the trivial solution is found). From the axis, for a given k and ω , we use the adaptive step Runge-Kutta method in order to integrate the equation to the outer boundary, which should be as far as possible to the transition (convergence tests have to be undertaken for this), what depends on the value of m (steepness of the layer). Solutions satisfying the Sommerfeld radiation conditions (no incoming waves from infinity and wave amplitudes decaying towards infinity) are selected:

$$P_1(x = x_f) + \frac{i P_1'(x = x_f)}{k_x} = 0 \quad (\text{B.17})$$

where x_f is the x -coordinate of a point far enough from the jet. A convergence value of 10^{-8} is required. If our selected values of k and ω do not fulfill equation (B.17), Muller method looks for another value of ω and the integrating process starts again. A large loop sweeping wavenumbers is given to the program, and, as there may be many modes present at a given wavenumber, also a grid of starting points in ω is given for each k , in such a way that solutions around that initial pair of numbers (k, ω) are found.

Appendix C

Special relativity in extragalactic jets

Special relativity theory is 100 years (1905-2005), and this thesis deals on *relativistic flows*, words which appear on the title followed by *application to extragalactic jets*. How have we reached the knowledge that relativity is to be applied in this case? After one century of theoretical and observational research, special relativity has been confirmed both experimentally (in particle accelerators) and observationally (in the atmosphere -cosmic rays- and in the Universe). Several astrophysical scenarios (gamma-ray bursts, galactic superluminal sources and jets in AGN's) have been explained on the basis of this theory. Not only due to the anniversary, but also to its central role in this work, we will review the evidences of relativity acting in extragalactic jets. For a review on this topic see Ghisellini (2000).

Observational features of extragalactic jets which are not understood on the basis of non-relativistic motion:

- **One-sidedness.** If we consider the scenario of jet formation in the way that most accepted theories explain it, it consists of an accretion disk around a compact object, out of which matter is taken by magnetorotational processes. The disk-compact object is an up-down symmetric system, and therefore we should expect that one jet is formed on each side; however, most of extragalactic jets appear to be only one-sided in the parsec scales.
- **Inverse Compton.** Inverse Compton scattering is a process by which

a photon colliding with a relativistic particle gains an amount of energy which is proportional to the square of the particle's Lorentz factor. This scattering makes that synchrotron photons typically emitted from radio to optical, are turned into X-ray photons. Observed radio emission from many jets implies larger X-ray emission than observed.

- **Brightness temperature.** This magnitude (T_b) is defined as $I_\nu \equiv 2k_B T_b \nu^2 / c^2$, where I_ν is the specific intensity of the source at frequency ν , k_B is the Boltzmann constant, and c is the speed of light. High values of T_b imply high values of specific intensity, i.e., a large number of photons (and emitting particles) at that frequency, and this makes the probability of inverse Compton scattering larger. It is known that for $T_b > 10^{12} K$, the amount of radiation produced by inverse Compton should be larger than that due to synchrotron radiation, and as a consequence, to a dramatic particle cooling known as *Compton catastrophe*. Despite this theoretical limit, many jets present brightness temperatures larger than $10^{12} K$.
- **Superluminal motion.** VLBI observations allowed to measure the velocity of individual blobs in parsec scale jets, which were derived to be larger than the speed of light.

C.1 Beaming and its effects

We know that radiation from jets in AGN's is synchrotron radiation from accelerated electrons by a magnetic field (Rybicki and Lightman 1979). Charged, accelerated, non-relativistic particles emit radiation following the equation:

$$P = \frac{2q^2}{3c^3} a^2, \quad (\text{C.1})$$

where P is the total power emitted, q is the charge, c is the speed of light and a is the acceleration. This radiation is emitted in dipole form ($\propto \sin^2 \Theta$, being Θ the angle to the direction of acceleration). However, if the radiating particle is moving relativistically, and the acceleration vector is perpendicular to the velocity vector (which is the case for synchrotron radiation, see section 1.3.4), emission suffers an aberration that makes a large part of the radiation to be emitted in a cone of semi-angle $1/\gamma$ (γ the Lorentz factor) with respect to the direction of velocity.

Another effect that occurs due to the relativistic motion of radiating particles is the contraction of arrival time of photons emitted by particles moving towards the observer (Doppler effect). The relation between both intervals is:

$$\Delta t_a = \gamma(1 - \beta \cos \theta) \Delta t_e \equiv \frac{\Delta t_e}{\delta} \quad (\text{C.2})$$

where Δt_a is the interval between the arrival of the two photons in the reference frame of the observer, β is the velocity of the flow in units of the speed of light, θ is the angle between velocity of the particle and the line of sight, and Δt_e is the interval between the emission of both photons, in the reference frame of the particle. We have also introduced δ , defined as $1/\gamma(1 - \beta \cos \theta)$, which is known as the beaming or Doppler factor.

If we take these effects into account, the fact that only one-sided jets are observed in many sources can be naturally explained by the jets moving relativistically and one of them closely to our line of sight; brightness temperature values have to be thus corrected, if emission is not isotropic, and they must therefore be much lower than estimated if we are observing the approaching jet. The same applies to inverse Compton scattering estimations, which have to be revised in terms of anisotropy of radiation by relativistic particles. When putting all these observations in the light of special relativity, they are easily explained. Moreover, these observations allow us to put limits on the Lorentz factor and viewing angle of jets.

C.2 Superluminal motion

One fact remains to be explained: superluminal motion of blobs in the jets. It can also be understood as a relativistic effect. Consider Figure C.1: a blob of matter is moving along the line A-B forming an angle θ with the line of sight, and it emits a photon at A, and later, another from B. Consider also that the observer is at an infinite distance. The time elapsed between two emissions is, in the reference frame of the observer Δt_e . The distance from A to B is $\beta c \Delta t_e$, and the distance from A to $(B \cos \theta)$ is thus $\beta c \Delta t_e \cos \theta$. Meanwhile, the photon emitted at A has reached position C, at a distance $c \Delta t_e$. Therefore, the distance between the photon emitted at A and that emitted at B is $AC - A(B \cos \theta) = c \Delta t_e (1 - \beta \cos \theta)$. As they are at a constant speed (of light), the difference in arrival times is $\Delta t_e (1 - \beta \cos \theta)$, i.e., shorter than Δt_e . Taking into account that the projected distance (the distance observed) between A

and B is $(B \cos \theta)B = \beta c \Delta t_e \sin \theta$, we can measure the *apparent velocity*:

$$\beta_{app} = \frac{\beta \sin \theta}{1 - \beta \cos \theta}. \quad (C.3)$$

We can see that $\beta_{app} > 1$ if β is close to 1, and θ is sufficiently small. This

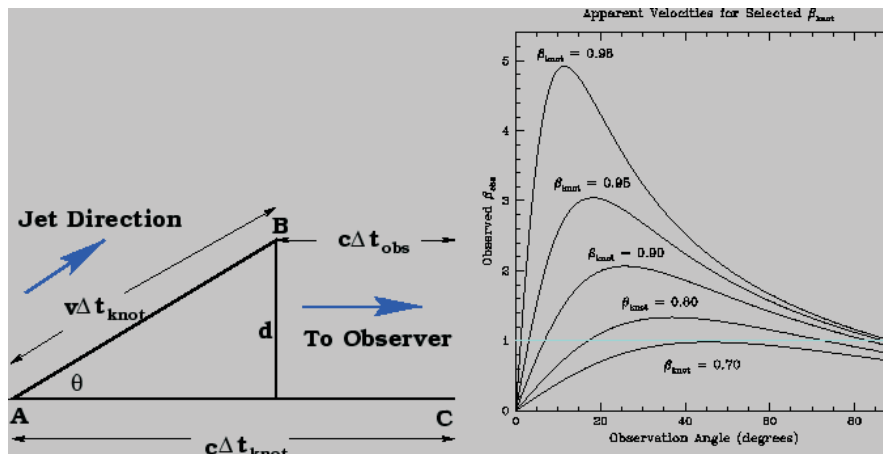


Figure C.1: Schematic view of superluminal motion and apparent velocity versus viewing angle for different flow speeds. Taken from web page <http://parsnip.wooster.edu/thesis/html/node14.html>

effect is, as we have seen, due to the contraction of arrival times of photons.

With this demonstration, we have shown that those previously unexplained observational features of extragalactic jets are easily fitted under the light of special relativity. This is nothing but the proof that these jets move at speeds close to the speed of light, and that special relativity is at action. Other observational features are not direct evidence of relativistic motion, but they confirm this point. The most characteristic are:

- Laing-Garrington effect: the lobe associated with the observed one-sided jet is less polarized, meaning that the light coming from it is travelling a shorter path, as light is depolarized by matter, i.e., it should be associated to the approaching jet, in agreement with beaming considerations.
- Jet bending: Many jets are observed to be curved, what generates problems of stability. However, this could be explained as apparent distortions caused by small viewing angles, also consistent with beaming.

Two nice examples of these distortions are shown in Ghisellini (2000) as a moving bar (which is apparently lengthened) or a square (which is apparently rotated).

Appendix D

Linear stability problem for sheared jets

In this Appendix, we present the development of the linear stability problem for sheared jets in several situations. In Section D.1, we develop the differential equation for a sheared slab, relativistic jet. This equation has been used in Chapter 3 in order to analyze the evolution of perturbations in this frame. Sections D.2 and D.3 are devoted to sheared cylindrical and conical jets, where the flow has an initial rotating velocity. None of both equations has been directly applied along this work (only that for cylindrical jets, and with no rotation was solved in several cases to be applied in Chapter 3). However, they have been derived for their theoretical interest and their potential application in astrophysical scenarios.

The first case will be of interest in order to study the influence of rotation in the stability of parsec and kiloparsec scale jets. The fact that jets present differential rotation is deduced from formation models which involve magnetocentrifugal processes (see the list of references in Hanasz et al. 2000). We plan to solve this equation in order to apply it to simulations like those shown in Section 4.1.

The second case is of direct application in cases like that in the simulation of 3C 31 presented in this work. In the simulation, the jet is initially overpressured with respect to the ambient. However, we need to make some assumptions to simplify the equations and in order to be able to solve them numerically. Due to this fact, we assume pressure equilibrium and constant opening angle of the jet. This is a simplifying approach to the real problem,

but it can give us some interesting conclusions of the effects of jet expansion through an external density gradient on its stability. This equation could also be applied in the case of Gamma Ray Bursts (GRBs), in which strong variability in the emission is thought to be associated with perturbations in the jet (see, e.g., Aloy et al. 2002).

D.1 Slab jet

This equation was first derived, for the case of cylindrical geometry, by Birkinshaw (1984), but we include here the derivation as it has not been published elsewhere. We start with the energy momentum tensor:

$$T^{\mu\nu} = (\rho + P)u^\mu u^\nu + P g^{\mu\nu}, \quad (\text{D.1})$$

where P is pressure of the fluid, ρ is the energy density, $g^{\mu\nu}$ is the metric tensor and u^μ is the four-velocity. We will use $u^\mu = \gamma(1, \mathbf{v})$ (γ is the Lorentz factor) and $\rho h = \rho + P$, with h the specific enthalpy. Doing $T_{;\nu}^{\mu\nu} = 0$, we find, for $\mu = i$:

$$\gamma \frac{\partial}{\partial t} (\rho h \gamma \mathbf{v}) + \gamma (\mathbf{v} \cdot \nabla) (\rho h \gamma \mathbf{v}) + \rho h \mathbf{v} \left(\frac{\partial \gamma}{\partial t} + (\mathbf{v} \cdot \nabla) \gamma + \gamma^2 \nabla \cdot \mathbf{v} \right) + \nabla P = 0, \quad (\text{D.2})$$

and for $\mu = 0$:

$$\gamma \frac{\partial}{\partial t} (\rho h \gamma) + \gamma (\mathbf{v} \cdot \nabla) (\rho h \gamma) + \rho h \left(\frac{\partial \gamma}{\partial t} + (\mathbf{v} \cdot \nabla) \gamma + \gamma^2 \nabla \cdot \mathbf{v} \right) - \frac{\partial P}{\partial t} = 0. \quad (\text{D.3})$$

Using both equations we can derive the momentum equation:

$$\rho h \gamma^2 \left(\frac{\partial \gamma}{\partial t} + (\mathbf{v} \cdot \nabla) \mathbf{v} \right) = -\nabla P - \mathbf{v} \frac{\partial P}{\partial t}. \quad (\text{D.4})$$

If we do the following contraction $u_\mu T_{;\nu}^{\mu\nu} = 0$, we obtain the equation for energy:

$$\gamma \left(\frac{\partial \rho}{\partial t} + \mathbf{v} \cdot \nabla \rho \right) = -\rho h \left(\frac{\partial \gamma}{\partial t} + \mathbf{v} \cdot \nabla \gamma + \gamma \nabla \cdot \mathbf{v} \right). \quad (\text{D.5})$$

From the expression $(nu^\mu)_{;\mu} = 0$, with n the number density, we obtain the continuity equation:

$$\gamma \left(\frac{\partial n}{\partial t} + \mathbf{v} \cdot \nabla n \right) + n \left(\frac{\partial \gamma}{\partial t} + \mathbf{v} \cdot \nabla \gamma + \gamma \nabla \cdot \mathbf{v} \right) = 0. \quad (\text{D.6})$$

Combining eqs. (D.5) and (D.6) we find the following relation between energy and number density:

$$\frac{1}{n} \left(\frac{\partial n}{\partial t} + \mathbf{v} \cdot \nabla n \right) = \frac{1}{\rho h} \left(\frac{\partial \rho}{\partial t} + \mathbf{v} \cdot \nabla \rho \right). \quad (\text{D.7})$$

We can write this expression in terms of entropy (s), by using the first law of thermodynamics ($d\rho = Tds + \rho h/n dn$),

$$\frac{\partial s}{\partial t} + \mathbf{v} \cdot \nabla s = 0, \quad (\text{D.8})$$

and, taking $s = s(\rho, P)$, we find the following adiabatic equation:

$$\frac{\partial P}{\partial t} + \mathbf{v} \cdot \nabla P = c_s^2 \left(\frac{\partial \rho}{\partial t} + \mathbf{v} \cdot \nabla \rho \right), \quad (\text{D.9})$$

with $c_s^2 \equiv \left(\frac{\partial P}{\partial \rho} \right)_s$ the relativistic sound speed.

Now we introduce a linear perturbation in the variables ($\rho = \rho_0 + \rho_1$, $P = P_0 + P_1$ and $\mathbf{v} = \mathbf{v}_0 + \mathbf{v}_1$). Perturbed, linearized Lorentz factor is $\gamma = \gamma_0 + \gamma_0^3 \mathbf{v}_0 \cdot \mathbf{v}_1 / c^2$, and $\gamma^2 = \gamma_0^2 + 2\gamma_0^4 \mathbf{v}_0 \cdot \mathbf{v}_1 / c^2$. Considering a steady slab jet like that in Figure 2.1 in pressure equilibrium with the ambient medium, and surrounded by a smooth transition or shear layer (with $v_{0z}(x)$ and $\rho_0(x)$), equation (D.5) results:

$$\gamma_0 \left(\frac{\partial \rho_1}{\partial t} + v_{0z} \frac{\partial \rho_1}{\partial z} + v_{1x} \frac{\partial \rho_0}{\partial x} \right) + \rho_0 h_0 \left(\frac{\partial \gamma_1}{\partial t} + \frac{\partial \gamma_1 v_{0z}}{\partial z} + \frac{\partial \gamma_0 v_{1x}}{\partial x} + \frac{\partial \gamma_0 v_{1z}}{\partial z} \right) = 0, \quad (\text{D.10})$$

equation (D.4):

$$\gamma_0^2 \rho_0 h_0 \left(\frac{\partial \mathbf{v}_1}{\partial t} + (\mathbf{v}_1 \cdot \nabla) \mathbf{v}_0 + (\mathbf{v}_0 \cdot \nabla) \mathbf{v}_1 \right) = -\nabla P_1 - \mathbf{v}_0 \frac{\partial P_1}{\partial t}, \quad (\text{D.11})$$

and equation (D.9):

$$\frac{\partial P_1}{\partial t} + \mathbf{v}_0 \cdot \nabla P_1 = c_s^2 \left(\frac{\partial \rho_1}{\partial t} + \mathbf{v}_0 \cdot \nabla \rho_1 + \mathbf{v}_1 \cdot \nabla \rho_0 \right). \quad (\text{D.12})$$

Assuming wave-like patterns for the perturbations $\propto x_1(x) e^{i(\omega t - k_z z)}$, where $x_1(x)$ contains the transversal dependence, we get, for equation (D.10):

$$i(\omega - k_z v_{0z}) \rho_1 + \frac{\partial(\rho_0 h_0 v_{1x})}{\partial x} + \rho_0 h_0 \left(i(\gamma_0^2 v_{0z}(\omega - k_z v_{0z}) - k_z) v_{1z} + \gamma_0^2 v_{0z} \frac{dv_{0z}}{dx} v_{1x} \right) = 0, \quad (\text{D.13})$$

equation (D.4), transversal direction (x):

$$\gamma_0^2 \rho_0 h_0 i(w - k_z v_{0z}) v_{1x} = -\frac{\partial P_1}{\partial x}, \quad (\text{D.14})$$

equation (D.4), axial direction (z):

$$\gamma_0^2 \rho_0 h_0 \left(i(w - k_z v_{0z}) v_{1z} + \frac{dv_{0z}}{dx} v_{1x} \right) = i(k_z - w v_{0z}) P_1, \quad (\text{D.15})$$

and equation (D.12):

$$i(wt - k_z z) P_1 = c_{s0}^2 \left(i(w - k_z v_{0z}) \rho_1 + \frac{d\rho_0}{dx} v_{1x} \right). \quad (\text{D.16})$$

Expressing P_1 in terms of the variables v_{1x} in equation (D.14), v_{1z} in equation (D.15) and ρ_1 in equation (D.16), bringing these expressions to equation (D.13), and after some algebra, we find the following differential equation for pressure perturbation:

$$\begin{aligned} \frac{\partial^2 P_1}{\partial x^2} + \left(\frac{2\gamma_0^2 \frac{dv_{0z}}{dx} (k_z - w v_{0z})}{(w - k_z v_{0z})} - \frac{\frac{d\rho_0}{dx}}{\rho_0 h_0} \right) \frac{\partial P_1}{\partial x} + \\ \gamma_0^2 \left(\frac{(w - k_z v_{0z})^2}{c_{s0}^2} - (k_z - w v_{0z})^2 \right) P_1 = 0. \end{aligned} \quad (\text{D.17})$$

D.2 Cylindrical rotating jet

If we consider a cylindrical jet, with angular velocity $v_\theta \neq 0$ ($v_{0z}(r)$, $v_{0\theta}(r)$ and $\rho_0(r)$), equation (D.10) would read:

$$\begin{aligned} \gamma_0 \left(\frac{\partial \rho_1}{\partial t} + \frac{v_{0\theta}}{r} \frac{\partial \rho_1}{\partial \theta} + v_{0z} \frac{\partial \rho_1}{\partial z} + v_{1r} \frac{\partial \rho_0}{\partial r} \right) + \\ \rho_0 h_0 \left(\frac{\partial \gamma_1}{\partial t} + \frac{1}{r} \frac{\partial (\gamma_1 v_{0\theta})}{\partial \theta} + \frac{\partial (\gamma_1 v_{0z})}{\partial z} \right) + \\ \rho_0 h_0 \left(\frac{1}{r} \frac{\partial (r \gamma_0 v_{1r})}{\partial r} + \frac{1}{r} \frac{\partial (\gamma_0 v_{1\theta})}{\partial \theta} + \frac{\partial (\gamma_0 v_{1z})}{\partial z} \right) = 0. \end{aligned} \quad (\text{D.18})$$

Considering wave-like perturbations $\propto x_1(r) e^{i(wt - n\theta - k_z z)}$, where $x_1(r)$ contains the radial dependence of the perturbation and n is the azimuthal wavenumber (an integer number of waves around the circumference of the cylinder),

previous equation would result:

$$\begin{aligned} & \gamma_0 i \left(w - \frac{n}{r} v_{0\theta} - k_z v_{0z} \right) \rho_1 + \gamma_0 v_{1r} \frac{d\rho_0}{dr} + \\ & \rho_0 h_0 \gamma_0^3 i \left(w - \frac{n}{r} v_{0\theta} - k_z v_{0z} \right) (v_{0\theta} v_{1\theta} + v_{0z} v_{1z}) + \\ & \rho_0 h_0 \left(\frac{\gamma_0 v_{1r}}{r} + v_{1r} \frac{d\gamma_0}{dr} + \gamma_0 \frac{\partial v_{1r}}{\partial r} - \frac{in}{r} \gamma_0 v_{1\theta} - ik_z \gamma_0 v_{1z} \right) = 0, \end{aligned} \quad (\text{D.19})$$

equation (D.4), radial direction (r):

$$\gamma_0^2 \rho_0 h_0 i \left(w - \frac{n}{r} v_{0\theta} - k_z v_{0z} \right) v_{1r} + \frac{\partial P_1}{\partial r} = 0, \quad (\text{D.20})$$

equation (D.4), azimuthal direction (θ):

$$\gamma_0^2 \rho_0 h_0 i \left(w - \frac{n}{r} v_{0\theta} - k_z v_{0z} \right) v_{1\theta} + \gamma_0^2 \rho_0 h_0 v_{1r} \frac{\partial v_{0\theta}}{\partial r} - \frac{in}{r} P_1 + iw v_{0\theta} P_1 = 0, \quad (\text{D.21})$$

equation (D.4), axial direction (z):

$$\gamma_0^2 \rho_0 h_0 i \left(w - \frac{n}{r} v_{0\theta} - k_z v_{0z} \right) v_{1z} + \gamma_0^2 \rho_0 h_0 v_{1r} \frac{\partial v_{0z}}{\partial r} - ik_z P_1 + iw v_{0z} P_1 = 0, \quad (\text{D.22})$$

and equation (D.12):

$$i \left(w - \frac{n}{r} v_{0\theta} - k_z v_{0z} \right) P_1 - c_{s0}^2 \left(i \left(w - \frac{n}{r} v_{0\theta} - k_z v_{0z} \right) \rho_1 + v_{1r} \frac{\partial \rho_0}{\partial r} \right) = 0. \quad (\text{D.23})$$

Substituting P_1 in terms of v_{1r} in equation (D.20), in terms of $v_{1\theta}$ in equation (D.21), of v_{1z} in equation (D.22) and ρ_1 in equation (D.23) and bringing all the resulting expressions to (D.19), we obtain:

$$\frac{\partial^2 P_1}{\partial r^2} + F_1(r) \frac{\partial P_1}{\partial r} + F_2(r) P_1 = 0, \quad (\text{D.24})$$

where $F_1(r)$ is:

$$F_1(r) = \frac{1}{r} - \frac{2 \frac{dv_{0\theta}}{dr} \left(\gamma_0^2 v_{0\theta} \left(w - \frac{n}{r} v_{0\theta} - k_z v_{0z} \right) + \frac{n}{r} \right)}{\left(w - \frac{n}{r} v_{0\theta} - k_z v_{0z} \right)} - \frac{2 \frac{dv_{0z}}{dr} \left(\gamma_0^2 v_{0z} \left(w - \frac{n}{r} v_{0\theta} - k_z v_{0z} \right) + k_z \right)}{\left(w - \frac{n}{r} v_{0\theta} - k_z v_{0z} \right)} - \frac{\frac{d\rho_0}{dr}}{\rho_0 h_0} + \frac{n}{r^2} \frac{v_{0\theta}}{\left(w - \frac{n}{r} v_{0\theta} - k_z v_{0z} \right)}, \quad (\text{D.25})$$

and $F_2(r)$:

$$F_2(r) = \frac{\left(w - \frac{n}{r} v_{0\theta} - k_z v_{0z} \right)^2 \gamma_0^2}{c_{s0}^2} + \left(\gamma_0^2 v_{0\theta} \left(w - \frac{n}{r} v_{0\theta} - k_z v_{0z} \right) + \frac{n}{r} \right) \left(w v_{0\theta} - \frac{n}{r} \right) + \left(\gamma_0^2 v_{0z} \left(w - \frac{n}{r} v_{0\theta} - k_z v_{0z} \right) + k_z \right) (w v_{0z} - k_z). \quad (\text{D.26})$$

D.3 Conical rotating jet

In the case of a jet expanding in a decreasing density/pressure atmosphere with constant opening angle, and following Hardee (1982), we use spherical coordinates. In this frame, r is the radial coordinate, θ is the polar angle, and ϕ is the azimuthal angle. We consider a pressure profile $P_0 = P_0(r)$, where the jet is in pressure equilibrium with the atmosphere at $r = ct..$ We consider polar density and velocity profiles, in order to account for shear layers, and radial velocity independent of the radius ($\rho_0 = \rho_0(r, \theta)$ and $\mathbf{v}_0 = \mathbf{v}_0(\theta)$). The velocity vector includes a rotation velocity: $\mathbf{v}_0 = (v_{0r}, 0, v_{0\phi})$, but we consider $v_{0\theta} = 0$, as a consequence of pressure equilibrium at constant radius. Equation (D.10) would thus be:

$$\begin{aligned} & \gamma_0 \left(\frac{\partial \rho_1}{\partial t} + v_{0r} \frac{\partial \rho_1}{\partial r} + \frac{v_{0\phi}}{r} \sin \theta \frac{\partial \rho_1}{\partial \phi} + v_{1r} \frac{\partial \rho_0}{\partial r} + \frac{v_{1\theta}}{r} \frac{\partial \rho_0}{\partial \theta} \right) + \\ & \rho_0 h_0 \left(\frac{\partial \gamma_1}{\partial t} + \frac{v_{1\theta}}{r} \frac{\partial \gamma_0}{\partial \theta} + v_{0r} \frac{\partial \gamma_1}{\partial r} + \frac{v_{0\phi}}{r \sin \theta} \frac{\partial \gamma_1}{\partial \phi} + \frac{2\gamma_1 v_{0r}}{r} + \frac{2\gamma_0 v_{1r}}{r} \right) + \\ & \rho_0 h_0 \left(\gamma_0 \frac{\partial v_{1r}}{\partial r} + \gamma_0 \frac{v_{1\theta} \cot \theta}{r} \frac{\partial v_{1\theta}}{\partial \theta} + \frac{\gamma_0}{r \sin \theta} \frac{\partial v_{1\phi}}{\partial \phi} \right) = 0. \quad (\text{D.27}) \end{aligned}$$

Considering wave-like perturbations $\propto x_1(\theta) e^{i(\omega t - n\phi - k_r r)}$, where $x_1(\theta)$ contains the radial dependence of the perturbation and n is the azimuthal wavenumber (an integer number of waves around the circumference of the conus), previous equation would result:

$$\begin{aligned} & \gamma_0 i \left(w - \frac{n}{r \sin \theta} v_{0\phi} - k_r v_{0r} \right) \rho_1 + \gamma_0 \left(v_{1r} \frac{\partial \rho_0}{\partial r} + v_{1\theta} \frac{\partial \rho_0}{\partial \theta} \right) + \\ & \rho_0 h_0 \left[\gamma_0^3 i \left(w - \frac{n}{r \sin \theta} v_{0\phi} - k_r v_{0r} \right) v_{0r} + \frac{2\gamma_0}{r} (\gamma_0^2 v_{0r}^2 + 1) - i k_r \right] v_{1r} + \\ & \rho_0 h_0 \left[\gamma_0^3 i \left(w - \frac{n}{r \sin \theta} v_{0\phi} - k_r v_{0r} \right) v_{0\phi} + \frac{2}{r} \gamma_0^3 v_{0r} v_{0\phi} - \frac{i n \gamma_0}{r \sin \theta} \right] v_{1\phi} + \\ & \rho_0 h_0 \left[\frac{1}{r} \frac{\partial \gamma_0}{\partial \theta} + \frac{\cot \theta}{r} \right] v_{1\theta} + \rho_0 h_0 \frac{\partial v_{1\theta}}{\partial \theta} = 0, \end{aligned} \quad (\text{D.28})$$

equation (D.4), polar direction (θ):

$$\gamma_0^2 \rho_0 h_0 i \left(w - \frac{n}{r \sin \theta} v_{0\phi} - k_r v_{0r} \right) v_{1\theta} + \frac{1}{r} \frac{\partial P_1}{\partial \theta} = 0, \quad (\text{D.29})$$

equation (D.4), radial direction (r):

$$\gamma_0^2 \rho_0 h_0 i \left(w - \frac{n}{r \sin \theta} v_{0\phi} - k_r v_{0r} \right) v_{1r} + \gamma_0^2 \rho_0 h_0 v_{1\theta} \frac{\partial v_{0r}}{\partial \theta} - i k_r P_1 + i w v_{0r} P_1 = 0, \quad (\text{D.30})$$

equation (D.4), azimuthal direction (ϕ):

$$\gamma_0^2 \rho_0 h_0 i \left(w - \frac{n}{r \sin \theta} v_{0\phi} - k_r v_{0r} \right) v_{1\phi} + \gamma_0^2 \rho_0 h_0 \frac{v_{1\theta}}{r} \frac{\partial v_{0\phi}}{\partial \theta} - \frac{i n}{r \sin \theta} P_1 + i w v_{0\phi} P_1 = 0, \quad (\text{D.31})$$

and equation (D.12):

$$\begin{aligned} & i \left(w - \frac{n}{r \sin \theta} v_{0\phi} - k_r v_{0r} \right) P_1 + v_{1r} \frac{\partial P_0}{\partial r} - \\ & c_{s0}^2 \left[i \left(w - \frac{n}{r \sin \theta} v_{0\phi} - k_r v_{0r} \right) \rho_1 + v_{1r} \frac{\partial \rho_0}{\partial r} + \frac{v_{1\theta}}{r} \frac{\partial \rho_0}{\partial \theta} \right] = 0. \end{aligned} \quad (\text{D.32})$$

Substituting P_1 in terms of $v_{1\theta}$ in equation (D.29), in terms of v_{1r} in equation (D.30), of $v_{1\phi}$ in equation (D.31) and ρ_1 in equation (D.32) and bringing all the resulting expressions to (D.28), we obtain:

$$\frac{\partial^2 P_1}{\partial \theta^2} + F_1 \frac{\partial P_1}{\partial \theta} + F_2 r^2 P_1 = 0, \quad (\text{D.33})$$

where F_1 is:

$$F_1 = -\frac{\partial \ln(\gamma_0)}{\partial \theta} - \frac{\partial \ln(\rho_0 h_0)}{\partial \theta} + \cot \theta - \frac{1}{i\sigma} \left(\frac{\partial v_{0r}}{\partial \theta} (C_r - ik_r) + \frac{\partial v_{0\phi}}{\partial \theta} \left(C_\phi - \frac{in}{r \sin \theta} \right) \right) - \frac{in v_{0\phi} \cot \theta}{\sin \theta}, \quad (\text{D.34})$$

and F_2 :

$$F_2 = -\frac{\gamma_0^2 (i\sigma)^2}{c_{s0}^2} + i(wv_{0r} - k_r)C_r + i \left(wv_{0\phi} - \frac{n}{r \sin \theta} \right) C_\phi, \quad (\text{D.35})$$

where we have used:

$$\sigma = w - \frac{n}{r \sin \theta} v_{0\phi} - k_r v_{0r}, \quad (\text{D.36})$$

$$C_r = \gamma_0^2 i\sigma v_{0r} + \frac{2}{r} (\gamma_0^2 v_{0r}^2 + 1) - ik_r + \frac{1}{c_{s0}^2 \rho_0 h_0} \frac{\partial P_0}{\partial r}, \quad (\text{D.37})$$

and

$$C_\phi = \gamma_0^2 i\sigma v_{0\phi} + \frac{2}{r} \gamma_0^2 v_{0r} v_{0\phi} - \frac{in}{r \sin \theta}. \quad (\text{D.38})$$

Equation (D.33) transforms into the following equation for the perturbation inside the jet, derived by Hardee (1982)

$$\sin^2 \theta \frac{\partial^2 P_1}{\partial \sin^2 \theta} + \sin \theta \frac{\partial P_1}{\partial \sin \theta} + P_1 \left[\beta^2(r) \frac{\sin^2 \theta}{\cos^2 \theta} - \frac{n^2}{\cos^2 \theta} \right] = 0, \quad (\text{D.39})$$

with:

$$\beta^2(r) = \frac{w^2 r^2}{c_{s0}^2} - k_r^2 r^2 - i \left(2k_r r + \frac{k_r r^2}{c_{s0}^2 \rho_0} \frac{\partial P_0}{\partial r} \right), \quad (\text{D.40})$$

if we consider a vortex sheet flow (no dependencies on θ), $v_{0\phi} = 0$, $\rho_0 h_0 \rightarrow \rho_0$, and $\gamma_0 \rightarrow 1$, i.e., sub-relativistic flows, both kinematically and thermodynamically.

Bibliography

- [1] Abraham, Z., Carrara, E.A., Zensus, J.A., Unwin, S.C. 1996, *A&AS*, **115**, 543
- [2] Abraham, Z., Romero, G.E. 1999, *A&A*, **344**, 61
- [3] Agudo, I., 2002, PhD Thesis, Instituto Astrofísico de Andalucía / Universidad de Granada
- [4] Agudo, I., Gómez, J.L., Martí, J.M^a, Ibáñez, J.M^a, Marscher, A.P., Alberdi, A., Aloy, M.A., Hardee, P.E. 2001, *ApJL*, **549**, 183
- [5] Aloy, M.A., 1999, PhD Thesis, Universitat de València
- [6] Aloy, M.A., Ibáñez, J.M^a, Martí, J.M^a, and Müller, E. 1999a, *ApJSS*, **122**, 151
- [7] Aloy, M.A., Pons, J.A., Ibáñez, J.M^a 1999b, *Comp. Phys. Comm.*, **120**, 115
- [8] Aloy, M.A., Gómez, J.L., Ibáñez, J.M^a, Martí, J.M^a, and Müller, E., 2000, *ApJL*, **528**, 85
- [9] Aloy, M.A., Ibáñez, J.M^a, Miralles, J.A., Urpin, V. 2002, *A&A*, **396**, 693
- [10] Amat, S., Aràndiga, F., Arnau, J.V., Donat, R., Mulet, P., Peris, R. 2002 *Aproximació numèrica*, Universitat de València
- [11] Appl, S. 1996, *A&A*, **314**, 995
- [12] Appl, S., Camenzind, M. 1992, *A&A*, **256**, 354
- [13] Asada, K., Inoue, M., Uchida, Y., Kamenno, S., Fujisawa, K., Iguchi, S., Mutoh, M. 2002, *PASJ*, **54**, L39

- [14] Attridge, J.M., Roberts, D.H., Wardle, J.F.C., 1999, *ApJL*, **518**, 87
- [15] Babadzhanlyants, M.K., Belokon, E.T. 1993, *AZh*, **70**, 241
- [16] Bahcall, J.N., Kirhakos, S., Schneider, D.P., Davis, R.J., Muxlow, T.W.B., Garrington, S.T., Conway, R.G., Unwin, S.C. 1995, *ApJL*, **452**, 91
- [17] Baum, S.A., Zirbel, E.L., and O'Dea, C.P. *ApJ*, 1995, **451**, 88
- [18] Begelman, M.C, Blandford, R.D., Rees, M.J. 1984, *RvMP*, **56**, 255
- [19] Blandford, R.D, Rees, M.J. 1974, *MNRAS*, **169**, 395
- [20] Blandford, R.D, Pringle, J.E. 1976, *MNRAS*, **176**, 443
- [21] Blandford, R.D, Znajek, R. 1977, *MNRAS*, **179**, 433
- [22] Blandford, R.D, Rees, M.J. 1978, *PhyS*, **17**, 265
- [23] Blandford, R.D., Königl, A. 1979, *ApJ*, **232**, 34
- [24] Blandford, R.D, Payne, D.G., 1982, *MNRAS*, **199**, 883
- [25] Blandford, R.D., 1994, in *ASP Conf. Ser., Vol. 54, Proc. 1st Stromlo Symp.: The Physics of Active Galaxies*, Bicknell, G.V., Dopita, M.A., Quinn, P.J., eds., 23
- [26] Blumen, W., Drazin, P., Billings, D. 1975, *J. Fluid Mech.*, **71**, 305
- [27] Bicknell, G.V. 1984, *ApJ* **286**, 68
- [28] Bicknell, G.V. 1994, *ApJ* **422**, 542
- [29] Biretta, J. A., Zhou, F., Owen, F. N., 1995, *ApJ*, **447**, 582
- [30] Biretta, J.A. 1996, in *Energy Transport in Radio Galaxies and Quasars*, Hardee, P.E., Bridle, A.H., and Zensus, J.A., eds., p.187
- [31] Biretta, J.A. 1999, Press Release.
- [32] Biretta, J.A., Junor, W., Livio, M. 2002, *NewAR*, **46**, 239
- [33] Birkinshaw, M. 1984, *MNRAS*, **208**, 887

- [34] Birkinshaw, M. 1991a, MNRAS, **252**, 505
- [35] Birkinshaw, M. 1991b, in *Beams and Jets in Astrophysics*, Hughes, P.A. ed., Cambridge, p.278
- [36] Bodo, G., Massaglia, S., Ferrari, A., and Trussoni, E. 1994, A&A, **283**, 655
- [37] Bodo, G., Massaglia, S., Rossi, P., Rosner, R., Malagoli, A., Ferrari, A. 1995, A&A, **303**, 281
- [38] Bodo, G., Rossi, P., Massaglia, S., Ferrari, A., Malagoli, A., Rosner, R. 1998, A&A, **333**, 1117
- [39] Bridle, A.H., Hough, D.H., Lonsdale, C.J., Burns, J.O., Laing, R.A. 1994, AJ, **108**, 766
- [40] Calvet , N. 2002, in *Accretion discs, jets and high energy phenomena in astrophysics*, Beskin, V., Henri, G., Menard, F., Pelletier, G., Dalibard, J., eds., EDP-Springer, p. 521
- [41] Camenzind, M. 2002, in *Accretion discs, jets and high energy phenomena in astrophysics*, Beskin, V., Henri, G., Menard, F., Pelletier, G., Dalibard, J., eds., EDP-Springer, p. 405
- [42] Celotti, A., Blandford, R.D. 2001, in Proceedings of *Black Holes in Binaries and Galactic Nuclei*. Kaper, L., van den Heuvel, E.P.J., Woudt, A.P., eds., 206
- [43] Celotti, A., Ghisellini, G., Chiaberge, M. 2001, MNRAS Letters, **321**, 1
- [44] Chandrasekhar, S., 1961, *Hydrodynamic and hydromagnetic stability*, Clarendon Press.
- [45] Colella, P., Woodward, P.R. 1984, J. Comput. Phys., **54**, 174
- [46] Cotton, W.D., Wittels, J.J., Shapiro, I.I., Marcaide, J., Owen, F.N., Spangler, S.R., Rius, A., Angulo, C., Clark, T. A., Knight, C. A. 1980, ApJL, **238**, 123
- [47] Courvoisier, T.J.L., Robson, E.I., Blecha, A., Bouchet,P., Falomo, R., Maisack, M., Staubert, R., Terasranta, H., Turner, M. J. L., Valtaoja, E., Walter, R., Wamsteker, W. 1990, A&A, **234**, 73

- [48] De Young, D.S., 1993, ApJL, **405**, 13
- [49] Donat, R., Font, J.A., Ibáñez, J.M^a, Marquina, A. 1998, J. Comput. Phys., **146**, 58
- [50] Donat, R., and Marquina, A. 1996, J. Comput. Phys., **125**, 42
- [51] Drazin, P.G., Davey, A., 1977, J. Fluid Mech., **82**, 255
- [52] Duncan, G.C., Hughes, P.A., 1994, ApJL, **436**, 119
- [53] Falle, S.A.E.G., 1991, MNRAS, **250**, 581
- [54] Falle, S.A.E.G., Komissarov, S.S. 1996, MNRAS, **278**, 586
- [55] Fanaroff, B.L., Riley, J.M. 1974, MNRAS, **167**, 31
- [56] Ferrari, A., Trussoni, E., and Zaninetti, L. 1978, A&A, **64**, 43
- [57] Ferrari, A., Trussoni, E., Zaninetti, L. 1981 MNRAS, **196**, 1051
- [58] Ferrari, A., Massaglia, S., Trussoni, E., MNRAS, 1982, **198**, 1065
- [59] Ferrari, A. 1998, ARA&A, **36**, 539
- [60] Font, J.A., Ibáñez, J.M^a, Marquina, A., and Martí, J.M^a 1994, A&A, **282**, 304
- [61] Ghez, A.M., Morris, M., Becklin, E.E., Tanner, A., Kremenek, T. 2000, Nature, **407**, 349
- [62] Ghisellini, G., Padovani, P., Celotti, A., and Maraschi, L., 1993, ApJ, **407**, 65
- [63] Ghisellini, G. 2000, in *Recent Developments in General Relativity*, Casciaro, B., Fortunato, D., Francaviglia, M., Masiello., A., eds., p.5
- [64] Ghisellini, G., and Celotti, A., A&A, 2001, **379**, L1
- [65] Gill, A.E., 1965, Phys. Fluids, **8**, 1428
- [66] Gómez, J.L., Alberdi, A., and Marcaide, J.M., A&A, 1993, **274**, 55
- [67] Gómez, J.L., Martí, J.M^a, Marscher, A.P., Ibáñez, J.M^a, Marcaide, J.M. 1995, ApJ, **449**, L19

- [68] Gómez, J.L., Martí, J.M^a, Marscher, A.P., Ibáñez, J.M^a, and Alberdi, A. 1997, ApJ, **482**, 33
- [69] Gómez, J.L., Marscher, A. P., Alberdi, A., Jorstad, S.G., García-Miró, C. 2000, Science, **289**, 2317
- [70] Hanasz, M., 1995, PhD Thesis, Nicholas Copernicus University, Toruń.
- [71] Hanasz, M., Sol, H. 1996, A&A, **315**, 355
- [72] Hanasz, M., 1997, in *Relativistic jets in AGNs*, Ostrowski, M., Sikora, M., Madejski, G., Begelman, M., eds, Kraków, p. 85 (astro-ph 9711275)
- [73] Hanasz, M., Sol, H. 1998, A&A, **339**, 629
- [74] Hanasz, M., Sol, H., Sauty, C. 2000, MNRAS, **316**, 494
- [75] Hardcastle, M.J., Worrall, D.M., Birkinshaw, M., Laing, R.A., Bridle, A.H. 2002, MNRAS, **334**, 182
- [76] Hardee, P.E. 1979, ApJ, **234**, 47
- [77] Hardee, P.E. 1982, ApJ, **257**, 509
- [78] Hardee, P.E. 1984, ApJ, **287**, 523
- [79] Hardee, P.E. 1986, ApJ, **303**, 111
- [80] Hardee, P.E. 1987, ApJ, **318**, 78
- [81] Hardee, P.E., Norman, M.L. 1988, ApJ, **334**, 70
- [82] Hardee, P.E., Rosen, A., Hughes, P.A., Duncan, G.C. 1998, ApJ, **500**, 559
- [83] Hardee, P.E. 2000, ApJ, **533**, 176
- [84] Hardee, P.E. 2001, in *Gamma-Ray Astrophysics*, Ritz, S., Gehrels, N., Shrader C.R., eds., 276
- [85] Hardee, P.E., Hughes, P.A., Rosen, A., Gomez, E.A. 2001, ApJ, **555**, 744
- [86] Hardee, P.E. 2003, ApJ, **597**, 798

- [87] Hardee, P.E., Hughes, P.A. 2003, ApJ, **583**, 116
- [88] Hardee, P.E., Walker, R.C., Gómez, J.L. 2005, ApJ, **620**, 646
- [89] Hartmann, L. 2002, in *Accretion discs, jets and high energy phenomena in astrophysics*, Beskin, V., Henri, G., Menard, F., Pelletier, G., Dalibard, J., eds., EDP-Springer, p. 549
- [90] Hazard, C., Mackey, M. B., Shimmins, A. J. 1963, Nature, **197**, 1037
- [91] Jester, S., Röser, H.J., Meisenheimer, K., Perley, R., Conway, R., 2001, A&A, **373**, 447
- [92] Jones, T.W., Tregillis, I.L., Ryu, D. 2002, NewAR, **46**, 381
- [93] Junor, W., Biretta, J.A., Livio, M. 1999, Nature, **401**, 891
- [94] Kataoka, J., Tanihata, Ch., Kawai, N., Takahara, F., Takahashi, T., Edwards, P.G., Makino, F. 2002, MNRAS, **336**, 932
- [95] Kirk, J.G., Duffy, P. 1999, J. Phys. G, **25**, 163
- [96] Koide, S., Shibata, K., Kudoh, T. 1998, ApJL, **495**, 63
- [97] Koide, S., Shibata, K., Kudoh, T., Meier, D.L. 2002, Science, **295**, 1688
- [98] Komissarov, S.S. 1990a, Ap&SS, **165**, 313
- [99] Komissarov, S.S. 1990b, Ap&SS, **165**, 325
- [100] Komissarov, S.S. 1994, MNRAS, **269**, 394
- [101] Komissarov, S.S. 2005, astro-ph/0501599 (submitted to MNRAS)
- [102] Körding, E., Falcke, H. 2001, in *The Role of VLBI in Astrophysics, Astrometry and Geodesy*, Mantovani, F., Kus, A., eds., NATO Science Series, **135**, p.107
- [103] Krichbaum, T.P., Witzel, A., Booth, R.S., Kus, A.J., Ronnang, B.O., Witzel, A., Graham, D.A., Pauliny-Toth, I.I.K., Quirrenbach, A., Hummel, C.A. et al. 1990, A&A, **237**, 3
- [104] Krichbaum, T.P., Alef, W., Witzel, A., Zensus, J.A., Booth, R.S., Greve, A., Rogers, A.E.E. 1998, A&A, **329**, 873

- [105] Krichbaum, T.P., Witzel, A., Zensus, J.A. 2000, in Proc. of the 5th EVN Symposium, J.E. Conway, A.J. Polatidis, R.S. Booth, Y.W. Philström, eds., Onsala Space Observatory, p.25
- [106] Krichbaum, T.P., Graham, D.A., Witzel, A., Zensus, J.A., Greve, A., Grewing, M., Marscher, A., Beasley, A. J. 2001, in *Particles and Fields in Radio Galaxies Conference*, Laing, A., Blundell, K.M., eds., Astronomical Society of the Pacific, 2001, p.184
- [107] Krolik, J.H., 1999. *Active Galactic Nuclei*. Princeton Series in Astrophysics.
- [108] Laing, R.A., 1996, IAUS, **175**, 147
- [109] Laing, R.A., Bridle, A.H. 2002a, MNRAS, **336**, 328
- [110] Laing, R.A., Bridle, A.H. 2002b, MNRAS, **336**, 1161
- [111] Lesch, H., Birk, G.T. 1998, ApJ, **499**, 167
- [112] LeVeque, R.J. 1992, *Numerical Methods for conservation Laws*, Birkhäuser Verlag, Basel
- [113] Lobanov, A.P., Zensus, J.A., Abraham, Z., Carrara, E., Unwin, S.C., Hirabayashi, H., Bushimata, T. 2000, AdSpR, **26**, 669
- [114] Lobanov, A.P., Zensus, J.A. 2001, Science, **294**, 128
- [115] Lobanov, A.P., Hardee, P.E., Eilek, J. 2003, NewAR, **47**, 629
- [116] Longair, M.S., 1994. *High Energy Astrophysics*, volume 2 (Stars, the Galaxy and the interstellar medium). Cambridge University Press.
- [117] Manolakou, K., Anastasiadis, A., Vlahos, L. 1999, A&A, **345**, 653
- [118] Marshall, H.L., Harris, D.E., Grimes, J.P., Drake, J.J., Fruscione, A., Juda, M., Kraft, R.P., Mathur, S., Murray, S.S., Ogle, P.M. et al. 2001, ApJL, **549**, 167
- [119] Marscher, A.P., Gear, W.K., 1985, ApJ, **298**, 114
- [120] Marscher, 1987, in *Superluminal Radio Sources*, ed. J.A. Zensus & T.J. Pearson (Cambridge: Cambridge University Press), 280

- [121] Marscher, A.P., Jorstad, S.G., Gómez, J.L., Aller, M.F., Teräsraanta, H., Lister, M.L., Stirling, A.M. 2002, *Nature*, **417**, 625
- [122] Martí, J.M^a, Müller, E., Font, J.A., Ibáñez, J.M^a 1995, *ApJL*, **448**, 105
- [123] Martí, J.M^a, Müller, E. 1996, *JCP*, **123**, 1
- [124] Martí, J.M^a, Müller, E., Font, J.A., Ibáñez, J.M^a, and Marquina, A. 1997, *ApJ*, **479**, 151
- [125] Meier, D.L., Godon, P., Edgington, S., Payne, D.G., Lind, K.R. 1998, in *ASP Conf. Ser., Vol. 144, IAU Colloquium 164: Radio Emission from Galactic and Extragalactic Compact Sources*, Zensus, J.A., Taylor, G.B., and Wrobel, J.M., eds., 51
- [126] Meier, D.L., Koide, S., Uchida, Y., 2001, *Science*, **291**, 84
- [127] Mimica, P., Aloy, M.A., Mller, E., Brinkmann, W. 2004, *A&A*, **418**, 947
- [128] Mirabel, I.F., Rodriguez, L.F. 1994, *Nature*, **371**, 46
- [129] Mirabel, I.F., Rodriguez, L.F. 1998, *Nature*, **392**, 673
- [130] Mirabel, I.F., Dhawan, V., Chaty, S., Rodriguez, L.F., Marti, J., Robinson, C.R., Swank, J., Geballe, T. 1998, *A&AL*, **330**, 9
- [131] Mirabel, I.F., Rodriguez, L.F. 1999, *Ann. Rev. A&A*, **37**, 409
- [132] Norman, M.L., Hardee, P.E. 1988, *ApJ*, **334**, 80
- [133] Payne, D.G, Cohn, H. 1985, *ApJ*, **191**, 655
- [134] Pearson, T.J., 1996, in *Energy Transport in Radio Galaxies and Quasars*, Hardee, P.E., Bridle, A.H., and Zensus, J.A., eds., p.97
- [135] Pearson, T.J., Unwin, S.C., Cohen, M.H., et al. 1981, *Nature*, **290**, 365
- [136] Penrose, R. 1969, *Nuovo Cimento*, **1**, 252
- [137] Perucho, M., Hanasz, M., Martí, J.M^a, Sol, H. 2004a, *A&A*, **427**, 415
- [138] Perucho, M., Martí, J.M^a, Hanasz, M., 2004b, *A&A*, **427**, 431

- [139] Perucho, M., Martí, J.M^a, Hanaasz, M., Miralles, J.A. 2005a, Phys. Rev. Lett., submitted
- [140] Perucho, M., Martí, J.M^a, Hanaasz, M. 2005b, A&A, submitted
- [141] Peterson, B.M., 1995. An Introduction to Active Galactic Nuclei. Cambridge University Press
- [142] Piran, T. 1999, PhR, **314**, 575
- [143] Press, W.H., Flannery, B.P., Teukolsky, S.A., Vetterling, W.T., 1992, *Numerical recipes*, Cambridge University Press.
- [144] Pudritz, R.E. 2002, in *Accretion discs, jets and high energy phenomena in astrophysics*, Beskin, V., Henri, G., Menard, F., Pelletier, G., Dalibard, J., eds., EDP-Springer, p. 187
- [145] Qian, S.J., Zhang, X.Z., Krichbaum, T.P., Zensus, J.A., Witzel, A., Kraus, A., Britzen, S., Ungerechts, H., Lisenfeld, U. 2001a, ChJAA, **1**, 236
- [146] Qian, S.J., Zhang, X.Z., Krichbaum, T.P., Kraus, A., Witzel, A., Zensus, J.A. 2001b, ChJAA, **1**, 296
- [147] Rawlings, S., Saunders, R. 1991, Nature, **349**, 138
- [148] Rawlings, S., Jarvis, M.J. 2004, MNRAS Letters, **355**, 9
- [149] Ray, T.P. 1982, MNRAS, **198**, 617
- [150] Rees, M.J. 1966, Nature, **211**, 468
- [151] Röser, H.J., Meisenheimer, K., Neumann, M., Conway, R.G., Perley, R.A. 2000, A&A, **360**, 99
- [152] Rybicki, G.B., and Lightman, A.P., 1979. Radiative processes in astrophysics. John Wiley and Sons, New York.
- [153] Rosen, A., Hughes, P.A., Duncan, G.C., Hardee, P.E. 1999, ApJ, **516**, 729
- [154] Roy Choudhury, S., and Lovelace, R.V.E. 1984, ApJ, **283**, 331
- [155] Sambruna, R.M., Urry, C.M., Tavecchio, F., Maraschi, L., Scarpa, R., Chartas, G., Muxlow, T. 2001, ApJL, **549**, 161

- [156] Scheck, L., Aloy, M.A., Martí, J.M^a, Gómez, J.L., Müller, E. 2002, MNRAS, **331**, 615
- [157] Scheuer, P.A.G. 1974, MNRAS, **166**, 513
- [158] Schmidt, M. 1963, Nature, **197**, 1040
- [159] Shibata, K., Uchida, Y. 1985 PASJ, **37**, 31
- [160] Shu, C.W., and Osher, S.J. 1988, J. Comput. Phys., **77**, 439
- [161] Snellen, I., and Best, P., 2003, New Atron. Rev., **47**, 225
- [162] Sol, H., Pelletier, G., Asseo, E., 1989, MNRAS, **237**, 411
- [163] Stawarz, L., Ostrowski, M., 2002, ApJ, **578**, 763
- [164] Stawarz, L. 2004, ApJ, **613**, 119
- [165] Swain, M.R., Bridle, A.H., and Baum, S.A., 1998, ApJL, **507**, 29
- [166] Synge, J.L. 1957, *The relativistic gas*, North-Holland, Amsterdam
- [167] Taub, A.H. 1978, Ann. Rev. Fluid Mechanics, **10**, 301
- [168] Trussoni, E. Ferrari, A., Zaninetti, L. 1983, in *Astrophysical jets. Proceedings of the International Workshop, Turin, Italy*, Dordrecht, Reidel, p. 281
- [169] Turland, B.D., and Scheuer, P.A.G. 1976, MNRAS, **176**, 421
- [170] Türler, M., Courvoisier, T.J.L., Paltani, S. 2000, A&A, **361**, 850
- [171] Urrin, V. 2002, A&A, **385**, 14
- [172] Urry, C.M., Padovani, P. 1995, PASP, **107**, 803
- [173] Walker, R.C., Benson, J.M., Unwin, S.C., Lystrup, M.B., Hunter, T.R., Pilbratt, G., Hardee, P.E. 2001, ApJ, **556**, 756
- [174] Wehrle, A.E., Pian, E., Urry, C.M., Maraschi, L., McHardy, I.M., Lawson, A.J., Ghisellini, G., Hartman, R.C., Madejski, G.M., Makino, F. 1998, ApJ, **497**, 178

[175] Woltjer, L., 1959, *ApJ*, **130**, 38.

[176] Zensus, J.A. 1997, *ARA&A*, **35**, 607

List of Figures

1.1	From the smallest to the largest. Jets in a forming star system (left, Hubble Space Telescope, HST) and in radiogalaxy Cygnus A (right, Very Large Array, NRAO).	6
1.2	Cygnus A, observed at different wavelengths. Extragalactic jets show strong self similarity in very different scales (Krichbaum et al. 1998).	7
1.3	Radiogalaxies 3C219 (FR II, left) and 3C31 (FR I, right) (NRAO).	9
1.4	The torus in the core of radiogalaxy NGC4261 (HST).	10
1.5	Schematic view of an AGN (Urry and Padovani 1995).	11
1.6	Caption from a simulation of jet formation in the surroundings of a SMBH; lines stand for magnetic field (Meier et al. 2001).	12
1.7	M87, from kiloparsec scales to the active nucleus (NRAO/AUI).	14
1.8	Observations of radio sources (quasar 3C279 at 22 GHz, left, and M87, right), showing superluminal motion. The outer component in 3C279 moved 25 projected light years during a six year interval and components in M87 move at about $6c$ (Wehrle et al. 1998, left, Biretta 1999, right).	15
1.9	Disk-jet connection. Emission at X-ray energies and radio wavelengths from an AGN., where correlation between X-ray dips and radio bursts was shown for 3C 120 (Marscher et al. 2002).	16
1.10	Jet in quasar 3C273 observed at different wavelengths.	17
1.11	Development of Kelvin-Helmholtz instability.	20
2.1	The geometry of the flow considered in the linear stability analysis and the numerical simulations (see Sect. 2.3), including a description of the boundary conditions.	28

- 2.2 Symmetric solutions of the dispersion relation for slab jets with $\gamma = 5$, $\varepsilon = 0.07 c^2$ and $\nu = 0.11$ (left panel) and $\gamma = 5$, $\varepsilon = 0.4 c^2$ and $\nu = 0.14$ (right panel). Top lines represent the real part of frequency, and lower lines stand for the corresponding imaginary part of the modes. In left panel colors identify real and imaginary parts of single modes as an example for the reader. 35
- 2.3 Same as Fig. 2.2 for jets with $\gamma = 5$, $\varepsilon = 6.1 c^2$ and $\nu = 0.44$ (left panel) and $\gamma = 5$, $\varepsilon = 60 c^2$ and $\nu = 0.87$ (right panel). . . 36
- 2.4 Same as Fig. 2.2 for jets with $\gamma = 10$, $\varepsilon = 0.4 c^2$ and $\nu = 0.14$ (left panel) and $\gamma = 20$, $\varepsilon = 0.4 c^2$ and $\nu = 0.14$ (right panel). . 37
- 2.5 Same as Fig. 2.2 for jets with $\gamma = 10$, $\varepsilon = 6.1 c^2$ and $\nu = 0.44$ (left panel) and $\gamma = 20$, $\varepsilon = 6.1 c^2$ and $\nu = 0.44$ (right panel). . 38
- 2.6 Same as Fig. 2.2 for jets with $\gamma = 10$, $\varepsilon = 60 c^2$ and $\nu = 0.87$ (left panel) and $\gamma = 20$, $\varepsilon = 60 c^2$ and $\nu = 0.87$ (right panel). . 39
- 2.7 Deformations of jets by Kelvin-Helmholtz instability modes (from Birkinshaw 1991b). 40
- 2.8 Linear growth of the amplitude of the pressure perturbation (in logarithmic scale) versus time (in units of R_j/c) for different resolutions. r_x stands for transversal resolution, r_z for longitudinal resolution, and m is the value which gives the shear layer steepness. 43
- 2.9 Evolution of the relative amplitudes of perturbations. Dotted line: pressure perturbation $((p_{max} - p_0)/p_0)$. Dashed line: longitudinal velocity perturbation in the jet reference frame $(0.5(v'_{z,max} - v'_{z,min}))$. Dash-dotted line: perpendicular velocity perturbation in the jet reference frame $(0.5(v'_{x,max} - v'_{x,min}))$. The search for maximum $((p_{max}, (v'_{x,max}, (v'_{z,max})$ and minimum $(v'_{x,min}, (v'_{z,min})$ values have been restricted to those numerical zones with jet mass fraction larger than 0.5. Solid line: linear analysis prediction for the growth of perturbation. Note that abscissae in the last column plots extend up to $t = 1000R_j/c$ and that ordinate values adapt to fit the scale of each plot. Arrows in the plot of Model A05 point to specific stages of evolution used to define t_{lin} , t_{sat} and t_{peak} (see text). 52

2.10	Pressure distribution at the end of linear phase for models B05 (left panel) and D05 (right panel). The continuous line corresponds to jet mass fraction equal to 0.5 and serves to distinguish jet and ambient media.	53
2.11	Snapshot around saturation of logarithmic maps of pressure, rest-mass density and specific internal energy and non-logarithmic Lorentz factor for model A05.	54
2.12	Same as Fig. (2.11) for models B05 (upper), C05 (middle) and D05 (lower).	55
2.13	Same as Fig. (2.11) for models B10 (upper), C10 (middle) and D10 (lower).	56
2.14	Same as Fig. (2.11) for models B20 (upper), C20 (middle) and D20 (lower).	57
2.15	Evolution of the mean width of the jet/ambient mixing layer with time for all the simulations. Different types of lines are used for models with different internal energies: Continuous line: model A; dotted line: model B; dashed line: model C; dashed-dotted line: model D. Line thickness increases with Lorentz factor (from 5, thinnest line, to 20 thickest one). A value of $5 R_j$ for the width of the mixing layer (horizontal dashed line) serves to classify the evolution of the different models.	59
2.16	Evolution of the jet particle fraction showing the development of mixing in two representative models. Left column (model B05): the ambient material carves its way through the jet making difficult the advance of the jet material which is suddenly stopped. Right column (model D05): the amount of ambient matter hampering the jet material is smaller and matter from the jet at the top of the jet crests is ablated by the ambient wind.	61
2.17	Pressure distribution at the onset of the jet/ambient surface distortion at the end of the saturation phase for models A05, B05, B10 and B20. The corresponding times are 355, 190, 370 and $765 R_j/c$. In the case of models A05, B05 and B10 this distortion leads to the formation of a shock.	62

- 2.18 Left panel: pressure perturbation amplitude in simulation D05 (dashed line) and D05 with the same initial relative amplitude as model A05 (dotted line); the similarity between pressure peak values can be observed. Right panel: normalized axial momentum in the jet versus time (the lines correspond to the same simulations as in left panel); the final axial momentum is around 40% in both cases. 63
- 2.19 Snapshot in the mixing phase of logarithmic maps of pressure, jet mass fraction and specific internal energy and non-logarithmic Lorentz factor for model D05, started with an initial relative amplitude of the pressure perturbation equal to that of model A05. Compare this figure with lower panel in Fig. 2.27. 64
- 2.20 Time evolution of the maxima of the transversal Mach number of the jet with respect to the unperturbed ambient medium, $M_{j,\perp}$. See text for further explanations. Lines are as in Figure 2.15. 65
- 2.21 Same as Fig. 2.20 for models F, G, H, I, J, K and L. Lines are as in Figure 2.22. 66
- 2.22 Same as Fig. 2.15, for models F, G, H, I, J, K and L. Different types of lines are used for models with different internal energies: Continuous line: model F; dotted line: model G; dashed line: model H; thick dotted line: model I; thick dashed line: model J; thick dashed-dotted line: model K; thick dash-dot-dot line: model L. A value of $5 R_j$ for the width of the mixing layer (horizontal dashed line) serves to classify the evolution of the different models. 67
- 2.23 Evolution of the total longitudinal momentum in the jet as a function of time for all the simulations. Lines represent the same models than in Fig. 2.15. The long-dashed horizontal line serves us to identify those models transferring more than 50% of the initial jet momentum to the ambient. 68
- 2.24 Same as Fig. 2.23 for models F, G, H, I, J, K and L. Lines represent the same models than in Fig. 2.22. The long-dashed horizontal line serves us to identify those models transferring more than 50% of the initial jet momentum to the ambient. . . 69

2.25 Evolution of the total transversal momentum in the jet as a function of time for all the simulations. Lines represent the same models than in Fig. 2.15. Left panel: models A05, B05, B10, C05, D05. Right panel: B20, C10, C20, D10, D20. Note the change in both horizontal and vertical scales between the two panels. 70

2.26 Snapshot in the mixing phase of logarithmic maps of pressure, jet mass fraction and specific internal energy and non-logarithmic Lorentz factor for model A05. Only the top half of the jet is shown. 71

2.27 Same as Fig. (2.26) for models B05 (upper; only top half of the model shown), C05 (middle) and D05 (lower). 72

2.28 Same as Fig. (2.26) for models B10 (upper; only top half), C10 (middle) and D10 (lower; only top half). 73

2.29 Same as Fig. (2.26) for models B20 (upper), C20 (middle) and D20 (lower; only top half of the model shown). 74

2.30 Same as Fig. (2.26) for models F (upper), G (middle) and H (lower). Only top half of the model shown. 75

2.31 Same as Fig. (2.26) for models I (upper), and J (middle) and K (lower); only top half of the model shown for I). 76

2.32 Same as Fig. (2.26) for model and L; only top half of the model shown. 77

2.33 Longitudinal averaged profiles of gas pressure for all models. Different types of lines are used for models with different internal energies: Continuous line: model A; dotted line: model B; dashed line: model C; dashed-dotted line: model D. Line thickness increases with Lorentz factor (from 5, thinnest line, to 20 thickest one). 78

- 2.34 Transversal averaged profiles of relevant physical quantities at the end of simulations B05 and D05. Left column: tracer, f (full line), rest mass density, ρ_0 (dotted line), specific internal energy ε (dashed line) and jet internal energy density, e ($= \rho_0 \varepsilon f$; dash-dot line). Right column: longitudinal velocity, v_z (full line), Lorentz factor normalized to its initial value, γ/γ_0 (dotted line) and longitudinal momentum normalized to its initial value, S/S_0 . The upper plots represent the model B05 and the lower plots represent D05. Note that the values of e are multiple by 10 for model B05 and divided by 10 for model D05. The values of ε for the model D05 are divided by 100. 79
- 2.35 Same plots as 2.15 (left) and 2.23 (right) for models C16 (solid line), C32 (dotted line), C64 (dashed line) and C128 (dash-dotted line). 83
- 2.36 Snapshots at $t = 375R_j/c$ of logarithmic maps of pressure, jet mass fraction and specific internal energy and non-logarithmic Lorentz factor for models for for models C16 (upper) and C32 (lower). 84
- 2.37 Same as Fig. 2.36 for models C64 (upper) and C128 (lower). . . 85
- 2.38 Longitudinal averaged profiles of relevant physical quantities for models C16 (thin lines) and C128 (thick lines) in the last snapshot of simulation C128 ($t = 375R_j/c$). Left panel: tracer (full line), rest mass density (dotted line) and internal energy divided by 10 (dashed line). Mixing produces a denser and colder jet in model C128. Right panel: longitudinal velocity (full line), Lorentz factor normalized to its initial value (dotted line) and longitudinal momentum normalized to its initial value (dashed line). 86
- 2.39 Square root of the jet-to-ambient enthalpy ratio versus jet Lorentz factor. Symbols represent different non-linear behaviors: crosses stand for shock disrupted jets (cold, slow jets, along with tenuous, hot, moderately fast or slow ones); diamonds for unstable, hot, fast jets; triangles for relatively stable hot, slow, and squares for stable, warm, fast, along with hot, tenuous, faster jets. 87

2.40 Antisymmetric solutions of Equation 2.26 for slab jets B05 (left panel) and B20 (right panel). In left panel colors identify real and imaginary parts of single modes as an example for the reader. 91

2.41 Same as Fig. 2.40 for models D05 (left panel) and D20 (right panel) 92

2.42 Evolution of the relative amplitudes of perturbations for models B05 (left panel) and B20 (right panel). Dotted line: pressure perturbation. Dashed line: longitudinal velocity perturbation in the jet reference frame. Dash-dotted line: perpendicular velocity perturbation in the jet reference frame. Definitions are like those in Fig 2.9. 92

2.43 Same as Fig 2.42 for models D05 (left panel) and D20 (right panel). 93

2.44 Upper left panel shows mixing layer width, upper right panel is for relative axial momentum. Dotted thin line stands for model B05, dotted thick for B20, dash-dot thin for D05 and dash-dot thick for D20. 93

2.45 Same as Fig. (2.26) for models B05 (upper) and D05 (lower) perturbed with first body antisymmetric mode, at the end of simulations. 95

2.46 Same as Fig. 2.45 for models B20 (upper) and D20(lower). 96

3.1 Dependence of mode growth rates with jet specific internal energy, jet Lorentz factor and shear-layer parameter m . Top panels correspond to Model D20 with $m = 25$ (panel a) and $m = 8$ (panel b). Panel c: Model B20 with $m = 25$. Panel d: Model D05 with $m = 25$ 101

3.2 Two-dimensional panels of different pressure perturbation structures for a detail of Model D20. Left panel: vortex sheet dominant mode (low order reflection mode) at a given wavelength (from linear solution). Central panel: Dominant mode (high order reflection mode) at the same wavelength when $m = 25$ shear layer is included (also from linear solution). Right panel: Pressure perturbation map from numerical simulation. 102

3.3 Solution for the shear layer stability problem of a slab jet with the parameters of B05 and $m = 8$. Left panel: antisymmetric; right panel: symmetric. 103

3.4	Same as Fig. 3.3 for B05 and $m = 25$. Left panel: antisymmetric; right panel: symmetric.	104
3.5	Same as Fig. 3.3 for the symmetric case of B05 and $m = 2000$ (left panel) compared to the vortex sheet solution (right panel)	104
3.6	Same as Fig. 3.3 for B20 and $m = 8$. Left panel: antisymmetric; right panel: symmetric.	105
3.7	Same as Fig. 3.3 for B20 and $m = 25$. Left panel: antisymmetric; right panel: symmetric.	105
3.8	Same as Fig. 3.3 for D05 and $m = 8$. Left panel: antisymmetric; right panel: symmetric.	106
3.9	Same as Fig. 3.3 for D05 and $m = 25$. Left panel: antisymmetric; right panel: symmetric.	106
3.10	Same as Fig. 3.3 for D20 and $m = 8$. Left panel: antisymmetric; right panel: symmetric.	107
3.11	Same as Fig. 3.3 for D20 and $m = 25$. Left panel: antisymmetric; right panel: symmetric.	107
3.12	Same as Fig. 3.3 for the symmetric case of D20 and $m = 200$ (left panel) compared to the vortex sheet solution (right panel).	108
3.13	Same as Fig. 3.3 for A2.5 (see Table 3.1) and $m = 25$. Left panel: antisymmetric; right panel: symmetric.	108
3.14	Same as Fig. 3.3 for A10 (see Table 3.1) and $m = 25$. Left panel: antisymmetric; right panel: symmetric.	109
3.15	Same as Fig. 3.3 for B2.5 (see Table 3.1) and $m = 25$. Left panel: antisymmetric; right panel: symmetric.	109
3.16	Same as Fig. 3.3 for B10 (see Table 3.1) and $m = 25$. Left panel: antisymmetric; right panel: symmetric.	110
3.17	Same as Fig. 3.3 for D2.5 (see Table 3.1) and $m = 25$. Left panel: antisymmetric; right panel: symmetric.	110
3.18	Same as Fig. 3.3 for D10 (see Table 3.1) and $m = 25$. Left panel: antisymmetric; right panel: symmetric.	111
3.19	Snapshot in the mixing phase of logarithmic maps of pressure, jet mass fraction and specific internal energy and non-logarithmic Lorentz factor for model C05 (see Chapter 2) with four symmetric eigenmodes excited.	114
3.20	Same as Fig. 3.19 but for the case four sinusoidal perturbations with the same wavelengths as eigenmodes excited there.	114

- 3.21 Evolution of the relative amplitudes of perturbations. Dotted line: pressure perturbation. Dashed line: longitudinal velocity perturbation in the jet reference frame. Dash-dotted line: perpendicular velocity perturbation in the jet reference frame. Definitions are like those in Fig 2.9. Left panel is for perturbed eigenmodes simulation and right panel is for that with sinusoidal perturbations. 115
- 3.22 Left panel: evolution of total longitudinal momentum in the jet versus time. Right panel: evolution of the mean width of the jet/ambient mixing layer with time. Dotted line: eigenmodes. Dashed line: sinusoidal perturbation. 115
- 3.23 Evolution of the relative amplitudes of perturbations (models **A2.5** and **B2.5**). Dotted line: pressure perturbation ($(p_{max} - p_0)/p_0$). Dashed line: longitudinal velocity perturbation in the jet reference frame ($0.5(v'_{z,max} - v'_{z,min})$). Dash-dotted line: perpendicular velocity perturbation in the jet reference frame ($0.5(v'_{x,max} - v'_{x,min})$). The search for maximum (p_{max} , $v'_{x,max}$, $v'_{z,max}$) and minimum ($v'_{x,min}$, $v'_{z,min}$) values have been restricted to those numerical zones with jet mass fraction larger than 0.5. 118
- 3.24 Same as Fig. 3.23 for models **D2.5** and **B05**. 118
- 3.25 Same as Fig. 3.23 for models **D05** and **A10**. 119
- 3.26 Same as Fig. 3.23 for models **B10** and **D10**. 119
- 3.27 Same as Fig. 3.23 for models **B20** and **D20**. 120
- 3.28 Upper panels: pressure and perpendicular velocity perturbation at late stages of linear phase (model D20). Lower panels: Generic perturbation distribution extracted from one resonant mode from linear stability analysis (pressure perturbation and perpendicular velocity perturbation). Oblique waves in upper panels are the result of longer wavelength modes, whereas in bottom panel, only the resonant mode has been plotted, so no oblique waves appear. See also 3.2. 122

- 3.29 Schlieren plots showing waves in the linear regime in models **B05** (left) and **B20** (right). Long wavelength structures in **B05** are apparent, contrary to small structures in **B20**. These plots represent a negative exponential of the density gradient times an arbitrary factor chosen for the sake of clarity ($\exp(-k|\nabla\rho|)$, with $k = 30$). Thus 1.0 means no density gradient and the lowest value stands for maximum density gradient. 123
- 3.30 Snapshots of logarithm of pressure (left) and Lorentz factor (right) for **B25** (upper panels), **D05** (center panels) and **D10** (bottom panels) at t_{sat} , where irregular structures caused by mode competition are observed. 125
- 3.31 Schlieren plots showing waves in the saturation phase and transition to non-linear regime for models **B05** (left panels) and **B20** (right panels). 126
- 3.32 Transversal Mach number in simulations (see text for definition). Solid line $\gamma = 2.5$; dotted line $\gamma = 5.0$; dashed line $\gamma = 10.0$; dash-dot line $\gamma = 20.0$. Thinner line is for models A and thickest is for models D, with B in between. Left panel shows models **A2.5**, **B2.5**, **B05** and **B10**, and right panel shows models **A10**, **B20**, **D2.5**, **D05**, **D10** and **D20**. 127
- 3.33 Evolution of the mean width of the jet/ambient medium layer (for tracer values between 0.05 and 0.95) with time for all simulations. Lines represent the same models as in Fig. 3.32. A value of $5 R_j$ for the width of the mixing layer (horizontal dashed line) serves to classify the evolution of the different models. . . 128
- 3.34 Evolution of the normalized total longitudinal momentum in the jet as a function of time. Lines represent the same models as in Fig. 3.32. The long-dashed horizontal line serves us to identify those models transferring more than 50 % of the initial jet momentum to the ambient. 129
- 3.35 Evolution of the total transversal momentum in the jet as a function of time for all the simulations. Lines represent the same models than in Fig. 3.32. 130

3.36	Longitudinal averaged profiles of gas pressure for all models. Different types of lines are used for models with different internal energies: Continuous line is used for Lorentz factor 2.5; dotted line for Lorentz factor 5; dashed line for Lorentz factor 10; dashed-dotted line for Lorentz factor 20. Line thickness increases with internal energy (from model A, thinnest line, to D thickest one).	131
3.37	Snapshot at the last frame of the simulation of logarithmic maps of pressure, jet mass fraction and specific internal energy and non-logarithmic Lorentz factor for model A2.5 (upper) and B2.5 (lower).	133
3.38	Snapshot at the last frame of the simulation of logarithmic maps of pressure, jet mass fraction and specific internal energy and non-logarithmic Lorentz factor for models D2.5 (upper) and B05 (lower).	134
3.39	Snapshot at the last frame of the simulation of logarithmic maps of pressure, jet mass fraction and specific internal energy and non-logarithmic Lorentz factor for models D05 (upper) and A10 (lower).	135
3.40	Snapshot at the last frame of the simulation of logarithmic maps of pressure, jet mass fraction and specific internal energy and non-logarithmic Lorentz factor for models B10 (upper) and D10 (lower).	136
3.41	Snapshot at the last frame of the simulation of logarithmic maps of pressure, jet mass fraction and specific internal energy and non-logarithmic Lorentz factor for models B20 (upper) and D20 (lower).	137
3.42	Schlieren plots showing waves in the non-linear regime for models B05 (left panels) and B20 (right panels).	138
3.43	Solutions for the temporal stability problem of the pinching mode in cylindrical coordinates. Left panel: model B05. Right panel: model D05.	139
3.44	Same as Fig. 3.43. Left panel: model B20. Right panel: model D20.	140

- 3.45 Left panel shows transversal relativistic Mach number as defined in Chapter 2 and right panel shows evolution of axial momentum in the jet and right panel stands for transversal momentum for one mode simulations. Dotted thin line stands for model B05, dotted thick for B20, dash-dot thin for D05 and dash-dot thick for D20. 140
- 3.46 Snapshot at the last frame of the simulation of logarithmic maps of pressure, jet mass fraction and specific internal energy and non-logarithmic Lorentz factor for one mode cylindrical models B05 (upper) and D05 (lower). 141
- 3.47 Snapshot at the last frame of the simulation of logarithmic maps of pressure, jet mass fraction and specific internal energy and non-logarithmic Lorentz factor for one mode cylindrical models B20 (upper) and D20 (lower). 142
- 3.48 Pressure and axial and radial velocity perturbation evolution for several modes simulations. Left panel: model B05. Right panel: model D05. 143
- 3.49 Same as Fig. 3.48. Left panel: model B20. Right panel: model D20. 143
- 3.50 Left panel shows transversal relativistic Mach number as defined in Chapter 2 and right panel is for relative axial momentum (several mode simulations). Dotted thin line stands for model B05, dotted thick for B20, dash-dot thin for D05 and dash-dot thick for D20. 144
- 3.51 Snapshot at the last frame of the simulation of logarithmic maps of pressure, jet mass fraction and specific internal energy and non-logarithmic Lorentz factor for cylindrical models B05 (upper) and D05 (lower). 145
- 3.52 Snapshot at the last frame of the simulation of logarithmic maps of pressure, jet mass fraction and specific internal energy and non-logarithmic Lorentz factor for cylindrical models B20 (upper) and D20 (lower). 146

- 3.53 Averaged transversal structure in the final state of the jets corresponding to models **A2.5** (upper panels), **D10** (middle) and **B20** (bottom). Left panels (thermodynamical quantities): solid line, tracer; dotted line, rest mass density; dashed line, specific internal energy. Right panels (dynamical quantities): solid line, longitudinal velocity; dotted line, lorentz factor normalized to the initial value in the jet; dashed line, longitudinal momentum normalized to the initial value in the jet. Specific internal energy for model **D10** has been divided by 100 to fit in the scale. 149
- 3.54 Relativistic Mach number (M_j) versus Lorentz factor (γ) of the simulated models here and in Chapter 2. Symbols represent different non-linear behaviors: crosses stand for UST1 disrupted jets (low relativistic Mach number and low Lorentz factor); triangles for UST2 jets (moderately fast and supersonic), and squares for ST jets (highly supersonic and fast jets). Models where two different points have been used are those with a different evolution in simulations presented here and those from Chapter 2 (see text). 151
- 4.1 Optical image of quasar 3C273 (left), where the jet is also seen, and composition of optical and radio images (right). 160
- 4.2 VSOP image of parsec scale jet in 3C 273 (from LZ01). In the left corner, we can see some transversal cuts to which the double gaussians are fitted. 162
- 4.3 Structure of perturbations (axial and transversal cuts) in a generic 3D jet, induced by eq (4.3). Top left: pinching mode ($n = 0$). Top right: helical mode ($n = 1$). Bottom left: elliptic mode ($n = 2$). Bottom right: triangular mode ($n = 3$). 165
- 4.4 Map of pressure perturbation transversal cuts in arbitrary units, values increasing from dark to lighter colors (to be compared with Fig. 4.3). Solid line indicates $v_z = 0.8c$ contour. Three left panels: Cuts at $35 R_j$, $t = 70, 140, 200 R_j/c$ where elliptical mode rotation is apparent. Three right panels: Cuts at $105 R_j$, $t = 210, 220, 240 R_j/c$ where helical mode rotation is apparent. 166
- 4.5 Longitudinal cut of pressure perturbation at $R_j/2$ in symmetric positions with respect to the jet axis at $t = 250 R_j/c$. Helical (antisymmetric) structures of 4 and $25 R_j$ and an elliptic (symmetric) one of $50 R_j$ are apparent. 166

4.6	Map of Lorentz factor distribution of a portion of the jet at a time before disruption, where a large amplitude wave is apparent (top panel, $t = 320 R_j/c$) and at the last frame (bottom panel, $t = 1097 R_j/c$). Coordinates are in jet radii. Note that the vertical scale size is increased by a factor of 4 for the sake of clarity.	168
4.7	Longitudinal cuts of pressure perturbation at $r \sim 0.0625 R_j$ in symmetric positions (dashed and dotted lines) with respect to the jet axis at $t = 40 R_j/c$	173
4.8	Longitudinal cuts of pressure perturbation at $r \sim R_j$ in symmetric positions (dashed and dotted lines) with respect to the jet axis at $t = 40 R_j/c$	174
4.9	Surface plot of Lorentz factor $\gamma = 2.5$ at $t = 40 R_j/c$	175
4.10	Surface plot of Lorentz factor $\gamma = 3.0$ at $t = 40 R_j/c$	175
4.11	Schematic plot of the jet 3C31 as shown in Laing and Bridle (2002a), compared with an image of the inner part of the source.	178
4.12	Initial profiles of atmospheric rest mass density (left) and pressure (right).	182
4.13	Left panel stands for bow shock position, and right panel for bow shock head pressure. See text.	185
4.14	Top left panel stands for bow shock velocity, and top right panel for bow shock Mach number. Bottom panels stand for mean cavity pressure (left) and cavity radius versus its length (right). See text.	186
4.15	Top left panel stands for the mean cavity radius, and top right panel for the mean jet radius (different lines stand for the different criteria used to fix the jet head position: solid line is for tracer $f = 0.01$, dotted line for $f = 0.1$, dashed line for $f = 0.5$ and dash-dotted line for $f = 0.9$). Bottom panels stand for cavity shape (left) and jet shape (right). See text.	187
4.16	Logarithm of rest mass density (upper panel) and jet mass fraction (tracer, lower panel) at the last frame of the simulation in this work. Coordinates are in parsecs (from injection in the grid), rest mass density ranges from $\rho = 3.1 \cdot 10^{-8}$ to $\rho = 0.38$ in the units specified in the text, and jet mass fraction ranges between $f = 0$ and $f = 1$	188

4.17	Lorentz factor (upper panel), and <i>emission</i> in arbitrary units (see text, lower panel) at the last frame of the simulation in this work. Coordinates are in parsecs (from injection in the grid), maximum Lorentz factor is $\gamma = 5.31$	190
4.18	Different profiles of variables on the jet axis at the last frame. (a) Rest mass density ($\rho_{a,c}$), (b) pressure ($\rho_{a,c} c^2$, dotted line is the original atmospheric pressure on the axis), (c) specific internal energy (c^2), (d) temperature (K). z' stands for the distance to the source ($z + 500$ pc).	192
4.19	Different profiles of variables on the jet axis at the last frame. (a) Emission (code units, see text), (b) Lorentz factor, (c) axial velocity (c), (d) tracer. z' stands for the distance to the source ($z + 500$ pc).	193
4.20	Profiles of radially averaged variables, weighted with the tracer and counting only those cells where the axial velocity is greater than zero. (a) rest mass density ($\rho_{a,c}$, in this plot, due to the logarithmic scale, material ahead of the shock -ambient material only- is not weighted with the tracer in order to avoid zeros), (b) pressure ($\rho_{a,c} c^2$, dotted line is the original atmospheric pressure on the axis), (c) emission (the inner part is omitted in order to stress the emission downstream), (d) Lorentz factor. z' stands for the distance to the source ($z + 500$ pc).	194
4.21	Jet radius versus distance in the last frame. Jet radius is computed taking the outermost position where the axial velocity is larger than $0.3c$. The boundaries between regions are marked with dashed vertical lines; dotted lines indicate fitted parts in order to obtain opening angles.	196
C.1	Schematic view of superluminal motion and apparent velocity versus viewing angle for different flow speeds. Taken from web page http://parsnip.wooster.edu/thesis/html/node14.html . . .	218

List of Tables

- 2.1 Equilibrium parameters of different simulated jet models. The listed parameters are: γ - jet Lorentz factor, ρ_{0j} - rest mass density, ε_j and ε_a - specific internal energies of jet and ambient medium, c_{sj} , c_{sa} - the sound speeds in jet and ambient medium, p - pressure, ν , η - relativistic density and enthalpy contrasts and M_j - the jet Mach number. All the quantities in the table, except the last column, are expressed in units of the ambient density, ρ_{0a} , the speed of light, c , and the jet radius, R_j . Parameters for the new set of simulations are shown in the lower part of the table. 46
- 2.2 Solutions of the dispersion relation (Eq. 2.26), corresponding to fastest growing first reflection mode, taken as input parameters for numerical simulations. The primes are used to assign wavenumber and complex frequency in the reference frame co-moving with jet. All the quantities in the table, except the last column, are expressed in units of the ambient density, ρ_{0a} , the speed of light, c , and the jet radius, R_j . Parameters for the new set of simulations are shown in the lower part of the table. . . 47

2.3	Times for the different phases in the evolution of the perturbed jet models. t_{lin} : end of linear phase (the amplitudes of the different quantities are not constant any longer). t_{sat} : end of saturation phase (the amplitude of the transverse speed perturbation reaches its maximum). t_{mix} : the tracer starts to spread. t_{peak} : the peak in the amplitude of the pressure perturbation is reached. t_{fmix} : external material reaches the jet axis. t_{mex} : the jet has transferred to the ambient a 1% of its initial momentum. t_{meq} : longitudinal momentum in the jet and the ambient reach equipartition. $t_{\text{sat}}^{\text{dyn}}$: saturation time in dynamical time units and in the jet reference frame. Δ_{peak} : relative value of pressure oscillation amplitude at the peak (see Fig. 2.9). Note that, as a general trend, $t_{\text{lin}} < t_{\text{mex}} \approx t_{\text{mix}} < t_{\text{sat}} < t_{\text{peak}} < t_{\text{fmix}} < t_{\text{meq}}$.	50
2.4	Times for different phases in the evolution of simulations C16, C32, C64 and C128. See Table 2.3 for the meaning of the times at the table entries.	82
3.1	Equilibrium parameters of different simulated jet models. The meaning of the symbols is as follows: γ : jet flow Lorentz factor; ε : specific internal energy; c_s : sound speed; p : pressure; ν : jet-to-ambient relativistic rest mass density contrast; η : jet-to-ambient enthalpy contrast; M_j : jet relativistic Mach number. Labels a and j refer to ambient medium and jet, respectively. All the quantities in the table are expressed in units of the ambient density, ρ_{0a} , the speed of light, c , and the jet radius, R_j .	112
3.2	$k_{0,1,2,3}$: excited longitudinal wavenumbers for each model (R_j^{-1}).	113
3.3	Dominant modes in the linear phase of the numerical simulations. w_{i,k_j} : maximum growth rate for the j -th wavenumber exited in the simulation (see Table 3.1). Left columns: symmetric mode; right columns: antisymmetric one. Growth rate values are in c/R_j units.	116
3.4	The dominant mode refers to the mode with the largest amplitude in rest mass density as derived from Fourier analysis of the box; they are written from larger to smaller amplitude when more than one is present. w_i : fitted pressure perturbation growth rate for the linear regime in the simulation. Growth rate values are in c/R_j units. *: Models where non regular growth affects the evolution (see text).	117

3.5 Growth of resonant modes. Models with maximum growth rate (according to the linear analysis) for all resonant modes (i.e., at any wavelength) above the growth rates of the perturbed modes are listed. $w_{i,max}$: maximum growth rate for all resonant modes from linear analysis; $w_{i,p,v_{\perp}}$: fitted growth rates of pressure and perpendicular velocity perturbations for the fast growth linear regime in the simulation, only for those simulations where it occurs; $w_{i,\parallel}$: same as $w_{i,p,v_{\perp}}$ for axial velocity. All values are in c/R_j units. 121

3.6 Times for the different phases in the evolution of the perturbed jet models. t_{lin} : end of linear phase (the amplitudes of the different quantities are not constant any longer). t_{sat} : end of saturation phase (the amplitude of the transverse speed perturbation reaches its maximum). t_{mix} : the tracer starts to spread. t_{peak} : the peak in the amplitude of the pressure perturbation is reached. t_{mex} : the jet has transferred to the ambient a 1% of its initial momentum. Δ_{peak} : relative value of pressure oscillation amplitude at the peak (see Figs. 3.23-3.27). 124

4.1 Identified wavelengths, modes and their amplitudes and relative phases from observations (LZ01). φ stands for the relative phase, and P1 P2 stand for both found helices (see text). H stands for helical, E for elliptical modes, and subscripts refer to surface (s , fundamental) or body modes (b , reflection). The latter are followed by the index identifying the exact body mode. 163

4.2 Jet parameters from the fit. γ_j is Lorentz factor, M_j is Mach number, η is rest mass density ratio, ϕ_j is jet half opening angle, θ_j is jet viewing angle, $c_{s,j,a}$ are sound speeds, and pc/mas is the projected linear scale. 163

4.3 First two columns give identified wavelengths and modes in LZ01 (H stands for helical, E for elliptical, s for surface mode and $b1$ and $b2$ for first and second body modes, respectively), third column gives the intrinsic wavelengths (see text), in the fourth column we have written observed wavelengths in the simulation, and the last three columns give the fourth column wavelengths as observed depending on the wave speed. ^a Computed assuming it propagates with the flow speed. 167

4.4	Relevant parameters (to be used in equations (4.1) and (4.2)) from Hardee et al. (1998) and Harde (2000). (H00) stands for the parameters of simulations B and C in Hardee (2000). . . .	169
4.5	Comparison of characteristic wavelengths of pinching surface and first three body modes, computed from equations (4.1) and (4.2) (first number), and those taken from the dispersion relation solution (second number) in Hardee et al. (1998). All wavelengths are in R_j units.	169
4.6	Comparison of characteristic wavelengths of helical and elliptic surface and first body modes, computed from equations (4.1) and (4.2) (first number), and those taken from the dispersion relation solution (second number) in Hardee et al. (2000). All wavelengths are in R_j units.	170
4.7	First column gives the observed wavelengths in the simulation, and the last three columns give this wavelengths as observed depending on the wave speed. We have used, for the wave speed, the underlying flow speed (second column), the maximum speed from the components (third column), and the corresponding speed to injection Lorentz factor ($\gamma = 5.$, fourth column). . . .	172
4.8	Table 1 in LB02b, where the ambient parameters are given (see text).	181
4.9	Parameters in the simulation. Different units are used in order to make comparisons with other works easier (see text). ¹ and ² stand for values at the injection and most external points in the grid, respectively, for the ambient medium.	183